

OPTICAL SYSTEMS FOR SOFT X RAYS

OPTICAL SYSTEMS FOR SOFT X RAYS

Alan G. Michette

*King's College
London, England*

PLENUM PRESS • NEW YORK AND LONDON

Library of Congress Cataloging in Publication Data

Michette, Alan G.

Optical systems for soft X rays.

Bibliography: p.

Includes index.

1. Grenz rays. 2. Optics. I. Title. [DNLM: 1. Optics. 2. Microscopy, Electron—instrumentation. 3. Radiation, Ionizing. QH 212.X2 M6230]

QC482.G68M53 1986 539.7'222 86-20446

ISBN-13: 978-1-4612-9304-0 e-ISBN-13: 978-1-4613-2223-8

DOI: 10.1007/978-1-4613-2223-8

© 1986 Plenum Press, New York
Softcover reprint of the hardcover 1st edition 1986
A Division of Plenum Publishing Corporation
233 Spring Street, New York, N.Y. 10013

All rights reserved

No part of this book may be reproduced, stored in a retrieval system, or transmitted in any form or by any means, electronic, mechanical, photocopying, microfilming, recording, or otherwise, without written permission from the Publisher

Preface

A fundamental problem in cell biology is the cause of aging. The solution to this problem has not yet been obtained because,⁽¹⁾ until recently, it was not possible to image living cells directly. The use of low-energy (soft) X rays has made such imaging possible, perhaps thereby allowing the aging process to be understood and possibly overcome (a result that may well generate further social, moral, and ethical problems). Fortunately this is not the only aspect of cell biology amenable to soft X-ray imaging, and it is envisaged that many less controversial studies—such as investigations of the detailed differences between healthy and diseased or malignant cells (in their natural states) and processes of cell division and growth—will be made possible. The use of soft X rays is not limited to biological studies—many applications are possible in, for example, fusion research, materials science, and astronomy. Such studies have only recently begun in earnest because several difficulties had to be overcome, major among these being the lack (for some purposes) of sufficiently intense sources, and the technological difficulties associated with making efficient optical systems. As is well known, the advent of dedicated synchrotron radiation sources, in particular, has alleviated the first of these difficulties, not just for the soft X-ray region. It is the purpose of this book to consider progress in the second. As well as discussing the optical properties of systems suitable for soft X rays, this book will address other fields of physics, such as thin-film phenomena and microlithographic processes, and it is hoped that the material presented will be understandable to those without specialized knowledge in these fields. Familiarity with standard optics and optical terminology will be assumed.

Many of the properties of suitable focusing devices—in particular those of diffraction gratings^(2,3)—have been covered in detail elsewhere and will only be discussed briefly here, for the sake of completeness. The topics discussed in more detail reflect, in many respects, the author's

particular interests in zone plate imaging and X-ray microscopy systems. In such rapidly advancing fields as soft X-ray physics and optics, it is impossible to cover all recent developments, and I apologize to anyone whose work has, unwittingly, been left unmentioned.

I must thank the many people who helped during the preparation of this book, even though many of them did so inadvertently. In particular, acknowledgments are due to my colleagues on the X-ray microscopy project at King's College, London, and the Daresbury Laboratory, especially Professor R. E. Burge and Professor P. J. Duke. The discussions in Chapters 8 and 9 on the properties of amplitude zone plates, and in Chapter 10 on zone plate optics for X-ray microscopy are largely based on the work Dr. M. J. Simpson did, under my supervision, for his doctoral thesis,⁽⁴⁾ and I am extremely grateful to him for allowing me to reproduce it here. It would have been impossible to complete this book without the support of my family, in particular my wife Margaret, and I look forward to being able to spend more time with them.

Alan G. Michette

Cumnor (Oxford) and King's College, London

Contents

1. Properties of Soft X Rays	1
1.1. Introduction	1
1.2. Interaction of Soft X Rays with Matter	3
1.3. Sources of Soft X Rays	7
1.4. Detectors of Soft X Rays	27
1.5. General Features of Soft X-Ray Optics	28
2. Reflective Optics for Soft X Rays I. Grazing Incidence	37
2.1. Total External Reflection	37
2.2. Focusing with Spherical Mirrors at Grazing Incidence . .	53
2.3. Focusing at Grazing Incidence with Single Aspheric Reflectors	57
2.4. Compound Systems	58
2.5. Resolution of Grazing Incidence Systems	65
3. Manufacture of Grazing Incidence Reflective Optics	67
3.1. Manufacturing Tolerances	67
3.2. Manufacturing Techniques	72
3.3. Metrology of Grazing Incidence Optical Components . .	89
4. Reflective Optics for Soft X Rays II. Multilayer Mirrors	95
4.1. Reflection of Soft X Rays by Multilayer Mirrors	96
4.2. Focusing with Multilayer Mirrors	110

5. Manufacture of Multilayer Mirrors	111
5.1. Manufacturing Tolerances	111
5.2. Manufacturing Techniques	117
6. Diffractive Optics I. Diffraction Gratings	127
6.1. Introduction	127
6.2. Plane Linear Gratings	127
6.3. Concave Spherical Gratings	131
6.4. Aspheric Gratings	139
7. The Design and Manufacture of X-Ray Diffraction Gratings . . .	147
7.1. Manufacturing Tolerances and Types of Grating	147
7.2. Manufacturing Techniques	157
8. Diffractive Optics II. Zone Plates	165
8.1. Fresnel and Soret Amplitude Zone Plates	165
8.2. Improvement of Image Quality—Modified Amplitude Zone Plates	188
8.3. Other Types of Modified Amplitude Zone Plate	203
8.4. Gabor Zone Plates	205
8.5. Phase-Modulating Zone Plates	207
9. Manufacture of Zone Plates	217
9.1. Manufacturing Tolerances	217
9.2. Manufacturing Techniques	224
9.3. Stability of Zone Plates	240
10. Applications of Soft X-Ray Focusing Systems	243
10.1. Introduction	243
10.2. Synchrotron Radiation Beam Lines and Monochromators	243
10.3. Small-Angle X-Ray Scattering	254
10.4. X-Ray Microscopy	254
10.5. Imaging of Laser Fusion Plasmas	269
10.6. X-Ray Astronomy	274
10.7. X-Ray Spectroscopy	282

11. Future Developments	283
11.1. Introduction	283
11.2. Sources of Soft X Rays	283
11.3. New Developments in Soft X-Ray Optics	285
11.4. New Uses of Soft X Rays	292
11.5. Conclusions	298
REFERENCES	299
INDEX.	321

Properties of Soft X Rays

1.1. Introduction

Whenever technological advances have enabled the formation of images using either new energy regimes of electromagnetic radiation or different types of radiation, outstanding, sometimes revolutionary, scientific progress has been made. Examples of this are the use of radio waves and, more recently, infrared radiation in astronomy, and the use of electrons (via electron microscopy) in the biological sciences.

Image formation usually implies some form of focusing. How this focusing occurs depends on the way in which the radiation interacts with its surroundings. Thus for visible light the well-known laws of reflection and refraction are utilized, while electrons are caused to travel in curved paths in electromagnetic fields. Low-energy (soft) X rays interact with matter in three ways (each causing attenuation of the X-ray beam)—elastic scattering, inelastic scattering, and absorption via the photoelectric effect.

Elastic scattering (in which exchange of energy is involved) is caused by two processes—Thomson scattering from single atomic electrons that may be considered as free in the low-energy limit, and Rayleigh (or coherent) scattering, which occurs from strongly bound electrons acting cooperatively. The scattered and incident beams have a definite phase relationship and interference can occur (Bragg diffraction). Inelastic, incoherent, or Compton scattering occurs from loosely bound (essentially free) electrons and involves the transfer of a small fraction of the energy of an incident X-ray photon. The scattered and incident beams do not have fixed phase relationships, and the atom is raised to a different quantum state due to the excitation of the electron. Absorption (through the photoelectric effect) occurs when the X-ray photon transfers all its energy to an inner atomic electron, thereby releasing it from the atom (ionization).

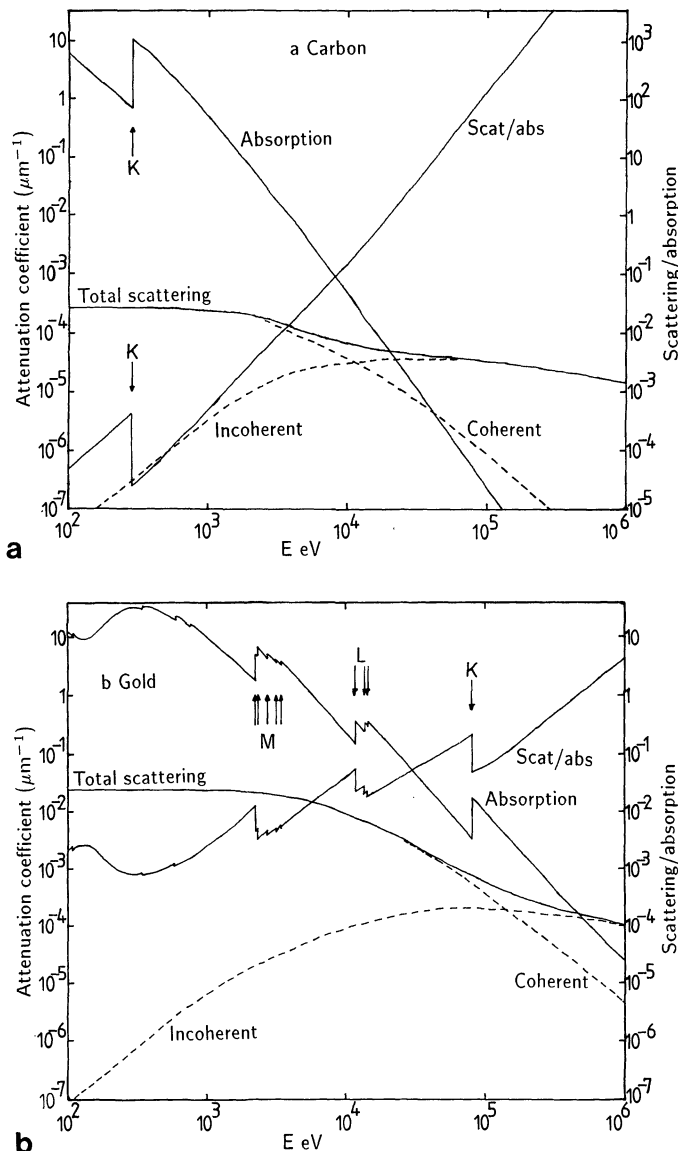


Figure 1.1. Linear attenuation coefficients for scattering and absorption of soft X rays in (a) carbon and (b) gold.

In Figure 1.1 the linear attenuation coefficient for these processes are plotted as functions of energy for two materials, carbon and gold, important in soft X-ray physics. For the soft X-ray regime, which may loosely be defined as the energy range from 100 to 2000 eV, incoherent scattering is completely negligible while coherent scattering contributes less than 1% to the total X-ray attenuation. Thus the dominant process in

the energy range of interest is X-ray absorption and it is this that determines the types of optics (mirrors, gratings, and zone plates) used for focusing.

Until recently, focusing of soft X rays was not of experimental interest because sources of sufficient intensity to be widely useful were not available. However, with the commissioning of several dedicated synchrotron sources, and the introduction of laser plasma sources, this is no longer the case and the necessary technological advances to enable the utilization of intense soft X-ray beams are being, and in some cases have been, made.

1.2. Interaction of Soft X Rays with Matter

When a beam of electromagnetic radiation passes through a material, the intensity is exponentially attenuated,

$$I = I_0 \exp(-\alpha x) \quad (1.1)$$

where x is the thickness of the material, α is the linear attenuation coefficient, and I_0 is the intensity at $x = 0$. The amplitude of the electromagnetic wave at x is

$$A = A_0 \exp(-2\pi\beta x/\lambda) \exp[-2\pi i(nx - ct)/\lambda] \quad (1.2)$$

where λ is the vacuum wavelength of the radiation, n is the refractive index of the material, and β is its absorption coefficient. The complex refractive index of the material, which governs the propagation of the electromagnetic wave, is

$$\tilde{n} = n - i\beta \quad (1.3)$$

Since, at soft X-ray wavelengths, absorption is the dominant process, α may be identified with a linear absorption coefficient, where

$$\alpha = 4\pi\beta/\lambda \quad (1.4)$$

Tabulations of X-ray absorption data usually give the mass absorption coefficient μ , where

$$\alpha = \mu\rho \quad (1.5)$$

and ρ is the density of the material. The mass absorption coefficient of a

compound is given by

$$\mu_{\text{com}} = \sum_j w_j \mu_j \quad (1.6)$$

where w_j is the weight fraction of the constituent with mass absorption coefficient μ_j . The linear absorption coefficient of the compound is then

$$\alpha_{\text{com}} = \mu_{\text{com}} \rho_{\text{com}} \quad (1.7)$$

where ρ_{com} is the density of the compound.

In the soft X-ray region, the energies of individual photons are much larger than the binding energies of outer atomic electrons (typically a few electron volts) and molecular binding energies. Absorbing atoms are therefore ionized by the radiation and most of the energy is transferred to the kinetic energy of the ejected electron. The energy of an X-ray photon may only be absorbed by an atomic electron in a particular atomic state if it is high enough to remove the electron from that state. Thus, as the X-ray energy increases, the absorption coefficient will undergo several relatively sharp increases (absorption edges) at energies corresponding to the binding energies of different atomic levels, as shown in Figure 1.1. In practice these increases are not so sharp as indicated, because of the finite energy widths of atomic states and because of the environment of the absorbing atoms.

There appears to be no standard nomenclature for the labeling of X-ray absorption edges and spectral lines. Although this is not important for the studies considered here, for definiteness the following notation will be used. The series $K, L, M \dots$ arise when an electron is removed from the level with principal quantum number $n = 1, 2, 3 \dots$. For $n > 1$ the energy levels corresponding to each principal quantum number are in general split according to their angular momentum values and are labeled $L_1, L_2, L_3, M_1, M_2, M_3 \dots$. The strongest unsplit line in each series (usually $n = 2 \rightarrow n = 1$) is then given the subscript α , the next strongest β , and so on. Under high resolution, these lines may be split into $\alpha_1, \alpha_2, \beta_1, \beta_2$, and so on. In many cases this nomenclature is largely historical and may seem arbitrary. A typical scheme is shown in Figure 1.2 (after Agarwal⁽¹⁾).

The theoretical treatment of X-ray scattering and absorption has been given in detail by many authors.⁽¹⁻³⁾ A brief summary is included here because the results have implications for the design of soft X-ray optical systems. The starting point of the calculations is to consider the scattering of X rays by free electrons (Thomson scattering). An electromagnetic wave whose electric vector has amplitude A_0 causes such an

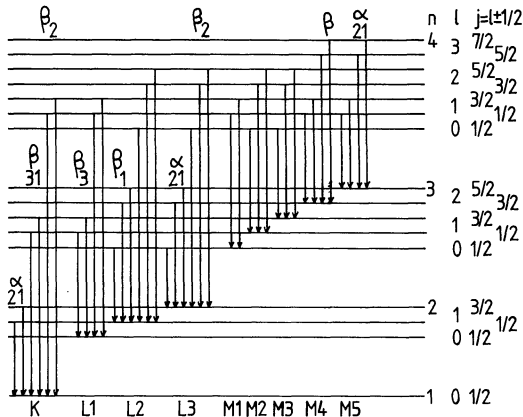


Figure 1.2. Schematic diagram of X-ray transitions for a one-valence electron atom. The transitions are governed by the selection rules $\Delta n \neq 0$, $\Delta l = \pm 1$, and $\Delta j = 0, \pm 1$ ($0 \rightarrow 0$ forbidden).

electron (of charge e and mass m_e) to be accelerated by an amount $A_0(e/m_e)$. Accelerated charges radiate, the amplitude of the electric vector at a distance r from the charge being⁽⁴⁾

$$A_T(\phi) = (e/4\pi\epsilon_0 c^2 r) a \sin \phi$$

where ϕ is the angle between the direction \mathbf{r} and the acceleration \mathbf{a} . Thus

$$A_T(\phi) = A_0(e^2/4\pi\epsilon_0 m_e c^2 r) \sin \phi \quad (1.9)$$

To describe the interaction of an electromagnetic wave with an electron bound in an atom, the Thomson amplitude $A_T(\phi)$ is multiplied by a complex atomic scattering factor $f_1 + if_2$, so that the scattered amplitude is given by

$$A(\phi, E) = A_T(\phi)[f_1(E) + if_2(E)] \quad (1.10)$$

where the factors f_1 and f_2 depend on the energy E of the incoming radiation but it is assumed that, to a first approximation, they do not depend on the scattering angle θ (i.e., the angle between the incoming and scattered radiation). This assumption is valid since the wavelengths of interest ($\sim 1-10$ nm) are large compared to typical dimensions of the atomic electron distribution ($\sim 1-50$ pm) so that the atomic electrons may be considered to scatter in phase. The factors f_1 and f_2 can be calculated in relativistic quantum dispersion theory^(5,6) and are given by

$$f_1(E) = Z + 4(\epsilon_0 m_e c / h e^2) \int_0^\infty [W^2 \sigma(W) / (E^2 - W^2)] dW - \Delta_{\text{rel}} \quad (1.11)$$

and

$$f_2(E) = 2(\epsilon_0 m_e c / h) E \sigma(E) \quad (1.12)$$

The first term in equation (1.11) describes Thomson scattering (Z is the atomic number of the scatterer) and, to describe the angular dependence of the scattering, may be replaced by the angle-dependent form factor⁽⁷⁾

$$f_0 = \int_0^{\infty} U(r) \operatorname{sinc} [(4\pi r/\lambda) \sin(\theta/2)] dr \quad (1.13)$$

where $U(r)$ is the radial charge distribution and $\operatorname{sinc}(x) = \sin(x)/x$. If the wavelength λ is in nanometers, then for $\sin(\theta/2) \leq 0.5\lambda$, $f_0 \approx Z$, while for $\sin(\theta/2) = \lambda$, $f_0 \approx 0.9Z$ for most elements.

The second term in equation (1.11), the anomalous dispersion integral, is the same as that given semiclassically by considering the electrons to be caused to oscillate by the incoming radiation. Because it neglects damping, this term results in imprecise values for f_1 close to absorption edges. The atomic photoionization cross section $\sigma(E)$ (in $\text{m}^2 \text{ atom}^{-1}$) is related to the mass absorption coefficient by

$$\sigma(E) = A\mu/N_0 \quad (1.14)$$

where A is the atomic weight and N_0 is Avogadro's number. In order to calculate $\sigma(E)$ theoretically the atomic wavefunctions must be known; these have to be obtained by approximation methods⁽⁸⁾ for all systems except hydrogen, leading to uncertainties in the expressions for f_1 and f_2 .

The third term in equation (1.11) is a relativistic correction, which is negligible at soft X-ray energies⁽³⁾ (except near absorption edges when f_1 is close to zero). It is given by⁽⁵⁾

$$\Delta_{\text{rel}} = (5/3)(|E_{\text{tot}}|/m_e c^2) + (Z/2)(E/m_e c^2)^2 \quad (1.15)$$

where $|E_{\text{tot}}|$ is the total (negative) energy of the atom. Most calculations of f_1 at low energies ignore this term.⁽³⁾

When considering photoabsorption by inner atomic energy levels in solids, it is a reasonable approximation (except near absorption edges) to assume that the solid state environment does not greatly affect the ionization process, since it is the outer atomic levels that are most modified when an atom is bound in a solid.⁽⁸⁾ Then, the atomic parameters f_1 and f_2 may be related to the macroscopic factors n and β by

$$\delta = 1 - n = (e^2 \hbar^2 / 2\epsilon_0 m_e E^2) \tilde{f}_1 \quad (1.16)$$

and

$$\beta = (e^2 \hbar^2 / 2 \epsilon_0 m_e E^2) \bar{f}_2 \quad (1.17)$$

where \bar{f}_1 and \bar{f}_2 are the average atomic scattering factors per unit volume,

$$\bar{f}_1 = \sum_j N_j f_{1j}, \quad \bar{f}_2 = \sum_j N_j f_{2j} \quad (1.18)$$

and N_j is the number of atoms of type j per unit volume. For energies well away from any absorption edges, equation (1.16) reduces to

$$\delta = (Ne^2 \hbar^2 / 2 \epsilon_0 m_e E^2) = (Ne^2 \lambda^2 / 8\pi^2 \epsilon_0 m_e c^2) \quad (1.19)$$

where N is the total number of electrons per unit volume. This equation, (1.19), is the same as that originally derived by Lorentz using classical ideas of absorption.⁽⁹⁾ In the soft X-ray region, δ is small (typically $\sim 10^{-3}$) and positive, i.e., the refractive index for soft X rays is slightly less than unity. Tables of values for f_1 and f_2 have been published,⁽¹⁰⁾ and these were used to generate Figure 1.1, along with the experimentally observed variation of the absorption coefficient away from an absorption edge:

$$\beta \sim Z^2 \lambda^3 \quad (1.20)$$

1.3. Sources of Soft X Rays

Soft X rays are produced in two types of process. The first is by emission from an atom or ion when an electron loses energy in the form of an X-ray photon when transferring from one atomic energy level to a lower level (from which an electron has previously been removed by some process such as photoionization). This gives a discrete line spectrum; examples are emission induced by electron bombardment of a low-atomic-number target and emission from a plasma formed from a low-atomic-number material. The second type of process is the acceleration of charged particles, usually electrons. This gives a continuous spectrum; examples are emission from electrons decelerated by bombarding a high-atomic-number target and emission from relativistic electrons constrained to travel in curved (essentially circular) paths by magnetic fields (synchrotron radiation). The latter is perhaps the most important laboratory source of soft X rays (it certainly gives the highest average intensity) and is also an important astrophysical source.

1.3.1. Synchrotron Radiation

It is a well-known result of classical physics that electrically charged particles emit electromagnetic radiation when they are accelerated. A magnetic field applied perpendicularly to the direction of motion of a charged particle causes it to move in a circular path, i.e., it is centripetally accelerated and so it emits radiation (in general the motion will be helical due to a component of velocity along the field direction). For a nonrelativistic particle (assumed to be instantaneously at rest), the radiation emitted into a solid angle $d\Omega$ about \mathbf{r} is

$$\frac{dP}{d\Omega}(\phi) = (e^2 a^2 \sin^2 \phi / 16\pi^2 \epsilon_0 c^3) \quad (1.21)$$

where ϕ is the angle between the acceleration \mathbf{a} and \mathbf{r} . The radiation is therefore emitted symmetrically about the axis of acceleration, as shown in Figure 1.3 (Larmor pattern). In order to obtain the radiation pattern for relativistic particles, a Lorentz boost is applied to equation (1.21) along the direction of instantaneous velocity \mathbf{v} . This gives

$$\begin{aligned} \frac{dP}{d\Omega}(\theta, \psi) &= \frac{e^2 a^2}{16\pi^2 \epsilon_0 c^3} \cdot \frac{1}{[1 - (v/c) \cos \theta]^3} \\ &\times \left\{ 1 - \frac{\sin^2 \theta \cos^2 \psi}{\gamma^2 [1 - (v/c) \cos \theta]^2} \right\} \end{aligned} \quad (1.22)$$

where θ is the angle between \mathbf{v} and \mathbf{r} and ψ is the angle between \mathbf{a} and the projection of \mathbf{r} onto the plane containing \mathbf{a} (see Figure 1.4), such that

$$\sin^2 \phi = 1 - \sin^2 \theta \cos^2 \psi \quad (1.23)$$

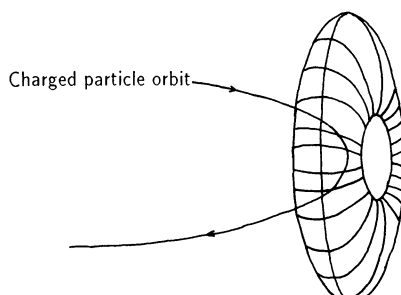


Figure 1.3. Radiation (Larmor) pattern for a centripetally accelerated nonrelativistic charged particle.

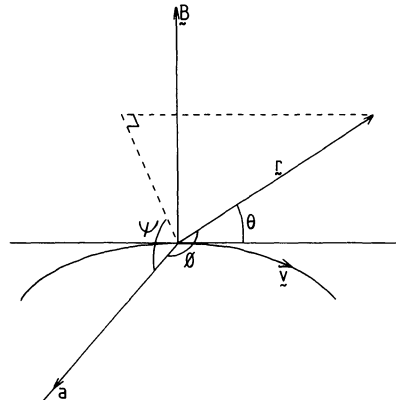


Figure 1.4. Definition of angles for the radiation pattern of a centripetally accelerated relativistic charged particle.

The relativistic factor γ in equation (1.22) is, as usual,

$$\gamma = (1 - v^2/c^2)^{-1/2} = E/m_0 c^2 \quad (1.24)$$

where E is the total energy and m_0 is the rest mass of the particle.

The expression (1.22) indicates some of the properties of synchrotron radiation. The radiation is peaked for small values of $[1 - (v/c) \cos \theta]$, i.e., in the direction of motion ($\theta = 0$), with

$$\frac{dP}{d\Omega}(0, \psi) = \frac{e^2 a^2}{16\pi^2 \epsilon_0 c^3} \cdot \frac{1}{(1 - v/c)^3} \quad (1.25)$$

Since θ is typically small, the approximations $\cos \theta \approx 1 - \theta^2/2$, and $\sin^2 \theta \approx \theta^2$ may be made in equation (1.22). Using also $v/c = (1 - 1/\gamma^2)^{1/2} \approx 1 - 1/2\gamma^2$ leads to

$$\frac{dP}{d\Omega}(\theta, \psi) \approx \frac{e^2 a^2}{2\pi^2 \epsilon_0 c^3} \cdot \frac{\gamma^6}{(1 + \gamma^2 \theta^2)^3} \cdot \left[1 - \frac{4\gamma^2 \theta^2 \cos^2 \psi}{(1 + \gamma^2 \theta^2)^2} \right] \quad (1.26)$$

This can be shown to be equal to half the value at $\theta = 0$ when

$$\theta = [(3 - \cos^2 \psi)/6]^{1/2}/\gamma \approx (4/9)^{1/2}/\gamma \approx 1/\gamma \quad (1.27)$$

for the average value (1/3) of $\cos^2 \psi$. Thus

$$\Delta\theta = 1/\gamma = m_0 c^2/E \quad (1.28)$$

is a measure of the angular divergence of the radiation. For relativistic

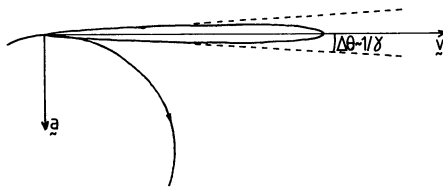


Figure 1.5. Angular distribution of synchrotron radiation.

particles, therefore, the radiation is concentrated in a very narrow cone about the forward direction (Figure 1.5).

The total power radiated in one revolution is found by integrating equation (1.22) over all angles ($0 \leq \psi \leq 2\pi$, $0 \leq \theta \leq \pi$), giving

$$P = (e^2 a^2 / 6\pi \epsilon_0 c^3) \gamma^4 = (e^2 a^2 / 6\pi \epsilon_0 c^3) (E/m_0 c^2)^4 \quad (1.29)$$

This shows that the total energy loss in one orbit is proportional to the fourth power of the particle energy, i.e., it is much greater for high energies, and inversely proportional to the fourth power of the rest mass. Thus the rate of energy loss is much higher for light particles: synchrotron radiation is usually only significant for electrons and positrons.

The relativistic gyrofrequency of an orbiting particle in a magnetic field of strength B perpendicular to the particle velocity is

$$\nu_g = eB / 2\pi \gamma m_0 \quad (1.30)$$

Relativistic time dilation means that to an observer, the particle will appear to return to the same point in its orbit at a time interval corresponding to a frequency

$$\nu_B = \gamma^3 \nu_g = \gamma^2 eB / 2\pi m_0 \quad (1.31)$$

This is the frequency at which a pulse of radiation, of angular width $1/\gamma$, will be observed. The Fourier components of this pulse give the frequency spectrum of synchrotron radiation; since $\gamma \gg 1$ the harmonics involved are very large multiples of ν_g and the spectrum merges into a continuum. The energy radiated by a relativistic electron of energy E over the frequency range ν to $\nu + d\nu$ in one turn is⁽¹¹⁻¹³⁾

$$I(\nu, E) d\nu = \frac{\sqrt{3} e^3 B}{15\pi^2 \epsilon_0 m_0 c^2} [(\nu/\nu_c) \int_{\nu/\nu_c}^{\infty} K_{5/3}(\eta) d\eta] d\nu \quad (1.32)$$

where the “critical frequency” ν_c is defined by

$$\nu_c = (3/2)\nu_B = 3\gamma^2 eB/4\pi m_0 \quad (1.33)$$

Half the total power is emitted at wavelengths less than $\lambda_c (=c/\nu_c)$ and half at longer wavelengths. The modified Bessel function $K_{5/3}(\eta)$ is defined by

$$K_{5/3}(\eta) = -2 \frac{d}{d\eta} [K_{2/3}(\eta)] - K_{1/3}(\eta) \quad (1.34)$$

$$K_{2/3}(\eta) = -\left(\frac{d}{d\eta} + \frac{1}{3\eta}\right) K_{1/3}(\eta) \quad (1.35)$$

and

$$K_{1/3}(\eta) = \sqrt{3} \int_0^\infty \cos [(3/2)\eta(x + x^3/3)] dx \quad (1.36)$$

Synchrotron radiation is polarized with components⁽¹⁴⁾

$$I_\perp(\nu, E)d\nu = \frac{\sqrt{3}e^3 B}{32\pi^2 \epsilon_0 m_0 c^2} \left[(\nu/\nu_c) \int_{\nu/\nu_c}^\infty K_{5/3}(\eta) d\eta + K_{2/3}(\nu/\nu_c) \right] d\nu \quad (1.37)$$

$$I_\parallel(\nu, E)d\nu = \frac{\sqrt{3}e^3 B}{32\pi^2 \epsilon_0 m_0 c^2} \left[(\nu/\nu_c) \int_{\nu/\nu_c}^\infty K_{5/3}(\eta) d\eta - K_{2/3}(\nu/\nu_c) \right] d\nu \quad (1.38)$$

perpendicular and parallel to the magnetic field direction. Equations (1.32), (1.33), (1.37), and (1.38) may be generalized to the case in which the field is not perpendicular to the electron motion by considering B to be the component of the field in that direction.

The radiated energy $I(\nu, E)$ is shown as a function of ν/ν_c in Figure 1.6. This clearly shows the very large spectral range of synchrotron radiation, with peak emission at $\nu = 0.3\nu_c$. The asymptotic variation goes as $(\nu/\nu_c)^{1/3}$ for $\nu \leq 0.01\nu_c$, and $(\nu/\nu_c)^{1/2} \exp(-\nu/\nu_c)$ for $\nu \geq 10\nu_c$. The two components $I_\perp(\nu, E)$ and $I_\parallel(\nu, E)$ are shown in Figure 1.7 as functions of $\gamma\psi$ (the factor γ makes the curves universal). These plots show that the radiation is elliptically polarized, except in the orbital plane when it is 100% linearly polarized.

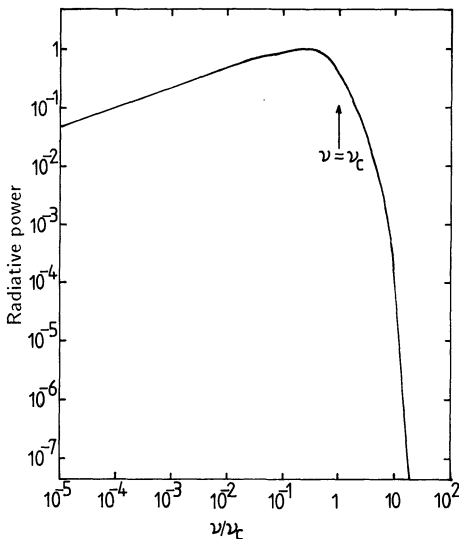


Figure 1.6. Spectral distribution of synchrotron radiation.

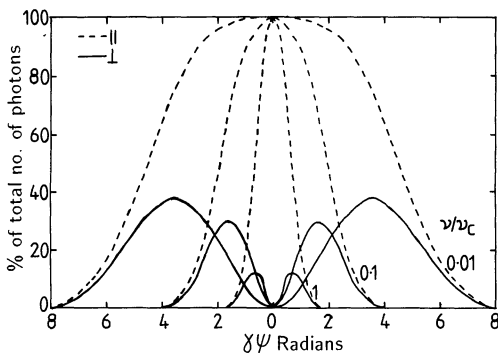


Figure 1.7. Angular distribution of the polarized components of synchrotron radiation.

1.3.1.1. Synchrotron Radiation Sources

Because of the mass dependence of synchrotron emission, equation (1.29), purpose-built synchrotron sources invariably use circulating beams of electrons. Sources are characterized by their critical frequencies, from equation (1.33),

$$\nu_c = 1.608 \times 10^{17} E^2 B \text{ Hz} \quad (1.39)$$

or their corresponding critical wavelengths

$$\lambda_c = 1.864/E^2 B \text{ nm} \quad (1.40)$$

where the electron energy E is in giga-electron volts and the magnetic flux density B is in teslas. If the radius of the electron orbit is R , then

$$R = (E^2 - m_0^2 c^4)^{1/2} / eBc = E/eBc \quad (\text{for } E \gg m_0 c^2) \quad (1.41)$$

and

$$\lambda_c = 0.559RE^{-3} \text{ nm} \quad (1.42)$$

with R in meters.

The electrons are kept in their orbit by series of bending (dipole) and focusing (quadrupole) magnets, the former to give the required orbit radii, from equation (1.41), and the latter to prevent beam divergence. To lessen losses through interactions with residual gas molecules, the beam circulates in an ultrahigh vacuum ($\sim 10^{-9}$ Torr)—typical $1/e$ lifetimes are several hours. The energy loss by synchrotron radiation is replaced in one or more radiofrequency cavities; because these can only accelerate the electrons when the rf field is in the correct direction, the electron beam circulates in a series of bunches. This gives a pulsed structure with typical pulse lengths of 50 psec—1 nsec and spacings 2–20 nsec. The rf cavities are also used to accelerate the electrons to their full energy after injection. This energy is determined primarily by the uses to which the synchrotron radiation is to be put. Magnetic fields of 1.2–1.5 T are optimum for synchrotron radiation⁽¹⁵⁾; thus for a critical

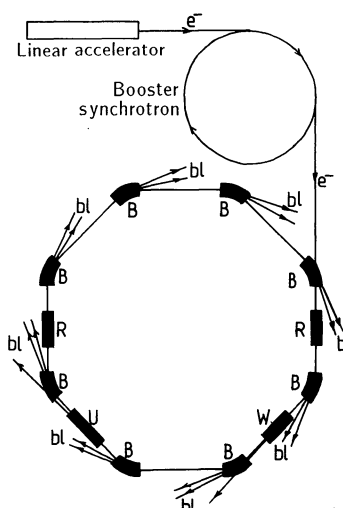


Figure 1.8. A schematic of a synchrotron radiation source. B = bending magnet; bl = beam lines; R = rf cavity; U = undulator; W = wiggler.

Table 1.1. Storage Rings Used in Synchrotron Radiation Research

Name(location)	<i>E</i> (GeV)	<i>B</i> (tesla)	<i>R</i> (m)	<i>I</i> _{max} (mA)	FWHM beam size (H × V, mm × mm)	<i>λ</i> _c (nm)	No. photons sec ⁻¹ mA ⁻¹ mm ⁻² mrad(H) ⁻¹ all vertical angles (4–5 nm) ^a
<i>N100^b</i> (Karkhov)	0.1	0.7	0.5	25		280	
TANTALUS ^b (Wisconsin)	0.24	1.3	0.64	200	0.85 × 0.21	26	3.97×10^{12}
SURF II ^b (NBS)	0.28	1.1	0.83	50	2.4 × 0.94	21	1.27×10^{11}
INS-SOR II ^b (Tokyo)	0.4	1.2	1.1	300	0.8 × 0.2	9.6	3.74×10^{12}
PLAMIA I ^c (Kurchatov)	0.45	1.5	1.0	100	3.8 × 0.31	6.1	1.07×10^{12}
UVSOR ^{c,d} (Okazaki)	0.6	0.9	2.2	500	0.71 × 0.47	5.7	5.32×10^{12}
MAX ^c (Lund)	0.55	1.5	1.2	200	0.2 × 0.5	4.0	2.09×10^{13}
TERAS ^c (Tsukuba)	0.66	1.1	2.0	100		3.9	
ACO ^b (Orsay)	0.55	1.7	1.1	150	1.2 × 1.2	3.7	1.50×10^{12}
ALADDIN ^c (Wisconsin)	0.75	1.2	2.08	500		2.8	
NSLS VUV ^{b,d} (Brookhaven)	0.5	1.3	1.9	150	0.68 × 0.26	2.5	2.05×10^{13}
HESYRL ^c (Hefei, China)	0.8	1.2	2.2	300		2.4	
VEPP-2M ^e (Novosibirsk)	0.67	1.8	1.22	100	2.24 × 0.14	2.3	3.09×10^{12}
BESSY ^b (Berlin)	0.78	1.45	1.78	230	0.45 × 0.45	2.1	1.85×10^{13}
SUPER SOR ^{d,f} (Tokyo)	1.0	0.9	3.66	500		2.05	
SUPER ACO ^{c,d} (Orsay)	0.8	1.5	1.75	500	0.26 × 0.31	2.0	4.87×10^{13}
ADONE ^{e,g} (Frascati)	1.2	0.8	5.0	50		1.6	
SRRC ^{d,f} (Taiwan)	1.0	1.2	2.78	200		1.55	
DUAL RING ^f (Stanford) (or	2.0	0.35	19.1	200		1.33	
COSY ^f (Berlin)	6.0	1.05		100		0.05)	
ESRF VUV ^f	0.56	4.9	0.38	300	0.7 × 0.7	1.2	6.21×10^{12}
SXRL ^c (Stanford)	1.0	1.7	2.0	>100		1.1	
SRS ^{b,h} (Daresbury) [with HBL]	2.0	1.2	5.56	500	12.7 × 0.7	0.39	1.04×10^{12}
DCI ^e (Orsay)					[1.75 × 0.31]		$[1.61 \times 10^{13}]$
IPPF (Moscow)	1.72	1.5	3.82	300		0.42	
VEPP-3 ^e (Novosibirsk)	2.0	1.33	5.0	1000		0.35	
	2.2	1.2	6.15	100		0.32	

Table 1.1. (Continued)

Name (location)	<i>E</i> (GeV)	<i>B</i> (tesla)	<i>R</i> (m)	<i>I</i> _{max} (mA)	FWHM beam size (H × V, mm × mm)	<i>λ</i> _c (nm)	No. photons sec ⁻¹ mA ⁻¹ mm ⁻² mrad (H) ⁻¹ all vertical angles (4–5 nm) ^a
KEK ^{b,g} (Tsukuba)	2.5	1.0	8.66	160	1.28 × 0.43	0.31	1.89×10^{13}
BEPC ^e (Beijing)	2.8	0.9	10.3	66		0.26	
NSLS X-RAY ^{b,d} (Brookhaven)	2.5	1.2	6.88	500	0.25 × 0.1	0.25	4.45×10^{14}
Doris ^e (Hamburg)	3.7	1.0	12.12	70	2 × 1.3	0.13	4.99×10^{12}
SPEAR ^{d,e} (Stanford)	3.0	1.05	12.7	100		0.11	
ESRF ^{b,d,f} (Grenoble)	5.0	0.75	22.36	500	0.17 × 0.11	0.10	8.38×10^{14}
CHESS ⁱ (Ithaca)	5.5	0.6	32	15		0.11	
VEPP-4 ^e (Novosibirsk)	7.0	1.4	16.5	10		0.03	
PEP ^j (Stanford)	15	0.3	165	100		0.03	
IND-I ^f (Pune)	1.5			200			
PLAMIA II ^{b,f} (Kurtchatov)	2.5			3000			
ALS ^{d,f} (LBL)	1.3			400			

^aValues quoted for soft X-ray (or nearest) beam line.

^bDedicated to synchrotron radiation.

^cUnder construction, will be dedicated.

^dSoft X-ray undulator planned.

^ePartly dedicated to synchrotron radiation, or parasitic.

^fProposed.

^gSoft X-ray undulator in operation.

^hSoft X-ray undulator under construction.

ⁱPart time.

^jSynchrotron radiation laboratory planned.

wavelength in the soft X-ray region, the electron energy should be, from equation (1.40), $\sim 0.3\text{--}1.6$ GeV, with bending radii in the range $\sim 0.7\text{--}4.4$ m. Since each bunch radiates independently, synchrotron radiation is temporally incoherent so long as the wavelength of the radiation is smaller than the bunch length. There is, however, some degree of angular coherence.⁽¹⁶⁾

A schematic diagram of a synchrotron radiation source is shown in Figure 1.8. Beam ports at the locations of the bending magnets allow the radiation to be directed along beam lines toward experimental stations. The optical layout of beam lines for soft X rays will be discussed in Chapter 10.

Table 1.1 gives a list of synchrotron sources currently in use, under construction, or proposed, together with an indication of the useful photon flux in the soft X-ray region (at $\lambda = 4.37$ nm). This depends on

the number of stored electrons per unit area,

$$n = 2\pi RI/Aec \quad (1.43)$$

where I is the stored current and A is the cross-sectional area of the beam, as well as on the critical wavelength.

The performance of a synchrotron source as described above is, to a certain extent, characterized by the requirement of keeping the electron beam in a closed orbit. The radiated power at certain wavelengths may be enhanced by causing the beam to deviate from its normal path, in such a way that there is no net deflection, by inserting extra magnets into straight sections of the synchrotron. Such devices are called wigglers and undulators.

1.3.1.2. Wigglers⁽¹³⁾

Wigglers are magnetic structures that, by use of local magnetic fields, cause the electron beam to move in a path with radius of curvature different from that in the bending magnets. Typically, the wiggler field B_w is larger than the bending magnet field, so that the radius of curvature is smaller and the critical wavelength is shifted to lower values. The simplest type of wiggler, three-pole or single-bump, is shown in Figure 1.9. By increasing the number of poles, as shown in Figure 1.10, to give a multipole wiggler, the intensity of radiation may be increased since an experiment can receive radiation from the same point on each of the wiggles. The form of the spectrum is the same as that from a dipole magnet except that, at long wavelengths, interference effects become noticeable. Since λ_c is typically much shorter than for bending magnets, these devices do not offer any advantages for soft X rays.

1.3.1.3. Undulators⁽²³⁾

Increasing the number of poles of a wiggler causes interference effects to become dominant, resulting in a line, rather than a continuous, spectrum. The device is then called an undulator; there are two types. The most common, planar undulators, cause the electrons to oscillate

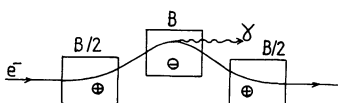


Figure 1.9. A three-pole wiggler.

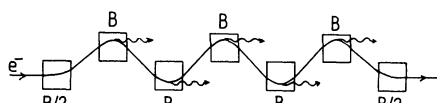


Figure 1.10. A multipole wiggler.

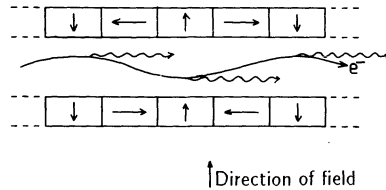


Figure 1.11. A planar undulator.

transversely in a plane (Figure 1.11). Helical undulators cause the electrons to describe a helix about the mean path. The angular deflection of the electron beam is smaller than the natural synchrotron radiation emission angle ($1/\gamma$), and the wavelengths of the quasi-monochromatic lines are given by

$$\lambda_n = (\lambda_0/2n\gamma^2)(1 + K^2/2)[1 + \gamma^2\theta^2/(1 + K^2/2)] \quad (1.44)$$

where θ is the angle of observation from the axis, $n = 1, 3, 5, \dots$ is the order of interference, λ_0 is the magnet period, K is the deflection parameter,

$$K = eB_0\lambda_0/2\pi m_0 c \quad (1.45)$$

and B_0 is the peak field.

The spectral width of the peak emission at $\theta = 0$ is

$$\Delta\lambda/\lambda \sim 1/nN \quad (1.46)$$

where N is the number of undulator periods. A typical undulator spectrum is shown in Figure 1.12. By suitable choice of field and period, spectral lines may be obtained in the desired wavelength range. Thus undulators are suitable sources for soft X rays, and photon fluxes several times higher than those from bending magnets are obtainable. Several of the sources listed in Table 1.1 have working or planned undulators, as indicated.

1.3.2. Nonsynchrotron Sources of Soft X Rays

A major disadvantage of synchrotron sources for many applications is their large size (and cost) so that they are normally multiuser facilities remote from an individual user's base. Smaller (and cheaper) soft X-ray sources, which can more easily be placed in a convenient location, fall into two main categories—solid target sources and plasma sources. There

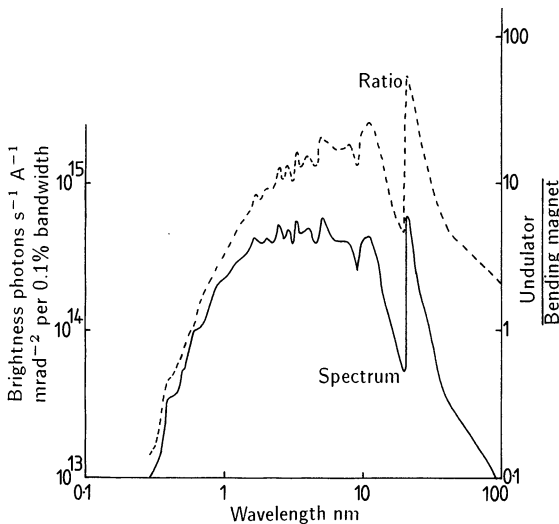


Figure 1.12. The spectral distribution of radiation from the SRS undulator, and a comparison with the ordinary synchrotron radiation spectrum.

are, in addition, some further processes (transition radiation,⁽¹⁷⁾ channeling radiation⁽¹⁸⁾) that cause emission of soft X rays but, as yet, sources utilizing these have not been constructed.

1.3.2.1. Solid-Target Sources

The conventional method of obtaining X rays is to bombard a solid target with a high-energy beam of electrons. This causes X-ray emission in two ways—deceleration of the incident electrons by coulomb interactions with the electrons and nuclei of the material (bremsstrahlung), and removal of an inner-level atomic electron. The former gives a continuous spectrum in a wavelength range characterized by the incident electron energy and the latter gives a line spectrum characterized by the target material.

The bremsstrahlung process may be described in a similar way to synchrotron radiation except that, on average, the acceleration a is against the direction of electron motion rather than perpendicular to it. The radiation emitted into a solid angle $d\Omega$ in the direction θ (relative to the direction of motion) is (for the electron being brought completely to rest)⁽¹⁹⁾

$$\frac{dP}{d\Omega}(\theta) = \frac{e^2 a^2}{64\pi^2 \epsilon_0 c^2} \cdot \frac{\sin^2 \theta}{\cos \theta} \left\{ \frac{1}{[1 - (v/c) \cos \theta]^4} - 1 \right\} \quad (1.47)$$

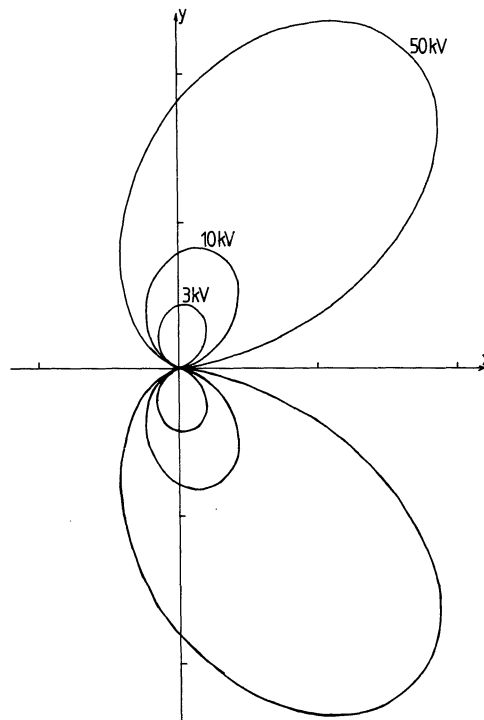


Figure 1.13. The angular distribution of X rays from a solid (electron impact) source.

This shows that there is no radiation directly forwards ($\theta = 0$), but that, as the electron kinetic energy increases, the radiation is emitted more toward the forward direction (Figure 1.13). Experimentally the intensity does not drop to zero at $\theta = 0$; this is because individual electrons may experience a deceleration with a component transverse to the direction of motion. This also affects the polarization; instead of the polarization being completely in the plane of the incident electrons, it is only partial. The shape of the continuous spectrum depends primarily on the kinetic energy T of the incident electrons (with only a small dependence on the nature of the target), with a short-wavelength cutoff

$$\lambda_{\min} = hc/T \quad (1.48)$$

corresponding to an electron losing all its energy in one collision. The more likely process is that the electrons undergo several collisions before coming to rest, resulting in a distribution of X-ray wavelengths given empirically by⁽²⁰⁾

$$I_B(\lambda) = (AcZ/\lambda^2)[c(\lambda - \lambda_{\min})/\lambda\lambda_{\min} + BZ] \quad (1.49)$$

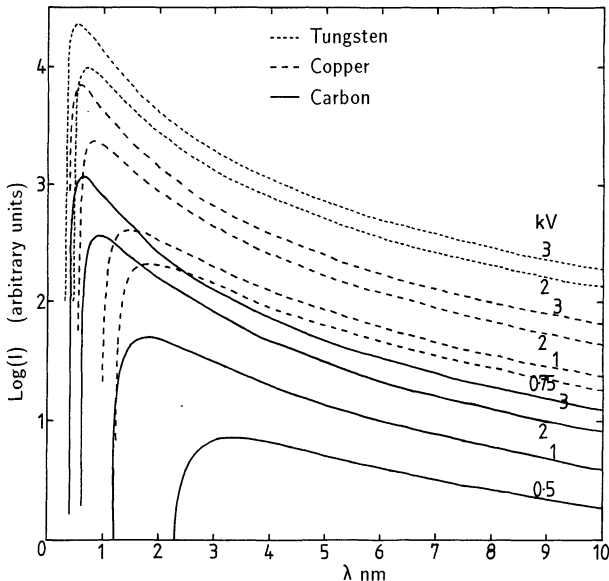


Figure 1.14. The spectral distribution of X rays from solid-target sources.

where A and B are constants and Z is the atomic number of the target material. The wavelength of maximum intensity is given by $dI_B/d\lambda = 0$, i.e., by

$$\lambda_m = (3/2)\lambda_{\min}/[1 + (BZ/c)\lambda_{\min}] \quad (1.50)$$

$$\simeq (3/2)\lambda_{\min} \quad (1.51)$$

if $BZ \ll c(\lambda - \lambda_{\min})/\lambda\lambda_{\min}$. This condition does not hold for small kinetic energies and high atomic numbers, in which case equation (1.49) does not accurately represent the intensity distribution. Even so equation (1.51) may be used to give an idea of the kinetic energies (~ 150 – 3000 eV) needed to give a peak wavelength in the soft X-ray region, and Figure 1.14 shows some calculated intensity distributions for the corresponding accelerating voltages (~ 150 – 3000 V).

The efficiency of conversion of incident electron kinetic energy into continuum X rays is given by⁽²¹⁾

$$\varepsilon = 1.1 \times 10^{-9} ZV \quad (1.52)$$

where V is the accelerating voltage. Thus for a high- Z target (e.g., tungsten, $Z = 74$), operated in the voltage range given above, $\varepsilon \simeq$

0.001–0.025%. The useful efficiency is even lower than this for many applications in which only a small-wavelength range is required.

X-ray line spectra are produced when the vacancy in an inner atomic level (caused in this case by electron impact) is filled by an electron from a higher level losing energy by radiating a photon. Using the nomenclature described in Section 1.1 this results in K_α , $K_\beta \dots$ spectral lines. The energy of an atomic level with principal quantum number n is given by

$$E_n = -hcR(Z - \sigma)^2/n^2 \quad (1.53)$$

where R is Rydberg's constant and σ is the screening parameter, which describes the reduction in the effective nuclear charge experienced by an electron due to the presence of other inner-level electrons. For a K -shell transition, $\sigma \approx 1$ and for an L -shell transition, $\sigma \approx 7.5$. Thus the frequency of, for example, K_α radiation is given by

$$\nu = hcR(Z - \sigma)^2(1/1^2 - 1/2^2)$$

i.e.,

$$\nu = (3/4)cR(Z - \sigma)^2 \quad (1.54)$$

A plot of $\nu^{1/2}$ against Z should therefore be, for a given transition, a straight line (Moseley diagram). This is generally found to be so, apart from small observed deviations (which are not important here) in the K_α series.

An X-ray line cannot appear in the spectrum unless the incident electron kinetic energy is greater than the ionization energy E_I . This is summarized in Table 1.2 for three target materials, carbon, copper, and tungsten. Apart from this, the wavelengths of observed spectral lines are independent of the incident electron kinetic energy, and depend only on

Table 1.2. Ionization Energies for Solid-Target Sources

Target/Z	Ionization energy (keV)								
	K	L1	L2	L3	M1	M2	M3	M4	M5
C/6	0.286								
Cu/29	8.996	1.104	0.955	0.935	0.122	0.078	0.076		0.003
W/74	69.64	12.11	11.56	10.22	2.821	2.574	2.279	1.870	1.807
	N1	N2	N3	N4	N5	N6	N7	O1	O2
	0.590	0.490	0.422	0.254	0.241	0.031	0.029	0.073	0.044
								O3	0.034

the nature of the target. However, the total number of X rays emitted in a particular line increases with increasing kinetic energy. For $T \geq E_l$, the intensity is given approximately by

$$I \sim (T - E_l)^n \quad (1.55)$$

with $n \approx 1.63$. For higher electron kinetic energies the increase falls off due to increasing penetration of the electrons into the target, resulting in increased reabsorption of the X rays in the target. Typically, each incident electron with $T \sim 3E_l$ produces an X-ray photon with a probability of $\sim 10^{-4}$ for low-Z targets and $\sim 10^{-3}$ for high-Z targets.

Most of the electron energy that does not produce X rays is dissipated in the target as heat. In order to obtain large X-ray fluxes, targets have to be cooled or otherwise have the heat dissipated. One way of doing this is to spread the heat load over a larger area by moving (rotating) the target. Even so, to prevent the target melting, the material and the amount of power (the product of electron current and accelerating voltage) are limited. Because the continuum spectrum is produced

Table 1.3. Solid-Target Soft X-Ray Sources

Target/Z	Line	Wavelength	
		λ (nm)	$\Delta\lambda/\lambda$
Al/13	K	0.834	4.5×10^{-4}
Mg/12	K	0.989	5.5×10^{-4}
Na/11	K	1.19	
Zn/30	L	1.23	
Cu/29	L	1.33	
Ni/28	L	1.46	
Co/27	L	1.60	
Fe/26	L	1.76	
F/9	K	1.83	
Mn/25	L	1.94	
Cr/24	L	2.16	
Mn/25	L	2.23	
O/8	K	2.36	
Ti/22	L	2.74	
Ti/22	L	3.14	
N/7	K	3.16	
C/6	K	4.47	
Rh/45	M	4.76	7.3×10^{-2}
W/74	N	5.84	
Mo/42	M	6.44	
B/5	K	6.76	
Nb/41	M	7.24	5.1×10^{-2}
Zr/40	M	8.19	4.3×10^{-2}
Y/39	M	9.38	3.5×10^{-2}

over a fairly wide angular range (Figure 1.13), and because the line spectrum is produced essentially isotropically (neglecting reabsorption in the target material), normally only a small fraction of the X rays produced can be used in focusing systems. The properties of some solid-target soft X-ray sources are summarized in Table 1.3.

1.3.2.2. Plasma Sources

Dense, high-temperature, plasmas emit both continuum radiation (due to bremsstrahlung or to an ion capturing a free electron) and line radiation (due to transitions between the energy levels of an ion). For soft X-ray production, most of the development of such sources has been concentrated on using pulsed lasers to produce the plasma.⁽²²⁻²⁶⁾ However, suitable plasmas have also been produced using electron beams,⁽²⁷⁾ vacuum sparks,⁽²⁸⁾ gas puff Z pinches,⁽²⁹⁾ tokamaks,⁽³⁰⁾ light ion beams,⁽³¹⁾ and imploding wires.⁽³²⁾

It is convenient to discuss laser-produced plasmas in two parts—those generated by relatively low-power ($\leq 10 \text{ J pulse}^{-1}$) lasers available in many laboratories, and those generated by high-power ($\geq 100 \text{ J}$) lasers, which are more likely to be national facilities.

The spectra of “low-power” laser-produced plasmas normally show some evidence of line emission (Figure 1.15). If the plasma is optically thin, the emitted power due to line radiation is⁽³³⁾

$$P_L = 7 \times 10^{-9} N_e N_{zg} T_e^{1/2} \sum_j f_{jz} \exp(-E_j/T_e) \text{ W m}^{-3} \quad (1.56)$$

where N_e is the electron density, N_{zg} is the density of ions of charge z in the ground state, T_e is the kinetic temperature of the electrons in electron volts, f_{jz} is the oscillator strength from the level j to the ground state (i.e., the number of bound electrons in the level j), and $v = E_j/h$ is the frequency of the emitted radiation. In realizable plasmas, P_L is reduced

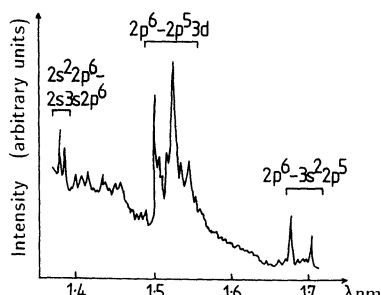


Figure 1.15. The spectral distribution of X rays from a low-power laser plasma source (laser wavelength 1064 nm, iron target, neon-like ions). (After Nagel *et al.*⁽²⁵⁾)

from the value given by equation (1.56) since collisional deexcitation can take place and since the plasma is not optically thin so that reabsorption occurs.⁽³⁴⁾ These effects lead to P_L being reduced by several orders of magnitude.

Under the conditions in which low-power plasmas are produced, the plasma equilibrium is normally intermediate between local thermodynamic equilibrium (LTE) and coronal equilibrium. The plasma is formed by collisional excitation and ionization, and LTE prevails when these processes are balanced by the inverse processes of collisional decay and recombination; while coronal equilibrium holds when they are balanced by line emission and radiative decay. Colombant and Tonon⁽³⁵⁾ have shown that the plasma equilibrium approaches LTE at very low z , while for high z coronal equilibrium is applicable. In the latter case, the emitted power from bremsstrahlung is⁽³³⁾

$$P_B = 1.5 \times 10^{-26} N_e T_e^{1/2} \sum_z N_z z^2 \text{ W m}^{-3} \quad (1.57)$$

where N_z is the density of ions of charge z in all states. The power emitted when ions (of charge $z + 1$) capture electrons (to level j) is

$$P_C = 1.5 \times 10^{-26} N_e T_e^{1/2} \sum_z \sum_j N_z z^2 \psi_{zj} \text{ W m}^{-3} \quad (1.58)$$

where ψ_{zj} is the ionization potential for removal of an electron from the level j .

The conversion efficiency (radiated X-ray energy/input laser energy) is given by

$$\epsilon \approx 4 \times 10^{-5} (P_T/P_B)(A T_e/z)^{1/2} \quad (1.59)$$

where P_T is the total radiated power and A is the atomic weight of the target.

For a particular target and type of laser, equations (1.56)–(1.59) allow predictions to be made about the type and amount of X-ray radiation expected. These agree reasonably well with experiment.⁽³⁴⁾ For example, a 1 J ruby laser focused onto a medium- Z (~ 70) target has $N_e \sim 10^{27} \text{ m}^{-3}$ and $T_e \sim 55 \text{ eV}$ with the most abundant ions having $z \sim 15$, corresponding to $\psi_{zj} \sim 300\text{--}400 \text{ eV}$. Assuming that recombination to the ground state predominates, $P_C \sim 6 P_B$. The continuum is observed to peak at a wavelength of $\sim 11 \text{ nm}$, to be compared to the

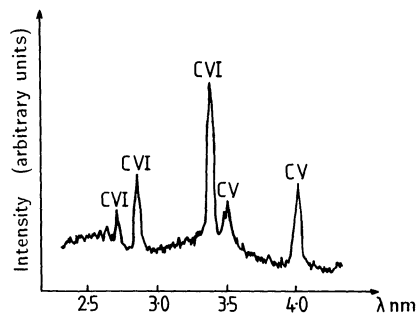


Figure 1.16. The spectral distribution from a high-power laser plasma source (laser wavelength 249 nm, carbon target, hydrogen- and helium-like ions).

bremsstrahlung theoretical peak at $620/T_e$ nm, and the observed conversion efficiency is $\sim 1\%$, while equation (1.59) gives $\sim 0.75\%$.⁽³⁴⁾ Very little line emission is observed, the value of P_L being reduced as discussed above.

Recent work using pulsed (≥ 10 Hz) Nd:YAG lasers, with $\sim 1 \text{ J pulse}^{-1}$, on a variety of targets has shown the feasibility of obtaining both line and continuum emission at reasonable intensities from laser-produced plasmas (Figure 1.15).⁽²⁵⁾

Plasmas produced by low-power lasers emit radiation essentially isotropically. As the laser power increases, some directionality of the radiation is obtained⁽²²⁾—if a disk is illuminated by the laser, the radiation is peaked normal to the disk. Because of the higher power, T_e increases and the bremsstrahlung continuum starts to dominate. Typical spectra are shown in Figures 1.16 and 1.17. Conversion efficiencies are also much higher, typically $\sim 20\text{--}30\%$.⁽²²⁾

The properties of typical laser-produced plasma sources are summarized in Table 1.4, along with those for other types of plasma source.

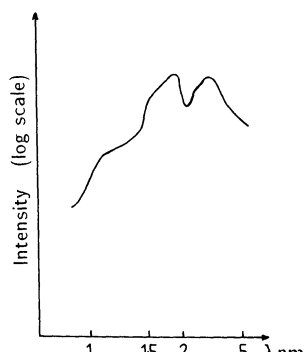


Figure 1.17. The spectral distribution from a high-power laser plasma source (laser wavelength 1064 nm, gold target). (After Slivinsky.⁽²²⁾)

Table 1.4. Plasma Sources of Soft X Rays

Plasma source	Wavelength range (peak emission) (nm)	Comments
Laser plasma ^a		
C target	~2–5	Strong lines at 2.7, 2.85, 3.37 nm (H-like), 3.5, 4.02 nm (He-like)
K, Ar, Cl target	~1–5	Line emission (Ne-like)
Al, Fe target	~6–20	Mainly line
Yb, Sm, etc. target	~4–60	Mainly continuum with weak lines
Electron beam ^b		
C-containing insulator	~2–25	Mainly continuum with weak lines
Z pinch gas puff	~1	Lines characteristic of gas superimposed on continuum

^aOther target materials can be used.^bOther insulators can be used.**Table 1.5.** Comparison of Soft X-Ray Sources

Source	Relative intensity (photons sec ⁻¹ mrad ⁻² in 1% bandwidth)	
	Peak	Average (synchrotron bending magnet = 1)
Synchrotron		
Bending magnet	1	1
Undulator	~10 ³	~10 ³
Solid-target		
Carbon K	≤5 × 10 ⁻¹²	≤5 × 10 ⁻¹¹
Copper L	≤10 ⁻¹⁰	≤10 ⁻⁹
Aluminum K	≤10 ⁻⁹	≤10 ⁻⁸
Laser plasma		
High power ^a	~10	~2 × 10 ⁻¹¹
Low power ^b	~10 ⁻²	~2 × 10 ⁻¹⁰
Electron beam ^c	~10 ⁻⁴	~2 × 10 ⁻¹¹
Gas puff ^d	~ 1	~2 × 10 ⁻⁸

^aLaser energy ~100 J, pulse repetition rate ~10⁻³ Hz.^bLaser energy ~1 J, pulse repetition rate ~10 Hz.^cRepetition rate ~100 Hz.^dRepetition rate ~20 Hz.

1.3.3. Comparison of Sources

Each of the types of source discussed above has certain relative advantages and disadvantages according to how the radiation is to be used. Any comparison between the sources, without considering the application, could therefore be misleading. Since the major part of the present work is to consider focusing of soft X rays, and because such focusing is commonly wavelength dependent, the comparison to be made here concerns the photon flux available for imaging in a 1% bandwidth at the middle of the soft X-ray range. This comparison is made in Table 1.5.

1.4. Detectors of Soft X Rays

Several types of detector are suitable in the soft X-ray range, as discussed in a recent comprehensive review,⁽³⁶⁾ in which detectors are classified as photographic or photoelectric. The former includes photographic film and X-ray resists (polymer lacquers) and the latter includes photoemissive detectors, such as ionization chambers, proportional counters, and microchannel plate arrays, and photoconductive detectors such as scintillation counters and charge-coupled devices. The properties of these are summarized in Figure 1.18 and Table 1.6.

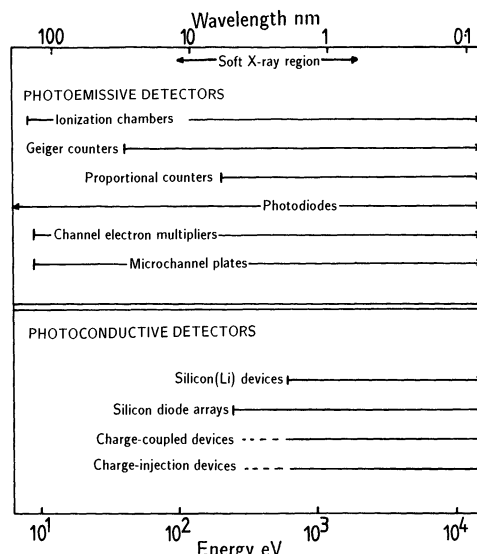


Figure 1.18. Properties and comparison of detectors for soft X rays. (After Timothy and Madden.⁽³⁶⁾)

Table 1.6. Detectors for Soft X Rays

Detector	Wavelength range (nm)	Energy/ spatial/ temporal resolution	Count rate (photons sec ⁻¹)/ gain/ efficiency ^a	Comments
Ionization counter	Whole ^b	-/-/-	$\geq 10^2$ / 1–100/100%	Windowless
Geiger counter	Whole ^b	-/-/25 nsec	$< 10^5$ / $> 10^5$	Window needed
Proportional counter (PC)	≤ 6	10–20%/-/ 25 nsec	$< 10^5$ / 10^3 – 10^5 /~100%	Window needed
Imaging PC	≤ 6	10–20%/ 0.1–0.2 mm/ 25–100 nsec	$< 10^4$ / 10^3 – 10^5 / ~100%	Window needed
Gas-scintillation PC	≤ 6	~10%/ ~2.5 mm/ ~100 nsec	$< 10^5$ / 10^5 – 10^8 / ~100%	
Photodiode	Whole ^b	-/-/-	$\geq 10^2$ /1/~10%	Opaque photocathode; windowless
Channel electron multiplier	Whole ^b	-/-/ <1 nsec	$> 10^6$ / 10^6 – 10^8 / ~10%	Grazing incidence for high efficiency
Microchannel plate	Whole ^b	-/~15 μm/ 200 psec	^c 10^5 – 10^6 / ~30%	Efficiency enhanced by MgF ₂ or CsI coating
Si (Li)	≤ 2	5–15%/-/ 10 nsec	$< 10^4$ /1/~60%	Operates at –170°C
Si diode array	≤ 5		/1	Operates at –(20–120°C)
Charge-coupled device	≤ 2	^d	/1	Thinned, back illuminated –(20–120°C)
Charge-injection device	≤ 2	^d	/1	Operates at 20 to –120°C

^aPeak quantum efficiency in soft X-ray range.^bWhole soft X-ray range covered.^c~ 10^5 counts mm⁻² sec⁻¹^dReadout dependent.

1.5. General Features of Soft X-Ray Optics

In Section 1.2, it was shown that the propagation of soft X rays in matter may be described by the complex refractive index

$$\tilde{n} = n - i\beta = 1 - \delta - i\beta \quad (1.60)$$

where δ is small and positive. Thus the real part of the refractive index is, unlike the case for visible light, less than one and so, if a normal refractive lens were to be used for focusing, it would have to be concave to give a real focus for an incident plane wave. For a plano-concave lens with central thickness d (Figure 1.19)

$$f/\rho = 1 + n/(\cos \phi - n \cos \phi') \quad (1.61)$$

where f is the focal length, ρ is the radius of curvature of the concave surface, and ϕ and ϕ' are the angles with respect to the normal to the concave surface as defined in Figure 1.19. For axial rays, this becomes

$$f/\rho = 1 + n/(1 - n) = 1/\delta \quad (1.62)$$

The depth of focus of such a lens is given by

$$\Delta f = \pm(1/2)(f/r)^2\lambda \quad (1.63)$$

where r is the radius of the lens aperture and λ is the illuminating wavelength. The maximum thickness of the lens is, from Figure 1.19,

$$t = \rho - (\rho^2 - r^2)^{1/2} + d \quad (1.64)$$

The closeness of the refractive index to unity, and the high absorption of soft X rays, means that lenses of the same sort of dimensions as those used for visible light would have impossibly long focal lengths (≥ 10 m), very small depths of focus (\sim tens of micrometers), and they would absorb essentially all of the incident radiation. Thus this type of lens is impractical for soft X rays, as has been stated by previous authors.^(37,38) However, optical components currently in use for soft X rays can have

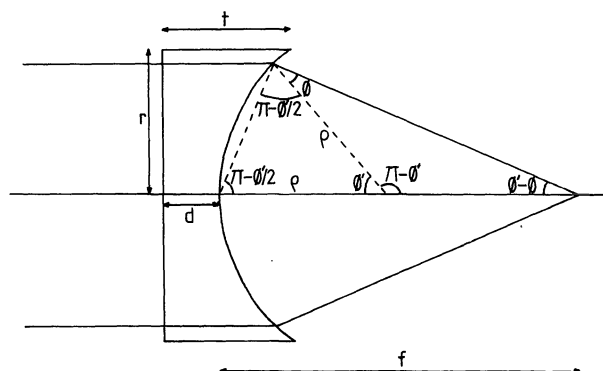


Figure 1.19. Parameters of a soft X-ray refractive plano-concave lens.

Table 1.7. Parameters of Possible X-Ray Refractive Lenses for a Wavelength of 3.5 nm^a

	Linear absorption coefficient (μm^{-1})	d (μm)	t (μm)	r (μm)	δ	β	ρ (μm)	f (mm)	Δf (mm)
Carbon	7	0.02	0.64	10	0.003	0.002	81	27	12
Gold	32	0.02	0.12	10	0.01	0.009	500	50	44

^aSee Figure 1.19 for definition of parameters.

focusing efficiencies of about 10% and effective aperture radii of about 10–50 μm . To match this efficiency, a refractive lens should have a mean thickness such that about 10% of the incident intensity is transmitted. Two possible lenses, for a soft X-ray wavelength of about 3.5 nm, are shown in Table 1.7. These results show that such lenses may not be unreasonable, although they have very large f-numbers and so very intense sources would be needed to prevent long imaging times. Calculations for biconcave lenses give similar results. However, the exact focusing properties of soft X-ray refractive lenses depend on better knowledge than currently available of the optical constants, and to date no attempts have been made to manufacture them.

The other conventional method of focusing at visible wavelengths is to use reflective optics. The reflected amplitude, a , at an interface between vacuum and a material is given by the Fresnel equations.⁽³⁹⁾ For radiation polarized so that the electric vector is perpendicular to the plane of incidence (s polarization)

$$a_{\perp} = [\cos \phi - (\tilde{n}^2 - \sin^2 \phi)^{1/2}] / [\cos \phi + (\tilde{n}^2 - \sin^2 \phi)^{1/2}] \quad (1.65)$$

where the angle of incidence ϕ is measured from the surface normal. In terms of the glancing angle, $\theta = 90^\circ - \phi$, this becomes

$$a_{\perp} = [\sin \theta - (\tilde{n}^2 - \cos^2 \theta)^{1/2}] / [\sin \theta + (\tilde{n}^2 - \cos^2 \theta)^{1/2}] \quad (1.66)$$

For parallel polarized radiation (p polarization)

$$a_{\parallel} = [\tilde{n}^2 \sin \theta - (\tilde{n}^2 - \cos^2 \theta)^{1/2}] / [\tilde{n}^2 \sin \theta + (\tilde{n}^2 - \cos^2 \theta)^{1/2}] \quad (1.67)$$

The reflectivity is given by

$$R = I/I_0 = aa^* \quad (1.68)$$

where I_0 is the incident intensity and I is the reflected intensity. For radiation incident normally on a surface, $\theta = 90^\circ$ and equations (1.66)

and (1.67) both lead to the normal incidence reflectivity

$$R_N = [(1 - \bar{n})/(1 + \bar{n})]^2 = (\delta^2 + \beta^2)/[(2 - \delta)^2 + \beta^2] \quad (1.69)$$

Using the values given in Table 1.7, and equation (1.4), gives, for a wavelength of 3.5 nm, $R_N = 3.3 \times 10^{-6}$ for carbon and $R_N = 4.6 \times 10^{-5}$ for gold. Normal incidence reflectivities are very small for all materials over the soft X-ray range, which means that conventional mirrors used in this way are impractical.

1.5.1. Enhancement of Reflectivity

The reflectivities of surfaces at soft X-ray wavelengths may be increased by using grazing angles of incidence or by causing multiple reflections to interfere constructively, as in Bragg diffraction from crystal layers.

If, in equations (1.66) and (1.67), the glancing angle is such that

$$(\bar{n}^2 - \cos^2 \theta)^{1/2} = 0 \quad (1.70)$$

then the reflectivity is identically equal to unity. For a non absorbing medium ($\beta = 0$), total reflection is obtained for glancing angles smaller than the critical angle θ_c , where

$$\cos \theta_c = n = 1 - \delta \quad (1.71)$$

For real media, the reflectivity approaches unity as $\theta \rightarrow 0$. If $\beta \ll \delta$ a sharp increase in reflectivity is obtained as θ falls below θ_c ; for $\beta \sim \delta$, a more gradual transition occurs. For $\theta < \theta_c$ no wave can propagate in the mirror material and the incident energy is reflected ("total external reflection"). Calculated grazing incidence reflectivities (for s polarization) are shown for beryllium, carbon, and gold at $\lambda = 3.5$ nm in Figure 1.20. The p-polarized reflectivities are not significantly different. A major problem with grazing incidence optics is their severe aberrations, especially astigmatism. How these may be overcome, and other properties of grazing incidence focusing systems, will be discussed in detail in Chapter 2.

The second way of enhancing reflectivity utilizes the same principles as employed in the quarter-wave stack (Figure 1.21a). In this, two nonabsorbing materials with refractive indices n_1 (high) and n_2 (low) are alternated, with optical thicknesses

$$n_i d_i = \lambda/4 \quad (1.72)$$

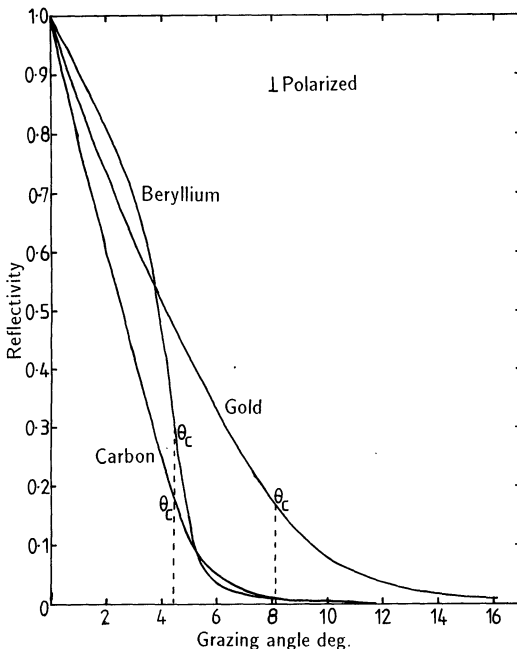


Figure 1.20. Grazing incidence reflectivities (single reflections) at a wavelength of 3.5 nm.

Reflections from all the boundaries add in phase and, for a sufficiently large number of layers, the reflectivity approaches unity. The actual number of layers necessary is obtained from knowledge of the amplitude reflection coefficient $|R|$, given by equation (1.69); thus if $|R| = 10^{-2}$, 100 interfaces are necessary. If one of the materials is absorbing, then it is no longer possible to use this arrangement to give high reflectivity, absorption losses occurring close to the antinodes of the standing wave given by the superposition of the incident and reflected waves. By restricting the absorbing material to regions close to the nodes of the standing wave (Figure 1.21b), absorption is minimized and, again, reflectivities approaching unity can be achieved, even if the two materials have equal refractive indices.⁽⁴⁰⁾

As discussed in Section 1.2, there are no absorption-free materials in the soft X-ray region and so the maximum reflectivities obtainable cannot approach unity. The optimum design of a high-reflectivity normal incidence mirror for soft X rays lies between the two cases discussed above. The detailed design and performance of these multilayer mirrors will be considered in Chapter 4.

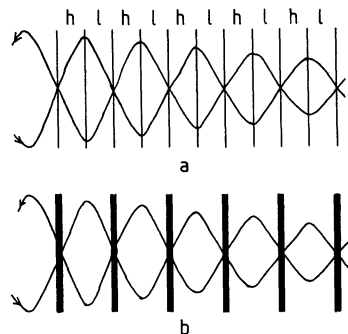


Figure 1.21. Ideal soft X-ray multilayer mirrors: (a) Absorption-free; (b) strong absorber with absorption-free spacer. Real X-ray multilayer designs lie between these two cases. (After Spiller.⁽³⁷⁾)

1.5.2. Diffractive Optics

For visible light, refracting and reflecting optics can be used to focus essentially all the incident radiation to one point. For focusing systems utilizing diffraction, this is not normally the case, due to the presence of an infinite number of diffraction orders. Thus diffraction systems have, traditionally, only curiosity value or, at best, limited applicability in the visible region.

However, in the soft X-ray region this is no longer the case. Because of the difficulties with refractive and reflective optics discussed above, diffraction-based systems may offer the best hope of achieving high resolutions. Diffraction gratings, usually at grazing incidence, are used in soft X-ray monochromators, while zone plates are used in focusing systems.

In their simplest form, zone plates are circular transmission gratings, with the concentric zone boundaries positioned so that the optical path difference from object to image point via two consecutive zones is $\lambda/2$. This means that the zones are of approximately equal area and the radius of the n th zone boundary is proportional to $n^{1/2}$. The zones are alternately totally opaque and completely transparent, leading to reinforcement of the radiation reaching the image point. For such a zone plate, 50% of the incident radiation is absorbed, and the diffraction efficiency to the m th-order focus is

$$\varepsilon_m = (10/m^2\pi^2)\% \quad (1.73)$$

where $m = 1, 3, 5, \dots$. A zone plate with perfectly positioned zone boundaries does not diffract radiation into even orders. The m th-order focal length is proportional to $1/m\lambda$, i.e., it is wavelength dependent, leading to severe chromatic aberration for polychromatic radiation. For zone plates with more than about 100 zones, imaging at a particular focus

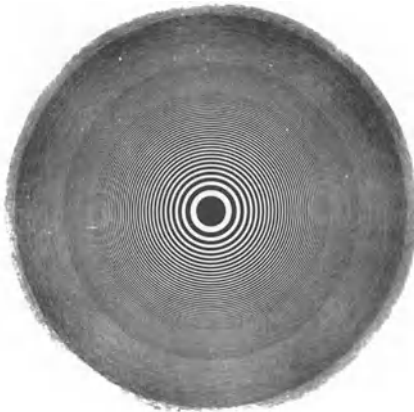


Figure 1.22. A Fresnel zone plate.

for monochromatic radiation can be treated in the same way as for refractive lenses. A typical zone plate structure is shown in Figure 1.22, and a full discussion of standard (Fresnel) and modified zone plates will be given in Chapter 8.

1.5.3. Resolution and Accuracy

The resolving power of an imaging system is given by the minimum distance between two points in the object that leads to distinct points in the image. For perfect optics this is governed by diffraction—diffraction-limited imaging. The diffraction patterns of the two points overlap, and the Rayleigh criterion⁽⁴¹⁾ for their resolution is that the inner dark ring of one diffraction pattern coincides with the central peak of the other. This corresponds to

$$d_R = 0.61\lambda/[n \sin(\theta_a/2)] \quad (1.74)$$

where d_R is the separation of the points, λ is the illuminating wavelength, n is the refractive index of the medium between the object and the imaging system, and θ_a is the angle subtended at the object by the edges of the optical system (Figure 1.23). The saddle to peak ratio in the combined diffraction pattern is 0.81. The Rayleigh criterion for resolution is somewhat arbitrary, and sometimes the Abbe criterion⁽⁴²⁾

$$d_A = 0.5\lambda/[n \sin(\theta_a/2)] \quad (1.75)$$

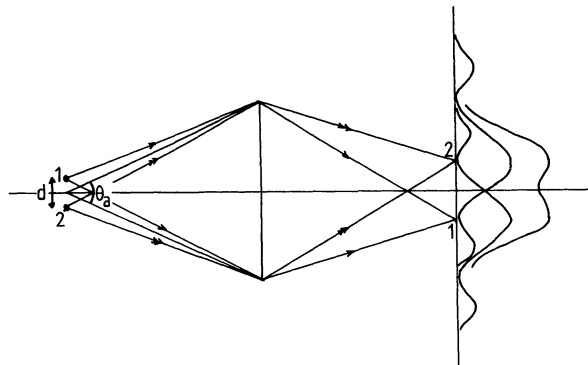


Figure 1.23. Resolution of two point objects (Rayleigh criterion).

is used instead. The numerical aperture of the system is

$$\text{NA} = n \sin (\theta_a/2) \quad (1.76)$$

—the resolution possible in an image increases as the numerical aperture increases and as the wavelength decreases. Thus, for equal numerical apertures, soft X-ray optical systems should be capable of much higher resolutions than visible light systems are.

The ultimate aim of a soft X-ray optical system is to produce diffraction-limited images, as indeed it is for any optical system. This means that aberrations introduced by inaccuracies in the manufacture of optical components must be small, i.e., the components must be accurately made. In addition, for reflecting optics, surfaces have to be very smooth. Typically, for grazing incidence optics, surface figures have to be accurate to about one-eighth of the required resolution (so that less than 50% of the incident light is diffusely scattered). For multilayer mirrors, accuracy and smoothness should be better than these figures by a factor of about two and, in addition, the accumulated thickness error over all the layers should be less than about $\lambda/10$. For zone plates, manufacturing tolerances of better than about one-third of the required resolution are necessary. Also, so that contributions from each alternate zone add in phase, any difference in phase change caused by thickness variations Δt of the zones (and, if applicable, the substrate) should be less than $\pi/4$, i.e.,

$$(2\pi/\lambda)\delta\Delta t < \pi/4 \quad (1.77)$$

giving

$$\Delta t < \lambda/8\delta \quad (1.78)$$

Aberrations introduced by such errors will be discussed in more detail in subsequent chapters, as will manufacturing methods and techniques for improving tolerances.

Reflective Optics for Soft X Rays I

Grazing Incidence

As discussed in Chapter 1, the reflectivities of single surfaces at normal or near-normal incidence for soft X rays are very small. High reflectivities from single surfaces are only obtained at grazing angles of incidence. This is because the refractive index of the reflecting medium is very close to, and slightly less than, that of the surrounding medium (vacuum)—the conditions under which total external reflection can occur.

2.1. Total External Reflection⁽¹⁾

Consider a plane wave traveling in a medium with complex refractive index

$$\tilde{n}_1 = 1 - \delta_1 - i\beta_1 \quad (2.1)$$

incident on a smooth planar boundary with a medium with

$$\tilde{n}_2 = 1 - \delta_2 - i\beta_2 \quad (2.2)$$

such that $\delta_2 > \delta_1$. In general, there will be a transmitted and a reflected wave, as illustrated in Figure 2.1. Initially, it will be assumed that both media are absorption free ($\beta_1 = \beta_2 = 0$) and that their magnetic permeabilities do not significantly differ from the permeability of free space. In terms of the glancing angles, Snell's law may then be written

$$(\cos \theta_i / \cos \theta_t) = (1 - \delta_2) / (1 - \delta_1) \quad (2.3)$$

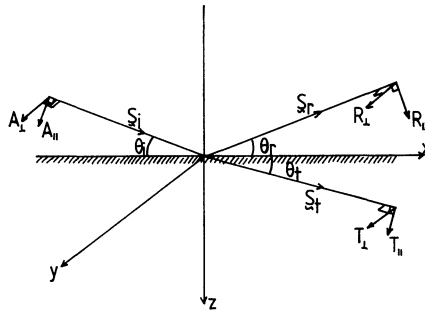


Figure 2.1. Total external reflection.

The coordinate system is defined so that the $x-z$ plane is the plane of incidence, and the z axis is normal to the boundary. The amplitudes of each of the incident, transmitted, and reflected fields may then be split into perpendicular components, along the y axis, and parallel components in the $x-z$ plane. The positive directions of the parallel components are defined in Figure 2.1. The components of the electric vectors of the fields may then be written

$$E_{ix} = -A_{\parallel} \sin \theta_i e^{-i\tau_i}, \quad E_{iy} = A_{\perp} e^{-i\tau_i}, \quad E_{iz} = A_{\parallel} \cos \theta_i e^{-i\tau_i} \quad (2.4a)$$

$$E_{tx} = -T_{\parallel} \sin \theta_t e^{-i\tau_t}, \quad E_{ty} = T_{\perp} e^{-i\tau_t}, \quad E_{tz} = T_{\parallel} \cos \theta_t e^{-i\tau_t} \quad (2.4b)$$

$$E_{rx} = R_{\parallel} \sin \theta_r e^{-i\tau_r}, \quad E_{ry} = R_{\perp} e^{-i\tau_r}, \quad E_{rz} = R_{\parallel} \cos \theta_r e^{-i\tau_r} \quad (2.4c)$$

where

$$\tau_i = \omega(t - \mathbf{r} \cdot \mathbf{s}_i/v_1) = \omega[t - (1 - \delta_1)(x \cos \theta_i + z \sin \theta_i)/c] \quad (2.5a)$$

$$\tau_t = \omega(t - \mathbf{r} \cdot \mathbf{s}_t/v_2) = \omega[t - (1 - \delta_2)(x \cos \theta_t + z \sin \theta_t)/c] \quad (2.5b)$$

$$\tau_r = \omega(t - \mathbf{r} \cdot \mathbf{s}_r/v_1) = \omega[t - (1 - \delta_1)(x \cos \theta_r + z \sin \theta_r)/c] \quad (2.5c)$$

ω being the angular frequency of the radiation and v_1, v_2 being the velocities of propagation in the two media,

$$v_1 = c/(1 - \delta_1), \quad v_2 = c/(1 - \delta_2) \quad (2.6)$$

The corresponding components of the magnetic vectors are

$$\begin{aligned} H_{ix} &= -A_{\perp}(1 - \delta_1) \sin \theta_i e^{-i\tau_i}, & H_{iy} &= -A_{\parallel}(1 - \delta_1) e^{-i\tau_i}, \\ H_{iz} &= A_{\perp}(1 - \delta_1) \cos \theta_i e^{-i\tau_i} \end{aligned} \quad (2.7a)$$

$$\begin{aligned} H_{tx} &= -T_{\perp}(1 - \delta_2) \sin \theta_t e^{-i\tau_t}, & H_{ty} &= -T_{\parallel}(1 - \delta_2) e^{-i\tau_t}, \\ H_{tz} &= T_{\perp}(1 - \delta_2) \cos \theta_t e^{-i\tau_t} \end{aligned} \quad (2.7b)$$

$$\begin{aligned} H_{rx} &= R_{\perp}(1 - \delta_1) \sin \theta_r e^{-i\tau_r}, & H_{ry} &= -R_{\parallel}(1 - \delta_1) e^{-i\tau_r}, \\ H_{rz} &= R_{\perp}(1 - \delta_1) \cos \theta_r e^{-i\tau_r} \end{aligned} \quad (2.7c)$$

Across the boundary, the tangential components of the electric and magnetic vectors must be continuous. Thus

$$E_{ix} + E_{rx} = E_{tx}, \quad E_{iy} + E_{ry} = E_{ty} \quad (2.8a)$$

and

$$H_{ix} + H_{rx} = H_{tx}, \quad H_{iy} + H_{ry} = H_{ty} \quad (2.8b)$$

From Figure 2.1 it is clear that $\theta_r = \theta_1$, and then equations (2.8a) and (2.8b) lead to

$$(A_{\parallel} - R_{\parallel}) \sin \theta_i = T_{\parallel} \sin \theta_t \quad (2.9a)$$

$$A_{\perp} + R_{\perp} = T_{\perp} \quad (2.9b)$$

$$(1 - \delta_1)(A_{\perp} - R_{\perp}) \sin \theta_i = (1 - \delta_2)T_{\perp} \sin \theta_t \quad (2.9c)$$

$$(1 - \delta_1)(A_{\parallel} + R_{\parallel}) = (1 - \delta_2)T_{\parallel} \quad (2.9d)$$

Equations (2.9) show that the parallel and perpendicular components are independent, since none of the equations contain both components. Solving for the reflected and transmitted components in terms of the incident components gives

$$\begin{aligned} R_{\parallel}/A_{\parallel} &= [(1 - \delta_2) \sin \theta_i - (1 - \delta_1) \sin \theta_t]/[(1 - \delta_2) \sin \theta_i \\ &\quad + (1 - \delta_1) \sin \theta_t] \end{aligned} \quad (2.10a)$$

$$\begin{aligned} R_{\perp}/A_{\perp} &= [(1 - \delta_1) \sin \theta_i - (1 - \delta_2) \sin \theta_t]/[(1 - \delta_1) \sin \theta_i \\ &\quad + (1 - \delta_2) \sin \theta_t] \end{aligned} \quad (2.10b)$$

$$T_{\parallel}/A_{\parallel} = [2(1 - \delta_1) \sin \theta_i]/[(1 - \delta_2) \sin \theta_i + (1 - \delta_1) \sin \theta_t] \quad (2.11a)$$

$$T_{\perp}/A_{\perp} = [2(1 - \delta_1) \sin \theta_i]/[(1 - \delta_1) \sin \theta_i + (1 - \delta_2) \sin \theta_t] \quad (2.11b)$$

Equations (2.10) and (2.11) are the Fresnel formulas for reflection at a plane surface. Using equation (2.3) they may be rewritten in the form

$$\frac{R_{\parallel}}{A_{\parallel}} = \frac{(1 - \delta_2)^2 \sin \theta_i - (1 - \delta_1)[(1 - \delta_2)^2 - (1 - \delta_1)^2 \cos^2 \theta_i]^{1/2}}{(1 - \delta_2)^2 \sin \theta_i + (1 - \delta_1)[(1 - \delta_2)^2 - (1 - \delta_1)^2 \cos^2 \theta_i]^{1/2}} \quad (2.12a)$$

$$\frac{R_{\perp}}{A_{\perp}} = \frac{(1 - \delta_1) \sin \theta_i - [(1 - \delta_2)^2 - (1 - \delta_1)^2 \cos^2 \theta_i]^{1/2}}{(1 - \delta_1) \sin \theta_i + [(1 - \delta_2)^2 - (1 - \delta_1)^2 \cos^2 \theta_i]^{1/2}} \quad (2.12b)$$

$$\frac{T_{\parallel}}{A_{\parallel}} = \frac{2(1 - \delta_1)(1 - \delta_2) \sin \theta_i}{(1 - \delta_2)^2 \sin \theta_i + (1 - \delta_1)[(1 - \delta_2)^2 - (1 - \delta_1)^2 \cos^2 \theta_i]^{1/2}} \quad (2.13a)$$

$$\frac{T_{\perp}}{A_{\perp}} = \frac{2(1 - \delta_1) \sin \theta_i}{(1 - \delta_1) \sin \theta_i + [(1 - \delta_2)^2 - (1 - \delta_1)^2 \cos^2 \theta_i]^{1/2}} \quad (2.13b)$$

If θ_i has the value θ_c given by

$$\cos \theta_i = (1 - \delta_2)/(1 - \delta_1) \quad (2.14)$$

then equations (2.12) reduce to

$$R_{\parallel}/A_{\parallel} = R_{\perp}/A_{\perp} = 1 \quad (2.15)$$

i.e., the incident wave is totally reflected. At this value of θ_i , $\theta_t = 0$ so that no radiation enters the second medium. If θ_i is less than θ_c , $\cos \theta_t$ becomes larger than unity, i.e., θ_t has unphysical values. Thus, again, no radiation can propagate in the second medium and the wave is totally reflected.

In most cases, this total external reflection takes place at a (near) vacuum/dense material boundary. Thus $\delta_1 = 0$ and the Fresnel equations become, with $\delta_2 = \delta$.

$$\frac{R_{\parallel}}{A_{\parallel}} = \frac{(1 - \delta)^2 \sin \theta_i - [(1 - \delta)^2 - \cos^2 \theta_i]^{1/2}}{(1 - \delta)^2 \sin \theta_i + [(1 - \delta)^2 - \cos^2 \theta_i]^{1/2}} \quad (2.16a)$$

$$\frac{R_{\perp}}{A_{\perp}} = \frac{\sin \theta_i - [(1 - \delta)^2 - \cos^2 \theta_i]^{1/2}}{\sin \theta_i + [(1 - \delta)^2 - \cos^2 \theta_i]^{1/2}} \quad (2.16b)$$

$$\frac{T_{\parallel}}{A_{\parallel}} = \frac{2(1 - \delta) \sin \theta_i}{(1 - \delta)^2 \sin \theta_i + [(1 - \delta)^2 - \cos^2 \theta_i]^{1/2}} \quad (2.17a)$$

$$\frac{T_{\perp}}{A_{\perp}} = \frac{2 \sin \theta_i}{\sin \theta_i + [(1 - \delta)^2 - \cos^2 \theta_i]^{1/2}} \quad (2.17b)$$

For an absorbing medium, $\beta_2 = \beta \neq 0$, the corresponding equations are⁽²⁾

$$\frac{R_{\parallel}}{A_{\parallel}} = \frac{\tilde{n}^2 \sin \theta_i - (\tilde{n}^2 - \cos^2 \theta_i)^{1/2}}{\tilde{n}^2 \sin \theta_i + (\tilde{n}^2 - \cos^2 \theta_i)^{1/2}} \quad (2.18a)$$

$$\frac{R_{\perp}}{A_{\perp}} = \frac{\sin \theta_i - (\tilde{n}^2 - \cos^2 \theta_i)^{1/2}}{\sin \theta_i + (\tilde{n}^2 - \cos^2 \theta_i)^{1/2}} \quad (2.18b)$$

$$\frac{T_{\parallel}}{A_{\parallel}} = \frac{2\tilde{n} \sin \theta_i}{\tilde{n}^2 \sin \theta_i + (\tilde{n}^2 - \cos^2 \theta_i)^{1/2}} \quad (2.19a)$$

$$\frac{T_{\perp}}{A_{\perp}} = \frac{2 \sin \theta_i}{\sin \theta_i + (\tilde{n}^2 - \cos^2 \theta_i)^{1/2}} \quad (2.19b)$$

Note that equations (2.18a) and (2.18b) are identical to equations (1.67) and (1.66), respectively.

For reflection at a curved surface, these equations can be used so long as the radius of curvature is much greater than the wavelength of the radiation. This condition is always satisfied for soft X rays. The reflectivities may be obtained from equations (2.18a) and (2.18b) as

$$R_p = (R_{\parallel}/A_{\parallel})(R_{\parallel}/A_{\parallel})^* \quad (2.20a)$$

and

$$R_s = (R_{\perp}/A_{\perp})(R_{\perp}/A_{\perp})^* \quad (2.20b)$$

using

$$\tilde{n}^2 = (1 - \delta)^2 - \beta^2 - 2i(1 - \delta)\beta \quad (2.21)$$

Values of the reflectivity R_p are shown for two values of δ and various

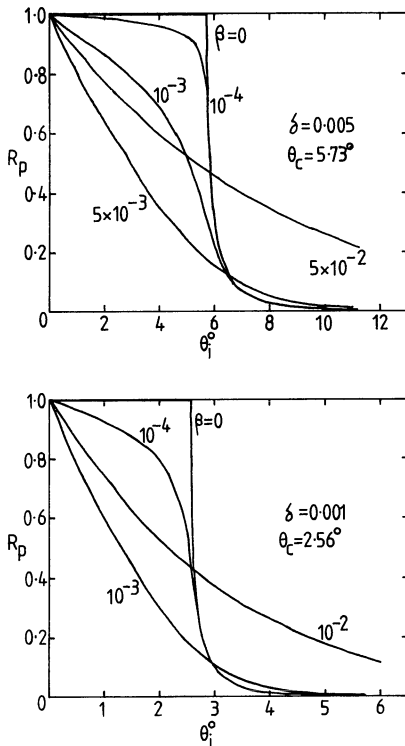


Figure 2.2. Calculated values of grazing incidence reflectivity for the parallel polarized component.

values of β in Figure 2.2. For small β (less than some fraction of δ), the reflectivity is high for grazing incidence angles less than the critical angle θ_c , and it drops off sharply for $\theta_i > \theta_c$. For larger values of β the reflectivity decreases more gradually for all $\theta_i > 0$. The reflectivity R_s behaves similarly; Figure 2.3 shows that $R_s \approx R_p$ for small θ_i (i.e., when the reflectivity is high). For glancing angles much larger than θ_c the reflectivities become very small (Figure 2.4). Since β is never zero for real materials, the incident radiation is never totally reflected. To determine which materials may be used to approach total external reflection, it is convenient to define the phenomenon as occurring when the reflectivity versus incidence angle curve contains a point of inflection.⁽³⁾ Figure 2.5 shows that the condition for this is

$$\beta < 0.63\delta \quad (2.22)$$

For reflection from real surfaces in the soft X-ray region, two modifications to the above discussion must be considered. The first of

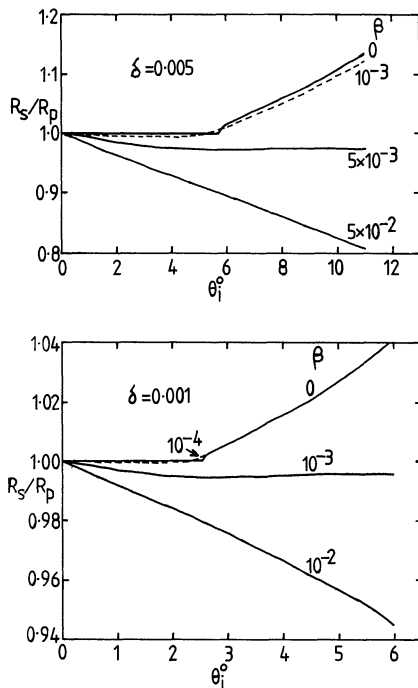


Figure 2.3. Calculated ratios of the parallel and perpendicular grazing incidence reflectivities.

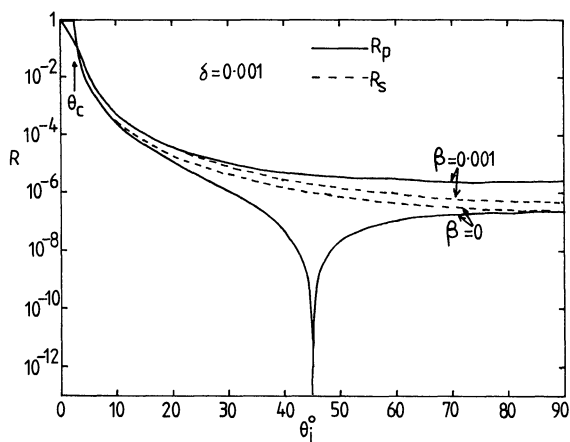


Figure 2.4. Calculated reflectivities over the whole range of incidence angles.

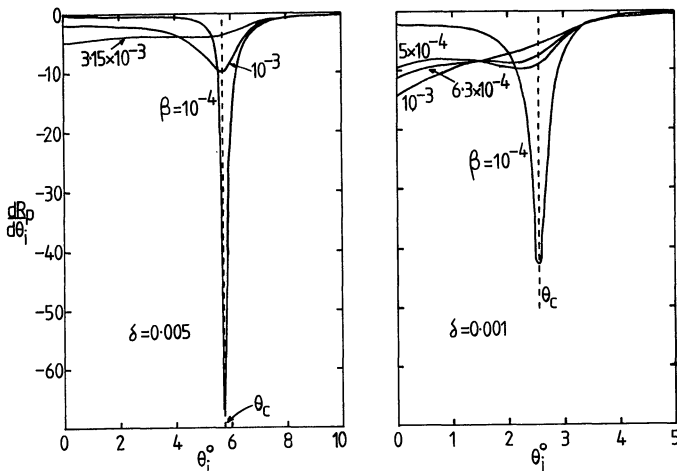


Figure 2.5. Slopes of the reflectivity curves as functions of grazing incidence angle, showing points of inflection when $\beta < 0.63\delta$.

these concerns the atomic nature of the reflecting medium, which is ignored in the solutions of Maxwell's equations leading to equations (2.4) and (2.7), and the second concerns surface roughness.

2.1.1. Reflection of X Rays from Atomic Surface Layers

In order to take into account the atomic nature of the reflecting medium, the approach of Smirnov⁽⁴⁾ may be followed. In this, the surface is modeled as a series of parallel layers, of thickness Δz small enough that the phase difference between successive reflections for grazing incidence angles is much less than 2π , i.e., $\Delta z \ll \lambda$. All the atoms of a layer may then be projected onto the upper boundary plane of the layer, which then contains all the scattering power of the layer. This reduces the problem to one of Bragg reflection. If N_a is the number density of atoms in the layer, the surface density of projected atoms is $N_a\Delta z$. The amplitude reflected by one such plane may be calculated by reference to Figure 2.6,^(5,6) where radiation of wavelength λ from P is reflected via O to P' . If Q is a point such that

$$PQP' = POP' + \lambda/2 = (r + r') + \lambda/2 \quad (2.32)$$

then the locus of points such as Q forms the boundary of the first (elliptical) Fresnel zone. If the Fresnel equations are to be valid, then the scattering points on the plane must be sufficiently close that they may be

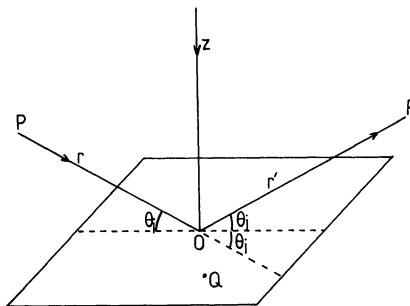


Figure 2.6. Reflection of X rays from a single atomic layer.

considered as having a continuous distribution compared to the areas of the Fresnel zones. The area of the first Fresnel zone is

$$\begin{aligned} A_1 &= \Pi \times (\text{semimajor axis}) \times (\text{semiminor axis}) \\ &= \pi \{[\lambda rr'/(r + r')]^{1/2}/\sin \theta_i\} \times [\lambda rr'/(r + r')]^{1/2} \end{aligned} \quad (2.24)$$

so that the condition for validity of the Fresnel equations is

$$N_a \Delta z \gg 1/A_1 = [(r + r')/\pi rr' \lambda] \sin \theta_i \quad (2.25)$$

Typically, for a grazing incidence X-ray microscope for example, $\lambda \approx 5-2 \text{ nm}$, $r \approx 4600-50 \text{ mm}$, $r' \approx 2600-2 \text{ mm}$, and $\theta_i \approx 0.17-25^\circ$,⁽⁷⁾ so that $1/A_1 \approx 10^5-4 \times 10^{10}$. Then condition (2.25) is satisfied for all real materials; typically there are about $10^{19} \text{ atoms m}^{-2}$. Thus the expression for the reflectivity obtained taking atomic effects into account should reduce to that obtained above, in Section 2.1.

The Fresnel construction shows that the resultant amplitude at P' due to the first zone is

$$a_{P'} = (2/\pi) \sum_j a_j \quad (2.26)$$

where a_j is the amplitude due to the j th scattering point. The total resultant amplitude at P' is just half that given by equation (2.26), and the phase of the resultant disturbance at P' is retarded by $\pi/2$ compared to the wavelet scattered by the point at O . All the atoms in the first Fresnel zone may be considered as lying at the same distance r' from P' , so that they each contribute an amplitude $a_j = a/r'$, where a is the amplitude at unit distance from O , assuming that all the atoms in the

plane are identical. The amplitude reflection coefficient is then given by

$$\begin{aligned} R &= (1/2)A_1(2/\pi)N_a\Delta z(a/r') \exp(-i\pi/2) \\ &= -(iN_a\Delta z\lambda a/\sin\theta_i)[r/(r+r')] \end{aligned} \quad (2.27)$$

If $r' \ll r$ (i.e., the incident wave is almost plane),

$$R = -iq \quad (2.28)$$

where

$$q = N_a\Delta z\lambda a/\sin\theta_i \quad (2.29)$$

For the perpendicular component of the reflected wave,

$$a_{\perp} = -f(2\theta_i)e^2/4\pi\varepsilon_0m_e c^2 \quad (2.30)$$

where $f(2\theta_i)$ is the atomic scattering factor of an atom (see Section 1.2) for scattering through a total angle $2\theta_i$, so that

$$q_{\perp} = -(N_a\Delta z\lambda/\sin\theta_i)f(2\theta_i)e^2/4\pi\varepsilon_0m_e c^2 \quad (2.31)$$

For a composite reflecting plane it is only necessary to replace f by F , the structure factor for the unit group of atoms, and N_a by N_u , the number density of unit groups. The parallel component of the reflected wave need not be considered separately since, as already noted, the two components are essentially equal for small θ_i .

It is clear that, to conserve energy, q must be less than one. Thus equation (2.31) cannot be completely general, since, in principle, N_a could be sufficiently large that $|q| > 1$. This is prevented by regarding f as dependent on N_a , so that the vibration of an atom is diminished by the presence of its neighbors. Typically, in the soft X-ray region, $f \leq Z$ so that $|q| \leq 10^{-2}/\sin\theta_i$, i.e., $|q| < 1$ except for very grazing incidence. Thus equation (2.31) is normally valid.

For reflection from the parallel series of layers (Figure 2.7), it is necessary to consider transmission through a layer, which is described by the amplitude transmission coefficient

$$T = 1 - iq_0 \quad (2.32)$$

where

$$q_0 = -(N_a\Delta z\lambda/\sin\theta_i)f(0)(e^2/4\pi\varepsilon_0m_e c^2) \quad (2.33)$$

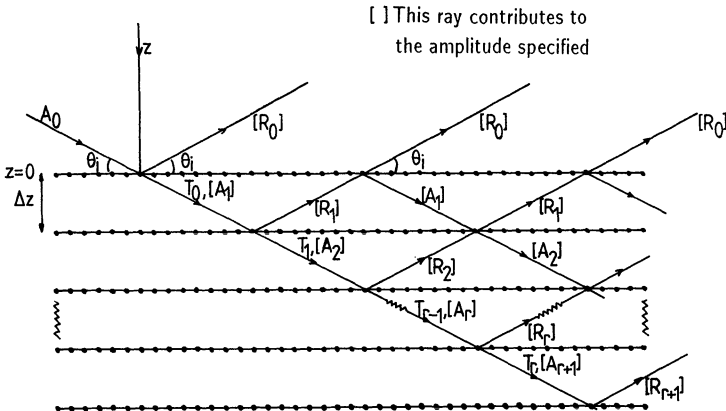


Figure 2.7. Reflection from a parallel series of atomic layers.

or the equivalent expression in terms of F and N_a . From equation (1.16), assuming no absorption ($\beta = 0$),

$$\delta = (e^2 \lambda^2 N_a / 8\pi^2 \epsilon_0 m_e c^2) f \quad (2.34)$$

so that, in the approximation that f is angle independent, and δ is independent of z (i.e., the number density of atoms remains constant),

$$q = -(2\pi\delta/\lambda \sin \theta_i) \Delta z = -\alpha \Delta z \quad (2.35)$$

and

$$q_0 = -(2\pi\delta/\lambda \sin \theta_i) \Delta z = -\alpha \Delta z \quad (2.36)$$

The phase difference ϕ between the waves reflected by successive planes may be written as

$$2\phi = 2\pi m + 2v \quad (2.37)$$

where $2v$ represents the excess over an integral number of half periods, i.e., $v = 0$ for reflection according to Bragg's law. Since in the model under discussion the phase difference between successive reflections is chosen to be much less than 2π , $m = 0$ and

$$\phi = v = (2\pi \Delta z / \lambda) \sin \theta_i = \gamma \Delta z \quad (2.38)$$

where $\Delta z \sin \theta_i$ is the path difference between reflections from successive layers.

The incident and reflected amplitudes for the r th layer are represented by A_r and R_r , respectively, as indicated in Figure 2.7, where $r = 0$ for the surface layer. To obtain the equivalent expression to equation (2.16b), it is necessary to determine R_0/A_0 . In order to obtain an expression for this, the multiple reflections and transmissions at each layer must be taken into account. Thus R_r consists of the part of A_r that is reflected at the upper surface of the r th layer, with reflection coefficient $-iq$, plus the part of $R_{r+1} \exp(-i\phi)$ that is transmitted from below, with transmission coefficient $1 - iq_0$. The phase difference ϕ is included here since R_{r+1} refers to the reflected amplitude just above the $(r + 1)$ th layer. Thus

$$R_r = -iqA_r + (1 - iq_0)R_{r+1} \exp(-i\phi) \quad (2.39)$$

and similarly

$$A_{r+1} = (1 - iq_0)A_r \exp(-i\phi) - iqR_{r+1} \exp(-2i\phi) \quad (2.40)$$

assuming that the reflection coefficient from the underside of a layer is the same as that from above (this is not necessarily valid for a composite material). Writing A_r and R_r as continuous functions of z , and using equations (2.35), (2.36), and (2.38) then leads to

$$R(z) = i\alpha\Delta z A(z) + (1 + i\alpha\Delta z)R(z + \Delta z) \exp(-i\gamma\Delta z) \quad (2.41)$$

and

$$\begin{aligned} A(z + \Delta z) &= (1 + i\alpha\Delta z)A(z) \exp(-i\gamma\Delta z) \\ &\quad + i\alpha\Delta z R(z + \Delta z) \exp(-2i\gamma\Delta z) \end{aligned} \quad (2.42)$$

Expanding A , R , and the exponential terms about z , and retaining only terms up to the first power in Δz , leads to

$$R(z) = -[\alpha/(\alpha - \gamma)]A(z) + [i/(\alpha - \gamma)]dR(z)/dz \quad (2.43)$$

and

$$A(z) = -[\alpha/(\alpha - \gamma)]R(z) - [i/(\alpha - \gamma)]dA(z)/dz \quad (2.44)$$

Defining

$$P(z) = A(z) + R(z) \quad (2.45)$$

and

$$Q(z) = A(z) - R(z) \quad (2.46)$$

leads to

$$P(z) = [-i/(2\alpha - \gamma)] dQ(z)/dz \quad (2.47)$$

and

$$Q(z) = (i/\gamma) dP(z)/dz \quad (2.48)$$

Solving equations (2.47) and (2.48) simultaneously gives [retaining only the decreasing exponential since $A(z)$ and $R(z)$ decrease with z]

$$P(z) = P(0) \exp(-Kz) \quad (2.49)$$

and

$$\begin{aligned} Q(z) &= (1 - 2\alpha/\gamma)^{1/2} P(0) \exp(-Kz) \\ &= [(\sin^2 \theta_i - 2\delta)^{1/2}/\sin \theta_i] P(0) \exp(-Kz) \end{aligned} \quad (2.50)$$

where

$$K^2 = \gamma(2\alpha - \gamma) \quad (2.51)$$

The reflectivity at the surface is thus

$$\begin{aligned} |R_\perp/A_\perp|^2 &= |R(0)/A(0)|^2 = |[P(0) - Q(0)]/[P(0) + Q(0)]|^2 \\ &= \{[\sin \theta_i - (\sin^2 \theta_i - 2\delta)^{1/2}]/[\sin \theta_i + (\sin^2 \theta_i - 2\delta)^{1/2}]\}^2 \end{aligned} \quad (2.52)$$

which agrees with equation (2.16b) since, for small δ , $(1 - \delta)^2 \approx 1 - 2\delta$. To take account of absorption, δ may be substituted by $\delta + i\beta^{(2)}$ as before.

The X-ray wavelengths for which this approach is valid may be estimated by expanding equations (2.41) and (2.42) up to the term containing the second power in Δz , and stipulating that this term is much smaller than those retained above. This leads to

$$\lambda \gg (\pi\delta/\sin \theta_i)\Delta z \quad (2.53)$$

For $\delta \sim 10^{-3}$ and $\Delta z \sim 0.1$ nm (crystal lattice spacing) this gives, for

$$\theta_i \approx 0.17 - 25^\circ,$$

$$\lambda \gg \sim 10^{-3} - 10^{-1} \text{ nm} \quad (2.54)$$

which is satisfied for the soft X-ray region.

2.1.2. Reflection of X Rays from Rough Surfaces

The model described in Section 2.1.1 may also be applied to the problems of surface roughness, using Figure 2.8.⁽⁸⁾ Now, the layers in the vicinity of the roughness are discontinuous, with full regions of dimension x_i and empty regions of dimension w_i . The mean period of the roughness is $\bar{s} = \bar{x} + \bar{w}$, where \bar{x} and \bar{w} are the means of x_i and w_i , respectively. The effect of this roughness is determined by calculating the disturbance at the point P' , situated in a layer of thickness Δz_1 , caused by the layer of thickness Δz_2 . The two layers are separated by a distance σ , which is a measure of the height of the roughness. The condition for validity of the Fresnel approach now becomes

$$\bar{s} \ll A_1^{1/2} \quad (2.55)$$

where A_1 is the area of the first Fresnel zone, given by equation (2.24). Using $r' = \sigma / \sin \theta_i$ ($\ll r$) this becomes

$$\bar{s} \ll (\pi \sigma \lambda)^{1/2} / \sin \theta_i \quad (2.56)$$

Using the range of values quoted previously for an X-ray microscope,

$$\bar{s} \ll (6 - 1350) \sigma^{1/2} \quad (2.57)$$

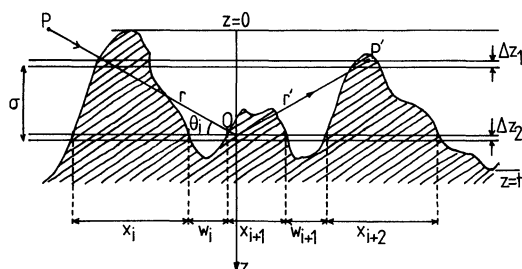


Figure 2.8. Reflection of X rays from a rough surface.

with \bar{s} and σ in nanometers. It is now possible to manufacture surfaces with $\sigma \sim 0.1 \text{ nm}$,⁽⁹⁾ so that the period of the surface roughness must be much less than 2 nm for large glancing angles. For small glancing angles the requirement is much less stringent. For visible radiation an optically smooth surface may have a period for the roughness of $\sim 20\text{--}30 \text{ nm}$; thus for soft X rays the period may have to be up to about ten times smaller.

If condition (2.56) is satisfied, then it is valid to assume that the material in the layer Δz_2 is uniformly distributed and has a mean number density of atoms $N_a(z)$. If the total thickness of the region of roughness is t , then $N_a(z)$ varies from zero at $z = 0$ to a maximum at $z = t$, remaining constant as z increases further. Since the number density of atoms is now dependent on z , so is the refractive index decrement δ , from equation (2.34), and the parameter α . Thus, the differential equation to solve for the amplitude becomes, combining equations (2.47) and (2.48),

$$d^2P(z)/dz^2 - \gamma[2\alpha(z) - \gamma]P(z) = 0 \quad (2.58)$$

with equation (2.48) remaining valid for obtaining $Q(z)$. Equation (2.58) cannot be solved without specifying a form for $\alpha(z)$. In some cases it may be approximately true that $\alpha(z)$ increases linearly with z , but this does not take into account, for example, crystal defects or oxidation of the reflecting surface. The procedure adopted by Smirnov *et al.*⁽⁸⁾ was to assume a form for $\alpha(z)$, compare the resulting calculated reflectivities with measured values, and then successively correct the form of $\alpha(z)$ until an (arbitrarily accurate) agreement was obtained. These calculations show that surface roughness on the scale indicated by equation (2.56) reduces the reflection coefficient in the region of the critical angle.

An alternative treatment of surface roughness is to use an approach similar to that taken by Debye⁽¹⁰⁾ when considering the effect of thermal vibrations of a crystal lattice on X-ray scattering. For an undisturbed lattice, the intensity at P' is, for unit incident amplitude,

$$\begin{aligned} I_u &= (1/r'^2) \sum_n \exp[(2\pi i/\lambda)\mathbf{r}_n \cdot \mathbf{S}] \sum_m \exp[-(2\pi i/\lambda)\mathbf{r}_m \cdot \mathbf{S}] \\ &= (1/r'^2) \sum_n \sum_m \exp[(2\pi i/\lambda)(\mathbf{r}_n - \mathbf{r}_m) \cdot \mathbf{S}] \end{aligned} \quad (2.59)$$

where \mathbf{r}_j is the position vector of the j th lattice point and

$$\mathbf{S} = \mathbf{s}_r - \mathbf{s}_i, \quad |\mathbf{S}| = 2 \sin \theta_i \quad (2.60)$$

(see Figure 2.1). If the lattice points are displaced by \mathbf{u}_j , then equation

(2.59) becomes

$$I_d = (1/r'^2) \sum_n \sum_m \exp [(2\pi i/\lambda)(\mathbf{r}_n - \mathbf{r}_m) \cdot \mathbf{S}] \exp [(2\pi i/\lambda)(\mathbf{u}_n - \mathbf{u}_m) \cdot \mathbf{S}] \quad (2.61)$$

To apply this to surface roughness, the mean value of $(\mathbf{u}_n - \mathbf{u}_m) \cdot \mathbf{S}$ is equated to σ^2 , the square of the mean surface displacement. Writing

$$P_{nm} = (2\pi/\lambda)(\mathbf{u}_n - \mathbf{u}_m) \cdot \mathbf{S} = (4\pi \sin \theta_i/\lambda)(u_{ns} - u_{ms}) \quad (2.62)$$

where u_{js} is the component of \mathbf{u}_j in the direction of \mathbf{S} , then

$$\begin{aligned} \exp(i\overline{P_{nm}}) &= 1 + i\overline{P_{nm}} - \overline{P_{nm}^2}/2! + \dots \\ &= 1 - \overline{P_{nm}^2}/2! + \overline{P_{nm}^4}/4! + \dots \end{aligned} \quad (2.63)$$

since, on average, terms involving odd powers of $\overline{P_{nm}}$ cancel. Hence, for small displacements (i.e., small $\overline{P_{nm}}$),

$$\exp(i\overline{P_{nm}}) \approx \exp(-\overline{P_{nm}^2}/2) \quad (2.64)$$

so that

$$\overline{I_d} = (1/r'^2) \sum_n \sum_m \exp [(2\pi i/\lambda)(\mathbf{r}_n - \mathbf{r}_m) \cdot \mathbf{S}] \exp (-\overline{P_{nm}^2}/2) \quad (2.65)$$

In order to calculate $\overline{P_{nm}^2}$, it is necessary to determine the mean value of $(u_{ns} - u_{ms})^2$. Expanding,

$$\overline{(u_{ns} - u_{ms})^2} = \overline{u_{ns}^2} + \overline{u_{ms}^2} - 2\overline{u_{ns}u_{ms}} \quad (2.66)$$

If the surface roughness is random, then

$$\overline{u_{ns}u_{ms}} = 0 \quad (2.67)$$

and

$$\overline{u_{ns}^2} = \overline{u_{ms}^2} = \sigma^2 \quad (2.68)$$

Thus

$$\overline{P_{nm}^2}/2 = (4\pi \sin \theta_i/\lambda)^2 \sigma^2 \quad (2.69)$$

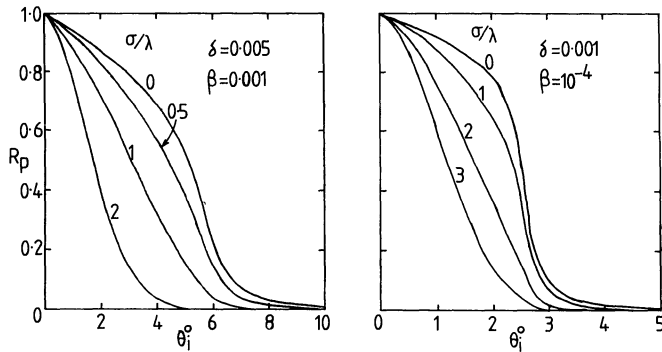


Figure 2.9. The effect of surface roughness on X-ray reflectivities.

and

$$\begin{aligned}\bar{I}_d &= (1/r'^2) \sum_n \sum_m \exp [(2\pi i/\lambda)(\mathbf{r}_n - \mathbf{r}_m) \cdot \mathbf{S}] \exp [-(4\pi\sigma \sin \theta_i/\lambda)^2] \\ &= I_u \exp [-(4\pi\sigma \sin \theta_i/\lambda)^2]\end{aligned}\quad (2.70)$$

The reflectivities, equations (2.20a) and (2.20b), are also reduced by this exponential factor; the results of this reduction are shown in Figure 2.9. It is clear from this that, in order to maintain high reflectivities at grazing incidence angles, the height of the surface roughness must be such that

$$\sigma \leq \lambda \quad (2.71)$$

which is not a stringent requirement for soft X-ray wavelengths, although it may restrict the materials that can be used.

2.2. Focusing with Spherical Mirrors at Grazing Incidence

In order to carry out any focusing using reflection, the reflecting surface must be curved. At near-normal incidence a concave spherical mirror can be used to form a good image of a point object on the optical axis. This is no longer the case as the object is moved away from the optical axis, and the aberrations become severe for grazing incidence angles.⁽¹¹⁻¹³⁾

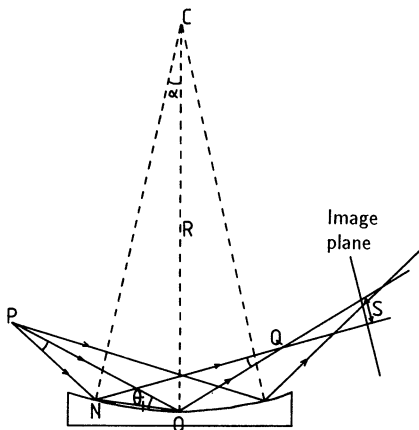


Figure 2.10. Image formation by a circular mirror.

2.2.1. Astigmatism

Consider Figure 2.10, in which a circular (i.e., two-dimensional) mirror of radius R is illuminated at a grazing incidence angle θ_i by radiation diverging at a small angle β from a point source P . The image of P is at Q and the object and image distances u (PO) and v (OQ) are measured from an arbitrary point O on the surface. The radiation is spread over a distance k (NO) on the surface of the mirror and β is chosen to be small enough that $k \ll R$. The chord NO subtends an angle α at C , the center of curvature, so that $k = R\alpha$, and γ is the convergence angle of the radiation at Q . The triangle PNO then gives, using small angle approximations,

$$\beta = R\alpha(\theta_i - \alpha/2)/(u - R\alpha) \quad (2.72)$$

Similarly, from triangle QNO ,

$$\gamma = R\alpha(\theta_i + \alpha/2)/(v + R\alpha) \quad (2.73)$$

From the law of reflection, $\beta + \gamma = 2\alpha$ and thus

$$(1 - \alpha/2\theta_i)/(u - R\alpha) + (1 + \alpha/2\theta_i)/(v + R\alpha) = 2/R\theta_i \quad (2.74)$$

which, for small α , reduces to

$$(1/u) + (1/v) = 2/R\theta_i = 1/f_m \quad (2.75)$$

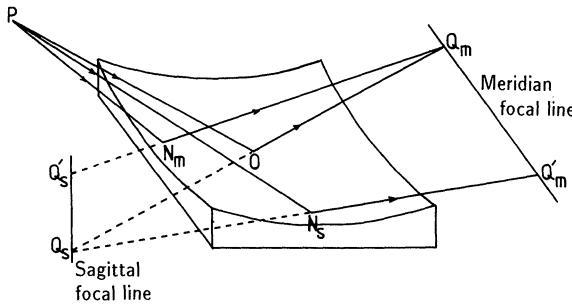


Figure 2.11. Image formation by a spherical mirror.

where $f_m = R\theta_i/2$ or, more generally,

$$f_m = (R \sin \theta_i)/2 \quad (2.76)$$

is known as the meridian focal length.

A spherical (three-dimensional) mirror gives a second image of P , as shown in Figure 2.11, corresponding to a focal length

$$f_s = R/2 \sin \theta_i \quad (2.77)$$

—the sagittal focal length. As shown in Figure 2.11 the two images of the point object at P are both lines, the meridian focal line being in the plane of the mirror and the sagittal focal line perpendicular to it. The two foci only coincide, resulting in a point image, if $\sin \theta_i = 1$, i.e., $\theta_i = 90^\circ$ —normal incidence. At grazing incidence angles, the images are severely astigmatic—for a grazing angle of about 2° , the sagittal focal length is about 10^3 times the meridian focal length.

2.2.2. Spherical Aberration

Spherical mirrors also suffer from transverse spherical aberration S , as shown in Figure 2.10, which may be determined by considering the variation of the image distance v with α , since

$$S = \Delta v \sin \gamma \approx \Delta v \gamma \quad (2.78)$$

From equation (2.74)

$$v_0 = f_m u / (u - f_m) \quad (2.79)$$

for $\alpha = 0$, while

$$v = v_0 + \Delta v = f_m u - (3uR\alpha/4 + R^2\alpha^2/2)/(u - 3R_\alpha/4 - f_m) \quad (2.80)$$

for $\alpha \neq 0$. Thus, for small α (ignoring terms in α^2)

$$\Delta v = (3R\alpha/4)(M + 1)^2 \quad (2.81)$$

where M is the magnification,

$$M = v/u \quad (2.82)$$

and, from equations (2.72) and (2.73),

$$\gamma = 2\alpha/(M + 1) \quad (2.83)$$

Thus

$$S = (3R\alpha^2/2)(M + 1) = (3k^2/2R)(M + 1) \quad (2.84)$$

—since S depends quadratically upon k , all rays are deviated to the same side of the $\alpha = 0$ image point.

2.2.3. Coma

Since at grazing incidence different parts of the mirror are at different distances from the object, the magnification varies across the mirror—the object distance u may vary by as much as the length of the mirror. As shown in Figure 2.12, an object is magnified more by the near

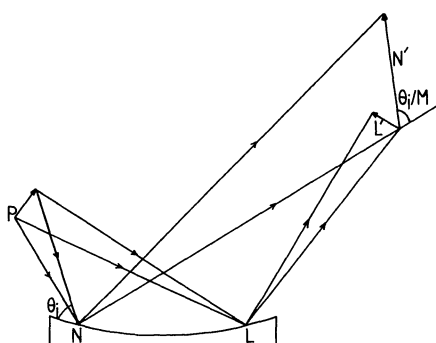


Figure 2.12. Coma and obliquity in the image formed by a spherical mirror.

edge of the mirror at N (forming an image at N') than by the far edge at L (forming an image at L'). Figure 2.12 also shows that the image is tilted at angle θ_i/M with respect to the object field—this is known as obliquity.

2.2.4. Reduction of Aberrations

To reduce the aberrations when using spherical mirrors it is necessary to use large grazing angles (to reduce astigmatism) and small apertures (to reduce spherical aberration and coma). To achieve the former condition a reflecting material with a large critical angle is necessary; since the refractive index decrement δ is proportional to the electron density, as shown by equation (1.19), this means a dense material such as platinum, which has 5.14×10^{30} electrons m^{-3} . The corresponding value of θ_i is 18° for carbon K_α radiation, which gives $f_s/f_m = 11$ so that astigmatism remains large.

Decreasing the aperture (i.e., decreasing k) to reduce spherical aberration and coma also reduces the collecting power of the mirror and leads to worsening of the diffraction limit to the resolving power—this is approximately equal to $\lambda/2\theta^{(14)}$ where θ is the maximum semiaperature angle, which is essentially equal to θ_i for grazing incidence.

It is possible to reduce the aberrations without using large grazing angles and small apertures in several ways. These include single aspheric mirrors, pairs of cylindrical mirrors with perpendicular axes of revolution, and systems of conic sections.

2.3. Focusing at Grazing Incidence with Single Aspheric Reflectors

A simple departure from a spherical surface that may be used to correct astigmatism at a given angle of incidence⁽¹⁵⁾ arises from defining a meridian radius of curvature R_m and a sagittal radius of curvature R_s such that

$$R_m \sin \theta_i = R_s / \sin \theta_i \quad (2.85)$$

i.e., the focal lengths are equal. Thus

$$R_s = R_m \sin^2 \theta_i \quad (2.86)$$

—the surface is toroidal, with optical axes coinciding with the axis of symmetry.

To avoid spherical aberration with a single mirror it is possible to use an elliptical mirror.⁽¹¹⁾ This does not, however, remove astigmatism, and the object has to be at one focus with the image at the other.

It is also possible to remove spherical aberration completely using a parabolic mirror⁽¹⁶⁾; however, field obliquity remains large. Methods of improving image quality include designing surfaces with small departures from parabolic form, thus giving the possibility of reducing field obliquity at the expense of a small amount of spherical aberration. These analyses show that the optimum reflector should have a cubic surface.⁽¹⁶⁻¹⁸⁾ Coma, however, cannot be corrected by a single surface of any shape. Also, as the form of the surface becomes more complicated, the manufacturing tolerances become more stringent and thus the mirrors are much more difficult to make. For these reasons, practical grazing incidence systems use combinations of mirrors to reduce the aberrations.

2.4. Compound Systems

Compound systems, in which the radiation is reflected at grazing incidence from two or more spherical or aspherical surfaces, are of two main types. The first, which are generally known as Kirkpatrick–Baez systems, involves reflectors whose meridian planes are at right angles (crossed). The second, known as Wolter systems, uses combinations of coaxial and confocal conic sections.

2.4.1. Kirkpatrick–Baez Systems⁽¹¹⁾

A simple Kirkpatrick–Baez system is shown in Figure 2.13. This uses, ideally, two cylindrical mirrors with equal radii of curvature R_m , and produces a real point image of a point object, and therefore a real extended image of an extended object. Thus astigmatism is removed. In

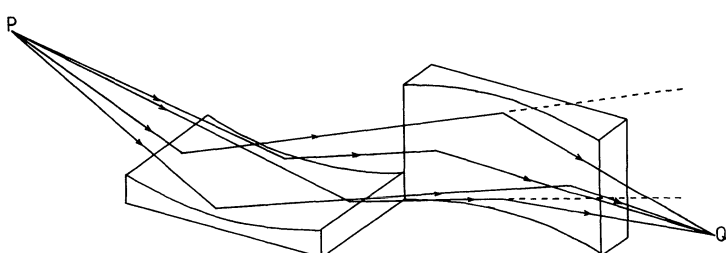


Figure 2.13. Two-mirror Kirkpatrick–Baez system.

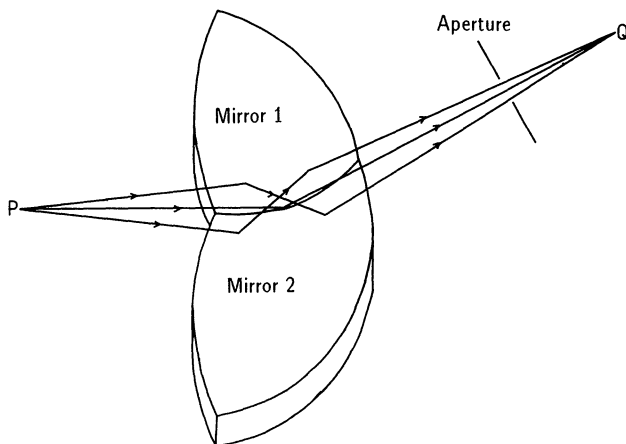


Figure 2.14. Hildenbrand–Montel mirror system.

practice spherical mirrors may be used since the sagittal focal lengths are so much greater than the meridian focal lengths.

This simple system, however, introduces another type of distortion, anamorphotism. Since the two mirrors are not coincident, the object distance for the meridian reflection in the first mirror is less than that for the sagittal reflection in the second mirror. Thus the magnification is different in the two directions. Corrections for this can be made in several ways, including placing the detector at an angle to the perpendicular to the optical axis,⁽¹¹⁾ or using a third reflector in the same plane as the first.⁽¹¹⁾ It is also possible, in principle, to devise systems in which both mirrors are at the same distance from the object,^(19,20) as shown in Figure 2.14. This sort of arrangement is extremely difficult to manufacture and its use has not been reported.

Kirkpatrick–Baez systems can be constructed to significantly reduce coma, although at least two pairs of crossed mirrors are necessary. This is so that the Abbe sine condition, which is equivalent to the requirement that all geometrical paths through the optical system result in the same magnification, is upheld. This is demonstrated in Figure 2.15, for two dimensions; the condition requires that $\sin \alpha / \sin \alpha'$ is constant, which cannot be upheld for a single reflection in two dimensions (Figure 2.15a), since as the angle α is increased α' decreases, whatever the surface shape. Two reflections are needed, as in Figure 2.15b, so that in the three-dimensional Kirkpatrick–Baez system four reflections in total are needed, two in each direction. Even this cannot completely remove coma if spherical mirrors are used—aspheric surfaces are necessary for this.⁽²¹⁾

Thus, although Kirkpatrick–Baez systems can be designed to considerably lessen the aberrations of reflecting systems at grazing incidence,

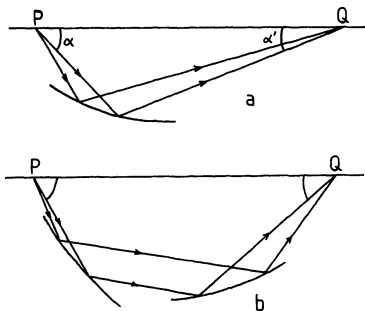


Figure 2.15. Reduction of coma in Kirkpatrick–Baez systems. In (a), the Abbe sine condition is not satisfied and coma is significant. In (b), coma is reduced by ensuring that the Abbe sine condition is satisfied.

rather complicated systems are usually necessary. Because of this, Wolter systems are now often preferred in practice.

2.4.2. Wolter Systems⁽²²⁾

Wolter systems exploit the well-known imaging properties of conicoidal surfaces, illustrated in Figure 2.16. Images of very good quality can

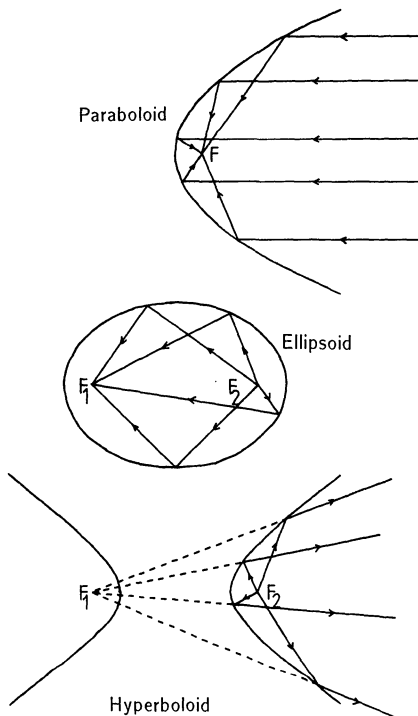


Figure 2.16. Reflections from single conicoidal surfaces.

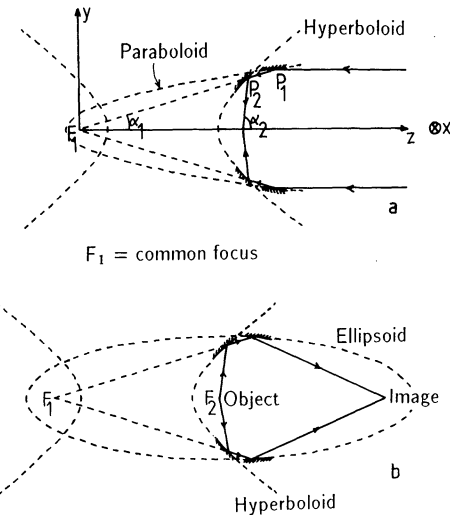


Figure 2.17. Wolter type I optics: (a) telescope; (b) microscope.

be obtained by successive reflections from sections of two such surfaces. In a Wolter type I system both reflections are from internal surfaces (Figure 2.17), while in a type II system the first reflection is internal and the second is external (Figure 2.18), and in a type III system the first is external and the second internal (Figure 2.19).

For radiation passing through the foci, because of the circular

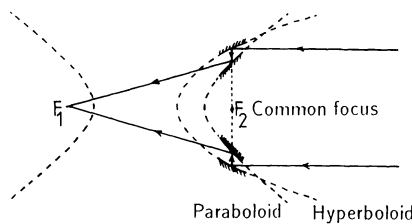


Figure 2.18. Wolter type II telescope.

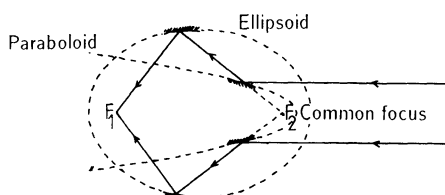


Figure 2.19. Wolter type III telescope.

symmetry, astigmatism and spherical aberration are eliminated for these systems. The Abbe sine condition can also be shown to hold to a good approximation. Consider, for example, Figure 2.17a,⁽²²⁾ where F_1 at $(y, z) = (0, 0)$ is the common focus of the paraboloid and the hyperboloid and F_2 is the second focus of the hyperboloid. The generating equation of the paraboloid is (in the plane $x = 0$)

$$y = [p(2z + p)]^{1/2} \quad (2.87)$$

where for a point $P_1(x_1, y_1)$ on the surface

$$p = F_1 P_1 - z_1 \quad (2.88)$$

The generating equation of the hyperboloid is

$$(z - e)^2/a^2 - y^2/b^2 = 1 \quad (2.89)$$

where for a point $P_2(x_2, y_2)$ on the surface

$$a = (1/2)(F_1 P_2 - F_2 P_2) \quad (2.90)$$

and the eccentricity e is given by

$$e^2 = a^2 + b^2 \quad (2.91)$$

If P_1 and P_2 are such that an incoming ray parallel to the z axis hits the paraboloid at P_1 and the hyperboloid at P_2 , then the line $F_1 P_2 P_1$ makes an angle α_1 with the z axis, where

$$\tan \alpha_1 = y_1/z_1 = y_2/z_2 \quad (2.92)$$

so that

$$F_1 P_1 = z_1 + p = y_1/\sin \alpha_1 \quad (2.93)$$

and

$$\cos \alpha_1 = z_1/(z_1 + p) \quad (2.94)$$

The line $F_2 P_2$ makes an angle α_2 with the z axis, and the Abbe sine condition is then (approximately) satisfied if the ratio $y_1/\sin \alpha_2$ is (approximately) independent of z_1 . From Figure 2.17a and equation

(2.93)

$$F_1 P_2 = y_2 / \sin \alpha_1 = (y_2 / y_1)(z_1 + p) \quad (2.95)$$

and

$$F_2 P_2 = y_2 / \sin \alpha_2 \quad (2.96)$$

Thus, from equations (2.90) and (2.92),

$$\begin{aligned} a &= (1/2)(y_2 / y_1)(z_1 + p - y_1 / \sin \alpha_2) \\ &= (1/2)(z_2 / z_1)(z_1 + p - y_1 / \sin \alpha_2) \end{aligned} \quad (2.97)$$

i.e.,

$$y_1 / \sin \alpha_2 = z_1 + p - 2az_1 / z_2 \quad (2.98)$$

For the point P_2 , equations (2.89) and (2.92) give

$$(z_2 - e)^2 / a^2 - (z_2^2 \tan^2 \alpha_1) / b^2 = 1 \quad (2.99)$$

which, solving quadratically and using equation (2.94), gives

$$z_2 = b^2 / [e \pm a(1 + p/z_1)] \quad (2.100)$$

The smaller of the two values of z_2 lies on the other branch of the hyperboloid, and thus the negative sign in equation (2.100) is the relevant one. Substituting this equation into equation (2.98) gives

$$y_1 / \sin \alpha_2 = p(e^2 + a^2) / b^2 + z_1[(e - a) / b]^2 \quad (2.101)$$

Since, from equation (2.91), a and e are of the same order, $y_1 / \sin \alpha_2$ is not strongly dependent on z_1 and so the sine condition is approximately satisfied. Thus coma is small.

2.4.2.1. Wolter-Schwarzchild Systems

It is possible to completely eliminate coma in a modified Wolter system by designing the two coaxial surfaces such that the Abbe sine condition is exactly satisfied. This problem was first treated by Schwarzchild,⁽²³⁾ and applied to grazing incidence systems by Wolter,⁽²⁴⁾ who considered small departures from the conicoidal forms. The elimination of coma leads to a corresponding improvement of resolution.⁽²⁵⁾

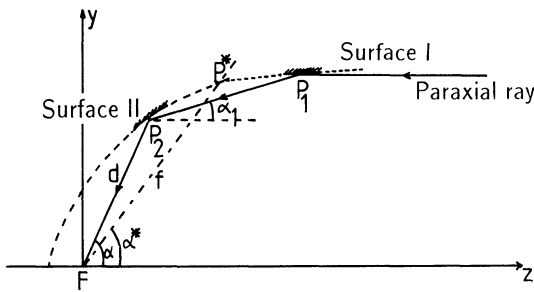


Figure 2.20. Wolter–Schwarzschild type I optical system.

The parameters of a Wolter–Schwarzschild system are defined in Figure 2.20. A point $P_1(y_1, z_1)$ on the first surface has coordinates

$$y_1 = f \sin \alpha \quad (2.102)$$

and

$$\begin{aligned} z_1 = D + (f^2 \sin^2 \alpha)/4D \\ + d_0[1 - (f/D) \sin^2(\alpha/2)]^{(2D-f)/(D-f)} [\cos^2(\alpha/2)]^{f/(D-f)} \end{aligned} \quad (2.103)$$

where the origin is at the focal point F and f is the distance between F and P^* , the intersection point of the two surfaces. For a point $P_2(y_2, z_2)$ on the second surface,

$$y_2 = d \sin \alpha \quad (2.104)$$

and

$$z_2 = d \cos \alpha \quad (2.105)$$

where

$$\begin{aligned} 1/d = (1/D) \sin^2(\alpha/2) \\ + (1/d_0)[1 - (f/D) \sin^2(\alpha/2)]^{-f/(D-f)} [\cos^2(\alpha/2)]^{D/(D-f)} \end{aligned} \quad (2.106)$$

In these equations, D is interpreted as the distance between the vertices of the two surfaces and d_0 as the distance of the focal point from the vertex of the second surface. Since $y_1/\sin \alpha$ is defined to be constant by equation (2.102), these surfaces naturally satisfy the Abbe sine condition.

2.5. Resolution of Grazing Incidence Systems

The performances of grazing incidence focusing systems deteriorate in resolution for off-axis image points. There are no simple analytical techniques for evaluating the imaging properties, and it is common to use ray-tracing methods. These depend on the parameters of individual systems and examples will be considered in Chapter 10.

Manufacture of Grazing Incidence Reflective Optics

3.1. Manufacturing Tolerances

In addition to the surface roughness effects discussed in the previous chapter, two other considerations must be taken into account when assessing the performances of real grazing incidence systems. These are geometric errors in the surface figures, and misalignments of the components of compound systems.

3.1.1. Surface Figure Errors

The departure of the surface figure from the ideal may be simulated by slight mathematical modifications to the equation describing the surface. These are normally assumed to take the form of elliptical deviations from the sagittal cross section and sinusoidal deviations from the meridional cross section.⁽¹⁾ An alternative, and more generalized, approach is to describe the surface figure errors as the superposition of two uncorrelated perturbations.⁽²⁾ These are the normal displacement and the misorientation of small segments of the tangent plane. This second approach is not in common use and will not be described here.

An undeformed conicoidal surface used at grazing incidence can be described by the equation⁽¹⁾

$$\rho_z^2 - \rho_0^2 = 2pz - (1 + \eta)z^2 \quad (3.1)$$

where

$$\rho_z^2 = x^2 + y^2 \quad (3.2)$$

ρ_0 is the central ($z = 0$) radius, η (known as the deformation parameter)

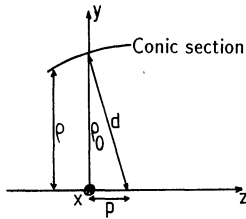


Figure 3.1. Definition of an ideal conicoidal surface.

defines the type of conicoid, and

$$p^2 = d^2 - \rho_0^2 \quad (3.3)$$

where d is the perpendicular distance from the center of the surface to the axis (Figure 3.1). Equation (3.2), a circle with radius ρ_z , gives the undeformed sagittal cross section. Elliptical deformations of this can be described in terms of a component with constant azimuthal orientation (Figure 3.2a) and one with a 90° azimuthal rotation from one end of the mirror to the other (Figure 3.2b). If Q_1 is the maximum deviation from the circular cross section of the component with constant orientation, the deformed cross section may be described by the equation

$$1 = x^2/(\rho_{z1} + Q_1)^2 + y^2/(\rho_{z1} - Q_1)^2 \quad (3.4)$$

or

$$\rho_{z1}^2 = \rho_z^2 - 2Q_1(x^2 - y^2)/\rho_0 \quad (3.5)$$

since, to maintain high-quality imaging, Q_1 must be much less than ρ_z for all z , and ρ_z does not change by a large amount along the mirror.

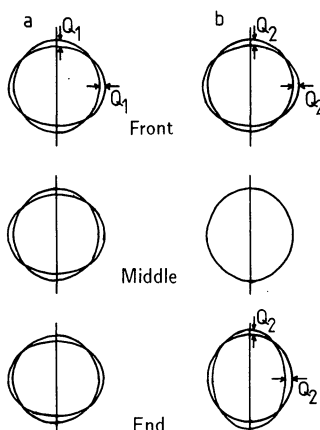


Figure 3.2. Elliptical deformation of a conicoidal surface: (a) constant azimuthal orientation; (b) 90° azimuthal rotation from end to end.

For the component with changing orientation, the maximum deviation Q_2 changes sign from one end of the mirror to the other, falling to zero in the middle. Thus the deviation may be described by

$$Q_{2z} = Q_2 z / z_m \quad (3.6)$$

where z_m is the maximum value of z ,

$$-z_m \leq z \leq z_m \quad (3.7)$$

Since, in equation (3.1), the term in z^2 is small (e.g., $\eta = -1$ for a paraboloid),

$$z \approx (\rho_z^2 - \rho_0^2)/2p \quad (3.8)$$

and

$$z_m \approx (\rho_m^2 - \rho_0^2)/2p \approx \rho_0(\rho_m - \rho_0)/p = \rho_0 T/p \quad (3.9)$$

so that

$$A = z/z_m \approx (\rho_z^2 - \rho_0^2)/2\rho_0 T \quad (3.10)$$

where

$$T = \rho_m - \rho_0 \quad (3.11)$$

The deformed sagittal cross section may then be described by

$$1 = x^2/(\rho_{z2} + Q_2 A)^2 + y^2/(\rho_{z2} - Q_2 A)^2 \quad (3.12)$$

which reduces to, using the approximation $Q_2 < \rho_z$,

$$\rho_{z2}^2 \doteq \rho_z^2 - 2Q_2 A(x^2 - y^2)/\rho_0 \quad (3.13)$$

The general surface equation for elliptical deformation is then given, using equations (3.1), (3.5), and (3.13), by

$$\rho_z^2 - \rho_0^2 - 2(x^2 - y^2)(Q_1 + Q_2 A)/\rho_0 = 2pz - (1 + \eta)z^2 \quad (3.14)$$

The sinusoidal deformation of the meridional cross section can be described in terms of three parameters—the amplitude of the variation, Q_3 , the number of periods per unit length, n , and the axial phase shift, ω (Figure 3.3). The sagittal cross-sectional radius then becomes

$$\rho_{z3} = \rho_z + Q_3 \sin(n\pi A + \omega) \quad (3.15)$$

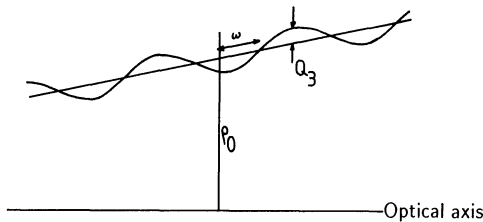


Figure 3.3. Sinusoidal deformation of a conicoidal surface.

and, since the sinusoidal variation is small, the surface equation is

$$\rho_z^2 - \rho_0^2 + 2\rho_0 Q_3 \sin(n\pi A + \omega) = 2pz - (1 + \eta)z^2 \quad (3.16)$$

A further type of surface deformation is obtained if the deformation parameter η is not constant, but varies with ρ_z (or z). The relationship between the change $d\eta$ in η and that, $d\rho_z$, in ρ_z is, from equation (3.1),

$$d\eta = -(2\rho_z/z^2) d\rho_z \quad (3.17)$$

If Q_4 is the maximum deviation at the ends of the mirror ($z = z_m$), then

$$d\eta = -2Q_4 \rho_m / z_m^2 \quad (3.18)$$

Using equation (3.9) for z_m and setting $\rho_m \approx \rho_0$ gives

$$d\eta \approx -2Q_4 p^2 / \rho_0 T^2 \quad (3.19)$$

Combining all the surface deformations into one surface equation gives

$$\begin{aligned} \rho_z^2 - \rho_0^2 - 2(x^2 - y^2)(Q_1 + Q_2 A)/\rho_0 + 2\rho_0 Q_3 \sin(n\pi A + \omega) \\ = 2pz - (1 + \eta - 2Q_4 p^2 / \rho_0 T^2)z^2 \end{aligned} \quad (3.20)$$

The spatial resolution δ of an image-forming system is given by

$$\delta = \lambda/2 \sin(\theta_a/2) \quad (3.21)$$

where θ_a is the largest aperture angle between rays contributing to the image and λ is the wavelength of the radiation. The effects that the deformations have on the resolution of a single paraboloidal reflector with $\rho_m = 1.01\rho_0$, $z_m = 1.5\rho_0$, and a focal length of $30\rho_0$ are shown in Figure 3.4. In order that the resolution is not worsened by more than

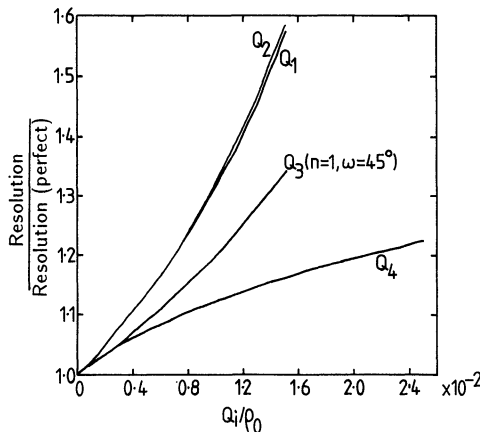


Figure 3.4. Effects of surface figure deformations on the resolution of a single paraboloidal mirror.

about 20%, the maximum deformations should be less than about 1% of the central radius. For compound systems the analysis is more complicated since the effects of the deformations of the individual surfaces can be made to cancel, or nearly so, by suitable orientations of the elements with respect to one another.⁽¹⁾ However, a useful rule of thumb would be to keep the deformations of each element to within about 1% of the corresponding central radius.

For diffraction-limited imaging, all waves contributing to an image point should have maximum phase deviations within $\pm\pi/4$ rad.⁽³⁾ The deformations discussed above could lead to much larger phase errors than this. These, however, can be removed by suitable orientations of the optical elements since the deformations vary smoothly along the surfaces. This cannot be done for surface irregularities such as roughness (with spatial periods of less than about one wavelength) as discussed in Chapter 2, or for lower frequency irregularities.

The superposition of the incident and reflected waves results in a standing wave with period δ given by equation (3.21). The fabrication tolerances for diffraction-limited imaging may be defined in terms of the spacings between the nodes of this standing wave, since a phase error of 2π rad in the reflected wave is caused by an element of the mirror being displaced by one period. The maximum aperture angle for a grazing incidence focusing element is $2\theta_c$ where θ_c is the critical angle. Thus the highest possible resolution is

$$\delta_{\max} = \lambda/2 \sin \theta_c \quad (3.22)$$

and the fabrication tolerance is one-eighth of this (corresponding to a $\pi/4$

phase deviation),

$$\delta_{\text{tol}} = \pm \lambda / 16 \sin \theta_c \quad (3.23)$$

or, more generally,

$$\delta_{\text{tol}} = \pm \lambda / 16 \sin \theta \quad (3.24)$$

where θ is the maximum glancing angle to be used by the element.

From equations (1.19) and (1.71), for small refractive index decrement,

$$\sin \theta_c = (Ne^2 / 4\pi^2 \epsilon_0 m_e c)^{1/2} \lambda \quad (3.25)$$

where N is the electron density, typically about 10^{30} m^{-3} . Thus, the tolerance (3.24) is about 1 nm, independent of the wavelength.

3.1.2. Misalignments

The positional errors of an element of a compound system with respect to a fixed system of coordinates can be divided into two categories. Linear misalignments are displacements of the element along (despace) and perpendicular to (decenter) the optical axis, and angular misalignments are tilts about the center of the element. Although angular misalignments in particular can cause severe degradation of image quality,⁽¹⁾ it is always possible, at least in principle, to optimize a compound system by allowing the positions of the elements to be freely adjustable with respect to one another.⁽⁴⁾ This also allows maximum cancellations of the surface figure errors.

Thus the performance of a compound system can be made to be primarily dependent on the quality of the individual mirrors, rather than on their relative positions. Linear misalignments typically increase the linear size of the point spread function by about 10% of the despace and 100% of the decenter, and angular misalignments increase the angular size of the point spread function by about twice the tilt angle.⁽¹⁾

3.2. Manufacturing Techniques

Grazing incidence optical components may be made in two ways—either by grinding, lapping, and polishing the surface to the required figure, which may then be used as the mirror itself or as a master in

replication techniques, or by producing a surface of simpler figure that is then bent in a controlled way to the required shape.⁽⁵⁾ Bent mirror optics, as well as being cheaper to manufacture, allow adjustments over ranges of curvature giving the possibility of finer adjustments. In addition, one system could be used for several applications.

For rigid mirrors, in order to achieve the tolerances established in Chapter 2 and Section 3.1, three areas of development have been necessary.⁽⁶⁾ The first of these is materials evaluation, for substrates and coatings, the main concern being that the surface must be polishable. The tolerances on surface figure and smoothness can only be achieved with materials of suitable mechanical, physical, and chemical stability. The second development is the manufacture of very precise mirror substrates, by diamond turning of metals and precision grinding of glasses and ceramic materials, followed by lapping and polishing. On flat disks, rms surface roughnesses as small as 0.2 nm are now possible. The third development, the metrology of the surfaces, allows the measurement of axial profiles to nanometer accuracy and of surface roughness to subnanometer accuracy, as well as diameter and circularity.⁽⁷⁾ For bent mirror optics accurate manufacture of bending blocks is also necessary.

3.2.1. Materials Evaluation⁽⁸⁾

There are many factors to be taken into account when evaluating the usefulness of a material for grazing incidence mirrors, some of which are dependent on the environment in which the mirror is to be used. Thus, for example, a mirror suitable for use in an X-ray telescope, with low incident fluxes, may be totally unsuitable in a synchrotron where the flux can be very high, possibly causing thermal distortion or damage to the surface. Apart from environmental considerations, the optical quality attainable depends on the microstructure and homogeneity of the material.

An important criterion is the polishability of the surface, i.e., the size of the residual roughness. Several materials can be polished to high degrees of smoothness, but not all of these are suitable for forming into the required figures. They can, however, be used as coatings on other materials and this type of mirror is commonly used. Typical values of roughness, after polishing, for several materials are shown in Table 3.1.⁽⁹⁾ By careful quality control, all the materials shown could, at least for the long-wavelength end of the soft X-ray range, satisfy the criterion (2.71) that the surface roughness should not exceed the wavelength. For short-wavelength soft X rays, however, the choice is more limited, and silicon carbide, fused quartz, or electroless nickel are the most suitable materials.

Table 3.1. Roughnesses of Candidate Mirror Materials⁽⁹⁾

Material	rms roughness (nm)	
	Average	Smallest measured
CVD silicon carbide	1.0	0.4
Fused quartz	1.3	0.4
Electroless nickel	1.8	1.1
Titanium	2.7	1.3
Copper	3.0	1.3
TZM	4.0	1.5
Stainless steel	4.0	3.3
Molybdenum	4.7	1.5
Invar	4.7	2.8
Diamond-turned copper	4.9	1.0
Aluminum	5.3	1.0
Monel	5.6	2.9
Beryllium copper	6.8	2.8
Potassium chloride	11.0	2.9

The material must be dimensionally, mechanically, thermally, and chemically stable. Residual internal stresses, which alter the form of the component as they gradually change or relax, are the cause of most macrodimensional instabilities. There are several possible causes of internal stresses, including the methods of manufacturing and machining the blank, microstructure, inhomogeneities, and atomic and thermal incompatibility of the substrate and coating. Small departures from metallurgical equilibrium and internal mechanical stresses can also cause microstructural changes, such as precipitation, grain growth, and ordering. As well as altering the surface figure, these factors can also give rise to micromechanical instabilities, which increase the surface roughness.

The mechanical properties of several mirror materials are shown in Table 3.2.^(8,10) Metals are ductile and deform permanently at low stresses (microcreep) and therefore should not be used in situations where external stresses are likely. On the other hand, beryllium has a higher specific stiffness than the glasses do and is therefore more suitable in a situation where it is important to have light components (e.g., telescopes). Silicon carbide also has a high specific stiffness. If the optical component is tubular, then the diametric stiffness is a more relevant parameter, and beryllium and silicon carbide are still superior. These properties also show why heavy metals are not commonly used (except for coatings)—although they can have higher reflectivities at larger glancing angles due to their larger critical angles, they are not so stable mechanically as lighter materials are. A further mechanical consideration is the ability to withstand vibration. Under conditions of severe vibration,

Table 3.2. Mechanical Properties of Mirror Materials^(8,10)

Material	Density ρ (kg m^{-3})	Young's modulus E (Pa)	Specific stiffness (E/ρ)	Diametric stiffness (E/ρ^3)	Microcreep strength (Pa)
Beryllium	1850	2.9×10^{11}	1.57×10^8	45.8	$14\text{--}60 \times 10^6$
Copper	8930	1.3×10^{11}	1.46×10^7	0.18	
Titanium	4500	1.2×10^{11}	2.67×10^7	1.3	
Nickel	8900	2.0×10^{11}	2.25×10^7	0.28	
PHAA ^a	2700	6.9×10^{10}	2.56×10^7	3.5	30×10^6
PSVS ^b	2200	7.4×10^{10}	3.35×10^7	6.9	
TMSVS ^c	2210	6.7×10^{10}	3.03×10^7	6.2	
Pyrex	2230	6.1×10^{10}	2.74×10^7	5.5	
SiC (CVD)	3200	4.5×10^{11}	1.40×10^8	13.7	

^aPrecipitation-hardened aluminum alloy.^bPure synthetic vitreous silica (trade names Spectrosil, Suprasil, and Corning 7940). Remelted quartz (Vitreosil, Herasil, and Homsil) is similar.^cTitanium-modified synthetic vitreous silica (trade name ULE Silica).

such as rocket launches, metal mirror surfaces can be seriously degraded, while Pyrex and ceramic surfaces are slightly degraded. No such effects have been observed for most glasses. Finally, harder materials are to be preferred because of their higher resistance to surface damage.

Table 3.3 gives the thermal properties of the materials.^(8,10) Metals have larger coefficients of thermal expansion than the glasses or silicon carbide do, and therefore undergo larger dimensional changes with changes of temperature. On the other hand, beryllium distorts far less in conditions that cause thermal spiking than most glasses do, although the best materials in this respect are silicon carbide and titanium-modified synthetic vitreous silica. It is clear that Pyrex is unsuitable in such conditions.

Chemical stability of mirror surfaces is important for two reasons—the capability of resisting any corrosive environment and, for surfaces that become contaminated, withstanding the action of chemicals used for refurbishment. This refurbishment, usually carried out by recoating the component, could also be necessary after the mirror has been subject to vibration. For metal optics, removal of the original coating prior to recoating causes significant degradation of the surface, and repolishing and sometimes refiguring is necessary.

If possible, mirrors should be constructed from materials having little or no microstructure since, after machining, the surface will always retain a memory of the microstructure of the substrate. All the metallic materials used for grazing incidence mirrors do have significant microstructure, and then it is important that this does not alter with age,

Table 3.3. Thermal Properties of Mirror Materials

Material	Thermal expansion coefficient α (K^{-1})	Thermal conductivity λ ($W\ m^{-1}\ K^{-1}$)	Specific heat C ($J\ kg^{-1}\ K^{-1}$)	Thermal spiking distortion ($\alpha\rho C/\lambda$)
Beryllium	1.15×10^{-5}	310	1700	0.117
Nickel	1.28×10^{-5}	59	444	0.857
PHAA	2.3×10^{-5}	170	920	0.336
PSVS	5×10^{-7}	1.4	670	0.526
TMSVS	3×10^{-8}	1.3	750	0.038
Pyrex	3.3×10^{-6}	1.1	750	5.02
SiC (CVD)	2.9×10^{-6}	200	710	0.033

environment, or applied stress, since macrodimensional and volumetric changes often accompany microstructural changes. An example of this is precipitation hardening in aluminum alloys. The materials that have least microstructure are remelted quartz, titanium-modified synthetic vitreous silica, and, the best, synthetic vitreous silica.

As well as having less microstructure, glasses are much more homogeneous than metals are. It is also easier to assess their homogeneity because of their optical transparency. Apart from some types of bubble, it is extremely rare to find inclusions with dimensions less than a few millimeters in glasses. This is because small inclusions are very soluble in molten glass. None of the glasses listed have grain boundaries or internal cracks.

3.2.2. Mirror Manufacture

In order to make a grazing incidence mirror to the required accuracy, at least three stages of manufacture are required. First, a suitable blank must be prepared. It is desirable to keep both the wall thickness and the volume of the blank as small as compatible with the finished mirror, since the homogeneity of materials tends to become worse with increasing size. This is because, in addition to purely statistical reasons, larger pieces of material are, in general, more difficult to treat in a uniform manner. Second, the surface must be machined, at least roughly, to the required figure, the techniques for this depending on the type of material. The machined surface may then be coated to improve the quality of the mirror performance; this coating may in turn be machined. Finally, the surface is lapped (to improve or correct the figure) and polished.

3.2.2.1. Blank Manufacturing Methods⁽¹¹⁾

Metal and ceramic blanks can be produced by sintering of finely divided powder followed by hot isostatic pressing. Beryllium, for example, made in this way contains few inclusions and is of low porosity. It has, however, some grain boundary concentrations of beryllium oxide and metallic impurities, which produce growth structures in any coating.

This process is expensive, and metal (especially aluminum alloy) blanks are often prepared by other means, such as casting, casting and forging, and spinning or fabricating from rolled sheets. Since materials tend to be homogenized by rolling and spinning (and forging), blanks spun from rolled sheets tend to be very homogeneous.

Ceramics, such as silicon carbide, produced by sintering tend to have high (1–5%) porosities.⁽¹²⁾ Hot pressing,⁽¹³⁾ in which fine silicon carbide powder is inductively heated in a graphite die, and reaction bonding,⁽¹³⁾ in which fine silicon carbide and graphite powders are isostatically pressed and then siliconized in a furnace, can lead to better finishes. However, the best ceramic surfaces are made by chemical vapor deposition of silicon carbide, either as a coating (see below) or as thin-walled free-standing components—this is, however, difficult to manufacture in large pieces.

Glass blanks are made by fusing. This needs considerable care, since differential strains can be developed by nonuniform cooling of the melt. Nonuniform cooling rates can also cause local variations in the thermal expansion coefficient, again leading to internal strains. A change of shape will then be caused when part of such a blank is machined off. The magnitude of this “springing” depends on the level and distribution of the residual stress, and on the orientation of the stress axis relative to the removed part. For example, a tubular blank containing a rotationally symmetric stress distribution would change shape very little if external or internal machining was used to reduce the wall thickness, while if the stress axis intersected the tube wall the blank would undergo an asymmetric shape change. Thus, if it is not possible to reduce residual stresses to negligible proportions, the blank should be manufactured so that the stresses do not cause significant springing during machining. Rotationally symmetric tubular blanks, for example, can be made in a furnace that rotates about a vertical axis.⁽¹¹⁾

3.2.2.2. Diamond Turning of Metal Blanks^(14,15)

Diamond turning is a metal cutting process using specially modified⁽¹⁴⁾ or purpose-built⁽¹⁵⁾ lathes with single-crystal (natural) diamond cutting tools. Several very stringent requirements need to be met to

allow optical-quality surfaces of the required figures to be machined. The important material properties in this context are being free of voids and inclusions, having uniform grain sizes at boundaries, and being stress-free. In addition, the material must be compatible with the diamond cutting tool and should not distort while rotating on the machine. Metals exhibiting good diamond turning characteristics include aluminum, copper, brass, magnesium, silver, gold, and some nickel alloys. Iron and steels, however, are not suitable since they cause rapid tool degradation. It is normally considered that the tool edge should appear flawless at a magnification of 425 to enable accurate turning.⁽¹⁴⁾

The component support must not cause any distortion. Possibilities include a three-point system that does not introduce compensating loads, floating stress-free in liquid rubber (which holds the component in place when it solidifies), and holding the component against a fixture by vacuum (this requires very accurate mating surfaces). Vibrations, which are generated either by the lathe itself or are transmitted from nearby machinery through the floor or the atmosphere, must be removed or compensated for since they can cause surface variations of about the same size as the vibration amplitude. Other detrimental environmental influences, notably heat, must be compensated for or, better, prevented. Thermal transients can seriously degrade the accuracy of the surface figure, and therefore it is important to allow the operating conditions to stabilize before machining a surface.

The final requirement is that the cutting motion should be definable and repeatable, ideally controlled by a computer. However, even when all these requirements are met, surface finishes contain slight periodic roughness, caused by the curvature of the cutting tool and the feed rate of the tool across the surface. The magnitude and periodicity of this is controllable. Typical surface finishes have rms roughnesses of about 25–60 nm for modified lathes,⁽¹⁴⁾ or as low as 1.2 nm for purpose-built machines,⁽¹⁵⁾ while figure accuracies of about one part in 10^6 are possible.

3.2.2.3. Grinding of Glass Blanks^(16,17)

On Moh's hardness scale, glass has a scratch resistance of between 4.5 and 6.5, while that of quartz is 7. Thus, harder materials can be used to initially shape, by abrasion, the surfaces of glass and quartz blanks. This may be done using grinding wheels coated with, for example, silicon carbide (known as carborundum in this context) with a hardness of 9. Alternatively, loose abrasive grinding is used. In this, small, irregularly shaped particles of, for example, carborundum or corundum (mainly Al_2O_3 , hardness 9) tumble between a tool and the blank while they are moved about relative to one another. This causes small chips to be

broken out of the blank (and the tool) due to shear strains being set up in the material. The grinding process also causes fissures and flaws in the surface and, as more fissures are produced, the flaws connect with one another, causing removal of material. In addition, loose abrasive entering a fissure can exert lateral forces on the sides, causing the fissure to deepen. To reduce the surface roughness and fissure depth, progressively smaller abrasive particles (down to around $10\text{ }\mu\text{m}$ in diameter) are used. Typically this leaves surface irregularities several micrometers deep and the strained regions can be larger than this.

A grinding technique that is becoming more common is precision multipoint grinding.⁽¹⁸⁾ For this, precision machines of the type used in diamond turning are used, with the diamond tool replaced by a grinding wheel. Glasses, which are not normally considered to be machineable, can then be shaped to near-optical finishes and accuracies. This process relies on a low indentation load (less than about 10^{-2} N per cutting point), or a small scratch depth (less than about $0.1\text{ }\mu\text{m}$) together with a high scratch speed. In these cases, cracking and fracturing as described above do not occur, and grinding is due to plastic flow. Provided that wear of the grinding wheel is very much less than the required contour accuracy, or that the wheel is continually dressed so that its size is known, departures from the desired form can be as low as $0.5\text{ }\mu\text{m}$.

3.2.2.4. Coating of Surfaces

In order to obtain the best results from grazing incidence metal optics, the substrates are usually overcoated with a thin layer of a material that can be finished to a higher degree. The most common coating materials are electroless (and electroplated) nickel⁽⁸⁾ and chemical vapor-deposited silicon carbide.^(13,19) The major inaccuracies of plated optics arise from mismatches of the thermal expansion coefficients and from internal stresses in the coating caused by the plating process. Since silicon carbide coatings are usually deposited on silicon carbide substrates, there is no (or little) thermal mismatch. As shown in Table 3.3, however, there is a large mismatch between nickel and aluminum, so that this combination is not often used. Nickel and beryllium are more compatible thermally. This combination is also favored over nickel and aluminum because the Young's modulus of beryllium is much higher than that of aluminum; however, plating-induced stresses have not been reduced below 35 MPa ,⁽²⁰⁾ at least three orders of magnitude higher than in the glasses used for grazing incidence components.

Normally, nickel plating must be preceded by complex cleaning and pretreatment of the substrate, consisting of a large number of chemical and electrochemical stages. For large components it becomes increasingly

difficult to avoid contaminants and cross-contamination, and physical pretreatment is to be preferred.⁽⁸⁾ In this the substrate is cleaned by sputter-etching, which typically removes about $0.2\text{ }\mu\text{m}$ of the surface. A thin layer of an activating material such as copper, palladium, or gold is then sputter-deposited onto the surface. The two processes are overlapped for a short time to prevent contamination between them. On removal from the vacuum chamber used for the pretreatment the component is either immediately placed in a dedicated plating bath or stored in an inert (argon) atmosphere.

Chemical vapor deposition (CVD) is accomplished by introducing at least one, and usually more, gaseous reactants into a deposition chamber that contains a heated ($1100\text{--}1800\text{ }^{\circ}\text{C}$) substrate. The most common combination of gases used for CVD of silicon carbide is methyltrichlorosilane (MTS— CH_3SiCl_3) with hydrogen; other combinations include SiCl_4 or SiH_4 with hydrocarbons and hydrogen, and $(\text{CH}_3)_2\text{SiCl}_2$ with hydrogen, at pressures of between 10^{-3} and 1 atm, with the reduced pressures used to avoid vapor phase nucleation. The major difficulty with CVD systems lies in the control of the reactant delivery rates to the deposition chamber, necessary to obtain reproducible results. For reactants that are gases at room temperature this is not a problem since they can be (automatically) controlled using flow meters. MTS is, however, liquid at room temperature and so must be placed in a heated retort and transported by a carrier gas. The delivery rate is then only controllable indirectly since it depends on the flow rate of the carrier gas, as well as on retort pressure and temperature.

Either graphite or silicon carbide made in various ways⁽¹⁹⁾ can be used for the substrate, the advantage of the former being its cheapness. It is possible to form a mirror from solid CVD silicon carbide, but this is an extremely slow process because in order to obtain a stoichiometric material, deposition rates cannot be higher than $400\text{--}600\text{ }\mu\text{m hr}^{-1}$. Typically CVD layers a few millimeters thick are laid down.

3.2.2.5. Lapping and Polishing

Lapping refers to the generation of a surface of a particular form,⁽¹⁶⁾ and is achieved by working a tool conforming to the desired figure against the component, which has previously been approximately shaped as discussed in the previous sections. A thin layer of abrading material, usually a water-based slurry, is introduced between the tool and the component. In order to prevent the surface of the component retaining a memory of the lapping, the movement of the tool over the component should be random. If the tool and the component are both rigid, then they can remain in contact, for random motion, only if all the elements of

the surfaces are congruent. Thus true lapping is only possible for plane and spherical surfaces, and also for cylindrical surfaces with the loss of one degree of freedom of motion. For other initial tool and component shapes, lapping, if allowed to take its own course, will produce spherical surfaces.⁽²¹⁾ By making the tool as large as possible compared to the component, the change of shape of the tool may be minimized since the wear is proportional to the surface area. Even so, it is often necessary to restore the tool to its original figure during the lapping process.

Initially both the tool and the component have local protuberances and deviations from the ideal figure. During lapping the high spots are worn away faster, thus decreasing the magnitudes of the deviations, which can be made as small as about 5 nm.

Polishing refers to the removal of scratches, pits, and protuberances on a fine scale and need not involve any change in the surface figure. It is, however, a process very similar to lapping and it is not normally possible to distinguish when lapping finishes and polishing starts. The classical polisher material used for lapping is pitch. Other possible materials, which, however, do not produce such good finishes,⁽¹⁶⁾ are wax polishers, polyurethane, Teflon FEP, and felt (possibly impregnated with pitch). In the polishing stage pitch can again be used, while for glass surfaces rouge (Fe_2O_3), zirconium oxide, and cerium oxide suspended in water are the only widely used materials. For electroless nickel, γ -alumina is one of the more commonly used materials.⁽¹¹⁾

For pitch-polished CVD silicon carbide, surface finishes of better than 2 nm are possible.⁽¹²⁾ For pitch-polished reaction-bonded silicon carbide, the finish can be subnanometer.⁽¹²⁾ For electroless nickel, residual roughnesses of about 1 nm are possible,⁽⁷⁾ while for some glasses, very small roughnesses have been obtained—about 1 nm for ULE silica⁽⁸⁾ and about 0.1 nm for Spectrosil.⁽⁶⁾

3.2.3. *Replica Optics*

A major disadvantage of the production techniques discussed so far is that the whole process has to be gone through for each component, which is time-consuming and costly. This may be overcome, especially for complicated surface figures, by replicating from an accurately made master.

The principle of the replication technique is illustrated in Figure 3.5.^(22,23) A master of glass, ground, lapped, and polished as described in the previous sections, is made in the negative shape of the final mirror, and coated with a layer of metal (usually gold), typically 50–90 nm thick. The substrate, normally made of beryllium because of weight considerations—replica mirrors have, to date, only been used in

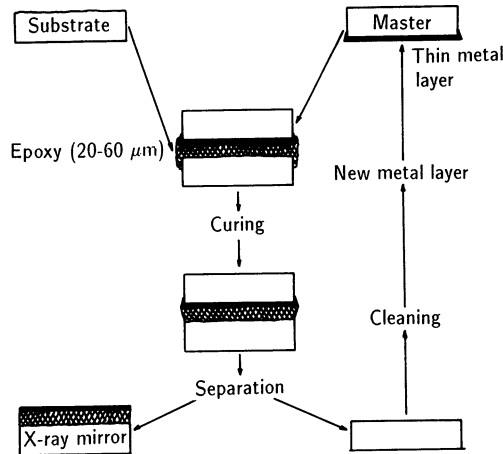


Figure 3.5. The principle of epoxy replication. (After Lainé *et al.*⁽²²⁾)

telescopes—is turned on a high-precision lathe to the approximate shape (within a few micrometers) of the desired final surface figure. To avoid print-through effects it is necessary to smooth the surface to about 300 nm. The coated master is then placed onto the substrate with a thin epoxy layer separating the surfaces, and after curing of the epoxy the master is removed (by thermal shock), leaving the metal layer molded into the mirror. After cleaning and recoating, the master can be used for further replication—up to ten replicas have been made without impairing the surface quality of the master.

During the epoxy molding stage, it is essential that the substrate is mounted in a stress-free way, especially during the curing phase, to avoid any deformation. Also, to give a uniform epoxy thickness, the master should be allowed to float in the epoxy. This, in addition, allows the master to, in part, follow the shrinkage of the epoxy. During the separation, it is necessary for the master and substrate to move freely along their concentric axis with no movement along the other axes.

Replica quality may be assessed by the shape, surface finish, and stability of the surface.⁽²³⁾ While the profile of the replica is a very good copy of the master, there are clear deviations in roundness, which are less than a micrometer in the master but several micrometers in the replicas. This can be improved by using a stiffer substrate or a more fluid epoxy. The surface finish of the replica depends mainly on two parameters, the surface roughness of the substrate and the thickness of the epoxy layer. Because the epoxy shrinks by about 2.5% during curing, an attenuated print of the substrate surface is formed on the replica surface. For a substrate roughness of 300 nm, the replicas have surface roughnesses of

0.3–0.5 nm for epoxy layers between 20 and 60 μm thick. As the epoxy layer becomes thinner, the replica surface roughness quickly increases, while for thicker layers shape distortion becomes measurable. Replica surface roughness can be decreased by polishing the substrate surface.

The surface roughness of replica optics tends to increase with time, with the percentage scatter increasing exponentially. This is represented by

$$\text{Scatter}(t) = \text{scatter}(0) \exp(bt) \quad (3.26)$$

where t is the time in years and b depends on how the epoxy is cured. For curing at 40 °C, $b = 0.6$ while at 80 °C, $b = 0.06$,⁽²³⁾ although the length of cure does not appear to be important. The amount of degradation is also reduced if the mirrors are stored in vacuum or under dry nitrogen.

3.2.4. Bent Mirror Optics^(24,25)

Another way of reducing the time and cost of manufacturing grazing incidence optics is to bend surfaces of simpler figure (flats, cylinders, or spheres), which are easier to produce and polish to a high degree of accuracy. A second advantage of bent mirror optics is that, by suitable choice of bending mechanism, it is possible to work with a large range of focusing conditions. The main disadvantages are in the stability and precision of the mirror and the bending block, which are both under stress. The mirror material is also likely to have a thermal expansion coefficient different from that of the bending mechanism. In order not to cause distortions in the mirror, the bending mechanism has, normally, to be made to optical quality.

3.2.4.1. Bending of Flats

The analysis given here follows closely that of Franks,⁽²⁴⁾ who considered the bending of a rectangular glass strip into a section of a right circular cylinder by applying equal bending couples to the ends. The underlying principles are the same for forming elliptical and parabolic surfaces by applying unequal bending couples, or by varying the width of the strip along its length, or by a combination of these.^(26,27)

The principles of a bending block are shown in Figure 3.6. The kinematic (three ball) mounting is to isolate the mirror from distortions, which may affect the base or the screw support. The thin-beam approximation, in which the thickness t of the strip is less than any other distance, is used in the analysis. It is usually assumed that the horizontal distance s between the load pins and the support pins must be greater

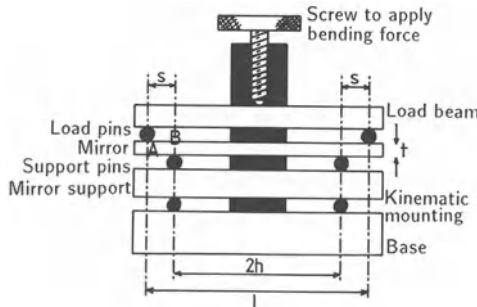


Figure 3.6. The design principle of mirror bending blocks. (After Franks.⁽²⁴⁾)

than $4t$, in order to minimize shear forces and displacements, for this approximation to be valid. If the screw applies a load P midway between the supports, then there is a uniform bending moment m of $Ps/2$ in the central region, and the beam bending equation is

$$m = Ps/2 = EI/R \quad (3.27)$$

where E is Young's modulus, R is the radius of curvature, and I is the moment of inertia,

$$I = wt^3/12 \quad (3.28)$$

for a strip of width w . The solution of the beam bending equation gives, for the deflection d of the point A (at a load pin) below the fixed point B (at a support pin),

$$d = Ps^2(31 - 4s)/Ewt^3 = s(31 - 4s)/6R \quad (3.29)$$

so that, in order to displace the ends of the beam by a distance d , the load must be

$$P = Ewt^3d/[s^2(31 - 4s)] \quad (3.30)$$

A beam bent to a radius of curvature R has a surface stress

$$\sigma = \pm Et/2R = \pm 3Etd/[s(31 - 4s)] \quad (3.31)$$

which, since R is usually large, is very small⁽²⁴⁾ (much less than the static fatigue limit).

To form a parabolic surface, as in Figure 3.7,⁽²⁷⁾ w and the bending

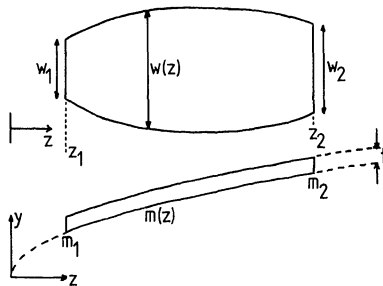


Figure 3.7. Formation of a parabolic surface by bending.

moment m are allowed to vary with z , i.e., along the length of the strip. If m_1 and m_2 are the moments at the ends z_1 and z_2 , then, by interpolation,

$$m(z) = m_2[(rz_2 - z_1) - (r - 1)z]/(z_2 - z_1) \quad (3.32)$$

where r is the ratio of the end moments. For grazing incidence optics, the radii of curvature are large and, to a good approximation,

$$1/|R| = d^2y/dz^2 \quad (3.33)$$

For a parabola, $y^2 = 4az$ so that

$$|R| = 2a^{-1/2}z^{3/2} \quad (3.34)$$

The variation of width of the strip with z to give a parabolic profile is, from equations (3.27), (3.28), (3.32), and (3.34),

$$w(z) = 24m_2z^{3/2}[(rz_2 - z_1) - (r - 1)z]/[Ea^{1/2}t^3(z_2 - z_1)^2] \quad (3.35)$$

A similar analysis can readily be undertaken for other profiles, by determining the relevant expression for d^2y/dz^2 .

If, in equation (3.35), the Young's modulus and thickness of the strip, and the end coordinates and ratio of end moments, are kept constant, then $w(z)$ remains unchanged if $m_2/a^{1/2}$ is also constant. The same strip can therefore be bent to give a series of parabolic cylinders with a range of values of the parameter a , by changing the magnitudes of the end moments while keeping their ratio constant. As a is changed, the focal length of the mirror will remain effectively constant since the value of z_1 is fixed. However, the mirror will have to be tilted to obtain the correct angle of incidence.

Using equation (3.35) to determine the end widths w_1 and w_2 and taking the ratio gives

$$w_1/w_2 = r(z_1/z_2)^{3/2} \quad (3.36)$$

Thus, for equal end widths, the ratio of the end moments is $(z_2/z_1)^{3/2}$, while if equal end moments are required the ratio of the end widths is $(z_1/z_2)^{3/2}$. Variation of r can be obtained by displacing the load application point from the center, or by having different distances between the load and support pins at the two ends.

Bending block design is complicated by the fact that the load beam, as well as the mirror, will bend. Typically, the deflection d required to give a suitable radius of curvature is less than $1\text{ }\mu\text{m}$.⁽²⁴⁾ Thus the allowable tolerances in the bending block manufacture are very small. In particular, to prevent twisting forces on the mirror, the pins and the mirror should be coplanar and parallel. Since there will always be some bending block manufacturing errors, the mirror should be flexible enough that any twisting is mainly accommodated at the ends of the strip. However, the mirror must be stiff enough to allow polishing. In order to prevent the load beam itself twisting, it is usual to specify that its compliance, $\partial d/\partial P$, is less than 10% that of the mirror.⁽²⁴⁾ Then, any relaxation of the mirror that may occur during use, will cause the radius of curvature to change by less than 10%. Typical mirror compliances are about $0.1\text{ }\mu\text{m N}^{-1}$ so that of the bending block should be less than $0.01\text{ }\mu\text{m N}^{-1}$. This can be achieved, for a steel bending block, if all components subject to bending are greater than about 12 mm thick.⁽²⁴⁾

The choice of a noncompliant system, in which ideally the load beam does not bend, or a compliant system is dependent on the application. In a compliant system the bending of the load beam demagnifies the motion of the screw mechanism, which may therefore be quite coarse, and thus the manufacturing tolerances of the bending block can be, relatively, low. The advantage of a noncompliant system is that relaxation of the mirror does not cause a change of curvature. However, the mechanical tolerances of the bending block must then match those of the mirror.

3.2.4.2. Bending of Cylinders⁽²⁵⁾

Bent cylindrical mirrors can be used as good approximations to ellipsoids, which are useful in synchrotron radiation beam lines where the horizontal and vertical divergences of the X-ray beam are usually different. The two radii of curvature of an ellipsoid may be derived from equations (2.75)–(2.77) by setting the meridian and sagittal focal lengths

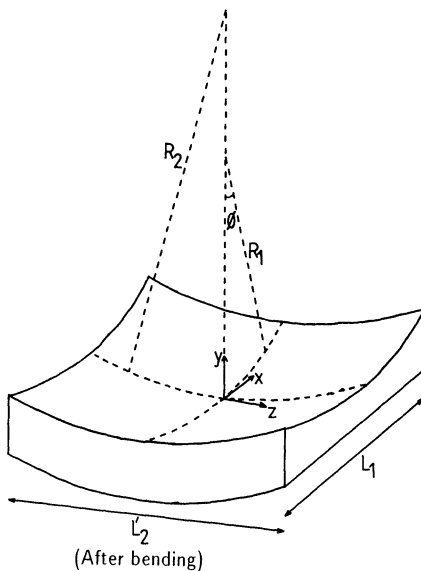


Figure 3.8. Bending of a cylindrical mirror.

equal,

$$R_1 = 2uv(\sin \theta_i)/(u + v) \quad (3.37)$$

and

$$R_2 = R_1/\sin^2 \theta_i \quad (3.38)$$

where u and v are the object and image distances and θ_i is the grazing incidence angle. Since θ_i is small, R_2 will be much larger than R_1 , and thus a cylindrical mirror of radius R_1 is bent so that the perpendicular radius is R_2 (Figure 3.8). For grazing incidence, the unbent lengths of the mirror satisfy $L_2 \gg L_1$ so that R_1 remains essentially unchanged after bending. A mirror of uniform cross section supported at each end and stresses downwards at the center gives a bent shape⁽²⁸⁾

$$y(x = 0, z) = 4S(1.5L_2z^2 - |z|^3)/L_2^3 \quad (3.39)$$

where S depend on the applied stress. The best imaging conditions are given by the smallest image of a point source, and S may be adjusted to give this. The radius of curvature R_2 of equation (3.38) is given, at the center of the mirror, if

$$S = S_0 = L_2^2/12R_2 \quad (3.40)$$

and this should be close to the value for best imaging. A rather larger value of S ,

$$S = kS_0 \quad (3.41)$$

with $k = 1 + 1/\sqrt{2} = 1.707$ in fact gives a smaller image of a point source, i.e., a better approximation to an ellipsoidal figure. An image point (x_i, y_i) formed from a source point (x_s, y_s) is moved by an amount

$$\begin{aligned}\delta x &= \{(1 + M)z[k(1 - |z|/L_2) - 1] \\ &\quad + 2v(1 - M)(1 - \cos \phi)/(1 + M)\} \sin \phi \sin \theta_i \quad (3.42)\end{aligned}$$

$$\delta y = -\delta x / \tan \phi \quad (3.43)$$

where $M = v/u$ is the magnification and ϕ is the angular displacement along the short mirror axis (Figure 3.8). These expressions show that the deviation of the image depends on the position of the reflection along the mirror and thus each longitudinal slice of the mirror (x, ϕ constant) contributes a line, inclined at an angle ϕ to the vertical, to the image. For magnifications close to unity, the second term in equation (3.42) is much smaller than the first, and the total size of the image is increased by

$$\Delta x \simeq 0.3L_2 \sin \phi \sin \theta_i \quad (3.44)$$

$$\Delta y = -\Delta x / \tan \phi \quad (3.45)$$

for the optimum value, 1.707, of k . Smaller or larger values of k produce

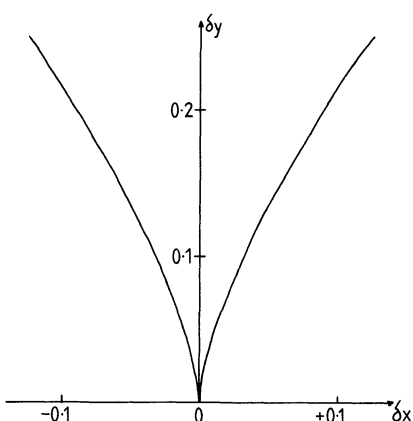


Figure 3.9. The image of a point source from a lateral slice of a bent cylindrical mirror (magnification not close to unity).

more blurring. If M is not close to unity, the second term in equation (3.42) dominates and the image becomes a cusped curve with, since the mirror dimensions are such that the angle ϕ is small,

$$\delta x \approx \pm v\phi^3 \sin \theta_i \quad (3.46)$$

$$\delta y \approx \pm (-v\phi^2 \sin \theta_i) \quad (3.47)$$

where the plus sign corresponds to $M \ll 1$ and the minus sign to $M \gg 1$. The image of a point source from a lateral slice of the mirror is as shown in Figure 3.9.

3.3. Metrology of Grazing Incidence Optical Components⁽⁷⁾

In the previous sections the importance of forming very precise surfaces, in terms of figure and residual roughness, and the accuracies that have been achieved were discussed. It is clear that the production of X-ray optical components cannot be carried out in isolation from their measurement and evaluation. It may be necessary to carry out a series of measurements, of increasing accuracy, throughout the various manufacturing stages. The interpretation of the measurements is often very complicated, since while parts of the mirror may be within the allowable tolerances, other parts may not be. It could then be difficult to determine whether the mirror as a whole is up to specification.

The types of measurement carried out can be classified into two groups. In the first of these the mirror surface is probed point by point in a sequential manner, while in the second the complete mirror, or large parts of it, are measured simultaneously by interferometry. Some tests have also been carried out using soft X rays. The coordinates of all points on the mirror surface must be known in order to predict its performance, and it is normal to consider that deviations from the ideal surface give rise to two categories of topography. Macrotopography refers to perturbations with wavelengths larger than a few millimeters, and with amplitudes greater than 100 nm. The most common macrotopographic measurements are of circularity, diameter, and axial profile. Perturbations of shorter wavelength and smaller amplitude are referred to as microtopography.

3.3.1. Probe Methods

Two types of probe are used for both macrotopography and microtopography—mechanical and optical. An advantage of optical

probes is that there is no physical contact with the surface; however, they are restricted to measurements on reflecting (i.e., polished) surfaces. Mechanical probes can be used, for example, to measure surface figures prior to polishing.

3.3.1.1. Macrotopography

Circularity and diameter are common measurements in optics and engineering, and measuring machines are commercially available. Axial profile measurements are more specialized and have required the development of special machines.^(22,29,30)

Circularity measurements⁽⁷⁾ are based on a precise axis of revolution, and departures from circularity are measured with a linear transducer in contact with the component. Either the component is stationary and the transducer is fixed to a rotating spindle, which can have radial accuracies of between 10 and 100 nm, or the component is on a precision rotation table with a stationary transducer. The output of the transducer may be fed directly into a computer, which can be used to determine, for example, the best fit, maximum inscribed and minimum circumscribed circles, as well as performing phase and amplitude analyses of the measured surface form.

Diameters are conventionally measured⁽⁷⁾ by adjusting the position of a probe to give the maximum reading when it contacts opposite faces. A less arbitrary and statistically more correct procedure is to use a two-axis measuring machine, similar to that described below for profile measurement. Normally several measurements, with a sensitivity of about 5 nm, are made close together at either end of a diameter, and the diameter is determined by a least-squares fit to a circle. Absolute measurements, to an accuracy of about 100 nm, are derived from secondary standards.

The principle of mechanical profile measuring machines is shown in Figure 3.10. A polished optically flat bar is used as a reference straight edge and allowed to move in the direction perpendicular to the surface

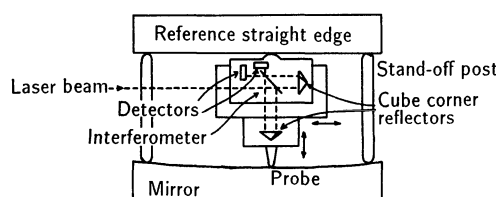


Figure 3.10. The principle of profile measuring machines. (After Franks.⁽⁷⁾)

being measured. The straight edge is referenced directly to the mirror surface through the stand-off posts. The separation of the straight edge and the mirror surface is measured by an interferometer that is mounted to refer directly to the straight edge. The moving arm of the interferometer carries a cube corner reflector and the detectors feed signals to register the sagittal position on an up-down counter. Overall measurement uncertainties of about 1 nm have been reported.⁽⁷⁾ The interferometric method of measuring the displacement of the probe has the advantage over analogue methods that the accuracy is independent of the range of motion.

Optical probe methods of assessing axial profile involve the measurement of the linear or angular displacements of a light beam reflected from the mirror surface. These displacements in fact measure changes in the slope, but so long as there are no discontinuities in the surface these can be converted to profile changes. An example of this type of probe, developed at the National Physical Laboratory U.K.,⁽⁷⁾ uses a laser beam parallel to a generator of the surface. After deflection through 90° by a pentaprism, this beam is reflected from the surface and is again deflected through 90° on passing through the pentaprism. Thus the angle between the incident and reflected beams is twice the slope angle, allowing the profile to be measured to within 5 nm at present and, ultimately, to about 1 nm.

Mechanical and optical probes can measure surface profile to the same order of accuracy, and thus can be used to cross-check one another. A potential disadvantage of mechanical techniques is damage to the surface along the line of contact, although this does not appear to be a problem in practice if the stylus loading is less than a few grams and its radius is on the order of 1 mm.

3.3.1.2. Microtopography

Small-scale microtopographic perturbations must be measured in an environment protected from temperature fluctuations and mechanical vibrations. The instruments are, typically, mounted on air-isolation tables, possibly underground, in rooms with temperature control to within 2°C.⁽³¹⁾ In addition, measurements must be made rapidly (about 100 points min⁻¹) to minimize any environmental changes. Both the surfaces and the measuring instruments have to be protected from contamination by dust particles and the rooms are therefore maintained clean to class 10,000.

Commercially available mechanical probes, such as the Rank Taylor Hobson Talystep,^(7,31) are equipped with diamond styli with ultrafine tips (0.2–1.0 μm) to enhance lateral resolution. A variable inductance transdu-

cer is used to monitor vertical movements of the stylus to an accuracy of better than 0.5 nm. So long as the stylus loading is less than 2 mg, no, or negligible, damage is caused to the surface. The Talystep cannot be used to measure inside bores so a modified version, called the Nanosurf, has been constructed at the National Physical Laboratory. In this the mirror surface is traversed along a very-high-quality optical flat over a range of 20 mm.⁽³¹⁾ The Nanosurf has the same sensitivity as the standard Talystep.

There are several optical probe methods for microtopography. A very useful instrument for inspecting surfaces during and after polishing is the Normarski differential interference contrast microscope. However, since this only gives semiquantitative results, it is not strictly a metrological tool. The Nomarski microscope uses a Wollaston prism⁽³²⁾ to give two polarized light beams that are recombined by the prism after reflection from the surface. Because of the birefringent properties of the prism, the two beams hit the surface at slightly different points, which, if they are at different heights, give rise to interference contrast due to the phase shift between the reflected beams. In this way height differences as small as 1 nm can be measured, while the lateral resolution is around 200 nm.

A second optical probe technique that may use birefringence is optical heterodyne profilometry. A double-focus microscope objective containing a birefringent element⁽³³⁾ produces two beams polarized orthogonally to one another. One of these, the reference beam, covers a large area of the surface being measured while the other, the probe, is focused to a fine spot on the surface. The two beams are recombined after reflection and converted to a linear polarization. The azimuth of the polarization depends on the optical path difference between the probe and reference beams, which in turn depends on the surface profile. This device has a lateral resolution of 0.8 μm and can detect profile variations of 0.1 nm.

A similar approach, which does not, however, use birefringence, focuses two orthogonally polarized beams of slightly different frequency onto the surface to be measured. The focused beams are separated by 100 μm and have diameters of 2 μm (which is thus the limit of the lateral resolution). After reflection the two beams are allowed to interfere, and the phase of the resulting beam frequency is proportional to the optical path difference between the beams. The reflecting surface is mounted on a precision rotary table with the reference beam centered on the rotation axis while the other beam is scanned over the surface. This method also has a height sensitivity of 0.1 nm.

These and similar methods that depend on measuring phase differences must be treated with caution since other effects can introduce phase differences between the beams. The local microstructure of the

surface or any thin films on the surface can cause phase changes in the reflected beams. Also, microscope objectives can introduce phase shifts, due to obliquity, which increase with increasing aperture,⁽³⁴⁾ so that if the reflected light does not uniformly fill the aperture a variable phase shift will be obtained.

Other optical probe methods have been reported, using scattering or multiple beam interferometry. However, scatter methods require comparison of the measurements with a hypothetical model of the surface. In the most common multiple beam technique, fringes of equal chromatic order (FECO),⁽³⁵⁾ the specimen and reference surfaces have to be thickly coated with metal in order to give sufficient reflectivity, and thus measurements are made of the roughness of the coating, which is not necessarily related to that of the underlying surface.

Better lateral resolutions than possible using optical probes have been obtained using transmission stereo electron microscopy.⁽³⁶⁾ Both lateral and vertical resolution are about 1 nm, but the technique can only be used to examine replicas of surfaces.

3.3.2. Interferometric Methods

Although large parts of a mirror surface can be examined at a time using interferometric techniques, in most cases the light path has to follow the X-ray path in order to be focused. At a grazing incidence angle θ_i , the sensitivity of interferometric measurements is reduced by a factor $\sin \theta_i$; for a grazing angle of 1°, one fringe corresponds to a contour change of 36 μm if a HeNe laser (wavelength 633 nm) is used. Use of a shorter wavelength can increase the sensitivity, as can multiple pass interferometry. In the latter case, however, if the mirror is imperfect, very complex and difficult-to-interpret interferograms are obtained. Most interferometric methods are less sensitive than the probe techniques. They also cannot be used if the surface is nonreflecting (i.e., prior to polishing) and are more difficult to use *in situ*.

Interferometric systems that have been used include normal incidence interferometry,⁽³⁷⁾ Linnik interferometry,⁽³⁸⁾ and Twyman-Green interferometry.⁽⁷⁾ These techniques have, to date, not yielded profile measurements to better than about 50 nm and will not be discussed further.

3.3.3. Surface Evaluation Using Soft X Rays

The ultimate test of grazing incidence optical components is their performance at the wavelengths for which they were designed.^(39,40) The concept of soft X-ray tests of mirrors is simple, given a sufficiently intense

source such as a synchrotron. However, the interpretation of the measurements is more difficult since, for comparison with predicted performances, precise knowledge of the optical constants of the mirror material is needed. Indeed, it is more common for this type of measurement to be used to obtain values for the optical constants.⁽⁴¹⁾

Higher-energy X rays (e.g., copper K_{α} , 8 keV) can be used to detect slow undulations, with wavelengths of a few millimeters and small slopes,⁽⁴²⁾ which quite often arise due to polishing. The undulations act as individual focusing elements when the surface is irradiated at grazing incidence, and the resulting secondary foci are observed photographically by film set at various distances from the mirror. The focal lengths provide dimensional information about the undulations.

Reflective Optics for Soft X Rays II Multilayer Mirrors

Reflectivities at nongrazing incidence angles, and in particular at normal or near-normal incidence, may be enhanced by causing multiple reflections to add in phase, in a manner analogous to Bragg reflection from a crystal. The Bragg condition for m th-order constructive interference is (Figure 4.1) that the angle θ that the incident radiation, of wavelength λ , makes with the crystal planes is equal to θ_m where

$$m\lambda = 2d \sin \theta_m \quad (4.1)$$

and d is the spacing between the planes. Typical crystals have spacings of a few tenths of a nanometer and therefore condition (4.1) cannot be satisfied for soft X rays with wavelengths of 1–10 nm. It is necessary to manufacture structures with the required spacings, and these are known as multilayer mirrors.

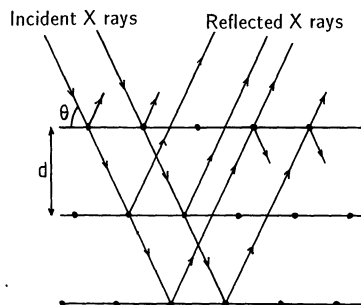


Figure 4.1. Bragg reflection from a crystal.

4.1. Reflection of Soft X Rays by Multilayer Mirrors

At an interface between two media, the Fresnel equations (2.18a) or (2.18b) can be used to calculate the reflectivities for glancing incidence angles greater than the critical angle. Typically, it is found that between 10^{-4} and 10^{-6} of the incident intensity is reflected, i.e., the coefficient of amplitude reflection is between 10^{-2} and 10^{-3} . Thus, neglecting absorption, if reflections from about 10^2 or 10^3 interfaces can be caused to add in phase, all of the incident intensity can be reflected. In practice, because of absorption, total reflection is not possible.

In its simplest form, a multilayer mirror consists of a substrate S onto which alternate layers of two different materials h and l, with refractive indices n_h (high) and n_l (low), are deposited. The thicknesses of the layers are d_h and d_l , so that the periodicity of the structure is $d = d_h + d_l$ (Figure 4.2). If the structure consists of L pairs of layers, then including the vacuum and the substrate, the total number of media involved is $2L + 2$.

In order to determine, theoretically, the performance of a multilayer mirror, it is necessary to solve Maxwell's equations for a system with a periodically varying dielectric constant. Two approaches, which can be shown to be equivalent, have been used. The first treats the reflections in a manner similar to that used for Bragg reflection from a crystal,^(1,2) although equation (4.1) must be modified in order to give the correct angles for the Bragg reflection peaks.⁽³⁻⁵⁾ This approach is valid because layers a few nanometers thick contain only a small number of atomic

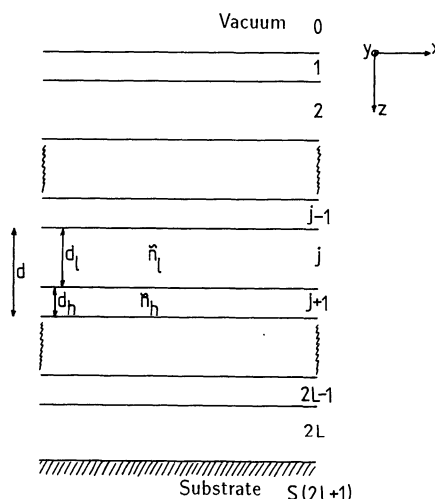


Figure 4.2. Structure of a multilayer mirror.

layers. The second approach uses an adaptation of the optical multilayer theory for the design of interference coatings for visible radiation.^(1,2,6,7) The description given here follows closely that of Underwood and Barbee.^(1,2)

4.1.1. Theory of Absorption-Free Multilayer Mirrors

Absorption in the layer materials may not be insignificant in terms of the forms of the Bragg reflections, but neglecting it leads to a simpler theory that gives expressions useful for estimating, for example, peak and integrated reflectivities and widths of the Bragg peaks. These estimates can be used in designing multilayer mirrors for particular applications.

The treatment of X-ray reflection from crystals may be undertaken in two ways, called kinematical and dynamical. In the kinematical theory, each volume element is considered to scatter the radiation independently of all other volume elements. This is appropriate to thin crystals and to crystals consisting of a large number of thin crystallites that are randomly oriented at small angles to the mean orientation (mosaic crystals). The kinematical theory neglects details of wave interactions within the structure, while the dynamical theory takes account of all these interactions, such as the reduction in amplitude of the incoming wave caused by reflection from successive planes (primary extinction).

From a crystallographic point of view, multilayer mirrors do not exhibit any mosaicity, the most obvious errors being variations in layer thicknesses caused by the manufacturing process. Thus their properties can be more suitably described via the dynamical theory, although for sufficiently thin multilayers the kinematical theory leads to the same approximations.

The complex refractive index of a layer consisting of a single element is

$$\tilde{n} = 1 - \delta - i\beta \quad (4.2)$$

where δ and β are related to the atomic scattering factors f_1 and f_2 via equations (1.16)–(1.18)

$$\delta = (e^2\lambda^2/8\pi^2\epsilon_0 m_e c^2) N f_1 \quad (4.3)$$

and

$$\beta = (e^2\lambda^2/8\pi^2\epsilon_0 m_e c^2) N f_2 \quad (4.4)$$

where N is the number density of atoms. For soft X rays, equation (4.1) requires $2d > 1 \text{ nm}$, i.e., $(\sin \theta)/m\lambda < 1 \text{ nm}^{-1}$ and thus, from equation (1.11),

$$f_1 \approx Z + \Delta f_1 \quad (4.5)$$

where Z is the atomic number. Thus all the electrons in an atom may be considered to scatter the radiation in phase. The scattering amplitude density ϕ is then defined by

$$\phi = N[(Z + \Delta f_1)^2 + f_2^2]^{1/2}(e^2/4\pi\epsilon_0 m_e c^2) \quad (4.6)$$

with $f_2 = 0$ for the absorption-free case.

In principle the crystalline structure of the individual layers will contribute to the reflected intensity. In practice, however, this structure can be neglected since the lattice spacing is such that equation (4.1) cannot be satisfied. Thus a unit area of one layer pair may be considered to be the unit cell for a multilayer mirror. The angle-dependent structure factor of a unit cell is then given by

$$F(\theta) = \int_0^d \phi(z) \exp [4\pi i (\sin \theta) z / \lambda] dz \quad (4.7)$$

where z is the direction normal to the multilayer surface (Figure 4.2).

For simple cases, $|F(\theta)|$ can be determined in an analytic way. If, for example, the layers h and l are homogeneous with constant scattering amplitude densities ϕ_h and ϕ_l , and the interfaces are perfectly sharp so that the transitions from ϕ_h to ϕ_l take place over negligibly small intervals, then

$$F(\theta) = \int_0^{d_l} \phi_l \exp(iQz) dz + \int_0^{d_h} \phi_h \exp(iQz) dz \quad (4.8)$$

where

$$Q = 4\pi(\sin \theta)/\lambda \quad (4.9)$$

Evaluating the integrals gives

$$F(\theta) = (1/iQ)[(\phi_l - \phi_h) \exp(iQd_l) - \phi_l + \phi_h \exp(iQd_h)] \quad (4.10)$$

so that

$$\begin{aligned}|F(\theta)| &= [F(\theta)F^*(\theta)]^{1/2} \\&= (\sqrt{2}/Q)[\phi_1^2(1 - \cos Qd_1) + \phi_h^2(1 - \cos Qd_h) \\&\quad - \phi_1\phi_h(1 + \cos Qd - \cos Qd_1 - \cos Qd_h)]\end{aligned}\quad (4.11)$$

If the layer thicknesses are equal, then $d_h = d_1 = d/2$ and

$$|F(\theta)| = (2/Q) \sin(Qd/4)[\phi_1^2 + \phi_h^2 + 2\phi_1\phi_h \cos(Qd/2)] \quad (4.12)$$

At the Bragg angle, $Q = 2m\pi/d$ and $\cos Qd = 1$. Thus equation (4.11) becomes

$$|F(\theta_m)| = (d/m\pi)(\phi_h - \phi_1) \sin(m\pi d_h/d) \quad (4.13)$$

which is zero for even orders if the layer thicknesses are equal, i.e., only the odd orders ($m = 1, 3, 5 \dots$) are allowed reflections.

For a real multilayer, the interfaces will not be perfectly sharp due to diffusion between the layers. If the transition of the scattering amplitude density from ϕ_h to ϕ_1 is sinusoidal, then the structure factor may be written as⁽⁸⁾

$$\begin{aligned}F(\theta) &= (\phi_1/2) \int_0^d [1 + \sin(2\pi z/d)] \exp(iQz) dz \\&\quad + (\phi_h/2) \int_0^d [(1 - \sin(2\pi z/d)] \exp(iQz) dz\end{aligned}\quad (4.14)$$

giving

$$\begin{aligned}|F(\theta)| &= \sin(Qd/2)[(\phi_1 + \phi_h)^2/Q^2 \\&\quad + (4\pi^2/d^2)(\phi_1 - \phi_h)^2/(Q^2 - 4\pi^2/d^2)^2]^{1/2}\end{aligned}\quad (4.15)$$

For first-order Bragg reflection, $Q = 2\pi/d$ and the first term of equation (4.15) vanishes. The second term, however, remains finite since

$$\lim_{Q \rightarrow 2\pi/d} \{[\sin(Qd/2)]/(Q^2 - 4\pi^2/d^2)\} = -d^2/8\pi \quad (4.16)$$

and thus

$$|F(\theta_1)| = (d/4)(\phi_h - \phi_1) \quad (4.17)$$

For higher-order reflections, $Q = 2m\pi/d$ ($m > 1$), both terms in equation (4.15) are zero so that only the first order is allowed in this case.

For diffraction of X rays by crystals, two solutions to the dynamical problem are known. The first of these, due to Darwin,⁽⁹⁻¹¹⁾ is for a thick crystal (large d) with negligible absorption, while the second, due to Ewald,⁽¹²⁻¹⁶⁾ assumes no absorption. The latter will, in the main, be used here.

For a plane parallel wave of wavelength λ and intensity I_0 incident on a multilayer mirror at glancing angle θ , the reflected intensity is⁽¹⁷⁾

$$I(\theta) = I_0 |p^2 + (p^2 - 1) \cot^2 [A(p^2 - 1)^{1/2}]|^{-1} \quad (4.18)$$

with

$$A = (2LKd/m) |F(\theta_m)| \quad (4.19)$$

$$p = (\pi m L / 2A \sin^2 \theta_m) [(\theta - \theta_m) \sin 2\theta_m - 2\bar{\delta}] \quad (4.20)$$

and

$$K = 1, \quad |\cos 2\theta_m|, \quad \text{or } (1 + |\cos 2\theta_m|)/2 \quad (4.21)$$

for perpendicular, parallel, and unpolarized radiation, respectively (see Figure 2.1). The refractive index decrement averaged over the multilayer structure which has, on average, number densities \bar{N}_j of atoms of type j is

$$\bar{\delta} = (e^2 \lambda^2 / 8\pi^2 \epsilon_0 m_e c^2) \sum_j N_j (Z + \Delta f_1)_j \quad (4.22)$$

If $|F(\theta_m)|$ is known, as in the cases discussed above, the factor A can be determined from equations (4.19) and (4.21).

The peak reflectivity for the m th-order Bragg reflection is, by definition, when $I(\theta)/I_0$ is maximum. Differentiating equation (4.18) with respect to p shows this maximum to be at $p = 0$ with the value

$$[I(\theta)/I_0]_{\max} = (-\cot^2 iA)^{-1} = \tanh^2 A \quad (4.23)$$

The integrated reflectivity for the m th-order reflection is⁽¹¹⁾

$$\begin{aligned} (I_m/I_0) &= \int_{\theta=0}^{\pi} [I(\theta)/I_0] d(\theta - \theta_m) \\ &= [A(\tan \theta_m)/\pi m L] \int_{-\infty}^{+\infty} [I(\theta)/I_0] dp \\ &= [(\tan \theta_m)/m L] A \tanh A \end{aligned} \quad (4.24)$$

Equation (4.20) shows that, since the peak reflectivity is at $p = 0$, the peak does not occur at the Bragg angle θ_m but at a slightly larger angle

$$\theta_m^p = \theta_m + 2\bar{\delta}/\sin 2\theta_m \quad (4.25)$$

This correction is due to refraction of the X rays ($\bar{\delta} \neq 0$) and the Bragg condition, equation (4.1), has to be modified to take account of it. In the medium, the wavelength of the radiation is λ' where

$$1 - \bar{\delta} = \lambda/\lambda' \quad (4.26)$$

the glancing angle is θ'_m where

$$m\lambda' = 2d \sin \theta'_m \quad (4.27)$$

and, by Snell's law,

$$1 - \bar{\delta} = \cos \theta_m^p / \cos \theta'_m \quad (4.28)$$

From equations (4.26)–(4.28), the modified Bragg condition

$$m\lambda = 2d[1 - (2\bar{\delta} - \bar{\delta}^2)/\sin^2 \theta_m^p]^{1/2} \sin \theta_m^p \quad (4.29)$$

$$\simeq 2d(1 - \bar{\delta}/\sin^2 \theta_m^p) \sin \theta_m^p \quad (4.30)$$

is obtained.

The limiting cases of the dynamical theory are given by $A \gg 1$ (e.g., large L giving a thick multilayer) and $A \ll 1$ (thin multilayer). Evaluation of the hyperbolic tangent function shows that, to within 5%, $\tanh A \approx 1$ for $A > 1.8$ and $\tanh A \approx A$ for $A < 0.4$. Thus multilayers are considered to be thick if $A > 1.8$ and thin if $A < 0.4$. In the former case, the peak reflectivity becomes

$$[I(\theta)/I_0]_{\max} \approx 1 \quad (4.31)$$

and this value is obtained for all $|p| < 1$, where the reflection is total. The integrated reflectivity is

$$I/I_0 \approx (A \tan \theta_m)/mL \quad (4.32)$$

In the thin approximation.

$$[I(\theta)/I_0]_{\max} \approx A^2 \quad (4.33)$$

and

$$I/I_0 \simeq (A^2 \tan \theta_m)/mL \quad (4.34)$$

It is also of interest to determine the range of angles about θ_m^p (i.e., about $p = 0$) for which the reflectivity is greater than a certain amount, say half the maximum, since this can be used to determine the range of wavelengths that will be reflected at a given incidence angle, i.e., the resolving power of the multilayer. For thick multilayers this means considering the case $|p| > 1$, for which equation (4.18) approaches no definite limit as A increases because of the presence of the (oscillatory) cotangent function. It is therefore necessary to adopt an averaging procedure⁽¹⁷⁾ for large values of A , i.e., for large numbers of layers, when it is to be expected that the thickness may vary across the multilayer structure. If the corresponding uncertainty ΔA in A is greater than $\pi/2$, then the average function found by integrating equation (4.18) over the range of uncertainty is

$$\overline{I(\theta)/I_0} = [1 - (1 - p^{-2})^{1/2}] \quad (|p| > 1) \quad (4.35)$$

which is equal to 0.5 when p is $\pm 2/\sqrt{3}$. Thus, for thick multilayers the full width at half-maximum intensity is

$$\Delta\theta_m = (4/\sqrt{3}\pi)(A \tan \theta_m)/mL \quad (4.36)$$

From equation (4.1)

$$\Delta\lambda = (2d/m)(\cos \theta_m)\Delta\theta_m \quad (4.37)$$

and thus the resolving power of a thick multilayer is

$$R_m = \lambda/\Delta\lambda = (\sqrt{3}\pi/4)mL/A \quad (4.38)$$

In the case of a thin multilayer, equation (4.18) reduces to

$$I(\theta)/I_0 \simeq (\sin^2 Ap)/p^2 \quad (4.39)$$

In order to estimate the full width at half-maximum intensity, equation (4.39) is approximated by⁽¹⁷⁾

$$I(\theta)/I_0 \simeq A^2 \exp(-A^2 p^2/\pi) \quad (4.40)$$

which has the same peak and integrated values. Then, at half maximum,

p is equal to $\pm(\pi \ln 2)^{1/2}/A$ and thus

$$\Delta\theta_m = 2[(\ln 2)/\pi]^{1/2}(\tan \theta_m)/mL \quad (4.41)$$

and the resolving power is

$$R = \lambda/\Delta\lambda = (1/2)(\pi/\ln 2)^{1/2}mL \approx mL \quad (4.42)$$

The effective number of layer pairs contributing to the reflection is, from equations (4.13) and (4.19),

$$L_{\text{eff}} = m^2\pi A/[2Kd^2(\phi_h - \phi_l)\sin(m\pi d_h/d)] \quad (4.43)$$

For a multilayer used at normal incidence, $\theta_m = \pi/2$, $K = 1$, and $d = m\lambda/2$. Thus

$$L_{\text{eff}} = 2\pi A/[\lambda^2(\phi_h - \phi_l)\sin(m\pi d_h/d)] \quad (4.44)$$

For use on the short-wavelength side of the carbon K_α absorption edge, with $\lambda \approx 4.3$ nm, a thick ($A = 1.8$) multilayer with equal thicknesses of rhenium–tungsten (scattering amplitude density = $\phi_h = 3.93 \times 10^{15} \text{ m}^{-2}$)⁽¹⁸⁾ and boron (scattering amplitude density = $\phi_l = 1.84 \times 10^{15} \text{ m}^{-2}$)⁽¹⁸⁾ has $L_{\text{eff}} \approx 290$ layer pairs for first-order reflections. If there is a sinusoidal variation of the scattering amplitude density, then using equation (4.17) in place of (4.13) gives $L_{\text{eff}} \approx 210$ layer pairs. (In references 1 and 2 it is stated, incorrectly, that a sinusoidal variation of the scattering amplitude density increases the effective number of layer pairs contributing to the reflection.) These values of L_{eff} will be reduced by absorption in the layer materials, but, along with the other results from the absorption-free treatment, may be used as a guide.

4.1.2. The Dynamical Theory with Absorption

In the soft X-ray region all materials are absorbing ($f_2 \neq 0$) so that $F(\theta)$ is complex. In principle this can be treated using the modification to the Darwin theory introduced by Prins⁽¹⁹⁾ as for X-ray diffraction by crystals. This is, however, most applicable to an infinite number of strictly periodic layers, and does not take into account reflections at the vacuum–multilayer and multilayer–substrate interfaces. As shown below, multilayers can have nonperiodic structures in order to minimize the effects of absorption, and they also have finite numbers of layers. A more appropriate approach is similar to that used by Parratt⁽³⁾ for the X-ray

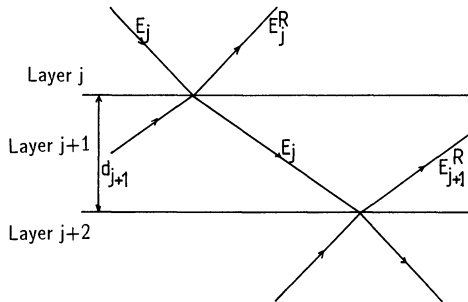


Figure 4.3. Continuity of the electric field at layer interfaces.

interference caused by contaminant layers on the surfaces of grazing incidence mirrors.

The tangential components of the electric (and magnetic) fields must be continuous at the interfaces between layers (Figure 4.3). Thus the vector amplitudes E_j (incident) and E_j^R (reflected) midway through the j th layer are related to those midway through the $(j + 1)$ th layer by

$$a_j E_j + E_j^R/a_j = E_{j+1}/a_{j+1} + a_{j+1} E_{j+1}^R \quad (4.45)$$

and

$$(a_j E_j - E_j^R/a_j)g_j = (E_{j+1}/a_{j+1} - a_{j+1} E_{j+1}^R)g_{j+1} \quad (4.46)$$

where E_{j+1} is the amplitude of the refracted wave at the interface,

$$g_j = (\tilde{n}_j^2 - \cos^2 \theta_j)^{1/2} \quad (4.47)$$

where θ_j is the glancing angle in the j th layer (it is related to the glancing angle θ at the vacuum–multilayer interface by Snell's law), and

$$a_j = \exp(-i\pi g_j d_j/\lambda) \quad (4.48)$$

is the amplitude factor over half the thickness d_j of the layer. The simultaneous equations (4.45) and (4.46) are solved by dividing one by the other, leading to

$$R_j = a_j^4(F_j + R_{j+1})/(1 + F_j R_{j+1}) \quad (4.49)$$

where

$$F_j = (g_j - g_{j+1})/(g_j + g_{j+1}) = E_j^R/E_j \quad (4.50)$$

and

$$R_j = a_j^2 F_j \quad (4.51)$$

Equation (4.49) is a recursion formula that can be applied successively at consecutive interfaces so long as a starting value of R_j is known. Equation (4.50) is the Fresnel coefficient for the reflection of the perpendicular component of polarization (see Section 2.1). For the parallel component, equation (4.49) may also be applied, using

$$F_j^{\parallel} = (\tilde{n}_{j+1}^2 g_j - \tilde{n}_j^2 g_{j+1}) / (\tilde{n}_{j+1}^2 g_j + \tilde{n}_j^2 g_{j+1}) \quad (4.52)$$

All the illustrative examples discussed below are for the perpendicular component.

If the substrate, which is the $(2L + 1)$ th layer, can be assumed to be infinitely thick, then $R_{2L+1} = 0$. Successive applications of equation (4.49) eventually lead to the reflectivity at the vacuum–multilayer interface (where $a_0 = 1$)

$$I(\theta)/I_0 = R_0^2 \quad (4.53)$$

For a rhenium–tungsten/boron multilayer (with equal thickness layers) for use at normal incidence with radiation of wavelength 4.3 nm (and $d = 2.168$ nm to take account of the longer wavelengths in the media), the reflectivity as a function of the number of layer pairs is shown in Figure 4.4. The values of the optical constants used to calculate these

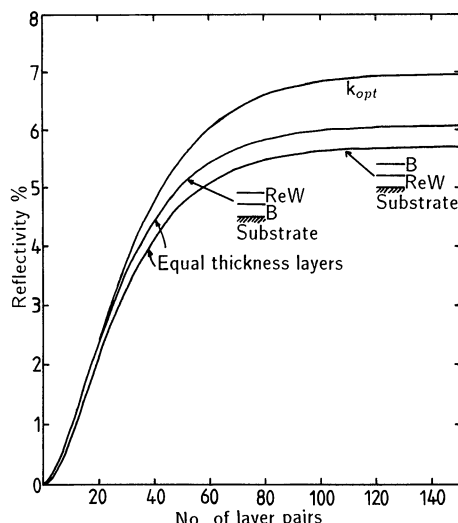


Figure 4.4. Reflectivity as a function of the number of layer pairs for rhenium–tungsten/boron multilayers used at normal incidence at a wavelength of 4.3 nm, showing the effect of optimized layer thicknesses.

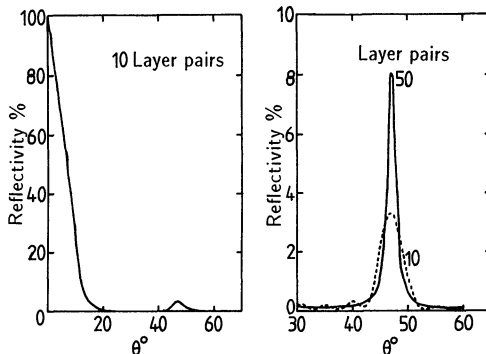


Figure 4.5. Variation of reflectivity with incidence angle for a rhenium-tungsten/boron multilayer with equal thickness layers designed for a wavelength of 4.3 nm and a Bragg angle of 47°.

curves, and those in the following examples, were, for rhenium–tungsten, $\delta = 1.16 \times 10^{-2}$ and $\beta = 1.26 \times 10^{-2}$, and, for boron, $\delta = 5.40 \times 10^{-3}$ and $\beta = 2.86 \times 10^{-3}$.⁽¹⁸⁾ The asymptotic reflectivity of about 5%, which is reached for $L \ll L_{\text{eff}}$ as given by equation (4.44), shows the effect of absorption. The curves show that the asymptotic efficiency for a multilayer with the least-absorbing material (boron) next to the substrate and the most absorbing next to the vacuum is higher (by a factor of about 1.07) than that for the alternative arrangement.

The variation of reflectivity with angle for a rhenium–tungsten/boron multilayer with ten layer pairs and $d = 3$ nm used with X rays of wavelength 4.3 nm is shown in Figure 4.5. This shows the grazing incidence peak as $\theta \rightarrow 0$ and the first-order maximum at $\theta_1^P \approx 47^\circ$, demonstrating the shift in the Bragg angle due to refraction ($\theta_1 = 45.8^\circ$ using the unmodified Bragg condition). The width of the first-order peak is about 5°, agreeing with that calculated using equation (4.41). Subsidiary interference peaks, as predicted by equation (4.39) for a thin multilayer, can also be seen. The reflectivity around the first-order maximum is also shown for a similar multilayer with 50 layer pairs, demonstrating that the first-order peak becomes higher and narrower and that the subsidiary peaks disappear as the number of layer pairs increases.

4.1.3. Choice of Layer Thicknesses and Materials

Because of absorption in the layers, it is possible to increase the reflectivity of a multilayer made from given materials by making the more-absorbing layers thinner and the less-absorbing layers thicker, while maintaining the overall periodicity d . The optimum value of the parameter d_i/d ($= k$) is found by differentiating equation (4.49) with respect to k and equating the result to zero. This gives the transcendental

equation

$$\operatorname{Re} [3g_l a_l^6(1 - a_h^2) - g_h(1 - a_l^6)] = 0 \quad (4.54)$$

where

$$g_l = (\bar{n}_l^2 - \cos^2 \theta_l)^{1/2} \quad (4.55)$$

$$g_h = (\bar{n}_h^2 - \cos^2 \theta_h)^{1/2} \quad (4.56)$$

$$a_l = \exp(-i\pi g_l dk_{\text{opt}}/\lambda) \quad (4.57)$$

and

$$a_h = \exp[-i\pi g_h d(1 - k_{\text{opt}})/\lambda] \quad (4.58)$$

The real part is taken in equation (4.54) since this governs absorption. For the normal incidence multilayer used as an example in Section 4.1.2, the optimum value of k is 0.603 and the reflectivities obtained using this value are shown in Figure 4.4. The asymptotic reflectivity is higher by a factor of about 1.15 than that for $k = 0.5$. For the multilayer used at $\theta_1^p \approx 47^\circ$, $k_{\text{opt}} = 0.601$, which gives the Bragg peak, for 50 layer pairs, shown in Figure 4.6. This peak is higher than the corresponding one for $k = 0.5$ by a factor of about 1.17.

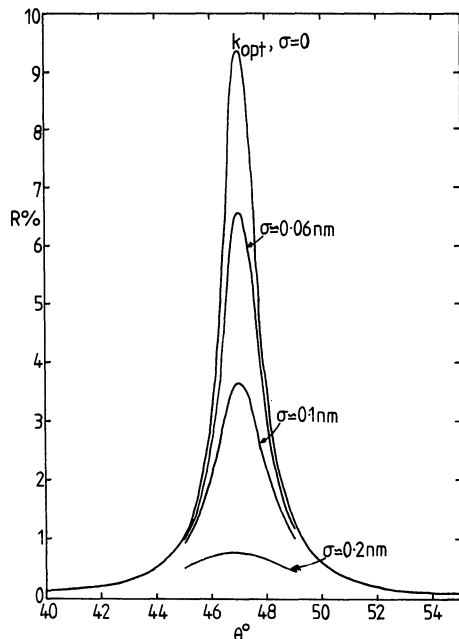


Figure 4.6. Reflectivity, near to the Bragg angle, for rhenium-tungsten/boron multilayers with optimized layer thicknesses, and showing the effect of rough interfaces.

The increase in reflectivity using the optimum value of k is the result of a trade-off between the constructive interference of successive reflections and absorption losses. However, this trade-off is counterproductive for small numbers of layer pairs, the use of k_{opt} decreasing the reflectivity. In fact, for small values of L , higher reflectivities are obtained if the layers with the larger value of δ (which are usually also more absorbing) are thicker, because the wavelength in these layers is longer, and constructive interference is enhanced by placing the interfaces at peaks of the waves. For one layer pair the highest reflectivity is obtained with $k = 0.486$. This suggests that higher reflectivities might be possible by gradually increasing k from this value for the lower layers to k_{opt} for the upper layers. However, in the soft X-ray region this has little effect on the reflectivity since for a large number of layers the lower layers do not contribute very much. For wavelengths greater than about 10 nm, longer than those of interest here, it is possible to increase the reflectivity significantly using such aperiodic designs.^(21,22)

For a normal incidence multilayer with a sinusoidal variation of the scattering amplitude density, the optimum value of k is given by⁽²⁰⁾

$$\tan(\pi k_{\text{opt}}) = \pi[k_{\text{opt}} - \beta_h/(\beta_h - \beta_l)] \quad (4.59)$$

This equation has been used^(1,2) for other angles of incidence and for multilayers with sharp interfaces. For rhenium–tungsten/boron multilayers, however, the resulting value of k_{opt} is 0.645, which is an overestimate according to equation (4.54).

Apart from k , the other free parameters in the design of a multilayer mirror for use at a particular wavelength and angle are the scattering amplitude densities ϕ_h and ϕ_l (i.e., the optical constants δ_h , β_h , δ_l , and β_l) and the number of layer pairs L . If the maximum possible reflectivity is required, then materials giving the largest value of $(\phi_h - \phi_l)$ should be chosen, and L should be large. For high resolving power, however, equation (4.38) shows that $(\phi_h - \phi_l)$ should be small and L large, while if a high bandpass is required so that the multilayer reflects over a large wavelength range, $(\phi_h - \phi_l)$ should be large and L small. More practical design considerations will be discussed in Chapter 5. One of the most important of these is the compatibility of the materials—ideally they should not react chemically or interdiffuse.

4.1.4. The Effect of Rough Interfaces

Even for perfectly deposited layers the interfaces will not, at the atomic level, be completely smooth. The effect of uncorrelated roughness can be treated in a manner similar to the analysis based on the Debye

theory⁽²³⁾ given in Section 2.1.2. Assuming that the roughness does not change the mean positions of the interfaces, the amplitude reflectivity at each interface is reduced by a factor

$$D_j = \exp \{-2[2\pi\sigma_j(\sin \theta_j)/\lambda_j]^2\} \quad (4.60)$$

where λ_j is the wavelength in the j th layer, θ_j is the glancing angle of incidence on the j th interface, and σ_j is the rms value of the effective roughness at the j th interface.

The effect of roughness is largest for normal incidence mirrors, since then $\sin \theta_j = 1$. Also, the roughness is then likely to be correlated since each layer will, to a certain extent, carry an imprint of the previous one. For nonnormal incidence, the long transverse paths ensure uncorrelated roughness distributions. For a small number of evaporated layers, $\sigma \geq 0.2 \text{ nm}$ typically,⁽²⁴⁾ i.e., $\sigma \geq 0.1d$ for the normal incidence rhenium-tungsten/boron multilayer being used as an example. As shown in Figure 4.7, a roughness of this magnitude dramatically reduces the normal incidence reflectivity. To obtain a useful reflectivity, a roughness less than about 0.1 nm is necessary. Fortunately the process of evaporating layers appears to have a smoothing effect⁽²⁵⁾ so that for total thicknesses of about 10 nm, roughness values of about 0.1 nm are possible. Figure 4.7 also shows the reflectivity for a multilayer with $\sigma = 0.3 \text{ nm}$ for the first layer pair, decreasing to 0.1 nm for the tenth and remaining constant thereafter.

For nonnormal incidence the smoothness requirements are not so stringent. The effect of rough interfaces on the first-order Bragg peak of

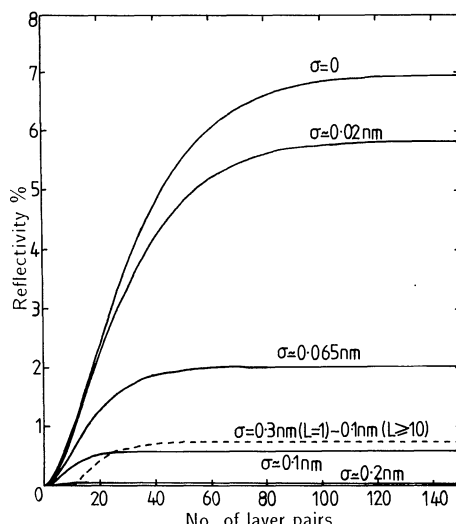


Figure 4.7. The effect of rough interfaces on the reflectivities of normal incidence rhenium-tungsten/boron multilayers.

the rhenium–tungsten/boron multilayer with $\theta_1^p \simeq 47^\circ$ is shown in Figure 4.6, where the peak is still obtained for a roughness of about 0.2 nm.

4.2. Focusing with Multilayer Mirrors

The aberrations of spherical mirrors have been discussed in Chapter 2. Using the analysis given there, it is clear that normal (or near-normal) incidence mirrors have smaller aberrations than do grazing incidence mirrors. A focusing system based on spherical (or only slightly non-spherical) multilayer mirrors can give high-quality images at normal or near-normal incidence. In addition, larger apertures and larger usable fields are possible at normal incidence.

The designs of normal incidence reflecting systems for soft X-ray wavelengths can be very similar to those for use at longer (e.g., visible) wavelengths. The conceptually simplest systems use one reflection from a conicoidal surface, e.g., ellipsoidal for a microscope or paraboloidal for a telescope. For small apertures the surfaces are almost spherical and although imaging is only perfect at the focal points, the usable fields are much larger than for equivalent grazing incidence systems. Because only one reflection is used, this type of system has the highest possible efficiency.

To obtain high resolution over a large field using spherical mirrors, it is necessary to use two reflections, as shown in the Schwarzschild⁽²⁶⁾ system of Figure 4.8. These have the advantage over single reflection systems that the object and image are on opposite sides of the focusing system, which makes them easier to use. However, they have lower efficiencies because of the two reflections needed. Practical designs of multilayer mirror focusing systems will be discussed in Chapter 10.

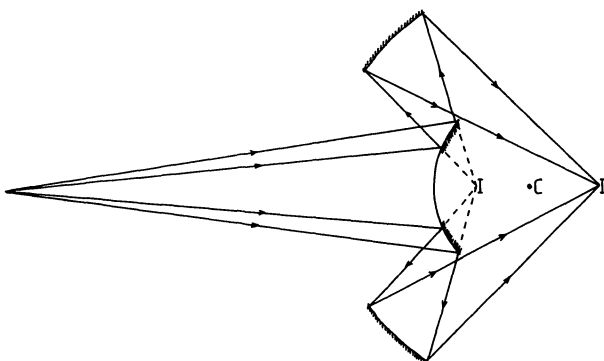


Figure 4.8. A Schwarzschild optical system, using two reflections from spherical multilayer mirrors.

Manufacture of Multilayer Mirrors

5.1. Manufacturing Tolerances

As discussed toward the end of Chapter 4, interfacial roughness causes significant reduction of the reflectivity of a multilayer element. Similarly, as shown below, if the layers are not deposited with accurately controlled thicknesses, the performances of the mirrors are adversely affected. Substrate figure errors will not be considered here—they may be treated in the same fashion as those of grazing incidence mirrors discussed in Chapter 3. It will be assumed that any figure errors are too small to significantly affect the reflectivities of multilayer mirrors, and that the layer boundaries are smooth.

5.1.1. Layer Thickness Errors

The effects of slight variations in layer thicknesses may be estimated using the method of Section 4.1.2 and introducing random shifts of the layer boundaries. For a rhenium–tungsten/boron multilayer used at normal incidence and a wavelength of 4.3 nm (for which the reflectivity was calculated in Section 4.1.2 for the case of no layer thickness errors), typical effects of random thickness variations of up to 0.03 and 0.05 times the correct layer thickness d are shown in Figures 5.1 and 5.2, respectively. It is not possible to predict the reflectivities, which are significantly decreased in both cases, with any certainty, and it is clear that layer thicknesses must not vary by more than about 0.03 d if reflectivity is to be maintained. In this case, which is typical, this corresponds to a maximum variation of less than 0.1 nm, i.e., less than an atomic layer. Such accuracies are clearly not possible, so mirrors with more than a few layers would not be feasible.

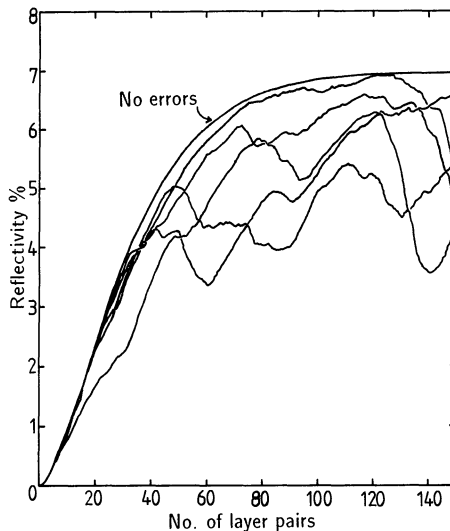


Figure 5.1. The effect on the reflectivity of normal incidence rhenium–tungsten/boron multilayers of random thickness variations up to a maximum of 3% of the layer thickness, with no *in situ* corrections.

For the other example given in Section 4.1.2, a rhenium–tungsten/boron multilayer for use at a Bragg angle of 47° , typical effects of random layer thickness variations are shown in Figures 5.3 and 5.4. Now, four effects occur, all of which increase with increasing maximum thickness variation. The peak is shifted, lowered, and broadened, and secondary maxima become more significant. The effects on the primary peak are summarized in Figure 5.5, where each data point is the mean of ten calculations with random layer thickness variations up to the maxima

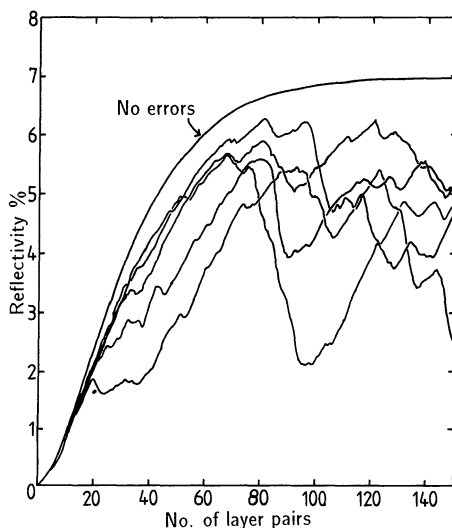


Figure 5.2. The effect on the reflectivity of normal incidence rhenium–tungsten/boron multilayers of random thickness variations up to a maximum of 5% of the layer thickness, with no *in situ* corrections.

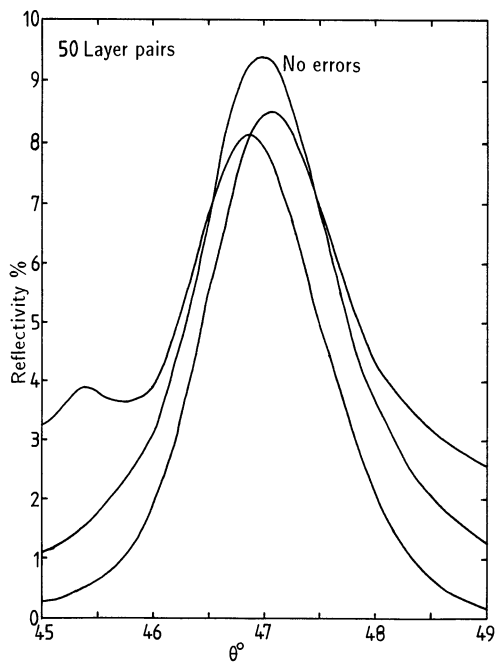


Figure 5.3. The effect on the reflectivity of 47° Bragg angle rhenium-tungsten/boron multilayers of random thickness variations up to a maximum of 3% of the layer thickness, with no *in situ* corrections.

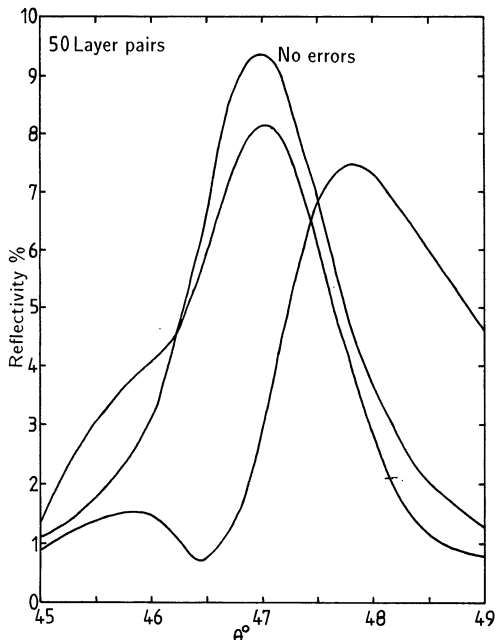


Figure 5.4. The effect on the reflectivity of 47° Bragg angle rhenium-tungsten/boron multilayers of random thickness variations up to a maximum of 5% of the layer thickness, with no *in situ* corrections.

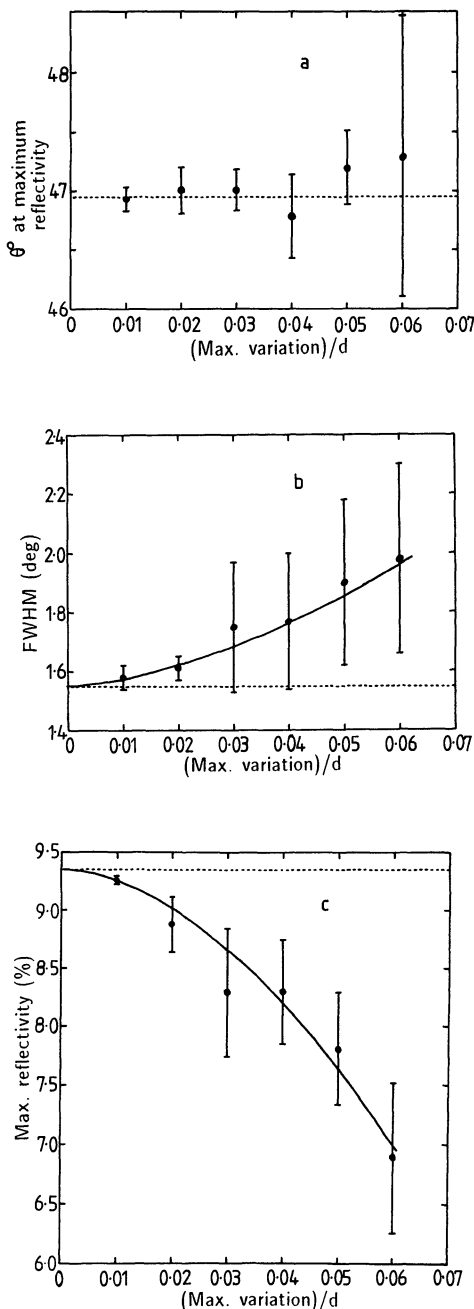


Figure 5.5. The dependence on layer thickness variations of (a) the angle, (b) the width, and (c) the peak value, of the reflectivity of 47° Bragg angle rhenium–tungsten/boron multilayers.

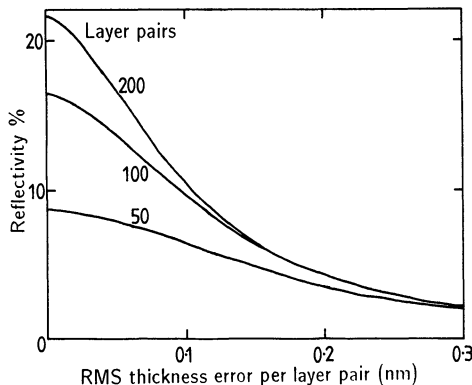


Figure 5.6. The decrease of reflectivity with layer thickness error for normal incidence tungsten/carbon multilayers. (After Rosenbluth and Forsyth.⁽¹⁾)

indicated. On average, the peak remains almost at the same position, although the spread of possible shifts gets larger as the thickness variations increase. The width of the peak increases quite rapidly with the thickness variation, while the peak reflectivity decreases rapidly (the curves in Figure 5.5b,c are “best fits” to the data points and should only be taken as guides). The same order of accuracy as necessary for the normal incidence example is indicated.

Results similar to those given above have been obtained for a tungsten/carbon multilayer mirror designed for use at normal incidence at a wavelength of 6.76 nm, with tungsten and carbon layer thicknesses of 0.76 and 2.65 nm, respectively.⁽¹⁾ As shown in Figure 5.6, the mean decreases in reflectivities are similar to those indicated in Figures 5.1 and 5.2 for the ReW/B multilayers. This analysis also shows that the resolving power $\lambda/\Delta\lambda$ of a multilayer is decreased by random thickness variations, as illustrated in Figure 5.7.

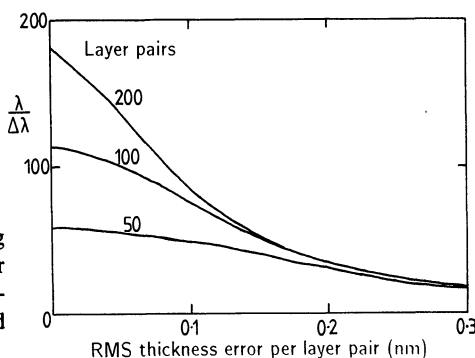


Figure 5.7. The decrease of resolving power with layer thickness error for normal incidence tungsten/carbon multilayers. (After Rosenbluth and Forsyth.⁽¹⁾)

5.1.2. Layer Thickness Errors with *in Situ* Corrections

The calculations discussed above relate to manufacturing processes where no attempt is made to correct for errors during the manufacture. If such corrections are made, the tolerances on each individual layer become much less stringent. This can be modeled by, for example, repeating the calculations described in the previous section but stipulating that alternate boundaries must be in the correct positions. With this restriction the allowable layer thickness variations can be about one order of magnitude larger, as shown in Figure 5.8.

The control of layer thicknesses may be carried out by measuring the reflectivity during the deposition process. As illustrated in Figure 5.9, during deposition of an absorbing layer the reflectivity increases to a maximum, at which point the deposition of the transmitting layer is started. During this part of the cycle, the reflectivity decreases, because the material cannot have zero refractive index decrement or absorption coefficient. When a minimum is reached, deposition of the next absorbing layer starts. The total reflectivity, when layers are complete, gradually rises since the increases during deposition of the absorbing layers are greater than the decreases during deposition of the transmitting layers. As will be discussed in more detail in Section 5.2.2.2, layers with thicknesses of the required accuracies can be deposited by monitoring the reflectivity. Alternative methods of determining layer thicknesses include use of a quartz microbalance⁽²⁾ and timing.⁽³⁾ The first of these has been

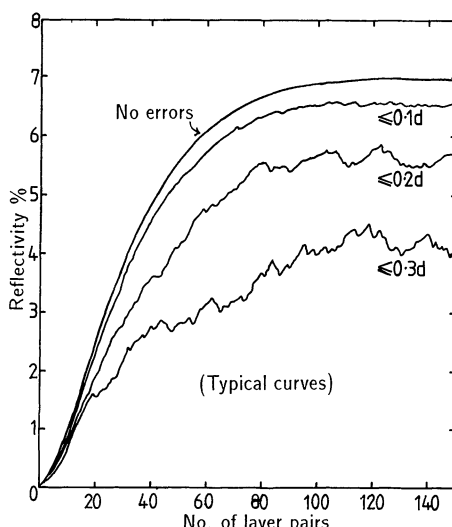


Figure 5.8. The reflectivities of normal incidence rhenium–tungsten/boron multilayers with *in situ* corrections of layer thickness errors.

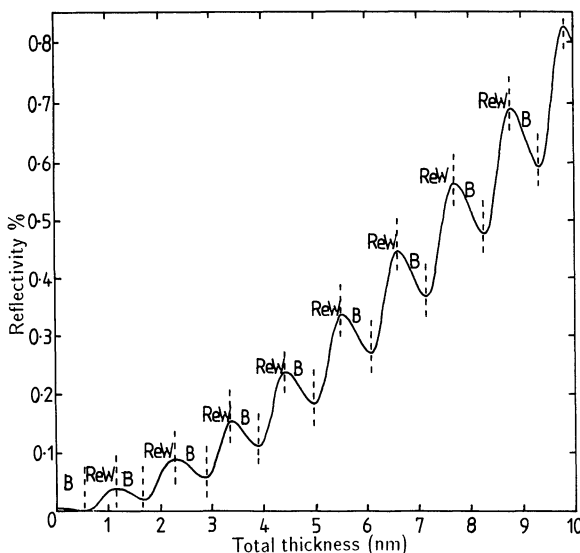


Figure 5.9. The variation of reflectivity of a normal incidence rhenium–tungsten/boron multilayer during deposition of the layers.

found to be unsuitable for large numbers of layers⁽²⁾ because of cumulative thickness errors, which must remain less than about $\lambda/10$.

5.2. Manufacturing Techniques

Because of the limited range of spacings available in natural crystals, the possibilities of manufacturing multilayer mirrors were considered soon after X-ray diffraction was first developed. Mainly because of technological difficulties, the earliest attempts were unsuccessful.^(4,5) The first multilayer mirrors to reflect X rays (molybdenum K_{α} , wavelength 0.07 nm) were made of vacuum-deposited layers of copper and gold with a period of about 10 nm.⁽⁶⁾ However, the layers were observed to interdiffuse within a few days, leading to a rapid decrease in reflectivity. Other combinations with similar instabilities are magnesium with lead or gold, while magnesium with iron is stable over periods longer than a year.^(7,8) All these combinations are, however, too absorbing in the transmitting layers to be of use at soft X-ray wavelengths.

Since these early attempts, advances in, principally, sputtering,⁽³⁾ evaporating,⁽⁹⁾ and laser deposition⁽¹⁰⁾ techniques have allowed efficient multilayer mirrors to be fabricated. In parallel with these advances has come a better understanding of materials evaluation and selection.

5.2.1. Materials Evaluation

Suitable materials for multilayer mirrors can be selected by consideration of the reflectivity properties of the mirrors discussed in Chapter 4 and Section 5.1. The criteria may be summarized in three rules^(11,12):

1. Select a material with a low absorption coefficient for the transmitting layer.
2. Select a second material that has a large reflection coefficient at a boundary with the first material. If several materials give similar reflection coefficients, that with the smallest absorption coefficient should be used.
3. Make sure that the boundaries are physically and chemically stable.

The first two rules may be satisfied by a search through the available data on soft X-ray optical constants.⁽¹³⁾ Since, in principle, any element or compound could be used, comprehensive searches can only be carried out by computer.⁽¹⁴⁾ The essential result is, however, that which has already been assumed—for the best reflectivity it is necessary to combine a low-atomic-number material, which normally means beryllium, boron, or carbon, with one of high atomic number, typically between tantalum and gold. Since carbon gives very smooth films and forms stable boundaries with nearly all heavy metals,⁽¹⁵⁾ it is commonly used. However, at wavelengths slightly shorter than its K_{α} absorption edge, carbon is highly absorbing and boron is more suitable. For wavelengths around 5 nm, combinations of the transition elements with carbon give theoretically higher reflectivities than tungsten/carbon or rhenium–tungsten/carbon.⁽¹⁶⁾

In order to assess the smoothness of the layers, changes in the roughnesses of films are estimated from the reflectivities during deposition.^(11,12) If a film exactly follows the substrate surface topology, the reflectivity will oscillate around an average determined by the amplitude reflectivity of the top surface, with damping determined by absorption in the film. Increasing roughness of the film during deposition will cause a decrease in the reflectivity at the top surface, leading to a reduction in the average between the maxima and minima of the oscillations. Similarly, decreasing roughness during deposition leads to the average increasing. Using an exponential factor as in equation (2.70) to describe the effect of roughness on reflectivity then allows the change in roughness during film deposition to be estimated. Typical results are shown in Table 5.1⁽¹²⁾—these are in qualitative agreement with other methods of assessing film roughness, such as electron microscopy.⁽¹⁷⁾ The

Table 5.1. Roughness of Films Assessed by Measuring the Change in Reflectivity during Deposition

	Material	Substrate	Increase in roughness of 10-nm-thick films (nm)
Low absorption	Boron	Re/W	0.1
	Carbon	Re/W	0
	LiF	Re/W	1.7
High absorption	Nickel	Silicon	0–0.3
	Tantalum	Silicon	0.52
	Tungsten	Silicon	0.3
	Rhenium	Silicon	0.52
	Osmium	Silicon	0.53
	Iridium	Silicon	0.42
	Platinum	Si/float glass	0.28–0.6
	Gold	Silicon	0.8
	Au/Pd	Silicon	0.33
	Re/W	Silicon	0–0.25
	Pt/Ir	Float glass	–0.3 to +0.2
		Silicon	0.7

results show that boron and carbon are suitable materials for the low-absorption layers, while lithium fluoride, although it has low absorption in the wavelength range 1.8–4.5 nm, is not. Of the high-atomic-number materials the best single element is tungsten, but films can be made smoother by using material combinations. For example, gold films can be made much smoother by adding palladium. The smoothest films obtained so far are made from rhenium–tungsten mixtures, with between 30% and 70% rhenium.⁽²⁾ Both these elements have high characteristic (Debye) temperatures

$$T_D = h\nu_m/k \quad (5.1)$$

where ν_m is the maximum frequency of the elastic vibrations of the material, h is Planck's constant, and k is Boltzmann's constant. Thus at room temperature there is little mobility of the atoms. Also, since the alloy grows as an amorphous film, there is no crystallization and therefore no microcrystals. Films 20 nm thick deposited on low-temperature substrates show voids only 0.5–1 nm across, to be compared with the 5-nm voids on 5-nm-thick gold films.⁽²⁾ For these reasons, rhenium–tungsten films have, under certain circumstances, been observed to show smoothing.

5.2.2. Mirror Manufacture

The first requirement for the manufacture of high-reflectivity multi-layer mirrors is a smooth substrate. These can be made as described in Chapter 3. The substrate can be either flat, in which case the multilayer mirror will have to be bent to perform focusing, or curved, in which case the layers will, in principle, follow the substrate figure. It is, however, more difficult to make uniform layers on curved substrates.

Although many different substrate materials have been used, the most consistent results have been obtained with single-crystal silicon wafers, with either (100) or (111) orientation. Cleaved mica, high-quality float glass, and, in some cases, plastic films can also be used.

5.2.2.1. Layer Deposition by Sputtering⁽³⁾

Since sputter deposition is a very complex process, it is not appropriate to consider it in detail here, as this is done in many books on thin-film technology.⁽¹⁸⁻²⁰⁾ Simply, sputtering is the deposition of particles evaporated from a cathode during electrical discharge through a gas such as argon. However, in addition to the conditions affecting the vapor deposition, the geometry of the system has to be considered.

Clearly, an important part of any apparatus is the sputter source, which should allow a high deposition rate to minimize the requirements of system stability. The source should also deposit small amounts of energy in the substrate and cause little radiation damage, since these can cause mixing of the materials extending several nanometers into a layer, thus degrading the sharpness of the interfaces. Available sources can be classified into three types, each of which can operate using direct current or radiofrequency power. Of these, standard diode sources are not suitable since they result in low deposition rates, a large fraction of the power is deposited in the substrate, and radiation damage is high. Triode sources give higher deposition rates but do not overcome the other problems. Magnetron sources also give large deposition rates, about an order of magnitude higher than possible with diodes, and, in addition, the source can be isolated from the substrate so that both energy deposition and radiation damage can be minimized. These advantageous properties arise from the construction of magnetron sources, which, behind the sputter source, have a magnet system that gives a fringing field that traps secondary electrons. These electrons, which are important in the ionization of the sputter gas, are trapped at the surface of the target and in turn trap the plasma, thus causing the plasma density at the surface to be increased. Because of this confinement the interaction of the sputtering plasma with the deposition surface is minimized and,

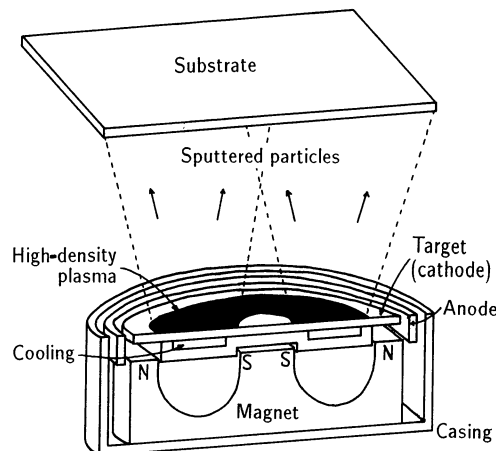


Figure 5.10. Construction of a suitable source, the ring gap plasmatron, for the manufacture of multilayer mirrors by sputtering. (After Vossen and Kern.⁽²⁰⁾)

because of the increase in plasma density, the rate of deposition is increased.

The construction of a typical source, the ring gap plasmatron, is shown in Figure 5.10.⁽²¹⁾ In this, a circular target (cathode), a permanent magnet that generates a magnetic field gap, and an anode are in a closed, grounded casing. Typically, field strengths of $(3\text{--}6) \times 10^{-2}$ T, cathode potentials of $-(300\text{--}700)$ V, and anode potentials of $+(0\text{--}35)$ V are used. The configuration of the electrodes and the magnetic field creates a high-density ring-shaped plasma with an inhomogeneous ion current distribution on the target surface. The mean current density in the ring gap field is greater than 200 A m $^{-2}$; because of this high power density at the cathode, the gap field zone must be cooled. Highest sputtering rates are obtained at an argon pressure of around 3×10^{-3} Torr when, at a power of 5 kW, deposition rates of greater than 10^{-4} kg min $^{-1}$ are possible.

A further factor affecting the nature of the deposited layers is the energy of the depositing atoms. Typically, their mean kinetic energy is about 8 eV, but there is a tail extending to about 80 eV. The distribution of energies can broaden the interfaces.

The most successful way of manufacturing multilayer mirrors by magnetron sputtering has been to use a triangular array of fixed sources with a rotating substrate table.⁽³⁾ The sources are arranged so that their deposition profiles do not overlap and then uniform rotation of the substrate results in the deposition of distinct layers. Alloys can be deposited by allowing the profiles to overlap, and layer thickness is controlled by monitoring the rotation rate. Rotation of the substrate has the added advantage that the depositing atoms arrive at the surface over a range of incidence angles, which minimizes shadowing and therefore

the effects of substrate roughness. This method has allowed the manufacture of mirrors with over 100 layer pairs with minimum thicknesses around 1.5 nm and very small layer thickness errors.

The behavior of these multilayer mirrors has been evaluated in many laboratories⁽³⁾ specifically for tungsten/carbon, vanadium/carbon, and titanium/carbon systems. The measured reflectivities are generally within a small factor (2 or 3) of those predicted, while the widths of the diffraction peaks are very close to the theoretical values. The departures from the predictions may be explained by poor knowledge of the optical constants used in the calculations, and by interfacial roughnesses of around 0.14–0.18 nm ($\sim 0.1\text{--}0.03d$) for the tungsten/carbon mirrors and about 0.8 nm ($\sim 0.06d$) for the vanadium/carbon mirrors.

5.2.2.2. Layer Deposition by Evaporation

Deposition by thermal evaporation is very simple and convenient and is described in detail in many books.^(18–20) The basis of the method is to heat a solid material to a sufficiently high temperature to vaporize it and then to allow the vapor to condense onto a cooler substrate. The important components of an evaporation system for manufacturing multilayer mirrors are the method of heating the materials and the monitoring of layer thicknesses. Also, in order to ensure straight line paths for the majority of the emitted vapor atoms, ambient pressures lower than about 10^{-5} Torr are necessary.

The mass evaporation rate of vapor atoms from a clean surface under vacuum is⁽¹⁸⁾

$$dm/dt = 0.583P(M/T)^{1/2} \text{ kg m}^{-2} \text{ sec}^{-1} \quad (5.2)$$

where P is the equilibrium vapor pressure in Torr of the evaporant under saturated vapor conditions at temperature T (K) and M is the molecular weight of the vapor species. This is an upper limit to the vapor deposition rate on the substrate, which also depends on the source geometry and position relative to the substrate and on the condensation coefficient. The properties of materials that have been used in the manufacture of evaporated multilayer mirrors are given in Table 5.2.⁽¹⁸⁾

Early attempts at manufacturing evaporated multilayer mirrors^(2,6–8,15) used quartz-crystal oscillator microbalances to monitor layer thicknesses, with the deposition of the layers controlled by shutters. In the later examples of this, gold/carbon, copper/carbon,⁽¹⁵⁾ and rhenium–tungsten/carbon⁽²⁾ mirrors were made. The gold/carbon and copper/carbon mirrors were made on glass (microscope objective) substrates, with the gold and copper being evaporated from a tungsten boat and the carbon

Table 5.2. Properties of Materials Used for Evaporated Multilayer Mirrors

Material	Melting point (K)	Temp (K) for vapor pressure of 10^{-4} Torr	Molecular weight	Evaporation rate ($\text{kg m}^{-2} \text{ sec}^{-1}$)
Boron	2303	2673	10.81	3.71×10^{-6}
Carbon	3773	2683	12.011	3.90×10^{-6}
Titanium	1953	1988	47.90	9.05×10^{-6}
Vanadium	2193	2093	50.942	9.10×10^{-6}
Chromium	2173	1703	51.996	1.02×10^{-5}
Manganese	1523	1293	54.938	1.20×10^{-5}
Iron	1812	1480	55.847	1.13×10^{-5}
Nickel	1726	1808	58.71	1.05×10^{-5}
Cobalt	1763	1803	58.9332	1.05×10^{-5}
Copper	1356	1305	63.54	1.29×10^{-5}
Niobium	2773	2823	92.906	1.06×10^{-5}
Ruthenium	2673		101.07	
Palladium	1825	1738	106.4	1.44×10^{-5}
Silver	1234	1378	107.870	1.63×10^{-5}
Tantalum	3269	3133	180.948	1.40×10^{-5}
Tungsten	3653	3303	183.85	1.38×10^{-5}
Rhenium	3440		186.20	
Platinum	2042	2293	195.09	1.70×10^{-5}
Gold	1336	1678	196.967	2.00×10^{-5}

with an electron gun. During the deposition of the metals, the pressure in the system rose only slightly from the base pressure of 5×10^{-7} Torr, while the carbon evaporation caused a pressure rise to 10^{-5} Torr. Also, during the carbon deposition, the quartz monitor became excessively heated, which caused it to drift. This meant that it was not possible to use the shutter and the thickness could only be obtained from the quartz monitor readings in the steady state before and after the deposition. In order to obtain the desired thickness, several evaporation were usually necessary. Layer thickness errors of up to 20% of the thickness were obtained—these large errors limited the number of layer pairs to less than ten. Even then, the measured reflectivities were worse than the predicted values by factors of 2.5 and larger—this could be attributed to interfacial roughness.

The same monitoring method applied to rhenium–tungsten/carbon multilayers on polished (111)-silicon wafers gave significantly better results, because of the smoother nature of the interfaces. In this case both types of layer were evaporated with an electron gun at pressures of about 10^{-6} Torr and a substrate cooled to 77 K. For some mirrors, the reflectivities were close to the theoretical values, but others did not

perform so well. This was again because of the accumulated thickness errors, resulting in a practical limitation of less than ten layer pairs. An important result from this work was the demonstration of the stability of these multilayers—little or no decrease in reflectivity was observed over a period of 6 months.⁽²²⁾

In order to increase the number of layers that can be accurately deposited, it is necessary to monitor the reflectivity *in situ*. This was done in the evaporation system described above by incorporating an X-ray source and an X-ray counter.^(9,11,12) The source gave characteristic X-ray wavelengths of 6.76 nm (boron), 4.47 nm (carbon), or 3.16 nm (nitrogen, in boron nitride), and angles of incidence around 60–65° were used. In addition to determining the point at which to change from one layer material to the other, as described in Section 5.1.2, this system allowed immediate recognition of any overshooting of the optimum thickness. The next layer could then be made thinner to compensate so that the following layer contributed with the correct phase. Also, the optical constants do not, in principle, need to be accurately known if the monitoring can be carried out at the design wavelength and incidence angle.

With this system, multilayer mirrors have been made with layers of rhenium–tungsten with carbon or boron, gold–palladium with carbon or boron, and vanadium, chromium, manganese, iron, nickel, cobalt, ruthenium, and platinum, all with carbon, on glass or silicon substrates. Of these, gold–palladium/boron and manganese/carbon do not give stable boundaries. All the other combinations give reasonably stable usable multilayer mirrors with up to about 100 layers. In the case of rhenium–tungsten/carbon the multilayer was observed to increase in thickness by about 0.5% year⁻¹ at room temperature. This aging can be accelerated by annealing at 400 °C for several hours in a vacuum furnace,⁽¹⁶⁾ after which some of the combinations (chromium, iron, cobalt, and nickel with carbon) show drops in reflectivity due to increases in the interfacial roughnesses and to the formation of microcrystallites in the metal layers.

All these mirrors give performances reasonably close to those predicted,^(11,16) with interfacial roughnesses ranging from 0.2–0.4 nm for rhenium–tungsten/carbon to about 0.8 nm for vanadium, chromium, and ruthenium with carbon. Other combinations with small values of roughness are platinum/carbon (<0.5 nm), and iron and cobalt with carbon (0.3–0.5 nm). Rhenium–tungsten/boron, which is a suitable combination for wavelengths just below the carbon K_{α} absorption edge, has a relatively high interfacial roughness (0.7 nm). These roughnesses appear to be larger than those obtained in the sputtering technique.⁽³⁾

5.2.2.3. Laser Evaporation

Both sputtering and thermal, or electron gun, evaporation are well-understood techniques that have been used in a wide variety of circumstances. As discussed above, they can be perfectly adequate for multilayer mirror manufacture from a range of materials. A technique that may be usable with a larger number of materials⁽²³⁾ is laser evaporation,⁽¹⁰⁾ alternatively known as laser sputtering.⁽²⁴⁾

Removal of material from a solid surface by pulsed laser bombardment has been observed at both infrared^(10,25,26) and ultraviolet⁽²⁴⁾ wavelengths. The input laser beam is focused onto a target to give a power density of $\sim 10^{13}$ – 10^{14} W m^{-2} , sufficient to vaporize the target but low enough so that a dense plasma is not formed (thermal sputtering or transient vaporization). At lower power densities, $\sim 10^{12} \text{ W m}^{-2}$, sputtering of metals in vacuum still occurs but this is now a hydrodynamical effect,⁽²⁷⁾ a result of transient melting. In order to understand which of the effects is important for a particular material, it is necessary to know the maximum surface temperature reached during each laser pulse. Thermal sputtering may need temperatures in excess of normal boiling points,^(24,27) which have no special meaning for short duration or vacuum heating, because vaporization is confined to the outer surface and occurs to a calculable extent at all temperatures. At the boiling temperature, vaporization of a surface atom typically takes several tens of nanoseconds, whereas a laser pulse is effective in causing vaporization over a few nanoseconds around the end of the pulse when the temperature is highest. Thus vaporization can be neglected for temperatures well above the boiling point.

It is, however, difficult to estimate the temperature attained by a surface since energy deposition efficiencies are not well understood. These efficiencies depend on the surface reflectivities at high temperatures and on the fraction of the laser pulse absorbed by the plasma above the target surface. Although surface reflectivities at high temperatures are typically less than about 20% and can be neglected, absorption in the plasma is significant though not well quantified. The surface temperature also depends on the energy loss efficiency, which is dominated by the well-understood process of thermal diffusion.

Several materials have been investigated for laser sputtering. These include aluminum, molybdenum, platinum, and gold,⁽²⁷⁾ carbon, tungsten, and rhenium,^(10,27) tantalum,⁽¹⁰⁾ and several compounds.⁽²⁴⁾ Multilayer mirrors of tantalum, tungsten, and rhenium with carbon have been made using the setup shown in Figure 5.11.^(10,25,26) No *in situ* monitoring was carried out, the layer thicknesses being estimated from measured

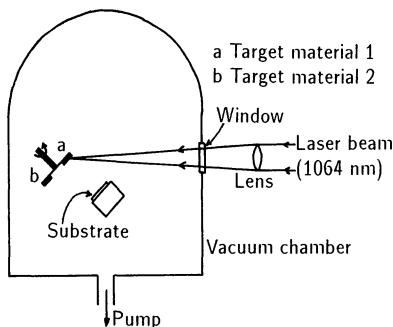


Figure 5.11. Manufacturing system for laser deposition of multilayers.

sputtering rates. Up to 50 layers with periods of 6–8 nm were deposited, the absorbing layers being 0.3–2.5 nm thick. Reflectivities of up to about 20% were obtained in the wavelength range 5–8 nm.

The evaporated atoms typically have velocities of a few times 10^4 m sec^{-1} and thus, for a substrate a few centimeters from the target, deposition takes place a few microseconds after the pulse. Suitable lasers have pulse repetition frequencies of around 10 Hz and thus it would be possible to use alternate pulses for deposition and for forming a plasma giving soft X-ray emission for monitoring. The use of this type of system has not yet been reported, and its possible implementation will be discussed in Chapter 11.

Diffractive Optics I

Diffraction Gratings

6.1. Introduction

Two types of diffractive optics are used in soft X-ray optical systems—linear gratings, on either plane or shaped substrates, and zone plates. The former are employed in, for example, soft X-ray monochromators and spectrometers, while the latter are of use in image-forming systems such as microscopes and telescopes. The general properties of diffraction gratings have recently been comprehensively discussed,⁽¹⁾ and in this chapter only those features important for the soft X-ray region will be considered. Since grating efficiencies are more dependent on the smoothness than the profiles of the grooves,⁽¹⁾ this topic will be discussed in Chapter 7.

6.2. Plane Linear Gratings

The properties of plane linear gratings, which have been dealt with in great detail by Stroke,⁽²⁾ are briefly discussed below following the approach of James.⁽³⁾ The treatment given is independent of whether the gratings are used in transmission or, more usually for X rays, reflection. Consider two grating lines L_1 and L_2 (Figure 6.1), which are assumed, for now, to be infinitely thin, separated by a distance \mathbf{d} . A plane monochromatic wave is incident from the direction \mathbf{p}_0 , at an angle α to the normal to \mathbf{d} , and is scattered by L_1 and L_2 through an angle $(\alpha + \beta)$, so that the reflected (or transmitted) wave travels in a direction \mathbf{p} at an angle β . The two scattered wavelets are assumed to arrive at a point Q at a distance R large compared to $|\mathbf{d}|$ so that the lines L_1Q and L_2Q may be considered

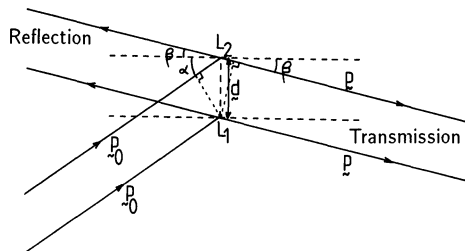


Figure 6.1. Derivation of the plane grating equation.

as parallel. The path difference between the two scattered wave fronts is, *in vacuo* (refractive index unity),

$$l = \mathbf{d} \cdot \mathbf{P} \quad (6.1)$$

and the corresponding phase difference is

$$\phi = (2\pi/\lambda)\mathbf{d} \cdot \mathbf{P} \quad (6.2)$$

where λ is the wavelength of the radiation, and $\mathbf{P} = \mathbf{p} - \mathbf{p}_0$. If A_0 is the amplitude of the scattered wave at unit distance from the scatterer L_1 , then the corresponding displacement at Q may be written

$$y_1 = (A_0/R) \exp(i\omega t) \quad (6.3)$$

while that at Q due to the scatter from L_2 is

$$y_2 = (A_0/R) \exp\{i[\omega t + (2\pi/\lambda)\mathbf{d} \cdot \mathbf{P}]\} \quad (6.4)$$

The resultant disturbance Y at Q due to the whole grating is obtained by summing equation (6.4) over all the grating lines (i.e., all distances d). Thus

$$Y = (A_0/R) \exp(i\omega t) \sum_{n=0}^{N-1} \exp\{i[(2\pi/\lambda)n\mathbf{d} \cdot \mathbf{P}]\} \quad (6.5)$$

$$= (A_0/R) \exp(i\omega t) \frac{1 - \exp\{i[(2\pi/\lambda)N\mathbf{d} \cdot \mathbf{P}]\}}{1 - \exp\{i[(2\pi/\lambda)\mathbf{d} \cdot \mathbf{P}]\}} \quad (6.6)$$

where N is the total number of lines. The intensity at Q is then

$$I = YY^* = (|A_0|/R)^2 \frac{\sin^2[(N\pi/\lambda)\mathbf{d} \cdot \mathbf{P}]}{\sin^2[(\pi/\lambda)\mathbf{d} \cdot \mathbf{P}]} \quad (6.7)$$

with maxima

$$I_{\max} = (|A_0|/R)^2 N^2 \quad (6.8)$$

when

$$(\pi/\lambda)\mathbf{d} \cdot \mathbf{P} = m\pi \quad (6.9)$$

with $m = 0, \pm 1, \pm 2$. Referring to Figure 6.1, this leads to

$$d(\sin \alpha + \sin \beta) = m\lambda \quad (6.10)$$

—the grating equation. A grating diffraction pattern, obtained from equation (6.10) with $N = 10$ to show up the form of the pattern, is given in Figure 6.2. This shows that between each main maximum there are $N - 2$ secondary maxima and the positions of the first minima are at

$$(\pi/\lambda)\mathbf{d} \cdot \mathbf{P} = (m \pm 1/N)\pi \quad (6.11)$$

In practice, gratings have very large N and so the intensity is only appreciable close to the main maxima. For a grating of width W ,

$$N = W/d \quad (6.12)$$

Due to the wavelength dependence of equation (6.10), radiation of a different wavelength is diffracted into order m at a different angle β for the same angle of incidence. Thus the resolving power of a grating can be expressed in terms of the wavelength discrimination. Using the Rayleigh criterion, the first dark ring of the diffraction pattern for wavelength

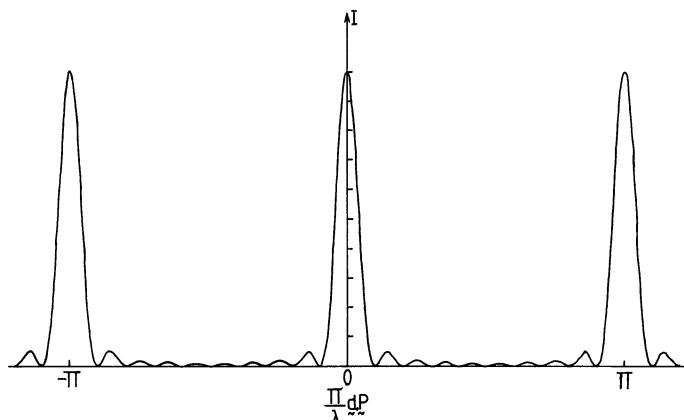


Figure 6.2. Diffraction pattern for a plane grating with ten lines.

$\lambda + \Delta\lambda/2$ should coincide with the peak of the central disk for wavelength $\lambda - \Delta\lambda/2$. This gives the resolving power in the m th order (for a perfect grating)

$$R_m = \lambda/\Delta\lambda = Nm - 1/2 \quad (6.13)$$

$$\simeq Nm = Wm/d \quad (6.14)$$

for large N . Thus, for high resolution, the grating must have a large number of lines (i.e., a large width). Using equations (6.10) and (6.14) gives

$$R_m = (W/\lambda)(\sin \alpha + \sin \beta) \quad (6.15)$$

i.e., for a given wavelength, high resolution is given by large angles of incidence.

By differentiating equation (6.10) with respect to β , the angular dispersion of a plane grating is found to be

$$d\beta/d\lambda = m/d \cos \beta \quad (6.16)$$

The above grating properties have been derived for a plane incident wave, i.e., a point source at infinity. For a source of finite size s at a distance r from the grating (Figure 6.3), the resolution limit $\Delta\lambda_s$ is given by

$$d[\sin(\alpha + \Delta\alpha) + \sin \beta] = m(\lambda + \Delta\lambda_s) \quad (6.17)$$

i.e.,

$$\Delta\lambda_s = (d/m) \Delta\alpha \cos \alpha = (ds/mr) \cos \alpha \quad (6.18)$$

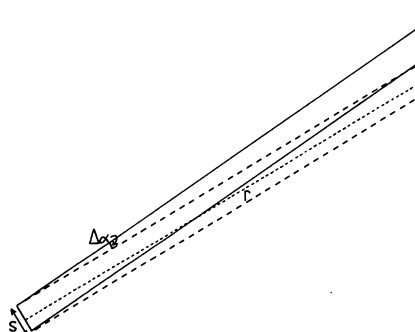


Figure 6.3. Illumination of a plane grating by a finite source at a finite distance.

6.3. Concave Spherical Gratings

Plane linear gratings do not focus the incident radiation but only disperse it. Thus they must be used in conjunction with other optical elements if focusing is required. Gratings on curved surfaces can be used as focusing elements; since this implies reflection, it is necessary to use grazing incidence to obtain high reflectivities at soft X-ray wavelengths, as discussed in Chapter 2. Despite this, it is instructive to consider the image-forming properties of gratings on curved surfaces for general angles of incidence.

The idea of combining a plane grating and a concave spherical surface was suggested by Rowland in 1882.⁽⁴⁾ The image-forming properties of such systems have been dealt with by many authors, notably Beutler⁽⁵⁾ and Namioka,⁽⁶⁾ and can be determined by reference to Figure 6.4, in which the coordinate origin is at the center of the grating. Consider radiation from an object point $P(x, y, z)$ forming an image at $P'(x', y', z')$ via the point $Q(\xi, \eta, v)$ on the grating. The coordinate ξ specifies the positions of the grating lines and so only has discrete values given by the integer ξ/d where d is the line spacing. For reinforcement of the image at P' , the path difference for two lines separated by ξ is $\xi m \lambda/d$ where m is the diffraction order, and so the optical path PQP' may be represented by the function

$$L = PQ + QP' + \xi m \lambda/d \quad (6.19)$$

PQ may be evaluated in terms of ξ , η , u , y , and α , and QP' in terms of ξ , η , v , y' , and β , using Figure 6.4.⁽⁶⁾ Then, using Fermat's principle, the

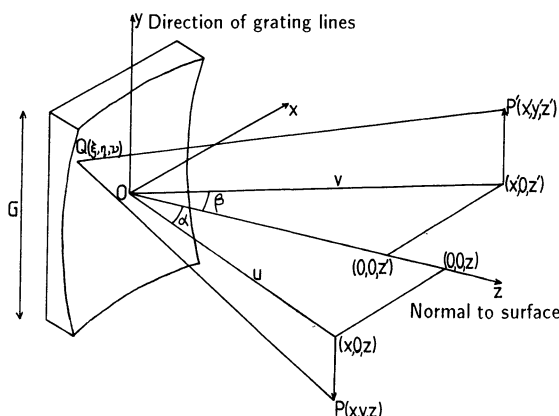


Figure 6.4. Image formation by a concave spherical grating.

image point P' is located by specifying that L has an extreme value for any point Q , i.e.,

$$\partial L / \partial \xi = 0 \quad \text{and} \quad \partial L / \partial \eta = 0 \quad (6.20)$$

In general, equations (6.20) do not have simultaneous solutions and so there is no perfect focus, i.e., a spherical grating does not form a perfect image. Radiation diffracted from the point $Q(\xi, \eta, v)$ goes in the direction specified by β and y'/v , which are both functions of ξ and η . Thus the direction of the diffracted radiation changes with the position of Q , so that different points P' on the focal plane are illuminated—a point source is focused into a vertical line at the horizontal focus and into a horizontal line at the vertical focus. In order to produce the least aberrated image, the dependence of β and y'/v on ξ and η must be minimized. For radiation via the center of the grating (POP'), equations (6.20) lead to

$$d(\sin \alpha + \sin \beta_0) = m\lambda(1 + y^2/u^2)^{1/2} \quad (6.21)$$

and

$$y/u = -y'_0/v_0 \quad (6.22)$$

where v_0 , β_0 , and y'_0 specify the image point for radiation via O . These equations give, respectively, the grating equation and the geometrical relation between object and image points. When $y \ll u$, equation (6.21) reduces to the plane grating equation. The general expressions obtained from equation (6.20) may be written in the following form by expanding about (v_0, β_0, y'_0) :

$$\begin{aligned} c_{\beta_0} \Delta \beta &= \frac{1}{2} \sum_{n=0}^{\infty} (n+2)\xi^{n+1} [(s_\alpha/u)^n (c_\alpha^2/u - c_\alpha/\rho) \\ &\quad + (s_\beta/v)^n (c_\beta^2/v - c_\beta/\rho)] + O(\xi^2/R^2) \end{aligned} \quad (6.23)$$

$$\Delta(y'/v) = \eta(1/u - c_\alpha/\rho + 1/v - c_\beta/\rho) + O(\xi^2/\rho^2) \quad (6.24)$$

where $\beta = \beta_0 + \Delta \beta$, $y'/v = y'_0/v_0 + \Delta(y'/v)$, ρ is the radius of curvature of the grating surface, $c_\theta = \cos \theta$, and $s_\theta = \sin \theta$. Thus, to minimize the dependence of β and y'/v on ξ and η , the largest terms in equations (6.23) and (6.24) should be made equal to zero by suitable mounting of the grating. From equation (6.23), the best horizontal focus satisfies

$$c_\alpha^2/u - c_\alpha/\rho + c_\beta^2/v - c_\beta/\rho = 0 \quad (6.25)$$

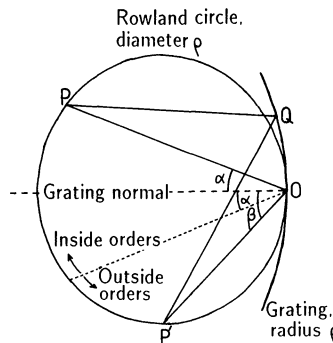


Figure 6.5. The Rowland circle.

which has solutions

$$u = \infty, \quad v = \rho c_\beta^2 / (c_\alpha + c_\beta) \quad (6.26)$$

and

$$u = \rho c_\alpha, \quad v = \rho c_\beta \quad (6.27)$$

Equation (6.26) represents an object at infinity, i.e., a plane incident wave, and gives the conditions for the Wadsworth mounting.⁽⁷⁾ Equation (6.27) shows that the diffracted light (of all wavelengths) is focused horizontally on the circumference of a circle of diameter ρ (the Rowland circle) equal to the grating radius of curvature, so long as the object and the grating lie on the circle (Rowland mounting) and the grating normal lies along a diameter (Figure 6.5).

The equation giving the best vertical focus is, from equation (6.24),

$$1/u - c_\alpha/\rho + 1/v - c_\beta/\rho = 0 \quad (6.28)$$

with solutions

$$u = \infty, \quad v = \rho / (c_\alpha + c_\beta) \quad (6.29)$$

and

$$u = \rho / c_\alpha, \quad v = \rho / c_\beta \quad (6.30)$$

For the Wadsworth mounting the horizontal and vertical foci coincide for any angle α so long as the images are viewed along the grating normal. For Rowland mountings⁽⁴⁾ the foci coincide for the trivial case $c_\alpha = c_\beta = 1$. Under these conditions a spherical grating gives stigmatic imaging. Since $\Delta\beta$ is related to image width and $\Delta(y'/v)$ to

astigmatism, in most cases it is better to satisfy equation (6.25), in which case the major aberration of a spherical grating is astigmatism. However, it is not possible to truly separate the aberrations since they are closely related to one another. Low-order aberration terms such as coma are identically zero for Rowland mountings, which are therefore preferred for high resolutions. Then, equations (6.19)–(6.22) lead to, with $t_\theta = s_\theta/c_\theta$, $Z^2 = 1 + (y/\rho c_\alpha)^2$, and $Z'^2 = 1 + (y'/\rho c_\beta)^2$,

$$\begin{aligned} L = & \rho(Zc_\alpha + Z'c_\beta) + \xi(m\lambda/d - s_\alpha/Z - s_\beta/Z') \\ & - (\eta/\rho)(y/Zc_\alpha + y'/Z'c_\beta) + (\eta^2/2\rho)(s_\alpha t_\alpha + s_\beta t_\beta) \\ & + (\xi/2\rho^2)[\eta^2(s_\alpha t_\alpha^2 + s_\beta t_\beta^2) - 2\eta(yt_\alpha/c_\alpha + y't_\beta/c_\beta)] \\ & + \{\eta^2\xi^2(s_\alpha t_\alpha^3 + s_\beta t_\beta^3) - 2\eta\xi^2(yt_\alpha^2/c_\alpha + y't_\beta^2/c_\beta) \\ & + \xi^2(y^2t_\alpha^2/c_\alpha + y'^2t_\beta^2/c_\beta) + (\xi^2 + \eta^2)^2(s_\alpha t_\alpha + s_\beta t_\beta)/4 \\ & - \eta^2[(\eta s_\alpha^2 - 2y)^2 + 2y^2s_\alpha^2]/4c_\alpha^3 - \eta[(\eta s_\beta^2 - 2y')^2 \\ & + 2y'^2s_\beta^2]/4c_\beta^3\}/2\rho^3 + O(\xi^5/\rho^4) \end{aligned} \quad (6.31)$$

$$\begin{aligned} \partial L / \partial \xi = 0 = & (m\lambda/d - s_\alpha/Z - s_\beta/Z') + [\eta^2(s_\alpha t_\alpha^2 + s_\beta t_\beta^2) \\ & - 2\eta(yt_\alpha/c_\alpha + y't_\beta/c_\beta)]/2\rho^2 \\ & + (\xi/\rho^3)[\eta^2(s_\alpha t_\alpha^3 + s_\beta t_\beta^3) - 2\eta(yt_\alpha^2/c_\alpha + y't_\beta^2/c_\beta) \\ & + (y^2t_\alpha^2/c_\alpha + y'^2t_\beta^2/c_\beta) + (\xi^2 + \eta^2)(s_\alpha t_\alpha + s_\beta t_\beta)/2] \\ & + O(\xi^4/\rho^4) \end{aligned} \quad (6.32)$$

$$\begin{aligned} \partial L / \partial \eta = 0 = & -(y/Zc_\alpha + y'/Z'c_\beta)/\rho + (\eta/\rho)(s_\alpha t_\alpha + s_\beta t_\beta) \\ & + (\xi/\rho^2)[\eta(s_\alpha t_\alpha^2 + s_\beta t_\beta^2) - (yt_\alpha/c_\alpha + y't_\beta/c_\beta)] \\ & + \{\eta\xi^2(s_\alpha t_\alpha^3 + s_\beta t_\beta^3) - \xi^2(yt_\alpha^2/c_\alpha + y't_\beta^2/c_\beta) \\ & + (\xi^2 + \eta^2)(s_\alpha t_\alpha + s_\beta t_\beta)/2 \\ & - \eta[(\eta s_\alpha^2 - 2y)(\eta s_\alpha^2 - y) + y^2s_\alpha^2]/c_\alpha^3 \\ & - \eta[(\eta s_\beta^2 - 2y')(\eta s_\beta^2 - y') + y'^2s_\beta^2]/c_\beta^3\}/\rho^3 \\ & + O(\xi^4/\rho^4) \end{aligned} \quad (6.33)$$

$$d(s_\alpha + s_\beta) = m\lambda Z \quad (6.34)$$

and

$$y/c_\alpha = -y'_0/c_{\beta_0} \quad (6.35)$$

6.3.1. Aberrations in Rowland Circle Mountings

If y_0 and y'_0 are the y coordinates of the center of the object and the corresponding image point for radiation via the center of the grating,

then the y coordinates of any point of the object and image are $y = y_0 + \Delta y$ and $y' = y'_0 + \Delta y'$, respectively. Also, if β_0 is the diffraction angle between y_0 and y'_0 , the diffraction angle via $Q(\xi, \eta, \nu)$ is $\beta = \beta_0 + \Delta\beta$. If it is assumed that the object is parallel to the direction of the grating lines (the case where it is inclined at a small angle has been considered by Namioka⁽⁶⁾), then, from equations (6.33)–(6.35), the coordinate η may be expressed by

$$\eta = [c_{\beta_0} \Delta y + c_\alpha \Delta y' + (\xi/\rho A) s_{\alpha-\beta_0} (y_0 A/c_\alpha + s_{\beta_0}^2 \Delta y - s_\alpha^2 \Delta y') + O(\xi^3/\rho^2)]/A \quad (6.36)$$

where

$$A = s_\alpha^2 c_{\beta_0} + c_\alpha s_{\beta_0}^2 \quad (6.37)$$

Similarly, from equations (6.32) and (6.34)–(6.36),

$$\begin{aligned} c_{\beta_0} \Delta\beta = & [By_0 \Delta y - Dy_0 \Delta y' + E(\Delta y)^2 + F(\Delta y')^2 - H \Delta y \Delta y']/2\rho^2 \\ & + (\xi/\rho^3) \{Jy_0 \Delta y - Ky_0 \Delta y' + M(\Delta y)^2 + N(\Delta y')^2 + P \Delta y \Delta y' \\ & + [\xi^2 A c_\alpha^2 + 4y_0^2 A - 4y_0^2 s_{\alpha-\beta_0}^2/A]/2c_\alpha^3 c_{\beta_0}\} + O(\xi^4/\rho^4) \end{aligned} \quad (6.38)$$

where

$$B = 2(s_\alpha - s_{\alpha-\beta_0}/A)/c_\alpha^2 \quad (6.39)$$

$$D = 2(s_{\beta_0} + s_{\alpha-\beta_0}/A)/c_\alpha c_{\beta_0} \quad (6.40)$$

$$E = (s_\alpha - s_\alpha c_{\beta_0}/A - s_{\beta_0}^2 c_\alpha s_{\alpha-\beta_0}/A^2)/c_\alpha^2 \quad (6.41)$$

$$F = (s_{\beta_0} - s_{\beta_0} c_\alpha/A + s_\alpha^2 c_{\beta_0} s_{\alpha-\beta_0}/A^2)/c_{\beta_0}^2 \quad (6.42)$$

$$H = 2s_\alpha s_{\beta_0} (s_\alpha + s_{\beta_0})/A \quad (6.43)$$

$$\begin{aligned} J = & 2t_\alpha/c_\alpha - s_{\alpha-\beta_0}[2s_{\alpha+\beta_0} + s_\alpha c_{\beta_0} \\ & + c_\alpha(s_{\beta_0}^2 s_{\alpha-\beta_0} - c_\alpha c_{\beta_0}^2)]/Ac_\alpha^3 c_{\beta_0} \end{aligned} \quad (6.44)$$

$$\begin{aligned} K = & [2s_{\beta_0}^2 c_\alpha + s_{\alpha-\beta_0}(2s_{\alpha+\beta_0} + s_{\beta_0} c_\alpha \\ & - c_\alpha^2 c_{\beta_0}^2/A)/A - s_\alpha^2 c_{\beta_0} s_{\alpha-\beta_0}^2/A^2]/c_\alpha^2 c_{\beta_0}^2 \end{aligned} \quad (6.45)$$

$$\begin{aligned} M = & c_{\beta_0}^2 (s_\alpha t_\alpha^3 + s_{\beta_0} t_{\beta_0}^3) + t_\alpha^3/c_\alpha \\ & + c_{\beta_0}(1 - 5s_\alpha^2)/2Ac_\alpha^3 - s_{\alpha-\beta_0} s_{\beta_0}^2 (t_\alpha/c_\alpha - c_{\beta_0}/A)/A^2 \end{aligned} \quad (6.46)$$

$$\begin{aligned} N = & c_\alpha^2 (s_\alpha t_\alpha^3 + s_{\beta_0} t_{\beta_0}^3) + t_{\beta_0}^2/c_{\beta_0} \\ & + c_\alpha(1 - 5s_{\beta_0}^2)/2Ac_{\beta_0}^3 + s_{\alpha-\beta_0} s_\alpha^2 (t_{\beta_0}/c_{\beta_0} - c_\alpha/A)/A^2 \end{aligned} \quad (6.47)$$

and

$$\begin{aligned} P = & 2c_\alpha c_{\beta_0} (s_\alpha t_\alpha^3 + s_{\beta_0} t_{\beta_0}^3) + (1 - 2t_\alpha^2 - 2t_{\beta_0}^2)/A \\ & + s_{\alpha-\beta_0} [s_\alpha t_\alpha^2 - s_{\beta_0} t_{\beta_0}^2 (s_\alpha^2 c_{\beta_0} - c_\alpha s_{\beta_0}^2)/A]/A^2 \end{aligned} \quad (6.48)$$

The object and image coordinates are restricted by, respectively,

$$-l/2 \leq \Delta y \leq l/2 \quad (6.49)$$

and

$$-AG/2c_\alpha - c_{\beta_0} \Delta y/c_\alpha \leq \Delta y' \leq AG/2c_\alpha - c_{\beta_0} \Delta y/c_\alpha \quad (6.50)$$

where l is the length of the object (in the y direction) and G is the illuminated length of the grating lines. For an object centered on the plane containing the grating center and the grating normal ($y_0 = 0$), equations (6.36) and (6.38) reduce to

$$\eta = [c_{\beta_0} \Delta y + c_\alpha \Delta y' + \xi s_{\alpha-\beta_0} (s_{\beta_0}^2 \Delta y - s_\alpha^2 \Delta y')/\rho A] \quad (6.51)$$

and

$$\begin{aligned} c_{\beta_0} \Delta \beta &= [E(\Delta y)^2 + F(\Delta y')^2 - H \Delta y \Delta y'] / 2\rho^2 \\ &+ (\xi/\rho^2)[M(\Delta y)^2 + N(\Delta y')^2 + P \Delta y \Delta y' + \xi^2 A/2c_\alpha c_{\beta_0}] \end{aligned} \quad (6.52)$$

The width of the image of a point on the object is given by equation (6.52). Since this varies with Δy and $\Delta y'$, the image of a straight object is curved. Astigmatism in the image is represented by equation (6.51), which gives

$$\Delta y' = [A\eta - \Delta y(c_{\beta_0} + s_{\alpha-\beta_0} s_{\beta_0}^2/\rho A)]/(c_\alpha - \xi s_{\alpha-\beta_0} s_\alpha^2/\rho A) \quad (6.53)$$

leading to the length of the image due to astigmatism

$$(\Delta y')_{\text{ast}} = AG/(c_\alpha - \xi s_{\alpha-\beta_0} s_\alpha^2/\rho A) \quad [=G(s_\alpha t_\alpha c_{\beta_0} + s_{\beta_0}^2) \quad \text{for } \xi = 0] \quad (6.54)$$

which is obtained by letting η vary from $-G/2$ to $+G/2$. For the object of length l , the total length of the image is therefore

$$(\Delta y')_{\text{tot}} = lc_{\beta_0}/c_\alpha + AG/(c_\alpha - \xi s_{\alpha-\beta_0} s_\alpha^2/\rho A) \quad (6.55)$$

For grazing incidence, $\alpha \rightarrow 90^\circ$ and so the astigmatic image length becomes very large. This is demonstrated in Figure 6.6 for a typical grating ($\rho = 1$ m, 1200 lines mm^{-1} , used at a wavelength of 4.4 nm in the first order).

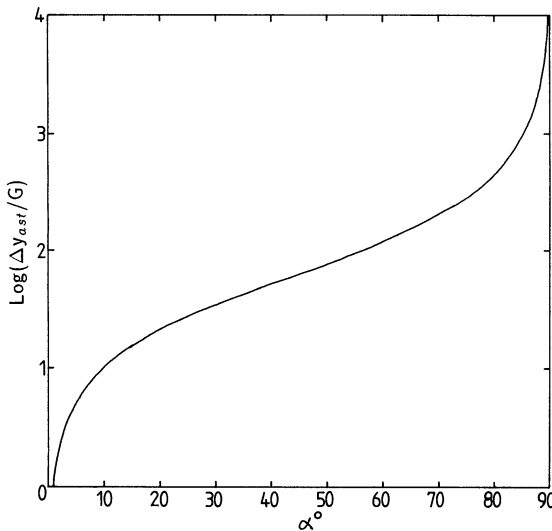


Figure 6.6. The astigmatic image length, as a function of incidence angle, for a concave spherical grating in the Rowland circle mounting.

6.3.2. Resolving Power of a Spherical Grating

In order to define the resolving power of a spherical grating, it is necessary to use a modified Rayleigh criterion, since the intensity distributions across the diffraction maxima are different from those of a plane grating. Using the Rayleigh criterion for a plane grating, the minimum total intensity between two just-resolved lines (of equal intensity) is $8/\pi^2$ times the intensity at the maxima. The resolving power of a curved grating may be defined in terms of the same minimum intensity,⁽⁶⁾ resulting in an expression involving the width of the grating. However, the optimum grating width is limited by spherical aberration; this width is given, to a good approximation, by the diameter of the first (widest) Fresnel zone on the grating at $\eta = 0$ for $y = y' = 0$. The path length from the center to the edge of this zone varies by $\lambda/4$ and so, from equation (6.31),

$$\lambda/4 = (\xi_1^4/8\rho^3)(s_\alpha t_\alpha + s_{\beta_0} t_{\beta_0}) \quad (6.56)$$

where ξ_1 is the x coordinate of the first zone edge at $\eta = 0$. Thus

$$\xi_1 = \pm[2\rho^3\lambda/(s_\alpha t_\alpha + s_{\beta_0} t_{\beta_0})]^{1/4} \quad (6.57)$$

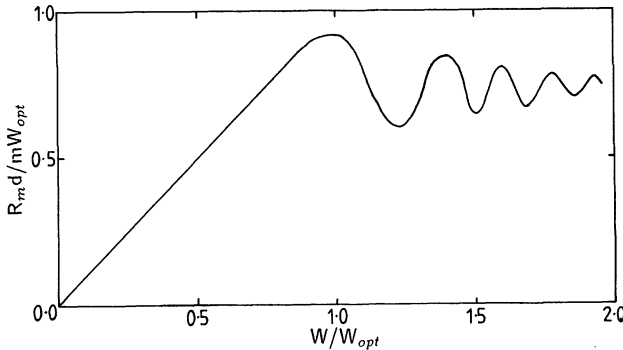


Figure 6.7. The resolving power of a spherical grating as a function of grating width.

and the optimum grating width is

$$W_{\text{opt}}^G = 2 |\xi_1| = 2[2\rho^3 \lambda / (s_\alpha t_\alpha + s_{\beta_0} t_{\beta_0})]^{1/4} \quad (6.58)$$

Using physical optics, rather than the above geometrical approach, i.e., obtaining the intensity distribution by evaluating

$$\int_{-W/2}^{W/2} d\xi \int_{-G/2}^{G/2} d\eta \delta_n \exp(2\pi i L/\lambda) \quad (6.59)$$

where δ_n is the amplitude of the contribution of the n th line of the grating to the total amplitude at the image point, gives⁽⁸⁾

$$W_{\text{opt}}^P = 2.36 [4\rho^3 \lambda / \pi (s_\alpha t_\alpha + s_{\beta_0} t_{\beta_0})]^{1/4} \quad (6.60)$$

Thus

$$W_{\text{opt}}^P / W_{\text{opt}}^G = 1.054 \quad (6.61)$$

so that the difference is usually unimportant, given the rather arbitrary definition of resolving power. The optimum width may be written

$$W_{\text{opt}} = 2.361 \Delta \quad (6.62)$$

with Δ given by either equation (6.58) or equation (6.60). Using the modified Rayleigh criterion, the resolution for a grating of width W is shown in Figure 6.7. This shows that

$$R_m = Wm/d \quad W \leq W_{\text{opt}}/1.18 \quad (6.63)$$

$$R_m^{\text{opt}} = 0.92 W_{\text{opt}} m/d \quad W = W_{\text{opt}} \quad (6.64)$$

$$R_m = 0.75 W_{\text{opt}} m/d \quad W \gg W_{\text{opt}} \quad (6.65)$$

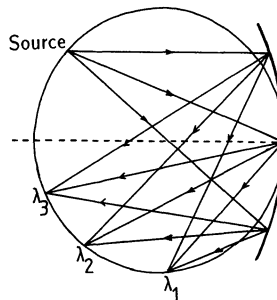


Figure 6.8. The angular dispersion, around the Rowland circle, of a spherical grating.

The angular dispersion of a spherical grating, derived in an analogous fashion to that for a plane grating, is illustrated in Figure 6.8—the different wavelengths are dispersed around the Rowland circle.

6.4. Aspheric Gratings

By modifying the shape of the grating surface it is, theoretically, possible to reduce all aberrations. In practice, such a surface may be difficult, if not impossible, to manufacture, and so only specific surfaces, toroidal and ellipsoidal, will be considered, although a generalized formulation has been published.⁽⁹⁾

6.4.1. Toroidal Gratings⁽¹⁰⁾

If a grating is ruled on a toroidal surface (Figure 6.9) with radii of curvature ρ_a and ρ_b , the horizontal focus condition, equation (6.25), becomes

$$c_\alpha^2/u - c_\alpha/\rho_a + c_\beta^2/v - c_\beta/\rho_a = 0 \quad (6.66)$$

and the vertical focus condition, equation (6.28), becomes

$$1/u - c_\alpha/\rho_b + 1/v - c_\beta/\rho_b = 0 \quad (6.67)$$

It is now possible to satisfy these conditions simultaneously, with

$$\rho_a/\rho_b = c_\alpha c_\beta = \cos \alpha \cos \beta \quad (6.68)$$

Thus, for each angle of incidence α , there are two stigmatic points on the Rowland circle given by the two angles of diffraction β and $-\beta$, as shown

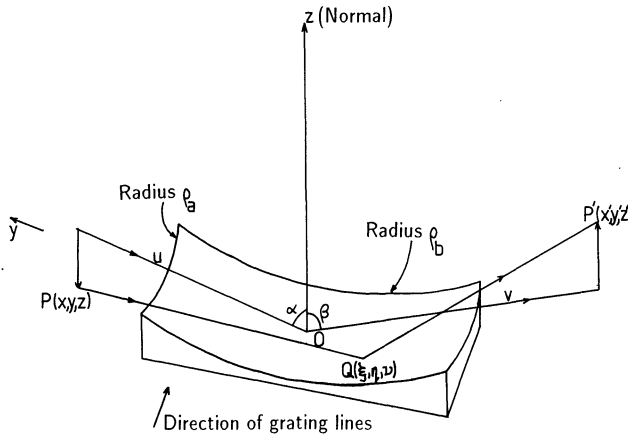


Figure 6.9. Image formation by a toroidal grating.

in Figure 6.10. Stigmatic images may be obtained at different wavelengths by varying α , and a quasi-stigmatic range of wavelengths may be defined over which the astigmatism is less than some defined limit. At the wavelength for which astigmatism is absent, higher-order aberrations are still present. An analysis of the path length function similar to that

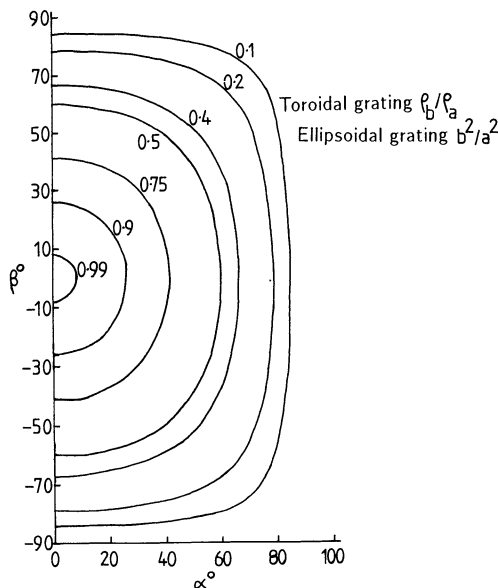


Figure 6.10. Stigmatic points of toroidal and ellipsoidal gratings.

presented for spherical grating gives the aberration terms⁽¹⁰⁾

Coma:

$$\begin{aligned}\Delta x &= [(t_\alpha/c_\alpha)(\rho_b - \rho_a c_\alpha^2) + (t_{\beta_0}/c_{\beta_0})(\rho_b - \rho_a c_{\beta_0}^2)]\eta^2/2\rho_a \rho_b \\ &\quad + [(t_\alpha^2/c_\alpha)(\rho_b - \rho_a c_\alpha^2) + (t_{\beta_0}^2/c_{\beta_0})(\rho_b - \rho_a c_{\beta_0}^2)]\eta^2\xi/2\rho_a^2 \rho_b\end{aligned}\quad (6.69)$$

$$\begin{aligned}\Delta y &= [(t_\alpha/c_\alpha)(\rho_b - \rho_a c_\alpha^2) + (t_{\beta_0}/c_{\beta_0})(\rho_b - \rho_a c_{\beta_0}^2)]\xi\eta/\rho_a \rho_b \\ &\quad + [(t_\alpha^2/c_\alpha)(\rho_b - \rho_a c_\alpha^2) + (t_{\beta_0}^2/c_{\beta_0})(\rho_b - \rho_a c_{\beta_0}^2)]\xi^2\eta/\rho_a^2 \rho_b\end{aligned}\quad (6.70)$$

Field curvature:

$$\Delta x = (\eta y'/\rho_a c_{\beta_0} \cos \phi)(t_\alpha - t_{\beta_0}) + (y'^2/2\rho_a c_{\beta_0}^2 \cos \phi)(s_\alpha + s_{\beta_0}) \quad (6.71)$$

$$\Delta y = (\xi y'/\rho_a c_{\beta_0} \cos \phi)(t_\alpha - t_{\beta_0}) \quad (6.72)$$

(where ϕ is the angle between QP' and the normal to the focal plane at P')

Toric aberration:

$$\begin{aligned}T &= (s_\alpha t_\alpha + s_{\beta_0} t_{\beta_0})(\xi^4/8\rho_a^3 + \xi^2\eta^2/4\rho_a^2 \rho_b) \\ &\quad + \eta^4(c_\alpha + c_{\beta_0})(\rho_b - \rho_a c_\alpha c_{\beta_0})/8\rho_a \rho_b^3 c_\alpha c_{\beta_0}\end{aligned}\quad (6.73)$$

The coma terms contribute significantly even at the stigmatic points. The toric aberration reduces to the spherical aberration of the spherical grating for $\eta = 0$. The term in η^4 becomes zero at the stigmatic points, but that in $\xi^2\eta^2$ can cause significant loss of resolution; for example, it contributes to the same degree as the spherical aberration term when $\eta^2 = \xi^2\rho_b/2\rho_a$. This means that the resolution attainable with a toroidal grating is lower than that possible with a spherical grating. To maintain high resolution, the aperture of a toroidal grating must be limited by stipulating

$$T \leq \lambda/4 \quad (6.74)$$

which leads to,⁽¹⁰⁾ similarly to the spherical grating,

$$W_{x\text{ opt}} = 2\{2\rho_a^3 \lambda t_{(\alpha+\beta_0)/2} c_\alpha c_{\beta_0} / [(s_\alpha + s_{\beta_0})(1 - c_\alpha c_{\beta_0})]\}^{1/4} \quad (6.75)$$

for the optimum width in the x direction, and

$$W_{y\text{ opt}} = 2\{2\rho_a^3\rho_b^3\lambda t_{(\alpha+\beta_0)/2}c_\alpha c_{\beta_0}/[(s_\alpha + s_{\beta_0})(\rho_b - \rho_a c_\alpha c_{\beta_0})]\}^{1/4} \quad (6.76)$$

for the optimum width in the y direction. Note that equation (6.75) gives the same result as equation (6.58) for the spherical grating.

6.4.2. Ellipsoidal Gratings⁽¹¹⁾

The conditions for imaging using an ellipsoidal grating may be established in a fashion analogous to that used for the spherical grating, using Figure 6.4. If a , b , and c are the semiaxes of the ellipsoid in the x , y , and z directions, respectively, then the focus conditions, equations (6.25) and (6.28), are replaced by

$$c_\alpha^2/u - c_\alpha c/a^2 + c_\beta^2/v - c_\beta c/a^2 = 0 \quad (6.77)$$

and

$$1/u - c_\alpha c/b^2 + 1/v - c_\beta c/b^2 = 0 \quad (6.78)$$

which have simultaneous solutions if

$$(b/a)^2 = c_\alpha c_\beta = \cos \alpha \cos \beta \quad (6.79)$$

These solutions are

$$u = c_\alpha a^2/c, \quad v = c_\beta a^2/c \quad (6.80)$$

which represent a circle of diameter a^2/c in the zx plane, which is similar to the Rowland circle of the spherical grating. For each value of α there are, as for the toroidal grating, two stigmatic points given by the angles β and $-\beta$, as shown in Figure 6.10. For angles other than these, the length of the astigmatic image is given by an analysis similar to that for spherical gratings,

$$(\Delta y')_{\text{ast}} = G(1 + c_{\beta_0}/c_\alpha) |1 - (a/b)^2 c_\alpha c_{\beta_0}| \quad (6.81)$$

where G is the illuminated length of the grating lines. Equation (6.81) is valid for gratings with widths smaller than the optimum defined below, and for imaging via the grating axis parallel to the lines ($\xi = 0$). Comparing this with equation (6.54), the astigmatism for an ellipsoidal grating is found to be less than that for a spherical grating if

$$(1 + c_{\beta_0}/c_\alpha) |1 - (a/b)^2 c_\alpha c_{\beta_0}| < s_\alpha^2 c_{\beta_0}/c_\alpha + s_{\beta_0}^2 \quad (6.82)$$

For $1 - (a/b)^2 c_\alpha c_{\beta_0} > 0$, equation (6.82) reduces to

$$(a/b)^2 > 1 \quad (6.83)$$

with no restriction on α and β_0 . For $1 - (a/b)^2 c_\alpha c_{\beta_0} < 0$, equation (6.82) gives

$$(a/b)^2 < 2/c_\alpha c_{\beta_0} - 1 \quad (6.84)$$

For a given grating (a/b fixed), this defines the range of values of α and β_0 for which the ellipsoidal grating gives less astigmatism than the spherical one does.

The optimum value of $(b/a)^2$ that minimizes astigmatism over a range of diffraction angles, $\beta_1 \leq \beta_0 \leq \beta_2$, for a given incidence angle is given by minimizing the function

$$g = \{(1 + c_{\beta_0}/c_\alpha)[1 - (a/b)^2 c_\alpha c_{\beta_0}]\}^2 \quad (6.85)$$

over the range of β_0 . This is done by solving

$$\frac{\partial}{\partial(a^2/b^2)} \int_{\beta_1}^{\beta_2} g d\beta_0 = 0 \quad (6.86)$$

resulting in, with $S_n = \sin(n\beta_2) - \sin(n\beta_1)$,

$$\begin{aligned} (b/a)_{\text{opt}}^2 &= \frac{(\beta_2 - \beta_1)(3 + 4c_\alpha^2) + 12S_1c_\alpha + 2S_2(1 + c_\alpha^2) + 4S_3c_\alpha/3 + S_4/4}{8(\beta_2 - \beta_1) + 2S_1(4c_\alpha + 3/c_\alpha) + 4S_2 + 2S_3/3c_\alpha} \end{aligned} \quad (6.87)$$

As for the spherical and toroidal gratings the optimum width of an ellipsoidal grating is obtained by specifying that the spherical aberration should not exceed $\lambda/4$,

$$(\xi^4 c^3 / 8a^6)[1/c_\alpha + 1/c_{\beta_0} - a^2(c_\alpha + c_{\beta_0})/c^2] = \lambda/4 \quad (6.88)$$

so that

$$W_{\text{opt}} = 2|\xi| = 2\{2a^6 \lambda c_\alpha c_{\beta_0} / [c^3(c_\alpha + c_{\beta_0}) |1 - a^2 c_\alpha c_{\beta_0} / c^2|]\}^{1/4} \quad (6.89)$$

If, in equation (6.89), c and a are equal, then the equation is the same as for a spherical grating of radius a , leaving the value of b to be chosen, via equation (6.87), to reduce astigmatism. Thus the ratio W_{es} of the

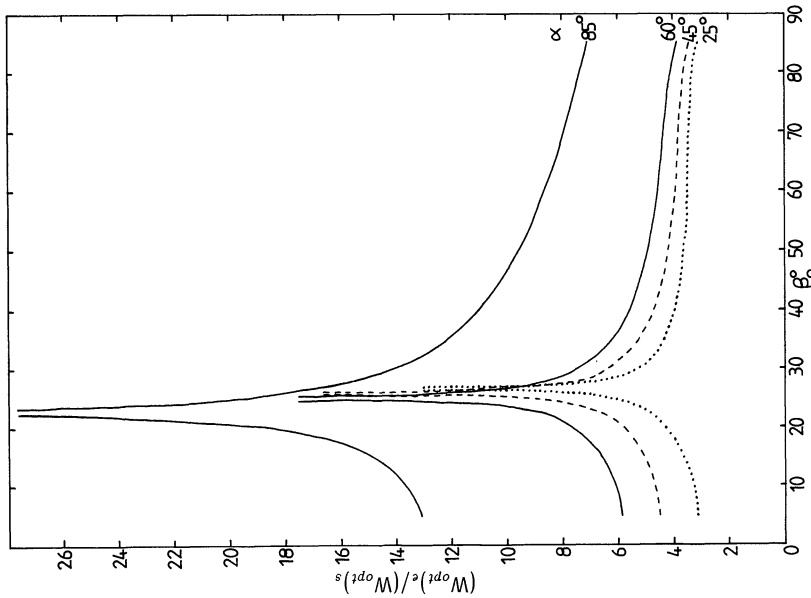


Figure 6.12. A comparison of the optimum widths of ellipsoidal and spherical gratings.

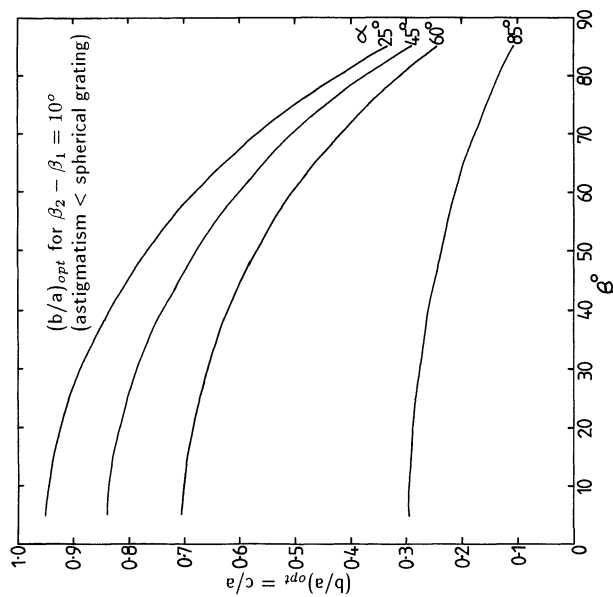


Figure 6.11. The optimum semiaxis ratio for ellipsoidal gratings.

optimum widths of ellipsoidal and spherical gratings is

$$W_{es} = [(a/c)^3(1 - c_\alpha c_{\beta_0})/(1 - a^2 c_\alpha c_{\beta_0}/c^2)] \quad (6.90)$$

If the grating is made so that $b = c < a$, then equation (6.87) may be used to obtain $(b/a)_{\text{opt}}^2 = (c/a)^2$ for a given range of β_0 , and then substituted into equation (6.90). In this way it can be shown that the astigmatism is reduced and the optimum width increased from the spherical grating values. This is demonstrated in Figures 6.11 and 6.12 for $\beta_2 - \beta_1 = 10^\circ$.

The Design and Manufacture of X-Ray Diffraction Gratings

7.1. Manufacturing Tolerances and Types of Grating

7.1.1. Reflection Gratings

For long-wavelength radiation such as visible light, gratings (used at near-normal incidence) typically have groove spacings d of between one and ten times the wavelength, i.e., a few hundred to one or two thousand lines per millimeter. These spacings are chosen to give large amounts of dispersion, which increases with λ/d . For X-ray gratings the criteria are modified by the necessity of using grazing incidence, which causes an apparent foreshortening of the grating features (and errors) by a factor of around the sine of the incidence angle. Thus, instead of 50,000 lines mm^{-1} (from five times a wavelength of 4 nm) or perhaps more, it is still possible to use gratings with a few hundred to a few thousand lines per millimeter. Large dispersion is not possible for X rays since if it is too high some of the diffracted radiation may fall outside the critical angle θ_c (Section 2.1)

$$\cos \theta_c = 1 - \delta \quad (7.1)$$

with, well away from absorption edges (Section 1.2),

$$\delta = Ne^2\lambda^2/8\pi^2\varepsilon_0m_ec^2 \quad (7.2)$$

where N is the number density of electrons. Rearranging these equations gives the minimum wavelength λ_{\min} reflected at a given grazing incidence angle θ_i

$$\lambda_{\min} = (4\pi^2\varepsilon_0m_ec^2/Ne^2)^{1/2} \sin \theta_i = A \sin \theta_i \quad (7.3)$$

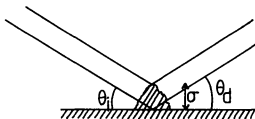


Figure 7.1. Introduction of a path difference into a diffracted beam by a surface deviation.

(it should be noted, however, that an effect of absorption is to allow wavelengths shorter than λ_{\min} to be reflected). As shown in Figure 7.1, a deviation of height σ from the local surface mean plane introduces a path difference of $\sigma(\sin \theta_i + \sin \theta_d)$ into a diffracted beam, where θ_d is the grazing angle of diffraction. According to the Rayleigh criterion, this path difference can be neglected if it is less than a quarter of a wavelength, i.e.,

$$\sigma(\sin \theta_i + \sin \theta_d) < \lambda/4 \quad (7.4)$$

or, at the minimum reflected wavelength and with $\theta_d \approx \theta_i$,

$$\sigma_{\max} \approx A/8 \quad (7.5)$$

The maximum allowable deviations for several materials suitable for the manufacture of X-ray gratings are given in Table 7.1. According to the analysis presented in Section 2.1.2, these deviations (roughness) will lead to reductions in the reflectivities,

$$R_r = R_s \exp \{ -[(4\pi\sigma/\lambda) \sin \theta_i]^2 \} \quad (7.6)$$

where R_s is the reflectivity of a completely smooth surface, with corresponding reductions in the grating efficiencies. In the soft X-ray range, for $\sigma = \sigma_{\max}$ the efficiencies are reduced to about 10% of their ideal values, and therefore it is desirable to keep the surface deviations

Table 7.1. Maximum Allowable Surface Roughnesses of Grating Materials

Material	Electron density $N (\text{m}^{-3})$	Maximum surface deformation (nm) (at $\theta_i = \theta_c$)	Percentage of ideal efficiency	
			$\lambda = 1 \text{ nm}$	$\lambda = 10 \text{ nm}$
Glass	7.8×10^{29}	4.7	8.5	8.9
Aluminum	7.83×10^{29}	4.7	8.5	8.9
Chromium	1.97×10^{30}	3.0	8.5	9.5
Silver	2.76×10^{30}	2.5	8.5	9.9
Gold	4.67×10^{30}	1.9	8.5	11.0
Platinum	5.18×10^{30}	1.8	8.5	11.3

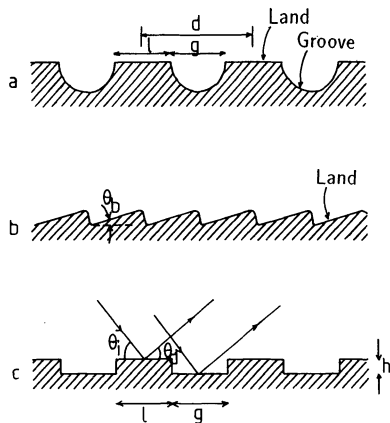


Figure 7.2. Types of X-ray diffraction grating: (a) amplitude; (b) blazed; (c) laminar.

much smaller than σ_{\max} . As shown in Table 3.1, it is possible to polish blanks to smoothnesses within these tolerances. However, the formation of the grating grooves can cause deviations in excess of σ_{\max} , and in this case it is necessary to choose groove profiles that can be made smooth rather than that give inherently high diffraction efficiencies.

X-ray gratings can be made by ruling, lithography, or interference techniques. The discussion above relates mainly to gratings or masters for replica made by ruling, and the profiles of interest are those shown in idealized forms in Figure 7.2. In the first of these, an amplitude grating, only the lands between the grooves contribute to the diffracted radiation, and the theoretical maximum *m*th-order absolute efficiency (i.e., the ratio of diffracted to incident intensity) is⁽¹⁾

$$\epsilon_0 = 25\%, \quad \epsilon_m = 100/(m\pi)^2 \% \quad m = \pm 1, \pm 3, \pm 5, \dots \quad (7.7)$$

when the land to groove ratio is unity and assuming that the grating material has a reflectivity of 100%. Half of the incident intensity is lost to the grooves. In practice, it is difficult to achieve these efficiencies because ruling processes displace rather than remove material, causing buildup along the groove edges. As well as scattering the incident radiation, this causes shadowing of the lands as shown in Figure 7.3, resulting in efficiencies at best two orders of magnitude lower than those given by equation (7.7). Since ruling in glass causes local collapse of the structure while in metals the material is just pushed to one side, glasses are normally preferred for ruled gratings since the displaced material occupies less volume.

In principle, blazed gratings (Figure 7.2b) can be used to diffract all

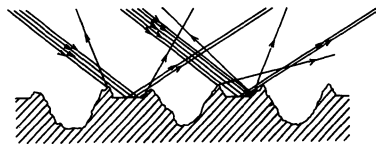


Figure 7.3. The rough profile of a ruled amplitude grating.

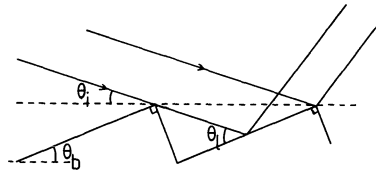


Figure 7.4. The parameters of a blazed grating, showing shadowing.

of the incident intensity into a given order. The optimum blaze angle θ_b is determined by the condition that the direction of the diffracted beam coincides with that of the beam specularly reflected from the land, with the restriction that the angle of incidence θ_1 on the land must be less than the critical angle.⁽²⁾ In addition, as shown in Figure 7.4, each groove shadows the next one so that the fraction of each land that is illuminated is

$$f = 1 - \tan \theta_b / \tan \theta_1 \quad (7.8)$$

This shows that the blaze angle must be less than the incidence angle, i.e., than the critical angle, and should be as small as feasible in order to illuminate as much of the land as possible. As the grating pitch becomes finer, less of the land is illuminated for a given incidence angle. Thus, in order to illuminate more of the land, the incidence angle θ_1 must be increased. However, if the pitch becomes too fine, θ_1 will exceed θ_c and the grating will become ineffective. Thus there is an upper limit to the pitch for a given wavelength. As less of the land becomes illuminated, the efficiency also becomes more sensitive to defects, which, because of the ruling process, are more significant at the tips of the grooves.

The third type of ruled X-ray grating is the laminar, or phase, grating (Figure 7.2c). In these, both the lands and the grooves contribute to the diffracted intensities and, by appropriate choice of the groove depth h and the incidence angle, the two contributions can be caused to destructively interfere in the zero order so that more energy is available for the other orders. The absolute efficiencies are, for the case in which the whole of the grating is illuminated and the land to groove ratio is

unity,^(3,4)

$$\epsilon_0 = 100 \cos^2 [\pi h(\sin \theta_i + \sin \theta_d)/\lambda] \% \quad (7.9)$$

and

$$\epsilon_m = 400 \sin^2 [\pi h(\sin \theta_i + \sin \theta_d)/\lambda]/(m\pi)^2 \% , \quad m = \pm 1, \pm 3, \pm 5 \dots \quad (7.10)$$

These efficiencies are plotted as functions of wavelength in Figure 7.5 for a groove depth of $0.02d$, a grazing incidence angle of 2° , and for $m = 0, +1$, and $+3$. The maximum efficiencies in any order are four times higher than those of the equivalent amplitude grating, and high efficiency over a large wavelength range can be obtained if the grating is used in the region of the primary maximum indicated in the figure. The position of the primary maximum as function of incidence angle, pitch, and groove depth is given by $\partial \epsilon_m / \partial (d/\lambda) = 0$, leading to⁽⁴⁾

$$\lambda/d = [2m \cos \theta_i + (\sin \theta_i)/p](1/4p^2 + m^2) \quad (7.11)$$

where $p = h/nd$ and n , an integer, is equal to unity for the primary maximum. The variations of λ/d at the primary maximum with θ_i and h/d are shown in Figure 7.6. Equation (7.11) may be used to design a grating for a particular wavelength.

For real gratings used at grazing incidence, the analysis described above must be modified in several ways. The first of these is the polarization of the diffracted radiation. However, as shown in Section 2.1, at small grazing incidence angles the two polarization directions

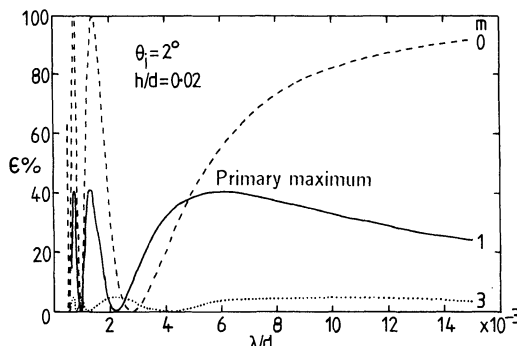


Figure 7.5. Diffraction efficiencies of an unshadowed laminar grating in the 0, +1, and +3 orders.

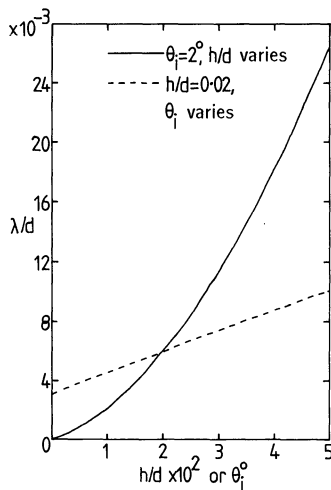


Figure 7.6. The positions of the primary maximum (value of λ/d) as functions of grazing incidence angle and land thickness for laminar gratings.

behave almost identically, so that in practice the diffracted radiation can be considered to be unpolarized. Two other effects—namely shadowing of the grooves by the lands, and the decrease of reflection coefficient with increasing grazing incidence angle—are, however, significant.

The effect of shadowing is shown in Figure 7.7—only a fraction g'/g of each groove contributes fully to the diffracted beam. In principle, radiation incident on a land can penetrate to the groove but, at soft X-ray wavelengths, absorption coefficients are sufficiently high that insignificant amounts of radiation penetrate the lands. Thus only the directly illuminated parts of the grooves contribute and the absolute efficiencies in the odd orders are given by⁽⁴⁾

$$\begin{aligned} \varepsilon_m = 100\{1 + \cos^2 \eta - 2 \cos \eta \cos [m\pi h(\cot \theta_i - \cot \theta_d)/d \\ + 2\pi h(\sin \theta_i + \sin \theta_d)/\lambda]\}/(m\pi)^2 \% \quad (7.12) \end{aligned}$$

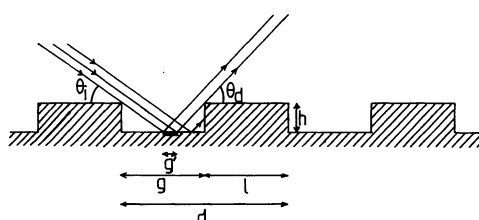


Figure 7.7. The effect of shadowing of a laminar grating.

where

$$\eta = m\pi h(\cot \theta_i + \cot \theta_d)/d \quad (7.13)$$

This gives the curve shown in Figure 7.8 for $m = 1$, $\theta_i = 2^\circ$, and $h/d = 0.01$. The primary maximum is shifted to longer wavelength but the most significant effect is the decrease in the maximum efficiency. In the limit that the grooves are completely shadowed, the efficiency drops to that of an amplitude grating. Higher peak efficiencies can be obtained than given by equation (7.12) by changing the land to groove ratio so that equal amplitudes are reflected from the lands and the grooves. This requires (Figure 7.7)

$$l = g' = g - h(\cot \theta_i + \cot \theta_d) \quad (7.14)$$

so that the pitch is effectively reduced by an amount $h(\cot \theta_i + \cot \theta_d)$, and the primary maximum is higher and narrower (Figure 7.8). Also shown in Figure 7.8 is the curve for a gold grating at a wavelength of about 4 nm, taking account of the reflectivity as described in Section 2.1.

A common error, particularly in ruled gratings, is periodic variations in the shapes or positions of the grooves.⁽¹⁾ These produce impurities in the grating spectra known as ghosts, of which two types are normally distinguished although there is no optical difference between them. Long-term errors in the grating periodicity lead to Rowland ghosts, which lie close to the corresponding diffracted order, while short-term errors (i.e., over a few grooves) give rise to Lyman ghosts, which are farther away. These ghosts arise from the periodic nature of the variations, which form a gratinglike structure superimposed on the main grating.

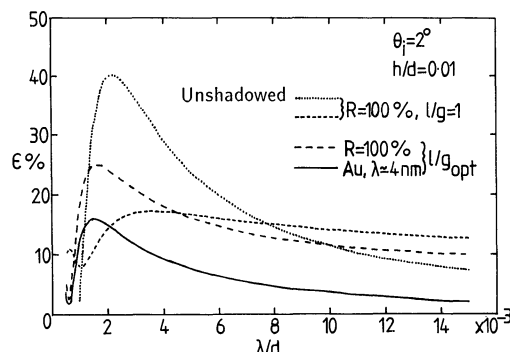


Figure 7.8. First-order diffraction efficiencies of shadowed laminar gratings.

Because Lyman ghosts are farther away from the main spectrum, they are more difficult to distinguish but less troublesome than Rowland ghosts. The intensity of Rowland ghosts relative to the corresponding main diffracted order is⁽⁵⁾

$$I_{\text{ghost}}/I_m \simeq (m\pi\delta x/d)^2 \quad (7.15)$$

where δx is the displacement of a groove. A general rule of thumb is that this ratio should be less than about 5% in the first order,⁽⁶⁾ so that δx must be less than about 7% of the grating period.

Nonperiodic errors in the grating structure give rise to satellites (for long-term errors), which are similar to Rowland ghosts but are not necessarily symmetrically placed about the main diffraction order, or to low-level continua known as grass for short-term errors perpendicular to the grooves. Random errors with no preferred direction, such as surface roughness, dust, or scratches, lead to diffuse scattering.

Gratings with profiles other than those discussed so far can be made by interference techniques.⁽⁷⁾ In particular, profiles consisting of sine waves or combinations of sine waves are produced in this way. Closed expressions for the efficiencies of sinusoidal gratings are not readily obtained and it is usual to use numerical approximations.⁽⁸⁾ The values obtained are similar to those for laminar gratings. For example, a gold sinusoidal grating used at a wavelength of 4.4 nm, and with $h/d = 0.012$, $\lambda/d = 2.64 \times 10^3$, and $\theta_i = 2.9^\circ$, has a calculated efficiency of about 13%.⁽⁶⁾

7.1.2. Transmission Gratings

Because transmission gratings have to be used at near-normal angles of incidence, they must have much finer pitches than do reflection gratings for the same amount of dispersion. Two types of transmission grating are shown in Figure 7.9, equivalent to laminar and blazed reflection gratings. For the rectangular profile grating, Figure 7.9a, the aperture size g_{opt} and thickness h_{opt} leading to maximum absolute efficiency in the m th order are given by⁽¹⁹⁾

$$g_{\text{opt}} = d/2m \quad (7.16)$$

and

$$h_{\text{opt}}/\lambda = \{\cos^{-1} \omega + \cos^{-1} [\omega \exp(-2\pi h_{\text{opt}}\beta/\lambda)]\}/2\pi\delta \quad (7.17)$$

where δ and β are the optical constants (Section 1.2) and $\omega^2 =$

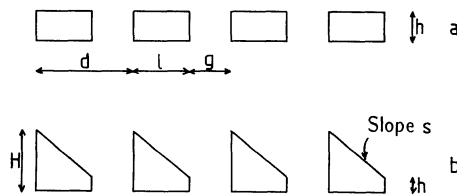


Figure 7.9. Types of X-ray transmission gratings: (a) rectangular profile; (b) optimized profile.

$\beta^2/(\beta^2 + \delta^2)$. The efficiency is then

$$\epsilon_m = 100[1 + (\delta/\beta)^2][\sin^2(2\pi h_{\text{opt}}d/\lambda)]/(m\pi)^2 \% \quad (7.18)$$

The variation of h_{opt} and ϵ_1 with wavelength for a rectangular transmission grating made of gold are shown in Figure 7.10.

For linearly blazed transmission gratings, Figure 7.9b, the optimum blaze slope is⁽⁹⁾

$$s_{\text{opt}} = -m\lambda/2d\delta \quad (7.19)$$

and the optimum aperture size is given by

$$G = g_{\text{opt}}/d = [|\cos^{-1} \gamma(\beta^2 + \delta^2)^{1/2}/\delta| - \cos^{-1} \omega + 2\pi h' \delta]/m\pi \quad (7.20)$$

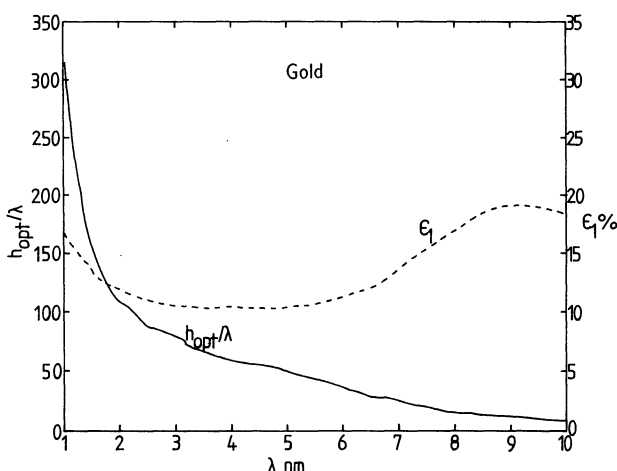


Figure 7.10. Optimum thicknesses and first-order diffraction efficiencies of rectangular profile transmission gratings in the soft X-ray region.

where $h = h'\lambda$ is the minimum thickness of the sawtooth and

$$\gamma = -\{\sinh [m\pi\beta(1 - G)/\delta]\} \operatorname{cosec}(m\pi G) \\ \times \exp \{-2\pi\beta[h' + m(1 - G)/2\delta]\} \quad (7.21)$$

The optimum maximum thickness is then

$$H_{\text{opt}}/\lambda = m(1 - G)/2\delta + h' \quad (7.22)$$

and the absolute efficiency is

$$\varepsilon_m = 100 G^2 [1 + (\delta/\beta)^2] [\operatorname{sinc}^2(m\pi G)] \sin^2(2\pi h'\delta - m\pi G) \% \quad (7.23)$$

Figures 7.11, 7.12, and 7.13 show, respectively, G , H_{opt}/λ , and ε_1 as

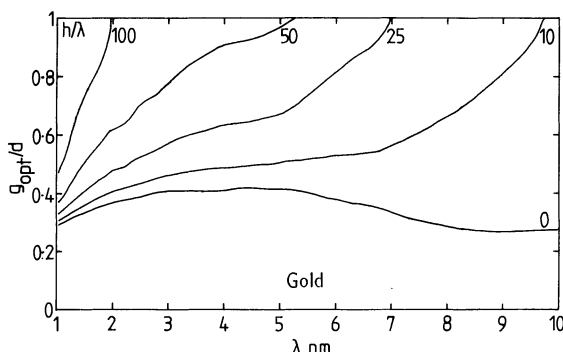


Figure 7.11. Aperture sizes of optimized profile transmission gratings.

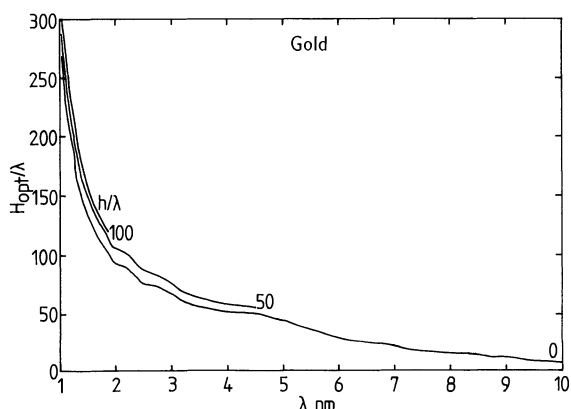


Figure 7.12. Maximum thicknesses of optimized profile transmission gratings.

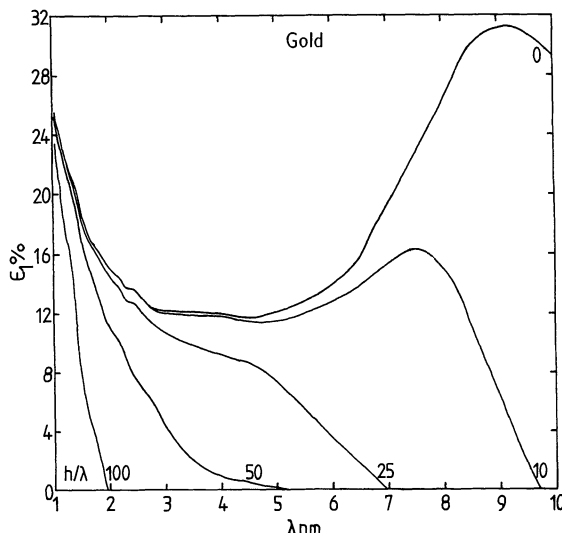


Figure 7.13. First-order diffraction efficiencies of optimized profile transmission gratings.

functions of wavelength for a gold grating and various values of h' . These show that if the minimum thickness is too large, equation (7.20) has no physical (i.e., $G < 1$) solutions and, to maintain high efficiency over the whole soft X-ray range, h' should be as small as possible.

7.2. Manufacturing Techniques

7.2.1. Reflection Gratings

7.2.1.1. Ruling

Because of the production of burrs in the ruling process, it is normally used in conjunction with other techniques, although directly ruled gratings have been used. In practice, the mechanical tolerances on ruling engines for X-ray gratings are less severe than those on engines for optical gratings⁽⁶⁾ because, as well as the foreshortening effect, high diffraction orders (where ruling errors are more noticeable) are not usually used for X rays. In addition, ruling times are generally shorter for X-ray gratings, because they are smaller (and lighter) than optical gratings, so that stability is less of a problem and errors caused by deformations of the engine are smaller.

Because of the optimum grafting width defined in Chapter 6, it is only necessary to rule lines over widths of a few centimeters. Even so, accuracy of groove position is required over a considerable total length.

For example, a 20×20 mm grating with 600 lines mm^{-1} has a total groove length of 240 m and the placement accuracy has to be better than about 120 nm. In typical ruling engines,⁽⁶⁾ both the tool carriage and the grating holder are made to move by a motor, flywheel, and gearbox, the carriage being controlled by a continuously moving lead-screw and the holder by a drive wheel giving a continuous reciprocating motion. This dual movement eliminates transient effects, which arise if the tool is kept stationary. The grating pitch is determined by the product of the gearbox ratio and the lead-screw pitch, and periodic grating errors arise from imperfections in these. Periodicity in the cumulative pitch error of the lead-screw can be eliminated using a Merton nut.^(10,11) This has no precut thread but is lined with strips of a resilient material, originally cork but now plastics such as PTFE being used. The tool attached to this nut moves continuously under the averaged influence of all the grooves of the lead-screw in contact with the strips, removing the effect of periodic errors for a sufficiently long nut. The Merton nut also minimizes the effect of nonstraightness in the unwrapped lead-screw thread—this can be further reduced by lapping the screw. Errors caused by the gearbox and bearings can be kept below the required limits by using components machined and aligned to within a few micrometers.⁽⁶⁾ Finally, errors caused by external influences must be minimized by housing the ruling engine in a clean, temperature-stabilized environment.

Measurements of the optical quality of directly ruled gratings indicate that the tolerances on ruling errors can be met. For example, a 295 line mm^{-1} grating was found to have a relative Rowland ghost intensity of 0.25% ⁽⁶⁾ and the grating was usable at soft X-ray⁽¹²⁾ and other^(12,13) wavelengths. By suitable choice of the ruling tool shape, either amplitude or blazed gratings can be made in this way. For high diffraction efficiencies, however, more complicated procedures are necessary.

7.2.1.2. Etching

Laminar gratings are made by generating masks to protect a smooth blank while grooves are being etched, the unetched portions forming the lands. The stages of an early process⁽⁴⁾ are shown schematically in Figure 7.14. The blank was made of a synthetic amorphous silica (Spectrosil) that, as discussed in Chapter 3, is very suitable for producing smooth surfaces. To prevent surface imperfections the whole process was carried out under clean room conditions, and all cleaning was done using stirred liquids rather than mechanical methods. To ensure smooth final grooves, the aluminum layer was very pure and evaporated slowly at near-normal incidence under low pressure. To minimize stresses in the substrate the rulings did not penetrate the aluminum, the substrate being exposed by

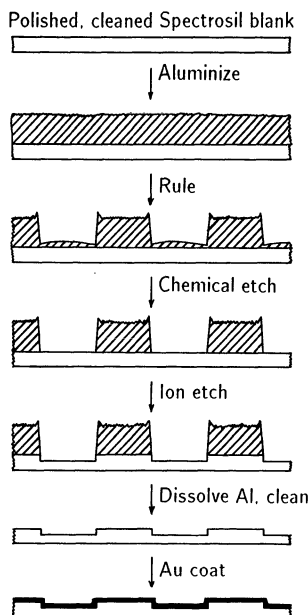


Figure 7.14. Manufacture of laminar diffraction gratings using ruled masks. (After Franks *et al.*⁽⁴⁾)

chemical etching. The remaining aluminum strips then formed the mask and the grooves were etched by argon ion bombardment. The aluminum strips were then removed by chemical dissolution, and, after cleaning, a gold layer was very slowly evaporated. A similar process has been used to manufacture transmission gratings.⁽¹⁴⁾

Indirect methods of assessing grating quality, such as electron microscopy⁽¹⁵⁾ and profilometry,⁽¹⁶⁾ indicate that good-quality gratings with $300\text{--}1200 \text{ lines mm}^{-1}$ can be made by this method. Spectroscopic evaluation of the gratings⁽⁴⁾ shows that peak first-order efficiencies of around 10% at the carbon K_{α} edge are possible.

The technique discussed above for generating the mask has now been superseded by interference methods,^(1,17) in which photoresist spun onto a (possibly metal-coated) substrate is exposed to interfering laser beams. These techniques have the advantage that they are faster, they can produce finer pitches, and gratings can be made on steeply curved substrates that could not be ruled. A typical process⁽¹⁷⁾ is shown in Figure 7.15. Peak first-order diffraction efficiencies of around 10% have also been observed for such gratings.

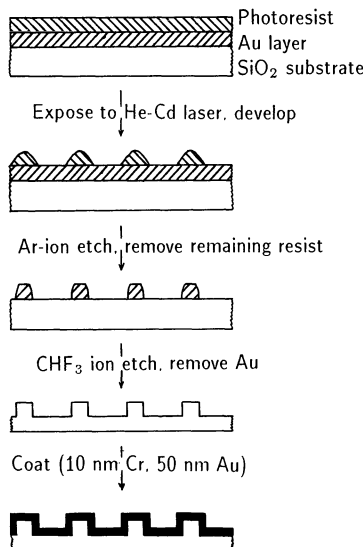


Figure 7.15. Manufacture of laminar diffraction gratings using masks made by interference methods. (After Aritome *et al.*⁽¹⁷⁾)

7.2.2. Transmission Gratings

7.2.2.1. Lithography

Many of the techniques to be discussed in Chapter 9 for the manufacture of zone plates can be adapted for making transmission gratings. For example, contamination lithography in a scanning transmission electron microscope has been used to make a gold transmission grating, on a carbon substrate, with $8000 \text{ lines mm}^{-1}$. This was small, about $11 \times 30 \mu\text{m}$, and made of a series of $5 \times 5 \mu\text{m}$ fields patched together and registered with respect to one another using the first grating line in each field. The original contamination pattern was gold coated at an angle to prevent the gaps being filled. An electron micrograph of part of the grating structure is shown in Figure 7.16. It was successfully used to analyze the spectrum from a rotating anode X-ray generator with a carbon-painted anode. Lines due to carbon K_α , oxygen K_α (probably from the carbon paint stabilizer), and silicon K_α (from vacuum grease) were observed.

Conventional electron-beam lithography has also been used to manufacture transmission gratings.⁽¹⁷⁾ This is summarized in Figure 7.17. Measurements of the diffraction intensities of such gratings show almost complete suppression of the even orders, demonstrating that the required

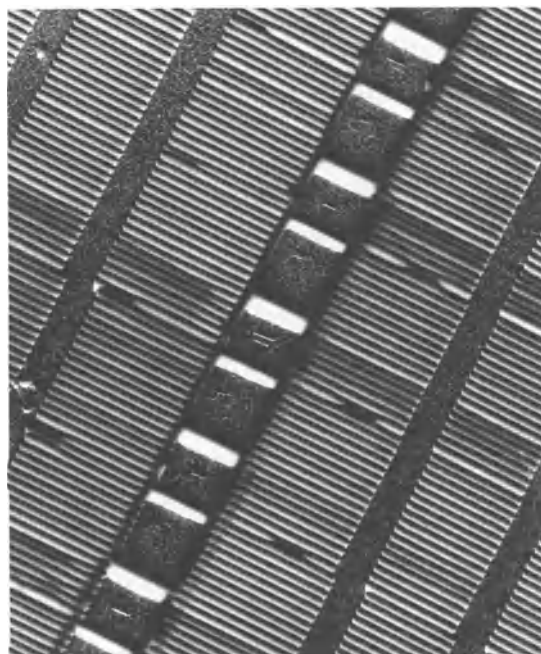


Figure 7.16. A transmission grating made by contamination lithography.

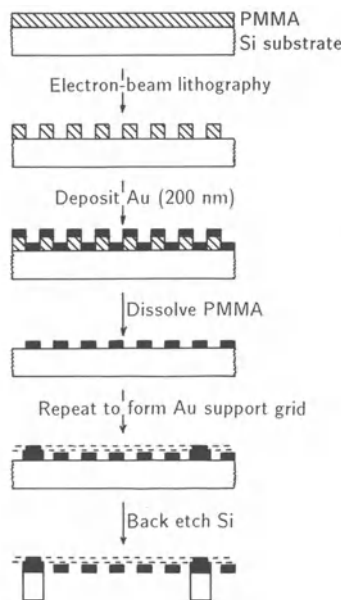


Figure 7.17. Manufacture of rectangular profile diffraction gratings by electron-beam lithography. (After Aritome *et al.*⁽¹⁷⁾)

relative slit opening of 0.5 was achieved, with good rectangular profiles of the grating bars.

7.2.2.2. Interference Methods

For many applications, large area transmission gratings are required. These cannot be written by lithographic systems in reasonable times and thus interference (holographic) methods, which can generate gratings with areas of around 100 mm^2 , are used.⁽¹⁹⁻²¹⁾ The exposure arrangement, of which several variations exist,⁽¹⁾ is shown schematically in Figure 7.18. In the arrangement shown, distortions of the wavefronts are avoided by eliminating the optional collimating lenses, so that the recording medium must be sufficiently far from the pinholes that the wavefronts are approximately planar in order to give constant groove spacing. Clearly the two light paths must be such that the two beams remain coherent. If they intersect at an angle 2θ , then interference fringes will be generated that may be recorded on a photoresist-coated substrate. If this is normal to the bisector of the two beams, then the fringe spacing and therefore the grating pitch is

$$d = \lambda/2n \sin \theta \quad (7.24)$$

where λ is the laser wavelength and n is the refractive index of the medium in which the interference takes place. In most cases it is convenient to record in air so that $n = 1$, and fine pitches are obtained

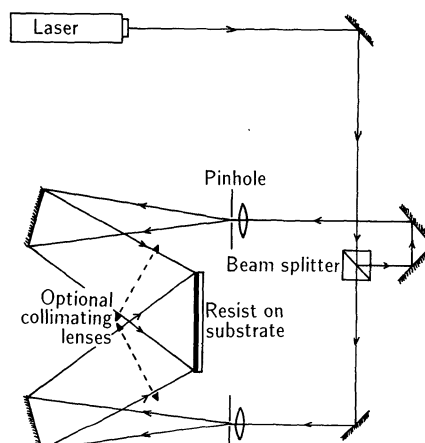


Figure 7.18. Schematic of an interference arrangement for the exposure of a grating pattern in photoresist.

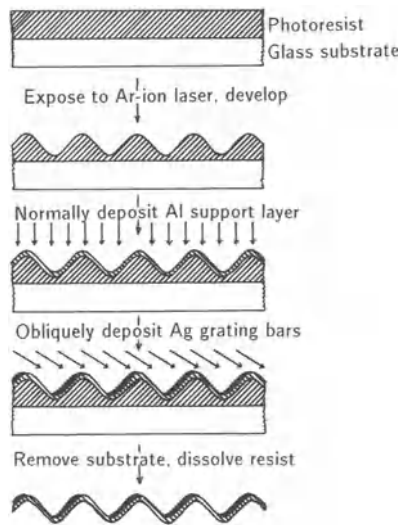


Figure 7.19. Coating of an interference pattern to give a transmission grating. (After Arakawa and Caldwell.⁽¹⁹⁾)

by using short wavelengths and large intersection angles. Because the photoresist response may not be linear, the recorded pattern may not be sinusoidal, but this does not cause any problems.

After the photoresist has been exposed, it is developed and may then be coated for direct use^(19,20) or used as a mask for, e.g., X-ray lithography.⁽²¹⁾ One coating method is illustrated in Figure 7.19.⁽¹⁹⁾ In this case, an argon ion laser ($\lambda = 457.9 \text{ nm}$) was used, and the beam intersection angle was 58° , resulting in gratings with about $2100 \text{ lines mm}^{-1}$, with silver bars $10\text{--}70 \text{ nm}$ thick on approximately 100-nm -thick aluminum layers, over areas of 64 mm^2 . The main problem with this method was due to the removal process, which caused slight (about 1%) distortions of the gratings. However, diffracted intensities of several percent were obtained.

Techniques involving X-ray lithography have been used to manufacture free-standing transmission gratings with $1000\text{--}3000 \text{ lines mm}^{-1}$.⁽²¹⁾ In these, a pattern is first produced on a thin polyimide membrane by interference methods, and this is then copied in the X-ray lithographic step. This allows the bar to space ratio to be adjusted, by over- or underdeveloping the X-ray resist [polymethylmethacrylate (PMMA)], the bar shape to be changed, and the thickness of the final grating to be controlled. In addition, once one good mask has been exposed, many replicas can be made.

Diffractive Optics II
Zone Plates**8.1. Fresnel and Soret Amplitude Zone Plates**

Zone plates may be considered to be circular diffraction gratings with radially increasing line densities. Their focusing properties have long been well known,⁽¹⁾ and they offer perhaps the best chance in the foreseeable future of diffraction-limited imaging using soft X rays, where they are used in transmission. Figure 8.1 shows the requirement for focusing, namely that radiation emitted from an object point P is focused to an image point P' . The complex disturbance at P' due to a spherical wavefront emitted by P is

$$Y(P') = A \exp [ik(R + R')]/(R + R') \quad (8.1)$$

where A is the amplitude at unit radius from P , R is the perpendicular distance from P to the focusing device, R' is the perpendicular distance from the focusing device to P' , and k is the wavenumber ($= 2\pi/\lambda$). In equation (8.1) the periodic time factor has been omitted since soft X-ray detectors only respond to time-averaged signals, and an inclination factor expressing the amplitude variation with distance has been ignored since (due to the small sizes of the optical components) only small angle diffraction need be considered. Using the Huygens–Fresnel wave propagation principle, each point on the wavefront emitted by P is considered to be a point source of spherical wavelets; all such points are in phase. The total effect at P' is found by summing the effects from all points on the wavefront with relative phases at P' determined solely by the optical distances from the wavefront to P' . If two signals on the wavefront have an optical path difference to P' of an integral number of wavelengths,

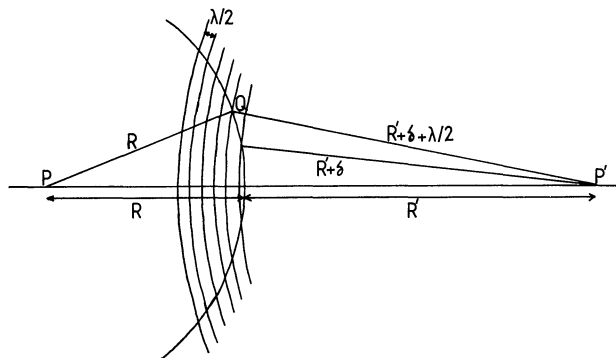


Figure 8.1. A propagating spherical wave, from the object point P , at radius R . The boundaries of the Fresnel half-period zones are defined by spheres of radius R' centered on the image point P' .

they will contribute in phase (i.e., interfere constructively), while if the optical path difference is an odd-integral number of half-wavelengths, they will contribute completely out of phase (i.e., interfere destructively). The wavefront may be imagined as being divided into a set of Fresnel (or half-period) zones by spheres differing in radius by $\lambda/2$ and centered on P' . Adjacent zones will then transmit radiation with opposite signs of phase—the resultant disturbance from these zones gives the propagating spherical wave in free space. If alternate zones are blocked, then the disturbances at P' will have the same sign of phase and the summation shows an increase proportional to the number of zones. Note that it is not necessary for the distance $R + R'$ between P and P' to be an integral number of half-wavelengths; in Figure 8.1, δ is introduced to take account of this, i.e., δ corresponds to an overall arbitrary phase.

A zone plate focusing element may be constructed following this analysis by projection onto a plane surface perpendicular to the optical axis joining P and P' . The resulting zones on this plane surface are of roughly equal area (except for the central zone if δ is not equal to zero or $\lambda/2$). This construction may be envisaged as the hologram formed by two point sources, at P and P' . Alternate areas are obstructed to give the Fresnel zone plate pattern, an example of which is given in Figure 1.22—a positive zone plate has an open center, while for a negative zone plate the center is closed. The convention to be used here is that each open or closed area is considered to be a complete zone—this has become the standard definition although some authors consider that each pair of open and closed areas forms a zone.

8.1.1. Basic Formulas

The radii of the zone boundaries are given by using the optical path difference of $\lambda/2$ for geometrical rays passing through adjacent boundaries. Using the notation of Figure 8.2, the optical path difference between an axial ray and one passing through the central (zeroth) zone boundary is

$$\delta = (s_0 + t_0) - (z + z') \quad (8.2)$$

while for the n th zone boundary

$$(\delta + n\lambda/2) = (s_n + t_n) - (z + z') \quad (8.3)$$

Rearranging and substituting for s_n in terms of r_n and z , and t_n in terms of r_n and z' gives

$$z + z' + n\lambda/2 = (r_n^2 + z^2)^{1/2} + (r_n^2 + z'^2)^{1/2} \quad (8.4)$$

where

$$n = Z + 2\delta/\lambda \quad (8.5)$$

Squaring equation (8.4) twice and rearranging gives, with $Z = z + z'$,

$$r_n^2 = [n\lambda Z z' Z + (n\lambda)^2 (Z^2 + zz')/4 + (n\lambda)^3 Z/8 + (n\lambda)^4/64]/(Z + n\lambda/2)^2 \quad (8.6)$$

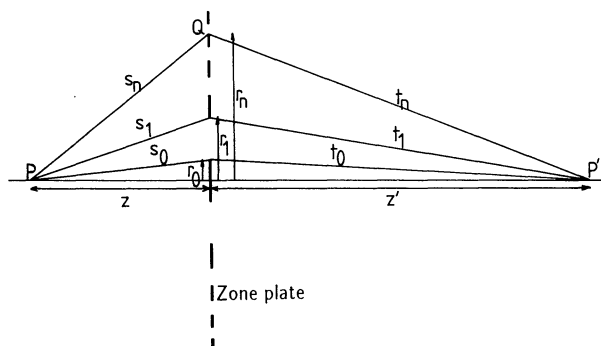


Figure 8.2. Definition of the zone boundary radii of a Fresnel zone plate.

This is an exact expression for the radius r_n of the n th zone. In the applications of zone plate imaging that are to be considered, $v\lambda \ll Z$ and equation (8.6) reduces to

$$r_n^2 = v\lambda zz'/Z + (v\lambda)^2(z^3 + z'^3)/4Z^3 + \dots \quad (8.7)$$

Considering the zone plate to be a thin lens of focal length f with conjugates at P and P' , then

$$1/f = 1/z + 1/z' \quad (8.8)$$

and the magnification is

$$M = z'/z \quad (8.9)$$

In terms of f and M , equation (8.7) becomes

$$r_n^2 = v\lambda f + (v\lambda)^2(M^3 + 1)/4(M + 1)^3 + \dots \quad (8.10)$$

The second term in equation (8.10) only becomes significant for zone plates with very large numbers of zones,

$$n \sim 4f/\lambda \quad (8.11)$$

i.e., high apertures, and can usually be ignored. Thus, to a good approximation,

$$r_n^2 = v\lambda f = n\lambda f + 2\delta f \quad (8.12)$$

The radius of the central zone is given by

$$r_0^2 = 2\delta f \quad (8.13)$$

so that

$$r_n^2 = r_0^2 + n\lambda f \quad (8.14)$$

or

$$r_n^2 = nr_1^2 - (n - 1)r_0^2 \quad (8.15)$$

When $\delta = 0$, then $r_0 = 0$ and the zone boundary radii are given by

$$r_n^2 = n\lambda f = nr_1^2 \quad (8.16)$$

which is the equation describing a Soret zone plate, a particular case of a Fresnel zone plate. The same equation holds when $\delta = \lambda/2$, since r_0^2 for $\delta = \lambda/2$ is equal to r_1^2 for $\delta = 0$ and so equation (8.16) arises for $\delta = \lambda/2$ by the obvious redefinition of n .

Since a zone plate is a form of diffraction grating, it is to be expected that there are higher-order foci. The position of an image point of order m is such that the optical path distances via adjacent zone boundaries differ by $m\lambda/2$. There are m Fresnel zones within each transmitting (or obstructing) area of the zone plate, which will cause cancellation if m is even, so that there is a resultant focus only if m is odd, and

$$r_n^2 = r_0^2 + mn\lambda f_m \quad (8.17)$$

where f_m is the m th order focal length,

$$f_m = f/m \quad (8.18)$$

Thus there is an infinite number of positive and negative foci with $m = \pm 1, \pm 3, \pm 5, \dots$. There is also some undiffracted radiation corresponding to $m = 0$.

The area A_n of the zone of outer radius r_n is

$$\begin{aligned} A_n &= \pi(r_n^2 - r_{n-1}^2) \\ &= \pi\lambda f + \pi(M^3 + 1)[(2n - 1)\lambda^2 + 4\delta\lambda]/4(M + 1)^3 \end{aligned} \quad (8.19)$$

which varies only slowly with n . To a good approximation,

$$A_n = \pi\lambda f = \pi(r_1^2 - r_0^2) \quad (8.20)$$

i.e., all the zones have the same area, except the central one with area πr_0^2 .

For large n , the widths dr_n of the zones are given by differentiating equation (8.14) and putting $dn = 1$, so that $2r_n dr_n = \lambda f$ i.e.,

$$dr_n = \lambda f / 2r_n \quad (8.21)$$

$$= (r_n^2 - r_0^2) / 2nr_n \quad \text{for } r_0 \neq 0 \quad (8.22)$$

$$= r_n / 2n \quad \text{for } r_0 = 0 \quad (8.23)$$

A plane wave focused at f/m is diffracted through a (small) angle β , given by $\sin \beta \approx \tan \beta = r_n/(f/m)$, i.e.,

$$2dr_n \sin \beta = m\lambda \quad (8.24)$$

—the diffraction grating equation for the local spacing dr_n and normal incidence [the factor of two difference between equations (8.24) and (6.10) is due to the definition of a zone that is used].

8.1.2. Diffraction Patterns

Although the above analysis indicates the positions of the zone plate foci, it does not give the forms of the diffraction patterns, which may be obtained using the Fresnel–Kirchoff diffraction integral.⁽²⁾ Referring to Figure 8.3, this gives the complex disturbance at P' as

$$Y(P') = - (iA/2\lambda) \iint \frac{\exp [ik(S + S')]}{SS'} (\cos \alpha - \cos \beta) da \quad (8.25)$$

where α, β are the angles between S, S' and the normal to the aperture, da is an element of area of the aperture, and the integral is carried out over the whole aperture. Under the conditions in which this is to be applied, the diffraction angles are small, and the diffracting aperture dimensions (the zone widths) are large compared to the wavelength but small compared to the object and image distances. Equation (8.25) then reduces to

$$Y(P') = -(iA/\lambda RR') \cos \gamma \exp [ik(R + R')] \iint \exp [ikL(\xi, \eta)] d\xi d\eta \quad (8.26)$$

where γ is the angle between PP' and the normal to the aperture. The

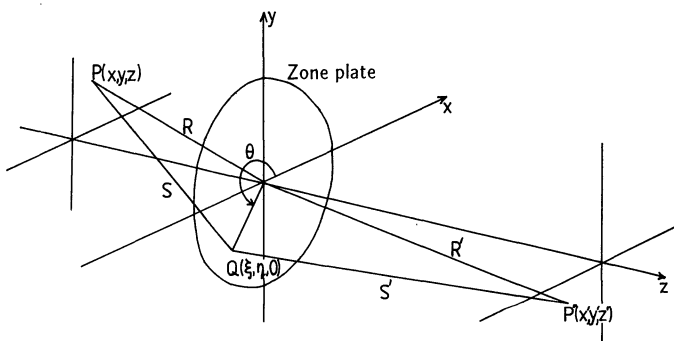


Figure 8.3. The coordinate system used in the calculation of the diffraction pattern of a circular aperture.

optical path length function via the point $Q(\xi, \eta, 0)$ in the aperture is

$$\begin{aligned} L(\xi, \eta) = & -(q + q') + (\xi^2 + \eta^2)(1/R + 1/R') \\ & - (q^2/2R - q'^2/2R') + \dots \end{aligned} \quad (8.27)$$

where $q = (x\xi + y\eta)/R$ and $q' = (x'\xi + y'\eta)/R'$. The Fresnel approximation to the integral is valid for the zone plates of low aperture that are being considered, so that $\cos \gamma \approx 1$ over the whole aperture, and the terms in $1/R^3$ and $1/R'^3$ can be ignored. A further simplification arises when considering an axial object (i.e., a point source) for which $x = y = 0$. This gives the point spread function of the zone plate. Using cylindrical polar coordinates for the aperture,

$$\xi = r \cos \theta = rc_\theta, \quad \eta = r \sin \theta = rs_\theta \quad (8.28)$$

leads to

$$\begin{aligned} Y(P') = & \frac{-iA \exp [ik(R + R')]}{RR'} \\ & \times \int_{\theta=0}^{2\pi} \int_{r=0}^{r_n} \exp \left\{ ik \left[-\frac{x'rc_\theta}{R'} - \frac{y'rs_\theta}{R'} + \frac{r^2(R + R')}{2RR'} \right] \right\} r dr d\theta \end{aligned} \quad (8.29)$$

where r_n is the radius of the aperture. Since zone plates are circularly symmetric, the diffraction pattern is radially symmetric so that the calculation can be carried out, without loss of generality, for $y' = 0$. Integrating over θ then gives

$$\begin{aligned} Y(P') = & \frac{-2\pi iA \exp [ik(R + R')]}{RR'} \\ & \times \int_0^{r_n} J_0 \left(\frac{krx'}{R'} \right) \exp \left[\frac{ikr^2(R + R')}{2RR'} \right] r dr \end{aligned} \quad (8.30)$$

where J_p is the Bessel function of order p . This integral may be evaluated⁽³⁾ in terms of the Lommel functions⁽⁴⁾

$$U_j(u_n, v_n) = \sum_{p=0}^{\infty} (-1)^p (u_n/v_n)^{j+2p} J_{j+2p}(v_n) \quad (8.31)$$

and

$$V_j(u_n, v_n) = \sum_{p=0}^{\infty} (-1)^p (v_n/u_n)^{j+2p} J_{j+2p}(v_n) \quad (8.32)$$

where u_n and v_n are the longitudinal and lateral dimensionless quantities

$$u_n = kr_n^2(R + R')/RR', \quad v_n = kr_n x'/R' \quad (8.33)$$

The contribution to the image due to an open aperture of radius r_n is given by, for $|u_n/v_n| \leq 1$,

$$Y(u_n, v_n, n) = (\Omega/u_n)(U_2 + iU_1) \exp(iu_n/2) \quad (8.34)$$

and, for $|u_n/v_n| \geq 1$.

$$Y(u_n, v_n, n) = (\Omega/u_n)[\exp(-iv_n^2/2u_n) + (V_0 + iV_1) \exp(iu_n/2)] \quad (8.35)$$

where

$$\Omega = -(Akr_n^2/RR') \exp[ik(R + R')] \quad (8.36)$$

To obtain the diffraction pattern of a zone plate, the disturbances due to the consecutive clear and opaque apertures are alternately added and subtracted. This is simpler if the equation (8.16) for the Soret zone plate is used; this results in the same expression for the intensity as using the more general equation (8.14). Although the dimensionless coordinates are different for each aperture, those of the central zone may be used for the whole zone plate by substituting

$$u_n = nu_1, \quad v_n = n^{1/2}v_1 \quad (8.37)$$

in the summation. Then, for a total number N of zones, the amplitude at the image point (u_1, v_1) is

$$Y_{ZP}(u_1, v_1, N) = \sum_{n=1}^N (-1)^{n+\mu} Y(nu_1, n^{1/2}v_1, n) \quad (8.38)$$

where $\mu = 1$ for a positive zone plate and $\mu = 0$ for a negative zone plate.

The distribution of intensity along the axis, to give the foci, is obtained by putting $v_1 = 0$ (since $x' = 0$), giving

$$V_0(nu_1, 0) = 1, \quad V_1(nu_1, 0) = 0 \quad (8.39)$$

so that

$$Y(nu_1, 0, n) = (\Omega/nu_1) \exp(inu_1/2) \quad (8.40)$$

and

$$Y_{\text{ZP}}(u_1, 0, N) = \sum_{n=1}^N (-1)^{n+\mu} (\Omega/n u_1) \exp(inu_1/2) \quad (8.41)$$

For an incident plane wave, $R = -\infty$, $\exp(ikR)/R = 1$, and $R' = f = r_n^2/n\lambda$. Thus

$$Y_{\text{ZP}}(u_1, 0, N) = -A \exp(ikR') \sum_{n=1}^N (-1)^{n+\mu} \exp(inu_1/2) \quad (8.42)$$

Note that evaluating this for an incident plane wave does not affect the forms of the diffraction patterns at the foci, but merely fixes the focal positions. The resulting intensity distribution is

$$\begin{aligned} I_{\text{ZP}}(u_1, 0, N) &= Y_{\text{ZP}} Y_{\text{ZP}}^* \\ &= I_0 \left[\sum_{n=1}^N (-1)^n \exp(inu_1/2) \right] \left[\sum_{l=1}^N (-1)^l \exp(-ilu_1/2) \right] \end{aligned} \quad (8.43)$$

where $I_0 = AA^*$, leading to⁽³⁾

$$I_{\text{ZP}}(u_1, 0, N) = I_0 \{[\sin(Nu_1/4)]/[\cos(u_1/4)]\}^2 \quad (8.44)$$

This distribution is shown in Figure 8.4 for the positive orders, showing the primary focus at $f(u_1 = 2\pi)$ and the higher-order foci at $f/3, f/5$, and so on. Note that the even orders are missing, as expected, and that the maxima all have the same peak value of $N^2 I_0$ but decrease in width with increasing order. This pattern is repeated for the negative orders (virtual foci).

In a focal plane, the radial intensity distribution is given by putting $u_1 = 0$. From equations (8.31) and (8.32),

$$\begin{aligned} \lim_{u_n \rightarrow 0} [U_1(u_n, v_n)/u_n] &= J_1(v_n)/v_n = J_1(n^{1/2}v_1)/n^{1/2}v_1 \\ \lim_{u_n \rightarrow 0} [U_2(u_n, v_n)/u_n] &= 0 \end{aligned} \quad (8.45)$$

so that

$$Y_{\text{ZP}}(0, v_1, N) = \sum_{n=1}^N (-1)^{n+\mu} i \Omega J_1(n^{1/2}v_1)/n^{1/2}v_1 \quad (8.46)$$

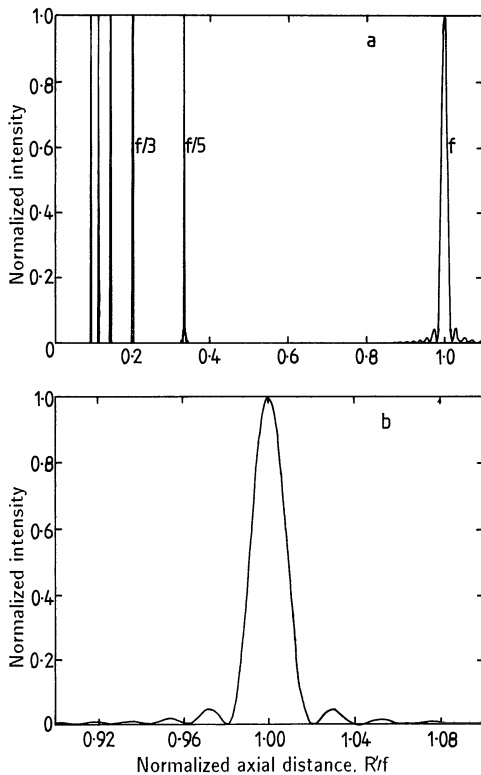


Figure 8.4. (a) The axial intensity distribution of an $N = 100$ Fresnel zone plate, illuminated with monochromatic radiation, showing the lowest positive diffraction orders. (b) The axial intensity distribution around the primary focus.

The resulting intensity distribution for an incoming plane wave is

$$I_{\text{ZP}}(0, v_1, N) = I_0 \sum_{n=1}^N (-1)^n J_1(n^{1/2}v_1) / n^{1/2} v_1 \sum_{l=1}^N (-1)^l J_1(l^{1/2}v_1) / l^{1/2} v_1 \quad (8.47)$$

which is shown in Figure 8.5 for several values of N . Also shown, for comparison, is the radial intensity distribution at the focus of a perfect lens, i.e., an Airy pattern

$$I(0, v) = I_0 [2J_1(v)/v]^2 \quad (8.48)$$

Clearly, as the number of zones increases, the zone plate pattern approaches the Airy pattern very closely; for $N \geq 100$ the difference is

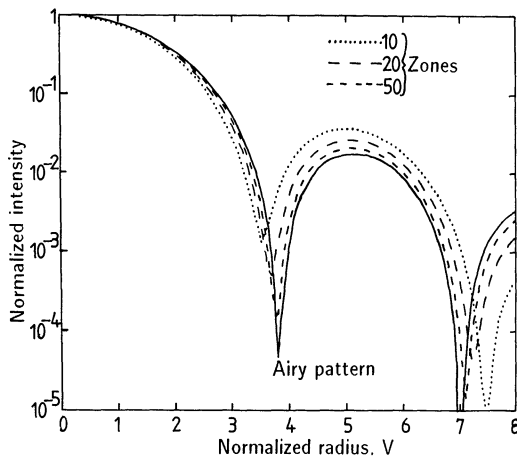


Figure 8.5. The radial intensity distributions of negative Fresnel zone plates.

negligible, as shown in Figure 8.6, in which the radii of the first minima are plotted as functions of N .

There is, however, a significant difference in the intensity distribution at the focus of a zone plate compared to that at the focus of a lens, which is not shown up by equation (8.47). This is that, for a zone plate, there is always a low-intensity background caused by the zero diffraction order and the out-of-focus other orders. The main contribution to this background is from the zero order, which, as will be shown below, has a diffraction efficiency of $1/4$. Thus, for an incoming plane wave, this contribution to the background is constant radially with a

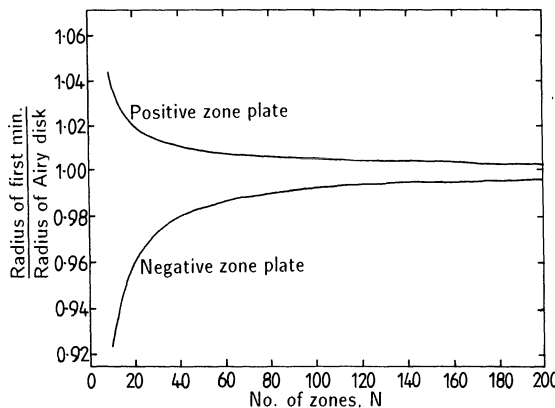


Figure 8.6. Ratios of the normalized radii of the first minima of the diffraction patterns of Fresnel zone plates to those of the Airy patterns of lenses of equivalent apertures.

value of $I_0/4$, and

$$(\text{Peak focused intensity})/(\text{background}) = 4N^2 \quad (8.49)$$

Although this is large and does not affect the imaging of point objects, it causes significant loss of contrast for extended objects.

8.1.3. Resolving Power and Chromatic Aberration

The resolving power of a zone plate may be defined using the Rayleigh criterion by rewriting the axial intensity distribution equation (8.44) in terms of the wavelength. For a plane wave, equation (8.33) gives

$$u_1 = 2\pi r_1^2/\lambda R' \quad (8.50)$$

and so

$$I_{ZP}(2\pi r_1^2/\lambda R', 0, N) = I_0 \{ [\sin(N\pi r_1^2/2\lambda R')] / [\cos(\pi r_1^2/2\lambda R')] \}^2 \quad (8.51)$$

This distribution is shown, schematically, in Figure 8.7 for two wavelengths, $\lambda + \Delta\lambda/2$ and $\lambda - \Delta\lambda/2$, just resolvable using the Rayleigh criterion. For the maximum of the distribution for $\lambda + \Delta\lambda/2$,

$$N\pi r_1^2/[2(\lambda + \Delta\lambda/2)R'] = p\pi/2 \quad (8.52)$$

where p is an odd integer, and for the minimum for $\lambda - \Delta\lambda/2$

$$N\pi r_1^2/[2(\lambda - \Delta\lambda/2)R'] = q\pi/2 \quad (8.53)$$

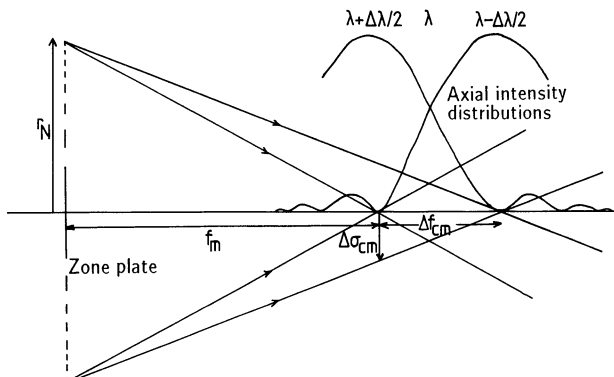


Figure 8.7. Longitudinal and transverse chromatic aberrations of a Fresnel zone plate.

where q is an even integer. For these to coincide, Np and q must differ by unity, i.e.,

$$Nr_1^2/[(\lambda + \Delta\lambda/2)R'] + 1 = Nr_1^2/[(\lambda - \Delta\lambda/2)R'] \quad (8.54)$$

At the m th-order focus, $R' = f_m = r_1^2/m\lambda$, and so

$$N\lambda m/[(\lambda + \Delta\lambda/2)] + 1 = N\lambda m/[(\lambda - \Delta\lambda/2)] \quad (8.55)$$

For $Nm \gg 1$ this leads to the resolving power

$$R_m = \lambda/\Delta\lambda = Nm \quad (8.56)$$

The longitudinal chromatic aberration Δf_{cm} (Figure 8.7) is given by the difference in the focal lengths for $\lambda - \Delta\lambda/2$ and $\lambda + \Delta\lambda/2$,

$$\begin{aligned} \Delta f_{cm} &= (r_n^2 - r_0^2)/[mn(\lambda - \Delta\lambda/2)] - (r_n^2 - r_0^2)/[mn(\lambda + \Delta\lambda/2)] \\ &= f_m/(1 - \Delta\lambda/2\lambda) - f_m/(1 + \Delta\lambda/2\lambda) = f_m/R_m \end{aligned} \quad (8.57)$$

The transverse chromatic aberration is given geometrically from Figure 8.7 as

$$\Delta\sigma_{cm}/r_N = \Delta f_{cm}/(f_m + \Delta f_{cm}) \quad (8.58)$$

i.e.,

$$\Delta\sigma_{cm} \approx r_N/R_m \quad (8.59)$$

The above discussion shows that the combination of a zone plate, illuminated with polychromatic light, and an axial pinhole will act as a monochromator. If the pinhole radius r_p is chosen to be equal to the transverse chromatic aberration $\Delta\sigma_{cm}$, then Figure 8.8 shows that all wavelengths that focus within

$$f_m[r_N/(r_N + r_p)] \leq f \leq f_m[r_N/(r_N - r_p)] \quad (8.60)$$

are transmitted. For wavelengths focused outside this range, the geometrical falloff in transmission is the ratio of the pinhole area to the blur circle area in the pinhole plane,

$$\pi r_p^2/\pi r_b^2 = (r_p/r_N)^2(1 + f_m/e)^2 \quad (8.61)$$

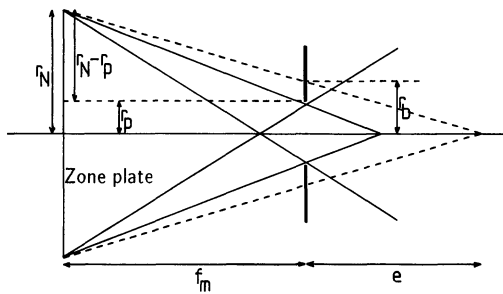


Figure 8.8. The use of a Fresnel zone plate as a monochromator.

where e is the distance of the focus from f_m . At half maximum, equation (8.61) leads to

$$e = \sqrt{2}r_p f_m / (r_N - \sqrt{2}r_p) \quad (8.62)$$

i.e., the focus is at

$$f_m + e = r_N f_m / (r_N - \sqrt{2}r_p) \quad (8.63)$$

corresponding to a wavelength $\lambda - \Delta\lambda'/2$ given by

$$f_m + e = r_N^2 / [Nm(\lambda - \Delta\lambda'/2)] = f_m / (1 - \Delta\lambda'/2\lambda) \quad (8.64)$$

From equations (8.63) and (8.64) the resolving power of the zone plate pinhole combination is

$$\lambda/\Delta\lambda' = r_N / 2\sqrt{2}r_p \quad (8.65)$$

8.1.4. Diffraction Efficiencies

For a point source, the peak intensity of the diffraction pattern is $N^2 I_0$ at each focus. However, as indicated in Figure 8.9, the convergence angles and sizes of the pattern vary and so different fractions of the incident energy are focused into the different orders. These fractions may be determined by expressing the amplitude transmission function of a Fresnel zone plate as a Fourier series

$$T(t) = c_0 + \sum_{-\infty}^{+\infty} c_{2q+1} \exp[i(2q+1)\pi Nt] \quad (8.66)$$

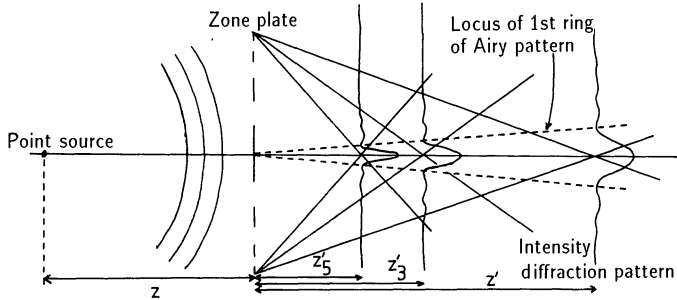


Figure 8.9. Schematic of the diffraction of a spherical wave by a Fresnel zone plate into the first three positive orders.

where

$$t = r^2/r_N^2 \quad (8.67)$$

is the square of the normalized radius. The m th ($m = 2q + 1$) coefficient of the series is given by

$$c_m = (N/2) \int_0^{2/N} T(t) \exp(-im\pi Nt) dt \quad (8.68)$$

leading to

$$c_0 = 1/2; \quad c_m = (-1)^m (i/m\pi) \exp(-im\pi Nt_0) \quad (8.69)$$

where t_0 is the value of t for the central zone, which contributes a phase shift to the coefficients. The coefficient c_m gives the complex amplitude diffracted to the m th focus for an incoming wave of unit amplitude, i.e., the diffraction efficiencies are given by $|c_m|^2$,

$$\text{Efficiency} = 1/4, 1/\pi^2, 1/9\pi^2, \dots, 1/m^2\pi^2 \quad (8.70)$$

for the orders $0, \pm 1, \pm 3, \dots, \pm m$. Summing the efficiencies over all values of m gives a total of $1/2$; the remaining 50% of the incident intensity is absorbed by the opaque zones. Only about 10% of the intensity is focused into the $m = +1$ order. Note that the size of the central zone does not affect the diffraction efficiencies.

8.1.5. Monochromatic Geometrical Aberrations

The third-order aberrations of zone plates may be calculated in the same way as for linear diffraction gratings,⁽⁵⁾ by applying Fermat's

principle to the zone boundaries. The optical path difference for radiation passing through the center of the zone plate is $nm\lambda/2$, so that the optical path PQP' (Figure 8.3) may be represented by

$$L = PQ + QP' + |nm\lambda/2| \quad (8.71)$$

i.e.,

$$L = PQ + QP' + |r_n^2 m\lambda/2r_1^2| \quad (8.72)$$

Using Figure 8.3,

$$PQ^2 = (x - \xi)^2 + (y - \eta)^2 + z^2 \quad (8.73)$$

leading to

$$PQ = zg + h/zg + [h(\xi^2 + \eta^2) - h^2 - (\xi^2 + \eta^2)^2/4]/2z^3 + O(\mu^6/z^5) \quad (8.74)$$

where $g^2 = 1 + (x^2 + y^2)/z^2$, $h = \xi x + \eta y$, and μ^6 represents combinations to the sixth power of x , y , and η . A similar expression is obtained for QP' by replacing (x, y, z) with (x', y', z') . Since Q lies on a zone boundary,

$$r_n^2 = \xi^2 + \eta^2 \quad (8.75)$$

and so applying Fermat's principle leads to

$$\begin{aligned} \partial L / \partial \xi = 0 &= (\xi - x)[1/zg + (2h - \xi^2 - \eta^2)/2z^3] \\ &+ O(\mu^5/z^5) + []' + |\xi m\lambda/r_1^2| \end{aligned} \quad (8.76)$$

$$\begin{aligned} \partial L / \partial \eta = 0 &= (\eta - y)[1/zg + (2h - \xi^2 - \eta^2)/2z^3] \\ &+ O(\mu^5/z^5) + []' + |\eta m\lambda/r_1^2| \end{aligned} \quad (8.77)$$

where $[]'$ represents similar terms with (x, y, z) replaced by (x', y', z') . Equations (8.76) and (8.77) cannot be simultaneously satisfied; the best that can be done is to make the lower-order terms in ξ and η zero. For radiation via the center of the zone plate, $\xi = \eta = 0$, so that equations (8.76) and (8.77) reduce to

$$x/zg + x'_0/z'_0 g'_0 = 0 \quad (8.78)$$

and

$$y/zg + y'_0/z'_0 g'_0 = 0 \quad (8.79)$$

where (x'_0, y'_0, z'_0) are the coordinates of the corresponding image point. The solutions of equations (8.78) and (8.79) are, respectively,

$$x/z = -x'_0/z'_0 \quad (8.80)$$

and

$$y/z = -y'_0/z'_0 \quad (8.81)$$

(Note that here z' is defined as positive for the positive orders.) For radiation via $Q(\xi, \eta, 0)$, the image point is specified by $x' = x'_0 + \Delta x'$ and $y' = y'_0 + \Delta y'$. Expanding equations (8.76) and (8.77) about (x'_0, y'_0) and using $\xi = r_N \cos \theta$, $\eta = r_N \sin \theta$ for the outermost zone leads to

$$\begin{aligned} \Delta x'/z'_0 &= \xi(1/z + 1/z'_0 + |m\lambda/r_1^2|) - 3r_N \cos \theta(x^2/z^3 + x'^2_0/z'^3_0)/2 \\ &\quad + r_N^2(1 + 2\cos^2 \theta)(x/z^3 + x'_0/z'^3_0)/2 \\ &\quad - r_N^3 \cos \theta(1/z^3 + 1/z'^3_0)/2 \\ &\quad + O(\mu^5/z^5, \mu'^5/z'^5_0) \end{aligned} \quad (8.82)$$

and

$$\begin{aligned} \Delta y'/z'_0 &= \eta(1/z + 1/z'_0 + |m\lambda/r_1^2|) - r_N \sin \theta(x^2/z^3 + x'^2_0/z'^3_0)/2 \\ &\quad + r_N^2 \sin \theta \cos \theta(x/z^3 + x'_0/z'^3_0) \\ &\quad - r_N^3 \sin \theta(1/z^3 + 1/z'^3_0)/2 \\ &\quad + O(\mu^5/z^5, \mu'^5/z'^5_0) \end{aligned} \quad (8.83)$$

To minimize the aberrations, the first terms in these expressions must be zero. Hence

$$1/z + 1/z'_0 + |m\lambda/r_1^2| = 0 \quad (8.84)$$

which corresponds to the thin lens formula, equation (8.8). The other terms in equations (8.82) and (8.83) represent the aberrations present when imaging with perfectly made zone plates.

8.1.5.1. Spherical Aberration

The spherical aberration is given by the terms in r_N^3 , i.e.,

$$(\Delta x'/z'_0)_{\text{SA}} = -r_N^3 \cos \theta (1/z^3 + 1/z'_0)^3 / 2 \quad (8.85)$$

$$(\Delta y'/z'_0)_{\text{SA}} = -r_N^3 \sin \theta (1/z^3 + 1/z'_0)^3 / 2 \quad (8.86)$$

The radius of the blur circle at the image plane, i.e., the lateral spherical aberration, is thus

$$\Delta l = (\Delta x'^2_{\text{SA}} + \Delta y'^2_{\text{SA}})^{1/2} = z' r_N^3 (1/z^3 + 1/z'_0)^3 / 2 \quad (8.87)$$

and the corresponding longitudinal aberration is (Figure 8.10)

$$\Delta z' = z'_0 \Delta l / r_N \quad (8.88)$$

As in the case of curved gratings, the presence of spherical aberration leads to an optimum zone plate radius. At $\eta = 0$ and for $y = y'_0 = 0$, equation (8.72) gives

$$\lambda/4 = r_{\text{opt}}^4 (1/z^3 + 1/z'_0)^3 / 8 \quad (8.89)$$

i.e.,

$$r_{\text{opt}} = [2\lambda/(1/z^3 + 1/z'_0)^3]^{1/4} \quad (8.90)$$

For a plane incident wave, $z = \infty$ and $z'_0 = f_m = r_1^2/m\lambda$. Thus

$$r_{\text{opt}} = r_1 (2r_1^2/m^3\lambda^2)^{1/4} \quad (8.91)$$

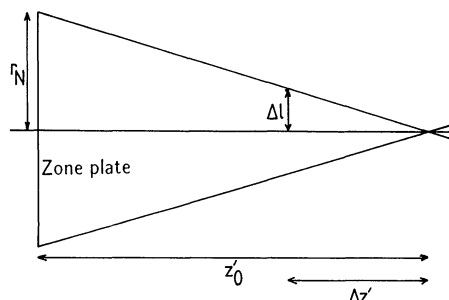


Figure 8.10. Lateral and longitudinal spherical aberrations of a Fresnel zone plate.

and the corresponding optimum number of zones is

$$N_{\text{opt}} = (r_{\text{opt}}/r_1)^2 = (2/m^3)^{1/2} r_1/\lambda \quad (8.92)$$

8.1.5.2. Coma

The coma is given by the terms in r_N^2 , i.e.,

$$(\Delta x'/z'_0)_C = r_N^2(1 + 2 \cos^2 \theta)(x/z^3 + x'_0/z_0'^3)/2 \quad (8.93)$$

$$(\Delta y'/z'_0)_C = r_N^2 \sin \theta \cos \theta (x/z^3 + x'/z_0'^3) \quad (8.94)$$

resulting in a series of coma circles obeying the equation

$$[(\Delta x'/z'_0)_C - r_N^2(x/z^3 + x'/z_0'^3)]^2 + (\Delta y'/z'_0)_C^2 = [r_N^2(x/z^3 + x'/z_0'^3)]^2 \quad (8.95)$$

8.1.5.3. Astigmatism

The astigmatism (and field curvature terms) are those in r_N ,

$$(\Delta x'/z'_0)_A = -3r_N \cos \theta (x^3/z^3 + x_0'^3/z_0'^3)/2 \quad (8.96)$$

$$(\Delta y'/z'_0)_A = -r_N \sin \theta (x^3/z^3 + x_0'^3/z_0'^3)/2 \quad (8.97)$$

so that

$$(\Delta x'_A/3)^2 + (\Delta y'_A)^2 = 4[r_N z'_0(x^2/z^3 + z_0'^2/z_0'^3)]^2 \quad (8.98)$$

—the equation of an ellipse with major and minor axes in the ratio 3:1. Thus the image is formed on two curved focal surfaces that, in the approximation that they are spherical, have curvatures

$$\Delta x'_A/r_N = x_0'^2/2z'_0 R_t \quad (8.99)$$

and

$$\Delta y'_A/r_N = x_0'^2/2z'_0 R_s \quad (8.100)$$

where

$$R_t = z'_0/3 \quad (8.101)$$

is the radius of the tangential focal surface and

$$R_s = z'_0 \quad (8.102)$$

is the radius of the saggital focal surface.

8.1.5.4. Distortion

Because of the condition, equation (8.84), that has been imposed, terms in x^3 representing distortion disappear from equations (8.76) and (8.77). Thus distortion does not appear in the image.

8.1.5.5. Relative Sizes of the Aberrations

For an object at infinity ($z = \infty$), $z'_0 = f_m$ and so

Δl : (radius of coma circle): (semimajor axis of astigmatism ellipse)

$$= r_N^2 : r_N x'_0 : 3x_0'^2 \quad (8.103)$$

Thus for image points close to the axis, spherical aberration is the largest aberration. For off-axis points, coma and astigmatism become more significant. For points more than about one zone plate radius away from the axis, astigmatism dominates.

8.1.6. Depth of Focus

For a lens the depth of focus is defined by the axial position at which the intensity has decreased to 80% of that at the focus. This gives,⁽⁶⁾ for a lens of radius r_N ,

$$\Delta f = \pm 3.2(\lambda/2\pi)(f/r_N)^2 \quad (8.104)$$

For a zone plate, the intensity requirement leads to [from equation (8.44)]

$$[\sin(Nu_f/4)/\cos(u_f/4)]^2 = 0.8N^2 \quad (8.105)$$

where

$$u_f = u_1 \pm \Delta u_{1m} \quad (8.106)$$

and u_{1m} is the normalized defocus for the m th order. For an incident plane wave, at a focus

$$u_1 = 2\pi r_1^2 / \lambda f_m = 2m\pi \quad (8.107)$$

Thus $u_f = 2\pi r_1^2 / \lambda (f_m \mp \Delta f_m)$, giving

$$\Delta f_m = (f_m / 2m\pi) \Delta u_{1m} = (f / 2m^2\pi) \Delta u_{1m} \quad (8.108)$$

and

$$\Delta f_m / \Delta f = (N / 3.2m^2) \Delta u_{1m} \quad (8.109)$$

using $r_N^2 = N\lambda f$ for a zone plate.

The values of Δu_{1m} satisfying equation (8.105) are

$$\sin^2(N\Delta u_{1m}/4) / \sin^2(\Delta u_{1m}/4) = 0.8N^2 \quad (8.110)$$

for N even, and

$$\cos^2(N\Delta u_{1m}/4) \sin^2(\Delta u_{1m}/4) = 0.8N^2 \quad (8.111)$$

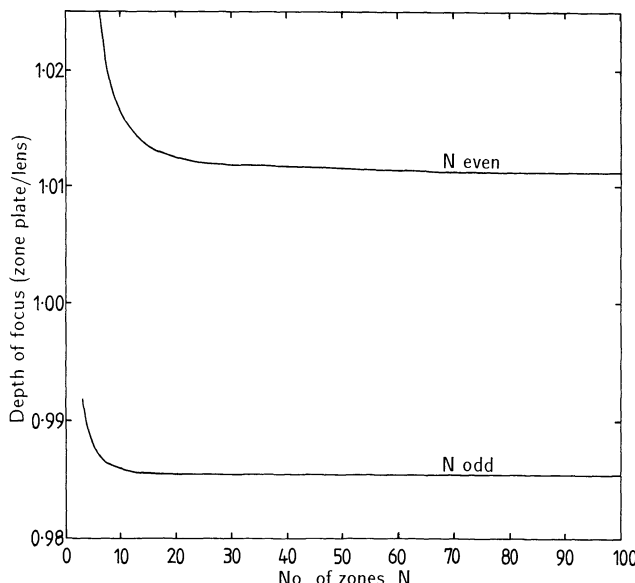


Figure 8.11. The ratio of zone plate depth of focus to lens depth of focus as a function of the number of zones.

for N odd. Using the values of Δu_{1m} found from these equations, the function (8.109) is plotted for N up to 100 for the first-order focus in Figure 8.11. Clearly for N sufficiently large it is a good approximation to use the lens formula, so that for the m th order

$$\Delta f_m \simeq \pm f_m / 2N \quad (8.112)$$

8.1.7. Resolution

8.1.7.1. Point Sources

Assuming that the number of zones N is sufficiently large that the diffraction pattern at a focus approximates to an Airy pattern, equation (8.48), the angular position of the first minimum is

$$\omega_1 = 0.61\lambda/r_N \quad (8.113)$$

By the Rayleigh criterion, the resolution is given by δ_m , the radius of the first dark ring of the Airy pattern in the m th order. For small angles,

$$m\delta_m/z' = \tan \omega_1 \simeq \omega_1 \quad (8.114)$$

and so the resolution is

$$\delta_m = 0.61z'\lambda/mr_N \quad (8.115)$$

For an object at infinity, $z' = f_m$ and using equation (8.21) gives the resolution in terms of the outermost zone width

$$\delta_m = 1.22 dr_N/m \quad (8.116)$$

Equation (8.116) shows that the point-to-point resolution depends on two things—the outermost zone width and the diffraction order. Higher resolutions can be obtained by manufacturing zone plates with smaller outer zone widths (thus the manufacturing method sets a limit on the resolution) or by using them in higher orders (but this leads to less focused intensity).

8.1.7.2. Extended Objects

The Airy pattern at any focus is surrounded by an extensive low-intensity background as discussed in Section 8.1.2. Thus, for a realistic assessment of image quality for extended objects, the classical optical view of resolution presented above is not sufficient. This can be

seen in a more quantitative way by considering the proportion of focused energy in the central peak of the point spread function; in an Airy pattern, 83.8% of the energy is within the first dark ring.⁽⁷⁾ Since, for a zone plate, $2/\pi^2$ of the focused energy forms the (approximate) Airy pattern in the first order, only 17% of the transmitted energy forms the principal imaging point.

A better criterion for image quality is obtained by using the modulation transfer function (MTF), which is the modulus of the optical transfer function (OTF).⁽⁸⁾ This is a measure of the faithfulness of transference of spatial frequencies from object to image. For an incoherent system, the OTF may be calculated in two ways—it is the Fourier transform of the intensity point spread function and it is the autocorrelation of the pupil function of the focusing element.⁽⁹⁾

To calculate the point spread function the methods of Section 8.1.2 may be used, leading to very complicated calculations since equations (8.34) and (8.35) have to be evaluated at a given focus for all orders. An approximate, simpler, method is to utilize equation (8.68), the Fourier coefficients giving the proportion of amplitude diffracted to each focus. Each focus may then be considered as a point source having this amplitude, except in the focal plane for which the calculation is being done where the Airy pattern gives the distribution. The total disturbance in the m th focal plane is the summation of the Airy pattern and the propagating spherical waves weighted by their relative amplitudes (Figure 8.12), and the square of this distribution gives the intensity point spread

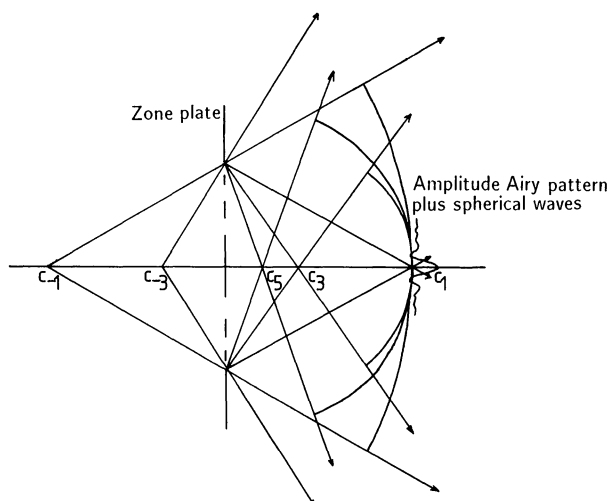


Figure 8.12. Illustration of an approximate method of calculating the point spread function of a zone plate with an extended object.

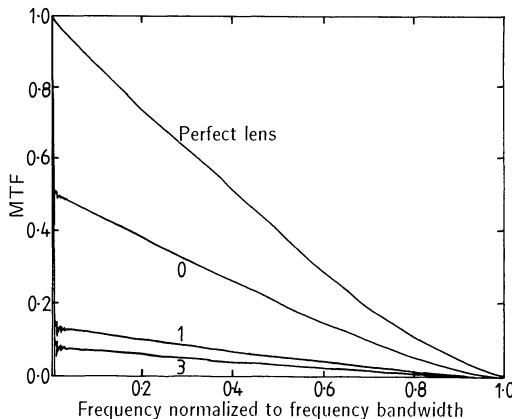


Figure 8.13. The incoherent modulation transfer functions for the zero and first and third positive diffraction orders of a Fresnel zone plate, compared to that for a perfect lens.

function. Since the point spread function is circularly symmetric, its Fourier transform may be found by taking the Hankel transform⁽⁸⁾ of the radial intensity distribution $I(0, v)$

$$F(t) = \pi \int_0^\infty v I(0, v) J_0(2\pi vt) dv \quad (8.117)$$

thus reducing a two-dimensional computation to a one-dimensional one. The resulting MTFs of the zero, first, and third orders of a zone plate are shown in Figure 8.13, compared to that for a perfect lens. The major feature of the zone plate MTFs is the large dc spike, present in all orders. Removal of the (unwanted) dc level would provide an improvement in the contrast—this may be done by subtracting a constant background level, which, however, takes no account of the variations in the background intensity.

8.2. Improvement of Image Quality—Modified Amplitude Zone Plates

Because of the problems of imaging with zone plates discussed above, it is worthwhile considering modifications to their basic structure that, for a particular purpose, may improve the imaging characteristics. Two types of modified zone plate^(10,11) that may be of use at soft X-ray wavelengths will be considered in this section. The first of these is when the zone plate center is obstructed, which eliminates the zero order from

a central (shadow) region of the image. The second is the addition of outer zones, which focus their higher-order diffracted intensity to the primary focus of the central zone plane, forming a composite zone plate.

8.2.1. Obstructed Zone Plates^(11,12)

An image formed (at the first-order focus) in the shadow of a circular obstruction at the center of the zone plate contains no contribution from the zero diffraction order (Figure 8.14). Thus the major contribution to the background is removed and so the contrast is improved. The radii of the zone boundaries are given by equation (8.14) where now r_0 is the radius of the central obstruction and may have any value up to r_N . In terms of the obstruction ratio

$$a = r_0/r_N \quad (8.118)$$

$$r_n^2 = n\lambda f[1 + (N/n)a^2/(1 - a^2)] \quad (8.119)$$

for $n = 1, 2 \dots N$.

8.2.1.1. The Point Spread Function

The diffraction patterns of an obstructed zone plate may be calculated using the method described in Section 8.1.2. For large N , the point spread function will be (approximately) the same as that of an equivalently obstructed lens, i.e.,⁽¹³⁾

$$I_{ZP}(0, v_N, N) = I_0[2J_1(v_N)/v_N - 2a^2 J_1(av_N)/av_N]^2/(1 - a^2)^2 \quad (8.120)$$

where v_N is the normalized radius

$$v_N = 2\pi r_N x' / \lambda f \quad (8.121)$$

from equation (8.33). Note that for $a = 0$, equation (8.120) reduces to the Airy pattern, equation (8.48), as would be expected. The distribution

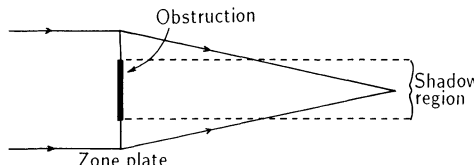


Figure 8.14. Image formation in the shadow of an obstructed zone plate.

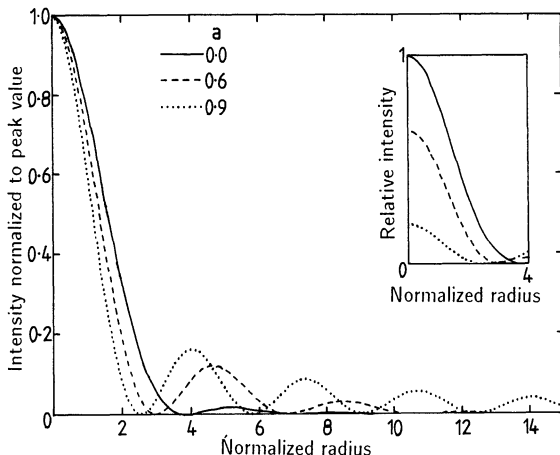


Figure 8.15. The point spread functions of obstructed zone plates.

(8.120) is shown in Figure 8.15 for various values of the obstruction ratio, showing that as it increases the width of the central peak decreases, thus improving the Rayleigh resolution, but this is offset by an increasing amount of energy in the side lobes (see Section 8.2.1.4). Also, since the transmitting area of the zone plate decreases as the obstruction ratio increases, the focused intensity decreases as shown in the inset to Figure 8.15.

The validity of using equation (8.120) to give the point spread function is demonstrated in Figure 8.16 where the radii of the first

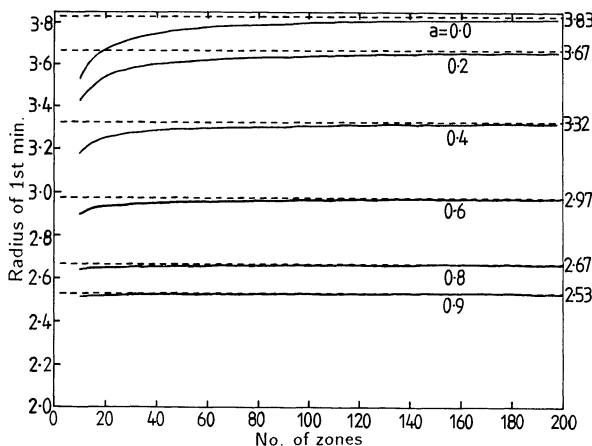


Figure 8.16. Positions of the first minima of the first-order diffraction patterns of obstructed zone plates (solid lines) compared to those of the equivalent obstructed lenses (dashed lines).

minima are plotted as functions of N for various values of the obstruction ratio. Clearly equation (8.120) gives a good approximation for sufficiently large N .

8.2.1.2. Resolving Power and Chromatic Aberration

The axial intensity distribution of an obstructed lens of radius r_N is⁽¹⁴⁾

$$I(z) = I_0 \{ \sin [p(1 - a^2)/2]/(p/2) \}^2 / (1 - a^2)^2 \quad (8.122)$$

where

$$p = \pi r_N^2 (z - f) / \lambda f^2 \quad (8.123)$$

Near to a focus the distribution for a zone plate may be taken to be the same as this. Thus the longitudinal chromatic aberration Δf_{cm} for the m th order is given when $\sin [\pi r_N^2 \Delta f_{cm} (1 - a^2) / \lambda f_m^2]$ is equal to zero, i.e.,

$$\Delta f_{cm} = f_m / [(1 - a^2) N m] \quad (8.124)$$

Comparing this with equation (8.57) gives the resolving power

$$\lambda / \Delta \lambda = f_m / \Delta f_{cm} = (1 - a^2) N m \quad (8.125)$$

Thus the resolving power of an obstructed zone plate is decreased compared to that of an unobstructed one [equation (8.56)].

8.2.1.3. Depth of Focus

The depth of focus of an obstructed lens is increased by a factor $1/(1 - a^2)$ compared to that of an unobstructed lens. Thus, for an obstructed zone plate, the depth of focus in the m th order is

$$\Delta f_m = \pm f_m / 2N(1 - a^2) \quad (8.126)$$

8.2.1.4. Energy in the Point Spread Function

The energy contained within a radius R of the point spread function is given by

$$E(R) = [C/(1 - a^2)^2] \int_0^R [2J_1(r)/r - 2a^2 J_1(ar)/ar]^2 r dr \quad (8.127)$$

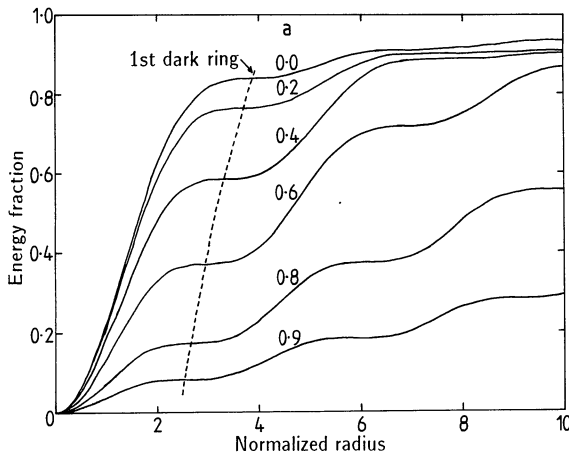


Figure 8.17. The energy contained within given radii of the first-order diffraction patterns of obstructed zone plates.

where the constant C is determined by stipulating that all the energy is contained within $R = \infty$. Thus the fraction of the energy within R is given by putting $C = 0.5$, since $E(\infty) = 2C$. Curves of $E(R)$ as functions of R are shown for various obstruction ratios in Figure 8.17. These show that as more of the zone plate is obstructed, the energy shifts into the outer rings of the diffraction pattern. Thus, using an obstructed zone plate to image an extended object leads to contrast reduction, since the energy of each object point is spread into a larger area of the image.

8.2.1.5. Modulation Transfer Function

The MTFs of obstructed zone plates may be obtained using equation (8.120) and proceeding as in Section 8.1.7.2. Figure 8.18 shows the results of such calculations when only the radiation focused to the m th order is considered (i.e., the background is neglected). This shows that, compared to an unobstructed zone plate, the contrast is degraded for most spatial frequencies but, because of the narrower central peak, improves slightly at high frequencies. Since, however, the effect of the central obstruction is to remove zero-order radiation from the image, the overall contrast will be improved.

8.2.1.6. Discussion

The above considerations show that the use of an obstructed zone plate leads to removal of a large part of the background intensity but also

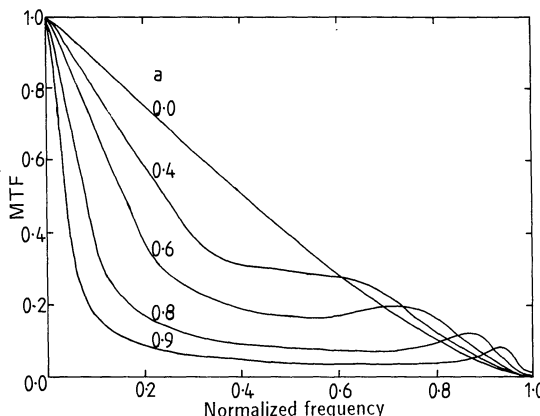


Figure 8.18. The modulation transfer functions for the central parts of the first-order diffraction patterns of obstructed zone plates.

to less faithful transfer of spatial frequencies from object to image. The former effect enhances the contrast while the latter degrades it. Thus, depending on the imaging application, the obstruction ratio must be chosen with care. In some applications (to be discussed in Chapter 10), obstructed zone plates have significant advantages over unobstructed ones.

8.2.2. Composite Zone Plates⁽¹¹⁾

As discussed above, a centrally obstructed zone plate gives increased resolution, but at the expense of a decrease in focused intensity. Higher-order foci can also be used to give better resolutions, but these have far less energy diffracted into them.

Certain manufacturing processes (see Chapter 9) offer an alternative way of increasing the resolution of a zone plate, without decreasing the focused energy. For a Fresnel zone plate, the highest possible resolution is achieved when the width of the outermost zone is equal to that of the finest line that the manufacturing instrument is capable of. If this central zone plate, of first-order focal length f , is surrounded with extra zones whose third-order focal length is also f , then increased resolution and increased energy focused at f are obtained. This idea may readily be extended to higher (fifth, seventh . . .) orders, but the gains become progressively less (see Section 8.2.2.6). The majority of the discussion will be restricted to first-/third-order composite zone plates.

The radii of the zone boundaries of a composite zone plate are, using

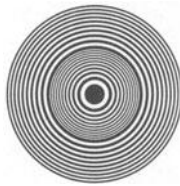


Figure 8.19. A (20,20) composite zone plate.

equation (8.16) (i.e., assuming that $r_0 = 0$),

$$r_n^2 = n\lambda f \quad n = 1, 2, \dots, N \quad (8.128)$$

and

$$r_n^2 = n\lambda f(3 - 2N/n) \quad N < n \leq N + M \quad (8.129)$$

A composite zone plate may be specified by the two numbers (N, M) where N is the number of zones in the inner (first-order) part and M is the number in the outer (third-order) part. The ultimate composite zone plate has equal-width finest zones of the inner and outer parts ($dr_{N+M} = dr_N$), i.e.,

$$3r_{N+M}/2(3M + N) = r_N/2N \quad (8.130)$$

the factors of three arising because of the third-order imaging of the outer part. Using equations (8.128) and (8.129) to give r_N and r_{N+M} respectively leads to the maximum value of M ,

$$M_{\max} = 8N/3 \quad (8.131)$$

Thus the maximum total number of zones is $11N/3$. An example of a (20,20) composite zone plate is shown in Figure 8.19.

8.2.2.1. Diffraction Patterns

As in the case of an obstructed zone plate, a composite zone plate has a counterpart in conventional optics, namely an apodized lens having the transmission function shown in Figure 8.20. Thus, although the diffraction pattern given by an incident plane wave may be calculated exactly following Section 8.1.2, for large numbers of zones the intensity

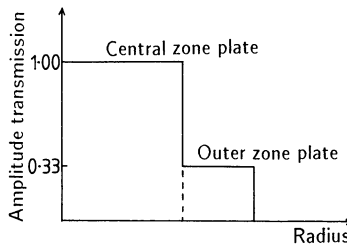


Figure 8.20. The effective transmission function of a composite zone plate.

distribution at f is given to a good approximation by, with $xB_L = J_1(xL)/xL$,

$$I_{CZP}(0, v_{N+M}, N, M) = I_0[1/(1 + 2a^2)]^2(2_1 B_{v_{N+M}} + 4a^2 {}_a B_{v_{N+M}}) \quad (8.132)$$

where

$$a = r_N/r_{N+M} \quad (8.133)$$

This is formed from the appropriately scaled sum of the amplitude from a lens and an annular lens, using $v_N = av_{N+M}$. In terms of N and M , equation (8.132) becomes, with $K = 3M + N$,

$$I_{CZP}(0, v_1, N, M) = I_0[N/(N + M)]^2(2K_k{}^{1/2}B_{V_1}/3N + 4N^{1/2}B_{V_1}/3) \quad (8.134)$$

where

$$v_1 = 2\pi x'r_1/\lambda f \quad (8.135)$$

The point spread functions for various $(100, M)$ composite zone plates are shown in Figure 8.21. The increase in peak intensity as M increases, due to the extra number of zones, is clearly shown. The peak intensity is still proportional to the square of the total number of zones, i.e., to $(N + M)^2$, the outer zones each having three times the area of the inner zones but being only one-third as efficient in focusing amplitude to f .

Figure 8.21 also shows that the central peak gets narrower as M increases, so that the classical resolution improves. Note, however, that the first minimum of equation (8.134) is nonzero for large values of M . This is the cause of the cusp in Figure 8.22, where the radius of the first dark ring is plotted as a function of M for $(100, M)$ composite zone plates.

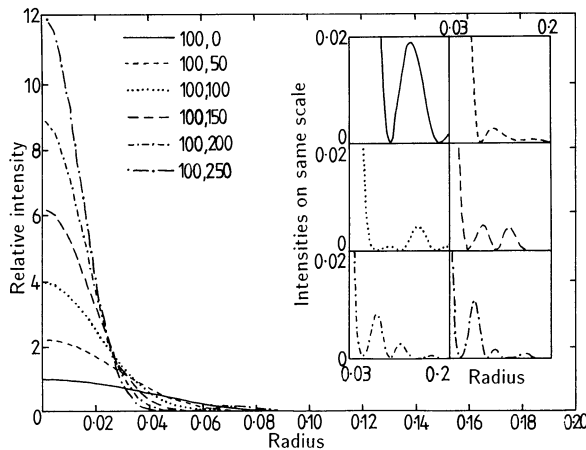


Figure 8.21. The point spread functions of composite zone plates.

The axial intensity is given by, following Section 8.1.2 and appropriately scaling the amplitudes,

$$I_{\text{CZP}}(u_1, 0, N, M) = I_0 |E(E^N - 1)/(1 + E) + E^{N+3}(E^{3M} - 1)/(1 + E^3)|^2 \quad (8.136)$$

where $E = \exp(-iu_1/2)$ and with

$$u_1 = 2\pi r_1^2/\lambda R' \quad (8.137)$$

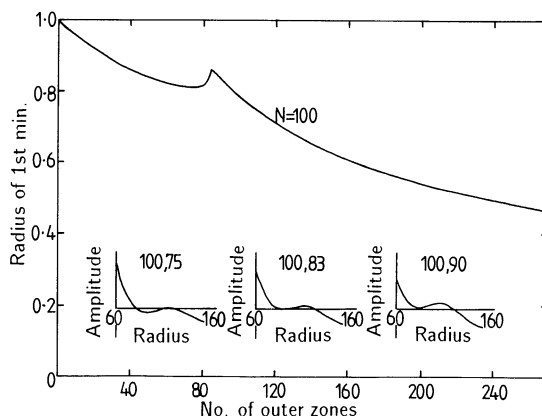


Figure 8.22. Radii of the first minima of the first-order diffraction patterns of $(100, M)$ composite zone plates.

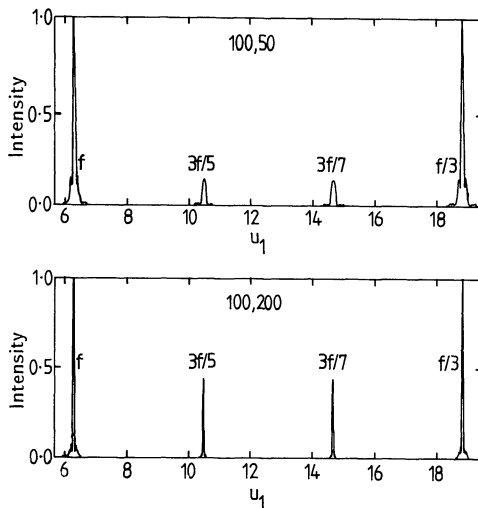


Figure 8.23. Normalized axial intensity distributions for (100,50) and (100,200) composite zone plates, showing the foci at f , $3f/5$, $3f/7$, and $f/3$.

The axial distribution, equation (8.136), is shown in Figure 8.23 for the two composite zone plates (100,50) and (100,200). This shows that the central zones focus to f , $f/3$, $f/5$, and so on, and the outer zones to $3f$, f , $3f/5$, $3f/7$, $f/3$, and so on. Only the common foci have peak intensities proportional to $(N + M)^2$, the remainder being proportional to M^2 .

8.2.2.2. Resolving Power

The axial intensity distribution about a focus of a composite zone plate may not have a clear first minimum, as shown in Figure 8.24, and so

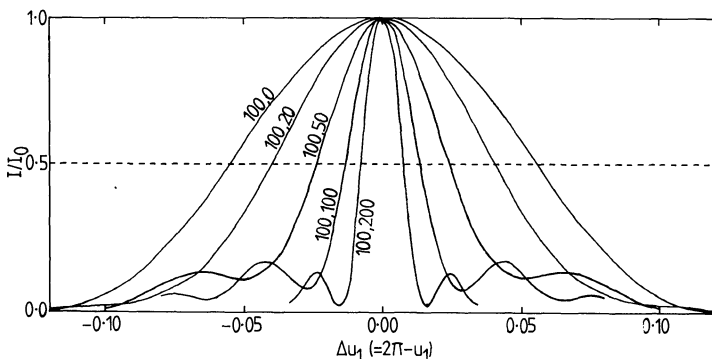


Figure 8.24. Normalized axial intensity distribution around the primary foci of composite zone plates.

Table 8.1. Resolving Power of Composite Zone Plates

Composite zone plate (N, M)	FWHM of central peak at f (rad)	Resolving power, $2\pi/(FWHM \times 9/16)$	$(N^2 + 9M^2)^{1/2} + M$
100,0	0.1113	100	100
100,20	0.0806	139	137
100,50	0.0479	233	230
100,100	0.0271	412	416
100,200	0.0147	760	808
200,0	0.0557	200	200
200,20	0.0484	231	229
200,50	0.0368	304	300
200,100	0.0241	463	461
200,200	0.0136	821	832
200,500	0.0061	1831	2013
300,0	0.0371	300	300
300,20	0.0341	328	326
300,50	0.0287	389	385
300,100	0.0211	529	524
300,200	0.0128	873	871
300,500	0.0058	1926	2030
300,800	0.00385	2901	3219

the positions of the first minima no longer give a good criterion for defining the spread of wavelengths transmitted. A more convenient criterion may be obtained by noting that, for a Fresnel zone plate, the resolving power at the primary focus is given by, from equation (8.50),

$$\lambda/\Delta\lambda = 2\pi/\Delta u_1 \quad (8.138)$$

The value of Δu_1 giving a resolving power of N is (by measuring from Figure 8.24) 9/16 times the full width at half maximum (FWHM). Assuming that the resolving power of a composite zone plate is given in the same way, the values in Table 8.1 are obtained. As shown there, these values are given to good approximation by

$$\lambda/\Delta\lambda = (N^2 + 9M^2)^{1/2} + M \quad (8.139)$$

except when M approaches its maximum value, when equation (8.139) is an overestimate of the resolving power.

8.2.2.3. Depth of Focus

The depth of focus of a composite zone plate may be obtained in a similar way to the resolving power, by determining the point at which the

Table 8.2. Depths of Focus of Composite Zone Plates

Composite zone plate (N, M)	Half width at 80% peak intensity	$\Delta f/f$	$[N/(N + M)]^2/2N$
100,0	0.0324	0.0052	0.0050
100,20	0.0231	0.0037	0.0035
100,50	0.0137	0.0022	0.0022
100,100	0.0079	0.0013	0.0013
100,200	0.0044	0.00070	0.00055
200,0	0.0162	0.0026	0.0025
200,20	0.0140	0.0022	0.0021
200,50	0.0105	0.0017	0.0016
200,100	0.0069	0.0011	0.0011
200,200	0.0040	0.00064	0.00063
200,500	0.00195	0.00031	0.00020
300,0	0.0108	0.0017	0.0017
300,20	0.0099	0.0016	0.0015
300,50	0.0083	0.0013	0.0012
300,100	0.0060	0.00095	0.00094
300,200	0.0037	0.00059	0.00060
300,500	0.00185	0.00029	0.00023
300,800	0.00138	0.00022	0.00012

intensity, equation (8.136), falls to 80% of its peak value. The depths of focus Δf given in this way are shown in Table 8.2 for the focus at f . As shown there, to a good approximation

$$\Delta f/f = [N/(N + M)]^2/2N \quad (8.140)$$

except, again, for large values of M , when equation (8.140) is an underestimate of the depth of focus.

8.2.2.4. Energy in the Point Spread Function

Compared to a normal lens of the same radius, the intensity distribution at the focus of an apodized lens has more energy in a broader central peak and less in the outer rings. In the case of a composite zone plate, the aperture is increased by the addition of the outer zones, which gives more energy in a narrower central peak while still decreasing the amount in the outer rings of the intensity distribution. The energy contained within a given radius R of the point spread function is

$$E(R) = C[3/(1 + 2a^2)]^2 \int_0^R [(2/3)J_1(r)/r + (4a^2/3)J_1(ar)/ar]^2 r dr \quad (8.141)$$

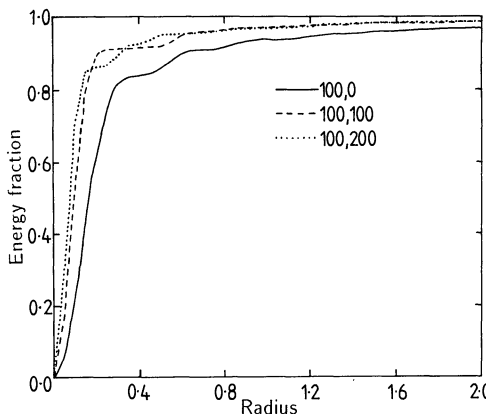


Figure 8.25. The energy contained within given radii of the first-order diffraction patterns of composite zone plates.

where C is determined in the same way as for the obstructed zone plate (Section 8.2.1.4). $E(R)$ is shown for three composite zone plates in Figure 8.25.

The fraction of the incident energy focused to f (i.e., the composite zone plate efficiency) can be calculated from the total areas of the inner and outer zones, which diffract $1/\pi^2$ and $1/9\pi^2$ respectively of the incident energy to f . For an incident plane wave, the total zone area is proportional to the incident energy and so, from equations (8.128) and (8.129), the diffraction efficiency is

$$\begin{aligned}\varepsilon &= (1/\pi^2)r_N^2/r_{N+M}^2 + (1/9\pi^2)(r_{N+M}^2 - r_N^2)/r_{N+M}^2 \\ &= (1/3\pi^2)(3N + M)/(N + 3M)\end{aligned}\quad (8.142)$$

For the maximum value of M , equation (8.131), this gives

$$\varepsilon = 17/81\pi^2 = 0.0213 \quad (8.143)$$

and the variation of ε with M for various values of N is shown in Figure 8.26. This shows that, although more energy is focused to f , the efficiency drops as M increases, and therefore the background increases.

8.2.2.5. Modulation Transfer Function

The MTFs of the focus at f for some composite zone plates are shown in Figure 8.27. When normalized to the aperture size, these show a reduction in the high-frequency response as M increases. This is to be

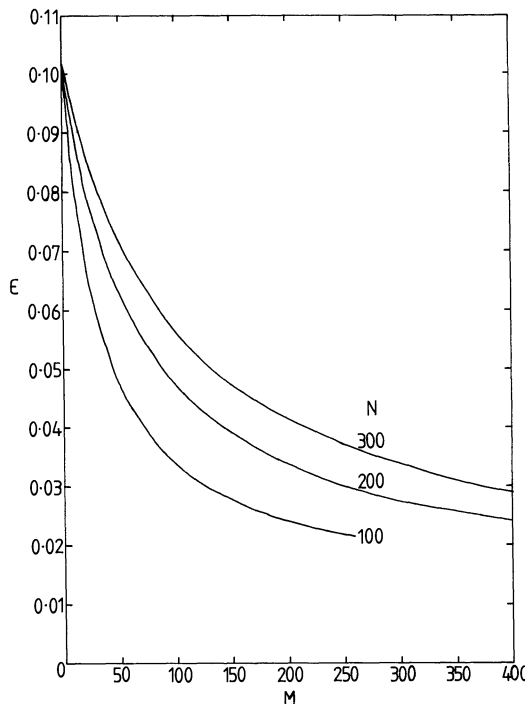


Figure 8.26. First-order diffraction efficiencies of composite zone plates.

expected because of the broader central peak and reduced energy in the outer rings caused by apodization. Since the purpose of the outer zones is to increase the zone plate aperture, to compare the MTFs they should be plotted on the same frequency scale, which shows up the improvement in resolution as M increases.

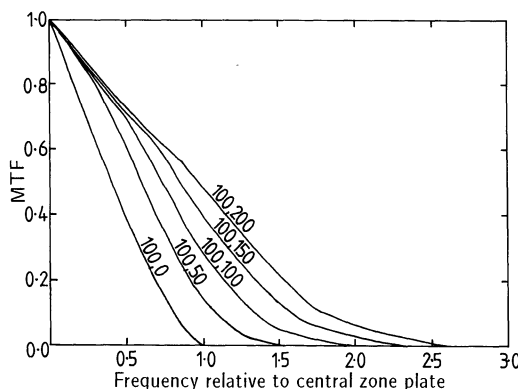


Figure 8.27. The modulation transfer functions of $(100, M)$ composite zone plates.

8.2.2.6. Higher-Order Composite Zone Plates

The idea of composite zone plates may readily be extended to include higher-order outer zones, either instead of or in addition to the third-order case already discussed. In the former case, equation (8.129) is replaced by

$$r_n^2 = n\lambda f[(2m + 1) - 2mN/n] \quad N < n \leq N + M \quad (8.144)$$

for the $(2m + 1)$ th order, $m = 1, 2, \dots$. For equal outer zone widths, the value of M is now given by

$$M_{\max} = N[(2m + 1)^2 - 1]/(2m + 1) \quad (8.145)$$

Adding higher-order zones outside the inner two parts is described by the equation, for a three-part composite zone plate,

$$\begin{aligned} r_n^2 = n\lambda f[(2l + 1) - 2(l - m)(N + M)/n - 2mN/n] \\ N + M < n \leq N + M + L \end{aligned} \quad (8.146)$$

and similarly for further added orders. The value of L for equal outer zone widths is found as before, using equation (8.145) to give M_{\max} ,

$$L_{\max} = N[(2l + 1)^2 - (2m + 1)^2]/(2l + 1) \quad (8.147)$$

For a composite zone plate consisting of first-, third-, and fifth-order zones, $M_{\max} = (8/3)N$ as before, and $L_{\max} = (16/5)N$. As shown in

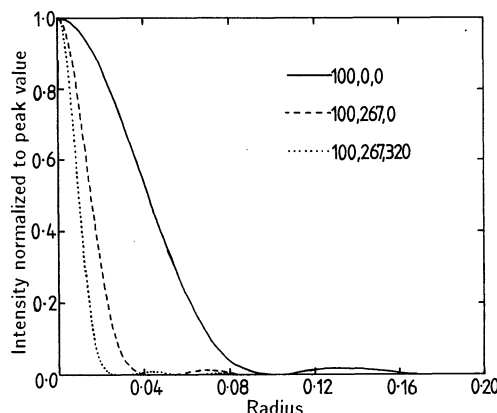


Figure 8.28. Comparison of the point spread functions of (100,267,320) and (100,267) composite zone plates with that of an $N = 100$ Fresnel zone plate.

Figure 8.28, such a zone plate further improves the resolution, but the gain is less than that obtained by the addition of the third-order zones. The background level is also further increased.

8.3. Other Types of Modified Amplitude Zone Plate

It is possible to envisage an almost infinite number of variations to the basic circular zone plate pattern. Most of these will be of limited or zero applicability in the soft X-ray region, and a few possibilities are merely listed below. Two important modifications to the basic pattern are, however, zone plates with supporting spokes and elliptical zone plates. The former of these allows freestanding zone plates to be manufactured, i.e., so that large areas of the transmitting zones are truly nonabsorbing, while the latter may arise from manufacturing errors or from a tilt with respect to the optical axis of the system.

The modifications that will not be discussed further here include

1. Linear zone plates, equivalent to cylindrical lenses^(15,16)
2. Square zone plates⁽¹⁷⁾
3. Hyperbolic zone plates⁽¹⁸⁻²⁰⁾
4. Zone plates with missing zones to emphasize certain foci⁽²¹⁾
5. Compound zone plates, which consist of two semicircular zone plates joined at their diameters⁽²²⁾

8.3.1. Zone Plates with Spokes

If a zone plate is to be freestanding with clear transmitting zones, then it must have a structure to hold the zones in the correct positions. The obvious type of structure is a set of thin radial spokes, the number and width of which are determined by the mechanical strength required. To minimize the effect on the point spread function, the spokes should be arranged in a circularly symmetric way (Figure 8.29). The reduction in intensity at a focus may be calculated from (for a normal amplitude zone plate)

$$\begin{aligned} I/I_0 &= \left(1 - \frac{\text{obstructing area of spokes}}{\text{zone plate transmitting area}}\right)^2 \\ &= \left\{1 - (2SW/\pi r_1 N) \sum_{n=1}^{N/2} [(2n)^{1/2} - (2n - 1)^{1/2}]\right\}^2 \quad (8.148) \end{aligned}$$

where I_0 is the focused intensity for no spokes, and S is the number of

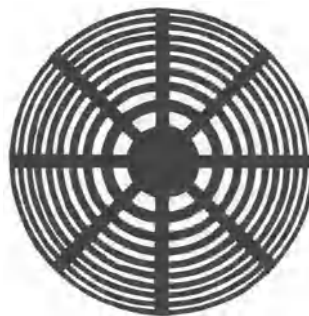


Figure 8.29. A freestanding zone plate with spokes.

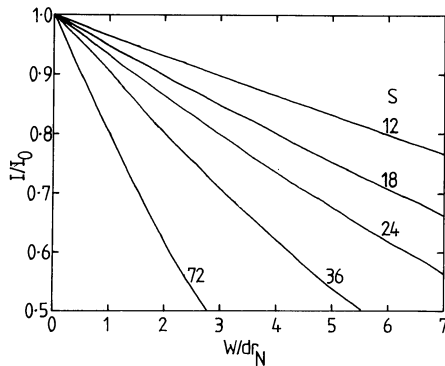


Figure 8.30. Reduction in intensity of a spoked zone plate as a function of the number of spokes and their width.

spokes of width W . Figure 8.30 shows this intensity ratio as a function of S and W for an $N = 100$ zone plate. For this particular case, the loss in intensity is only 20% for, e.g., 72 spokes each the same width as the outermost zone.

8.3.2. Elliptical Zone Plates

An elliptical zone plate consists of a series of ellipses, with constant ratio of major to minor axis, forming the zone boundaries. The semimajor axis a_n and semiminor axis b_n obey the relations

$$a_n^2 = n a_1^2 + n \lambda f_a \quad (8.149)$$

and

$$b_n^2 = n b_1^2 + n \lambda f_b \quad (8.150)$$

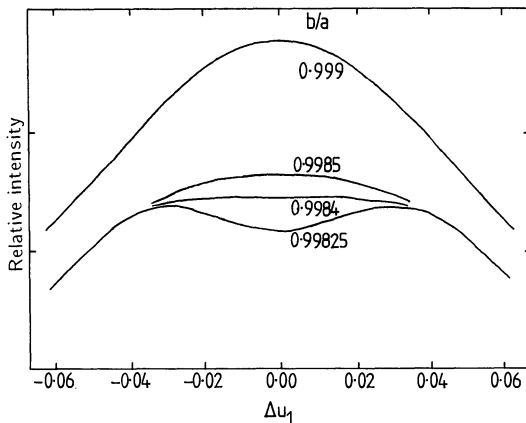


Figure 8.31. Intensity distributions around the best first-order foci of elliptical zone plates (with 20 zones).

The equation of the n th zone boundary is then

$$(x/a_1)^2 + (y/b_1)^2 = n \quad (8.151)$$

Thus an elliptical zone plate has two astigmatic foci in each order which, if the major to minor axis ratio is not too large, will lead to a best focus (peak axial intensity) between f_a and f_b . Using equation (8.42) gives the axial distributions around the primary focus shown in Figure 8.31.

8.4. Gabor Zone Plates

The contribution to the background in the first-order focus of a zone plate due to unfocused higher orders may be removed by replacing the square wave amplitude transmittance with an approximately sinusoidal one⁽²³⁾ (Figure 8.32)

$$T(r) = [1 + \sin(\pi r^2/\lambda f)]/2 \quad (8.152)$$

Referring back to Figure 8.3, the complex disturbance at the point P' for an incoming plane wave ($R = \infty$) is now given by

$$\begin{aligned} Y(P') = & -[iA \exp(ikR')/\lambda R'] \cos \gamma \\ & \times \iint T(\xi, \eta) \exp[ikL(\xi, \eta)] d\xi d\eta \end{aligned} \quad (8.153)$$

where the integral is carried out over the aperture. This integral is simple

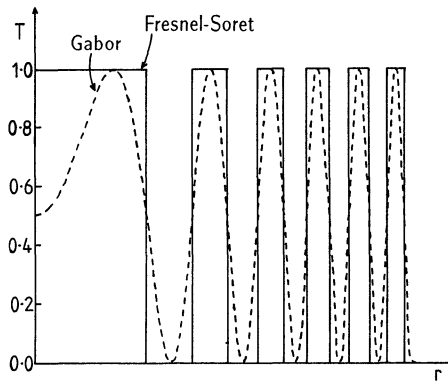


Figure 8.32. Amplitude transmission functions of Fresnel–Soret (square wave) and Gabor (sine wave) zone plates.

to evaluate for the focal point at f , when $\gamma = 0$, and $x' = 0$, $y' = 0$, $R' = f$ so that, from equation (8.27),

$$L(\xi, \eta) = (\xi^2 + \eta^2)/2f = r^2/2f \quad (8.154)$$

Thus, using cylindrical polar coordinates [equation (8.28)],

$$Y(P') = -[iA \exp(ikf)/\lambda f] \int_{\theta=0}^{2\pi} \int_{r=0}^{r_N} T(r) \exp(ikr^2/2f) r dr d\theta \quad (8.155)$$

$$= -[iA \exp(ikf)](C + iS) \quad (8.156)$$

where

$$C = (2\pi/\lambda f) \int_0^{r_N} T(r) \cos(\pi r^2/\lambda f) r dr \quad (8.157)$$

$$S = (2\pi/\lambda f) \int_0^{r_N} T(r) \sin(\pi r^2/\lambda f) r dr \quad (8.158)$$

Using $T(r)$ from equation (8.152) gives $C = 0$ and

$$S = \pi N/4 \quad (N \text{ even}) \quad (8.159)$$

$$= \pi N/4 + 1 \quad (N \text{ odd}) \quad (8.160)$$

Thus, for large N , to a good approximation

$$Y(P') = (A\pi N/4) \exp(ikf) \quad (8.161)$$

for all N , and the intensity at the focal point is

$$I = I_0 N^2 \pi^2 / 16 \quad (8.162)$$

Thus the intensity at the first-order focus is reduced by a factor $\pi^2/16$ from that for a Fresnel zone plate, i.e., the first-order efficiency is $1/16$. For other orders the same calculation may be made with $R' = f_m = f/m$. For undiffracted radiation ($m = 0$) this gives an efficiency of $1/4$; for the first virtual focus ($m = -1$) it gives $1/16$, and for all other values of m it gives zero—i.e., the higher-order foci do not exist. The remaining $5/8$ of the incoming radiation is absorbed.

Thus, although the Gabor zone plate only has one real focus, the total background (due to unfocused radiation) is relatively higher than for the corresponding Fresnel zone plate used in its first order.

8.5. Phase-Modulating Zone Plates

A better way of removing part of the background at the primary focus is to use phase-modulating zone plates in which alternate zones, instead of transmitting or absorbing the radiation, change its phase by specified amounts. In this way, at least in principle, the zeroth order can be completely removed and the focused intensities in other orders enhanced.

8.5.1. The Rayleigh–Wood Phase Reversal Zone Plate^(24,25)

The simplest type of phase-modulating zone plate (although un-realizable in practice for soft X rays) is one in which the absorbing zones are replaced by transmitting ones of optical thickness $\lambda/2$, equivalent to a phase change of π . The amplitude at P' (Figure 8.3) becomes, for an incident plane wave,

$$\begin{aligned} Y(P') = & -(2\pi i A / \lambda R') \cos \gamma \exp(ikR') \left\{ \int_0^{r_1} \exp(ikL)r dr + \dots \right. \\ & + \int_{r_{N-2}}^{r_{N-1}} \exp(ikL)r dr + \exp(i\pi) \left[\int_{r_1}^{r_2} \exp(ikL)r dr + \dots \right. \\ & \left. \left. + \int_{r_{N-1}}^{r_N} \exp(ikL)r dr \right] \right\} \end{aligned} \quad (8.163)$$

for a zone plate with an even number N of zones, and where

$L = L(\xi, \eta)$. The integration over θ in equation (8.163) has already been carried out. For axial rays, $R' \approx z'$ and $L \approx r^2/2z'$, and

$$Y(P') = -A \exp(ikz') \left\{ \left[2 \sum_{n=1}^N \exp(in\pi f/z') \right] - 1 - \exp(iN\pi f/z') \right\} \quad (8.164)$$

This amplitude is twice that of the corresponding amplitude zone plate, and thus the focused intensities are increased by a factor of four. The focal positions are, however, unchanged. In addition, there is no undiffracted radiation, as can be seen by summing the radiation diffracted to each focus ($m = \pm 1, \pm 3, \pm 5 \dots$)

$$2 \sum_{q=0}^{\infty} 4/[(2q + 1)^2 \pi^2] = 1 \quad (8.165)$$

The phase shift produced by a zone of thickness t is

$$\phi = (2\pi/\lambda)(1 - \delta)t \quad (8.166)$$

where $1 - \delta$ is the refractive index of the zone material. Thus if alternate zones are completely open ($\delta = 0$), a phase shift of π is obtained between adjacent zones if

$$t = \lambda/2\delta \quad (8.167)$$

For typical materials such as carbon and gold ($\delta \approx 0.003$ and 0.01 respectively for $\lambda = 3.5$ nm, see Table 1.7), thicknesses of $\sim 0.6 \mu\text{m}$ and $\sim 0.2 \mu\text{m}$ are required. Since no materials are absorption free in the soft X-ray region, the degree of enhancement obtained above is not possible in practice.

8.5.2. The Phase Reversal Zone Plate with Absorption⁽²⁶⁾

For the zone plates of small aperture that are used for focusing soft X rays, all pairs of adjacent zones contribute essentially equally to an image. Thus, in order to determine the properties of a phase reversal zone plate, only one pair need be considered. The first zone of the pair is left open, and the second is made of a thickness t of material that attenuates the incident amplitude by a factor $\exp(-2\pi\beta t/\lambda)$ and retards

the phase (with respect to the open zone) by

$$\Delta\phi = 2\pi\delta t/\lambda \quad (8.168)$$

where

$$\tilde{n} = 1 - \delta - i\beta \quad (8.169)$$

is the complex refractive index of the material. The amplitude from the open zone at the primary focus is

$$A_1 = iC/\pi \quad (8.170)$$

where $I_0 = C^2$ is the incident intensity on the pair of zones. The amplitude from the phase-shifting zone is

$$A_2 = -(iC/\pi) \exp(-i\Delta\phi) \exp(-2\pi\beta t/\lambda) \quad (8.171)$$

and thus the contribution from this pair of zones at the primary focus is

$$\begin{aligned} I_f &= |A_1 + A_2|^2 \\ &= (C/\pi)^2[1 + \exp(-4\pi\beta t/\lambda) - 2 \cos \Delta\phi \exp(-2\pi\beta t/\lambda)] \end{aligned} \quad (8.172)$$

which may be written in terms of

$$\eta = \beta/\delta = 2\pi t\beta/\lambda \Delta\phi \quad (8.173)$$

as

$$I_f = (C/\pi)^2[1 + \exp(-2\eta \Delta\phi) - 2 \cos \Delta\phi \exp(-\eta \Delta\phi)] \quad (8.174)$$

At the higher-order foci, the focused intensities are given by

$$I_{fm} = I_f/m^2 \quad m = \pm 1, \pm 3, \pm 5 \dots \quad (8.175)$$

The maximum focused intensity, in terms of the phase shift $\Delta\phi$, is then given by

$$\begin{aligned} \frac{\partial I_{fm}}{\partial(\Delta\phi)} &= 0 = 2(C/m\pi)^2[-\eta \exp(-2\eta \Delta\phi) \\ &\quad + (\sin \Delta\phi + \eta \cos \Delta\phi) \exp(-\eta \Delta\phi)] \end{aligned} \quad (8.176)$$

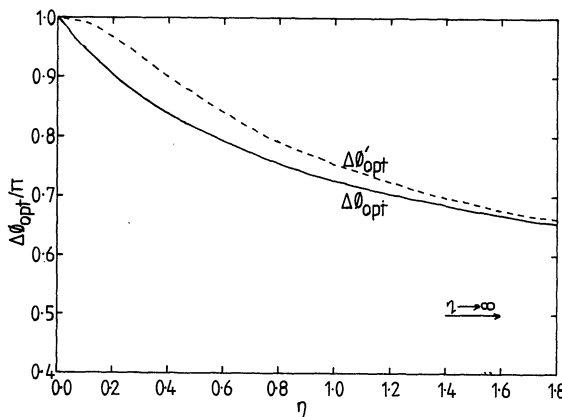


Figure 8.33. Optimum phase shifts as functions of η ($= \beta/\delta$) for phase reversal zone plates.

i.e., the optimum phase shift $\Delta\phi_{\text{opt}}$ is given by

$$\eta \exp(-\eta \Delta\phi_{\text{opt}}) = \sin \Delta\phi_{\text{opt}} + \eta \cos \Delta\phi_{\text{opt}} \quad (8.177)$$

The variation of $\Delta\phi_{\text{opt}}$ with η is shown in Figure 8.33. The two limiting cases are $\eta \rightarrow 0$ (Rayleigh–Wood phase reversal zone plate) for which $\Delta\phi_{\text{opt}} = \pi$, and $\eta \rightarrow \infty$ (Fresnel amplitude zone plate).

Since $I_0 = C^2$ is the incident intensity on the pair of zones being considered, $I_0/2$ is transmitted by the open zone and $(I_0/2) \exp(-2\eta \Delta\phi)$ is transmitted by the attenuating zone. Thus the total transmitted intensity is

$$I_t = (C^2/2)[1 + \exp(-2\eta \Delta\phi)] \quad (8.178)$$

Of this, the amount in each focus is given by equations (8.174) and (8.175). The zero-order undiffracted amplitude through the open zone is

$$A_{1u} = C/2 \quad (8.179)$$

while that through the attenuating zone is

$$A_{2u} = (C/2) \exp(-i \Delta\phi) \exp(-\eta \Delta\phi) \quad (8.180)$$

Thus the zero-order intensity is

$$\begin{aligned} I_u &= (C/2)^2 |1 + \exp(-i \Delta\phi) \exp(-\eta \Delta\phi)|^2 \\ &= (C/2)^2 [1 + \exp(-2\eta \Delta\phi) + 2 \cos \Delta\phi \exp(-\eta \Delta\phi)] \end{aligned} \quad (8.181)$$

For the optimum phase shift, $\Delta\phi_{\text{opt}}$, the intensities are

$$I_{t \text{ opt}} = (C^2/2)[2 - (1 - 1/\eta^2) \sin^2 \Delta\phi_{\text{opt}} + (1/\eta) \sin 2 \Delta\phi_{\text{opt}}] \quad (8.182)$$

$$I_{f \text{ opt}} = (C/\pi)^2(1 + 1/\eta^2) \sin^2 \Delta\phi_{\text{opt}} \quad (8.183)$$

and

$$I_{u \text{ opt}} = (C/2)^2[4 - (3 - 1/\eta^2) \sin^2 \Delta\phi_{\text{opt}} + (2/\eta) \sin 2 \Delta\phi_{\text{opt}}] \quad (8.184)$$

The fractional intensities absorbed ($I_a = 1 - I_t$), focused in the first order, and undiffracted at the optimum phase shift are shown in Figure 8.34 as functions of η . These tend, as would be expected, to the amplitude zone plate values for $\eta \rightarrow \infty$, and to the Rayleigh–Woods phase reversal zone plate for $\eta \rightarrow 0$.

Although the above analysis optimizes the intensity focused at the primary (first-order) focus, it does not optimize the imaging properties of the zone plate in terms of the signal to noise ratio at the focus. This is done by maximizing I_f/I_d where I_d is the defocused intensity, at the focus, due to all the other orders ($0, +3, +5, \dots, -1, -3, -5, \dots$),

$$I_d = F_u I_u/4 + \sum_{-1}^{\infty} F_p I_f / (2p + 1)^2 + \sum_1^{\infty} F_p I_f / (2p + 1)^2 \quad (8.185)$$

where F_u is the fraction of the unfocused radiation and F_p the fraction of the $(2p + 1)$ th-order radiation that falls within the focal spot. If the radius of the focal spot is taken to be that of the Airy disk, simple

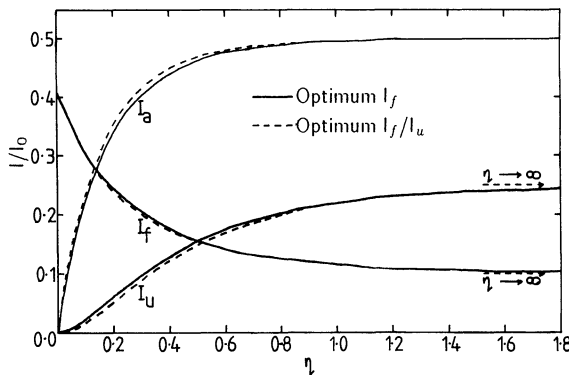


Figure 8.34. Optimum absorbed, focused (first-order), and undiffracted fractional intensities of phase reversal zone plates.

geometrical calculations show that, for a zone plate with N zones,

$$F_u = (0.61/N)^2 \quad (8.186)$$

and

$$F_p = (0.61/2Np)^2 \quad (8.187)$$

Thus

$$I_d/I_f = (0.61/2N)^2 \left\{ I_u/I_f + 2 \sum_1^{\infty} (4p^2 + 1)/[p^2(4p^2 - 1)^2] \right\} \quad (8.188)$$

and, since the summation term is a constant, maximizing I_f/I_d is the same as maximizing I_f/I_u , i.e.,

$$I_u[dI_f/d(\Delta\phi)] - I_f[dI_u/d(\Delta\phi)] = 0 \quad (8.189)$$

which gives the optimum phase shift $\Delta\phi'_{\text{opt}}$

$$\begin{aligned} (\sin \Delta\phi'_{\text{opt}} + \eta \cos \Delta\phi'_{\text{opt}}) + (\sin \Delta\phi'_{\text{opt}} - \eta \cos \Delta\phi'_{\text{opt}}) \\ \times \exp(-2\eta \Delta\phi'_{\text{opt}}) = 0 \end{aligned} \quad (8.190)$$

This is shown in Figure 8.33, and the resulting intensities I_a , I_f , and I_u in Figure 8.34; these show only a small difference from the values obtained by optimizing I_f .

8.5.3. The Gabor Phase Zone Plate

The phase-changing effect of the material of which a Gabor zone plate is made gives a distribution of phase changes

$$\Delta\phi(r) = -(1/\eta) \ln T(r) \quad (8.191)$$

with the resulting amplitude at the focus

$$\begin{aligned} Y(P') = -(2\pi i A/\lambda f) \exp(ikf) \int_0^{r_N} T(r) \exp[-i\Delta\phi(r)] \\ \times \exp(ikr^2/2f) r dr \end{aligned} \quad (8.192)$$

Evaluation of this integral shows that the focused intensity of a Gabor phase zone plate is four times that of the corresponding amplitude zone plate, i.e., 25% for the case of no absorption.

8.5.4. Optimized Zone Profiles

The above analyses have optimized the focused intensity of a zone plate without attempting to modify the basic square wave or sinusoidal structure. More of the incident intensity can be directed to the primary (or any desired) focus by designing the zone profile to cause gradual phase changes across each zone,⁽²⁷⁾ giving, for example, a structure analogous to that of a blazed linear grating. This is illustrated in Figure 8.35, where $t_i(r)$ is the thickness of the i th zone, as a function of r between r_i and r_{i+1} . This contribution to the amplitude at f from the i th zone is then

$$Y(P') = -(2\pi i A / \lambda f) \exp(ikf) \times \int_{r_i}^{r_{i+1}} T_i(r) \exp[-i \Delta \phi_i(r)] \exp(ikr^2/2f) r dr \quad (8.193)$$

where $T_i(r)$ is the amplitude transmittance and $\Delta \phi_i(r)$ the phase change associated with $t_i(r)$. In general, it is envisaged that part of each zone, of width d_i , may be made of a different material, or left open, as indicated in Figure 8.35. Tatchyn⁽²⁷⁾ shows that the optimum zone profile is, for the first zone,

$$t_1(r) = [(f^2 + r^2)^{1/2} - f]/\delta \quad 0 \leq r < [r_1 - d_1(\text{opt})] \quad (8.194)$$

$$= 0 \quad [r_1 - d_1(\text{opt})] \leq r \leq r_1 \quad (8.195)$$

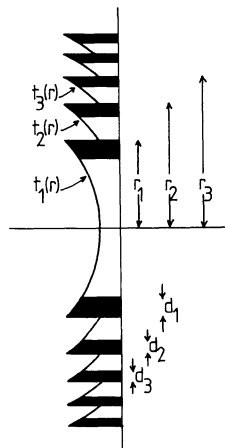


Figure 8.35. Profile of a generalized phase-modulating zone plate.

where $d_1(\text{opt})$ is found by solving the equations

$$L = r_1[(r_1/\lambda)^2 + 1]^{1/2} - r_1[(r_1/\lambda)^2 + (1 - a_1)^2]^{1/2} \quad (8.196)$$

$$\exp[-2\pi\eta(1 - L/\lambda)] = [\sin(2\pi L/\lambda + \gamma)]/\sin \gamma \quad (8.197)$$

with

$$\sin \gamma = (1 + \eta^2)^{-1/2} \quad (8.198)$$

and

$$a_1 = d_1(\text{opt})/r_1 \quad (0 \leq a_1 \leq 1) \quad (8.199)$$

The variation of a_1 with η is shown in Figure 8.36 for $r_1/\lambda = 500$ (a typical value for soft X rays). The corresponding efficiency, given by⁽²⁷⁾

$$I_f/I_0 = (1/\pi^2)(1 + 1/\eta^2)^2 \sin^4 \pi L/\lambda \quad (8.200)$$

is shown in Figure 8.37.

The generalizations of equations (8.194) and (8.195) for the i th zone are

$$t_i(r) = [(f^2 + r^2)^{1/2} - (f^2 + r_{i-1}^2)^{1/2}]/\delta \quad r_{i-1} \leq r < [r_i - d_i(\text{opt})] \quad (8.201)$$

$$= 0 \quad [r_i - d_i(\text{opt})] \leq r \leq r_i \quad (8.202)$$

The zone profiles for $\eta = 0.5$ and $\eta = 1.0$ (two examples of generalized blazed phase zone plates) are shown in Figure 8.38.

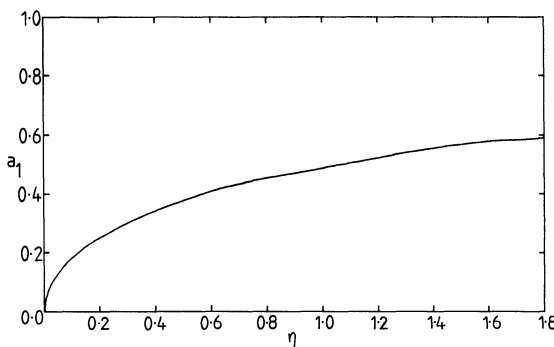


Figure 8.36. Variation, with η , of the width of the first open ring of an optimized profile phase zone plate.

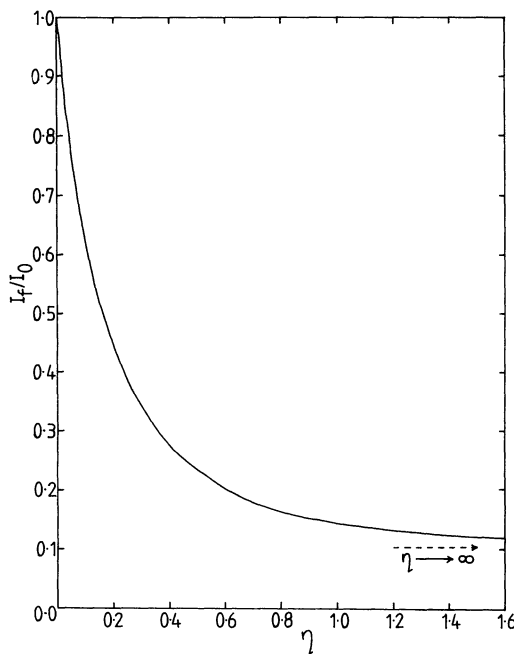


Figure 8.37. Diffraction efficiency of an optimized profile phase zone plate.

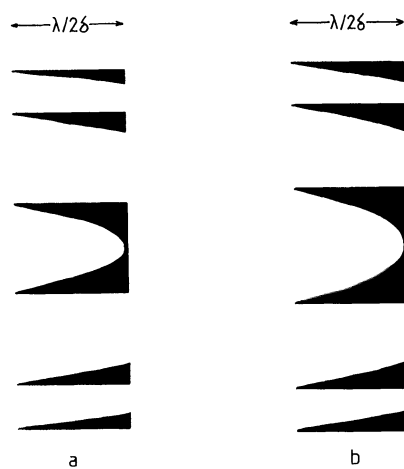


Figure 8.38. Profiles of optimized profile phase zone plates with (a) $\beta = 0.5\delta$ and (b) $\beta = \delta$.

Manufacture of Zone Plates

9.1. Manufacturing Tolerances

In the previous chapter the imaging properties of amplitude and phase zone plates were considered, on the assumption that the zone boundaries were correctly positioned. These properties will be modified for realizable zone plates, since the boundaries cannot be positioned with arbitrary accuracy. In particular, the intensity in each of the predicted foci will, in general, be decreased, the point spread functions will be changed, and further foci may be obtained. A normally less important modification may be to the positions of the foci. In addition, amplitude zone plates for soft X rays are normally made on a supporting substrate, causing the open zones to be partially absorbing, while the closed zones may not be thick enough to be totally absorbing. By placing limits on the effects of these changes, for example by stipulating that diffraction-limited imaging is required, manufacturing tolerances can be obtained. The types of manufacturing error, and the corresponding tolerances, depend on the method of making the zone plates. Some methods for manufacturing amplitude zone plates will be discussed later in this chapter, while in this section tolerances will be established. The manufacture of phase zone plates will be discussed in Chapter 11, since the optical properties of most materials in the soft X-ray region are not yet known with sufficient accuracy to enable them to be designed and made with any confidence.

Mispositioned or distorted zone boundaries will lead, on average, to zone plates that are still circularly symmetric, so that the major peaks of the diffraction patterns will remain on-axis. Thus an estimate of how closely the imaging properties of an aberrated zone plate approach the ideal may be obtained by using the Strehl ratio.⁽¹⁾ This is the ratio of the peak intensity of the aberrated point spread function (at a focus) to that of the equivalent perfect function (i.e., of a perfect zone plate). It is

generally accepted that the tolerance limit occurs when this ratio has a value of 0.8, the Strehl limit, which is equivalent to the Rayleigh $\lambda/4$ rule.⁽²⁾ Care has to be taken in calculating the Strehl limit, since altering the positions of zone boundaries also alters the zone plate focal lengths, and refocusing has to be carried out before obtaining the Strehl ratio.

9.1.1. Circular Zone Boundary Errors^(3,4)

The diffraction patterns for zone plates in which whole zone boundaries are shifted inwards or outwards may be calculated as described in Section 8.2, by integrating equation (8.30) over each modified aperture radius. It is convenient to express the zone boundary shifts in terms of fractions of the outermost zone width,

$$\varepsilon_n = |r_n - r'_n|/dr_n \quad (9.1)$$

where r_n is the correct radius and r'_n the modified radius of the n th zone. A simple case to consider is that any boundary may be left unshifted (0), be moved outwards by a fixed amount (+), or be moved inwards by the same fixed amount (-), i.e., $\varepsilon_n = \varepsilon$ and does not vary across the zone plate. If the manufacturing technique is such that alternate pairs of zones are moved in the same way, so that the boundary shifts may be expressed in pairs such as (+, -), which means that the odd-numbered zones are moved outwards by ε and the even-numbered zones inwards by ε , then four possibilities can be identified:

1. (0, 0): all zones are left unchanged, i.e., a perfect zone plate.
2. (0, +), (+, 0), (0, -), or (-, 0): every other boundary is moved outwards or inwards, resulting in the absorbing zones being too wide and the transmitting zones too narrow (or vice versa)—the zone centers are displaced.
3. (+, -) or (-, +): successive boundaries are moved in opposite directions, again resulting in zones that are too wide or too narrow, but with undisplaced zone centers.
4. (+, +) or (-, -): all boundaries are moved outwards or inwards, leading to a general Fresnel zone plate of the type described by equation (8.12).

The Strehl ratios for the first-order foci for each of these groups (for $N = 100$ zones) are shown in Figure 9.1, as functions of ε , and the amounts of refocusing necessary are shown in Figure 9.2. The Strehl limit is reached for $\varepsilon \approx 0.42$ for case (2), 0.21 for case (3), and 4 for case (4). Combinations of shifts involving more than two zones, e.g., (+, +, -) or (+, -, 0, -), give less stringent limits on ε .

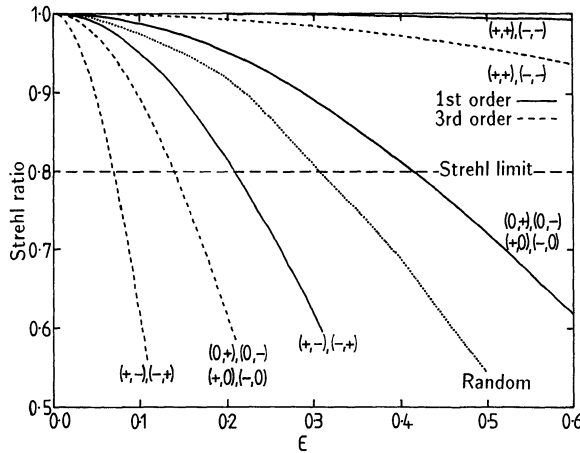


Figure 9.1. Strehl ratios for the first- and third-order foci of Fresnel zone plates with displaced zone boundaries.

A manufacturing process involving photographic development could lead to errors similar to case (3), the worst of the possibilities considered, if the recording medium is over- or underdeveloped. A more realistic evaluation of the errors involved in lithographic processes is to consider zone boundaries displaced in random directions with random values of ϵ_n . The lower limit on the displacement is also shown in Figure 9.1, giving the requirement $\epsilon \leq 0.3$. Thus a manufacturing process should be capable of placing the zone boundaries to an accuracy of within $\sim 20\text{--}30\%$ of the outermost zone width if the zone plate is to give

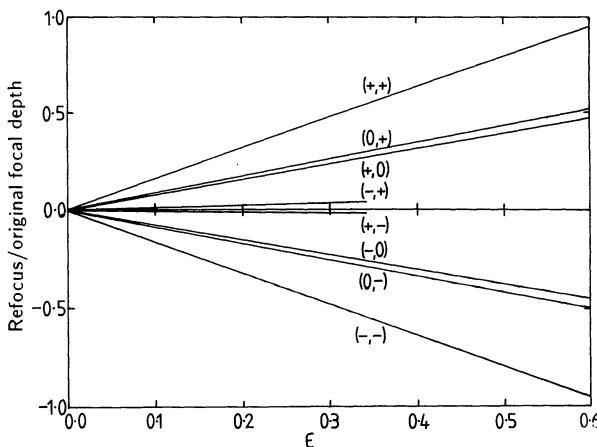


Figure 9.2. The fractional first-order focal length shifts as a result of zone boundary displacements.

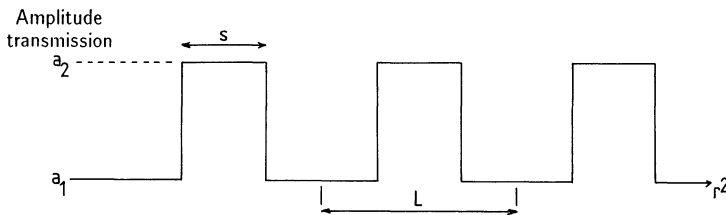


Figure 9.3. Amplitude transmission as a function of the square of the radius for Fresnel zone plates with displaced zone boundaries.

diffraction-limited imaging. The tolerances for higher-order foci are even stricter, as shown by the curves for the third order in Figure 9.1.

These types of error also cause a shift of the focused intensity from the foci of a perfect zone plate into even-order foci. The zone boundaries of a perfect zone plate are evenly distributed as a function of r^2 giving a mark to space ratio of 1:1. When the zone boundaries are mispositioned, the type of configuration shown in Figure 9.3 is obtained, and the Fourier coefficients, equation (8.69), are replaced by (with amplitude transmissions $a_1 = 0$, $a_2 = 1$)

$$c_0 = 1 - s/L \quad (9.2)$$

and

$$c_q = [\sin(\pi q s/L)]/\pi q \quad (9.3)$$

The coefficient c_q is no longer zero for even q , unless $s/L = 0.5$, which

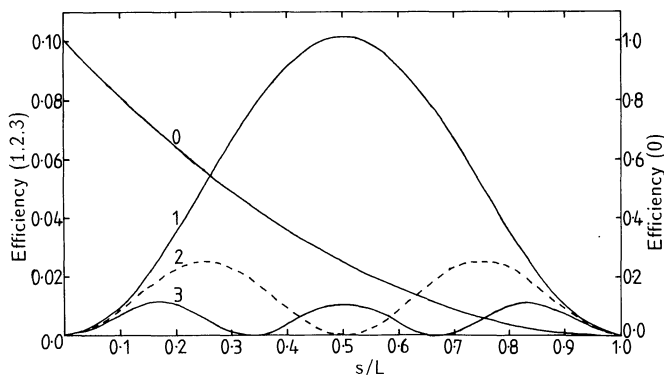


Figure 9.4. Diffraction efficiencies for a zone plate with displaced zone boundaries, showing that incorrect positioning moves energy into the even orders at the expense of, particularly, the first order.

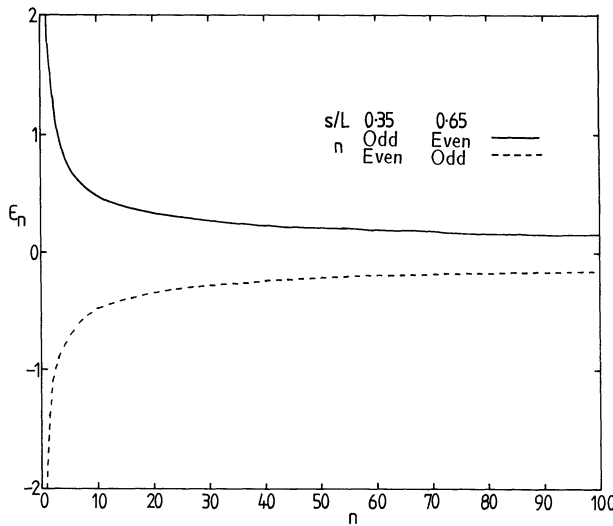


Figure 9.5. The variation of zone boundary displacement with zone number for a constant mark to space ratio in r^2 space.

corresponds to a perfect zone plate. The efficiencies, $|c_q|^2$, for the orders $q = 0, 1, 2$, and 3 are shown in Figure 9.4. This error, which has s/L constant, corresponds to ϵ_n varying radially and gives the Strehl limit, for the first-order focus, when $s/L = 0.35$ or 0.65 . The variation of ϵ_n with n , for $N = 100$, is shown in Figure 9.5.

9.1.2. Noncircular Zone Boundary Errors^(3,4)

In lithographic processes of zone plate manufacture, it is possible that the zone boundaries may be discontinuous. These discontinuities may be regular, if for example the zone plate is made as a series of sectors, or random, if for example the manufacturing system is subject to random fluctuations. In order to calculate the effects of such discontinuities, equation (8.29) has to be integrated over the angular range defined by two consecutive discontinuities. Possible configurations of the steps are shown in Figure 9.6, and the resulting Strehl ratios in Figure

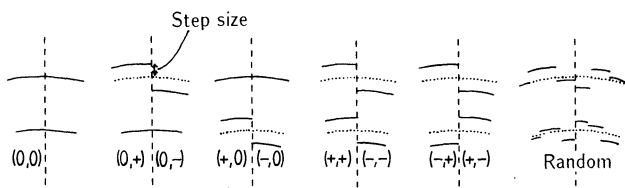


Figure 9.6. Configurations of stepped zone boundaries.

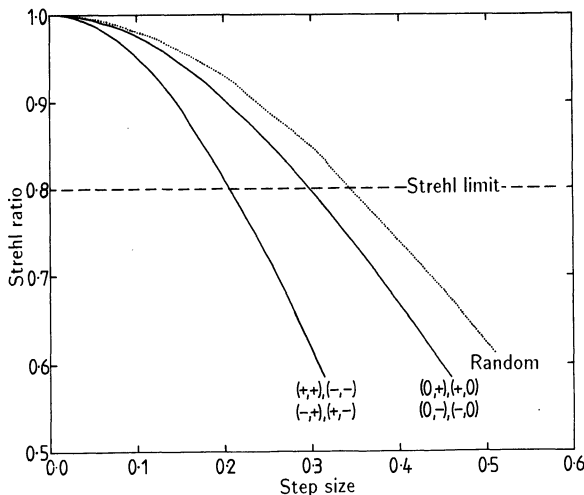


Figure 9.7. Strehl ratios for the first-order foci of Fresnel zone plates with stepped zone boundaries.

9.7. This shows that step sizes of $\sim 20\text{--}30\%$ of the outermost zone width are tolerable.

Another possible error in some lithographic processes is caused by the necessity to generate the patterns in several distinct parts (fields) that then have to be joined together (patched) using, for example, accurately positioned registration marks. Thus, although all the zone boundaries in one field may be correctly positioned with respect to one another, the fields themselves may be misaligned. The effects of such misalignments are difficult to assess in general, since the sizes and shapes of the fields need to be known. However, it should be expected that displacements similar to those obtained above, i.e., $\sim 20\text{--}30\%$ of the outermost zone width, will be tolerable.

9.1.3. Elliptical Zones

Elliptical zone plates have already been discussed (Section 8.3.2). They may be obtained as a result of manufacturing error if, for example, the recording medium is tilted with respect to its correct position. The Strehl ratio as a function of the semiminor to semimajor axis ratio is shown in Figure 9.8. The Strehl limit is reached for this ratio equal to 0.9964, corresponding to a tilt of 85 mrad (slightly less than 5°).

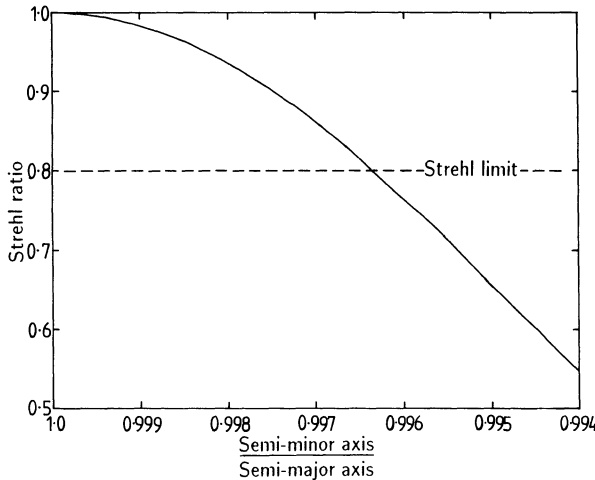


Figure 9.8. Strehl ratios for the first-order foci of elliptical zone plates as a function of the semiminor to semimajor axis ratio.

9.1.4. Zone Thickness and Substrate Effects

In general, for stability, zone plates for use with soft X rays will not be freestanding, but will be manufactured on substrates that absorb some of the incident radiation so that the transmitting zones are not completely open. Also, since it is not possible to manufacture zones of arbitrary thickness, the absorbing zones will, in general, be partially transmitting. This situation is shown in Figure 9.3, when $0 < a_1 < a_2 < 1$. Ignoring phase effects, the Fourier coefficients become

$$c_0 = a_1 s/L + a_2 (1 - s/L) \quad (9.4)$$

$$c_q = (a_2 - a_1)[\sin(\pi q s/L)]/\pi q \quad (9.5)$$

The amplitude transmission for a thickness t of material is

$$a = \exp(-\alpha t/2) \quad (9.6)$$

where α is the linear absorption coefficient [equation (1.4)]. Comparing equations (9.3) and (9.5), the energy diffracted into the q th order is a fraction $(a_2 - a_1)^2$ that for $a_2 = 1$, $a_1 = 0$. For $s/L = 0.5$ (i.e., perfectly positioned zones), and zone plates made of a combination of gold and carbon, the efficiencies as functions of thickness are shown in Figure 9.9 for X-ray energies of 300 and 600 eV. Clearly freestanding gold zone

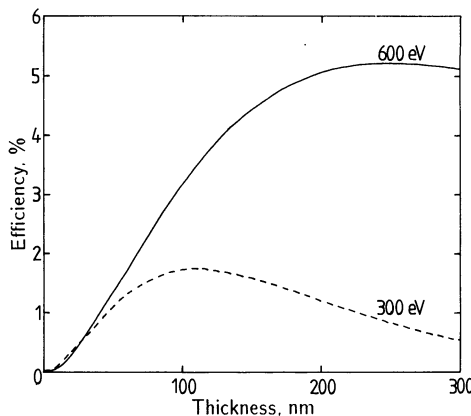


Figure 9.9. Diffraction efficiencies as functions of thickness for Fresnel zone plates with correctly positioned zones of, alternately, gold and carbon.

plates perform better than the other possibilities considered, but for certain thicknesses and wavelengths reasonable efficiencies can be obtained from the other configurations.

9.2. Manufacturing Techniques

Because of the small sizes of zone plates for soft X rays, the methods of manufacturing them are restricted to, mainly, two types: electron-beam lithography and optical (or ultraviolet) interferometry. Examples of these will be discussed in this section, as will a few methods that do not fall into these groups. Zone plates of two typical sizes have been made, with resolutions $\sim 1 \mu\text{m}$ or $\leq 100 \text{ nm}$. The former have been used in coded aperture imaging of fusing plasmas, in X-ray astronomy, as condenser lenses in X-ray microscopy, and in alignment systems for X-ray lithography, while the latter have been used as condenser and objective lenses in X-ray microscopy.

9.2.1. Electron-Beam Lithography

Many of the techniques used for fabricating microelectronic circuits⁽⁵⁾ can be applied to the manufacture of zone plates. However, the detailed requirements are somewhat different. Zone plate patterns are less complicated than microcircuit patterns and, usually, cover much smaller areas, while the accuracy requirements for zone plates are much stricter and, for the highest-resolution optics required, the minimum

linewidths are at least an order of magnitude less than currently employed in microcircuits.

Several methods of manufacturing zone plates using scanning electron-beam lithography (EBL) have been reported. These mostly involve using the electron beam to generate a master pattern in an electron-sensitive material (resist) that is subsequently copied, by various methods, into a more suitable material for absorption of X rays. Methods of directly writing zone plate patterns into materials suitable for use at certain wavelengths also exist.

Although individual EBL systems differ in detail, they all have the same basic components shown schematically in Figure 9.10. In systems that use EBL to directly write zone plate patterns, it is possible to view the pattern during the exposure by detecting the transmitted electrons. Resists are too thick to allow this, making it more difficult to control the tolerances.

The main difference between the resist exposure systems is the method used to replicate the zone plate pattern. These methods include using X rays (X-ray lithography), etching with liquids or with plasmas and ion beams through deposition followed by lift-off, plating processes, or combinations of these. Apart from this, these EBL methods of making zone plates are basically the same and so only one will be described—this

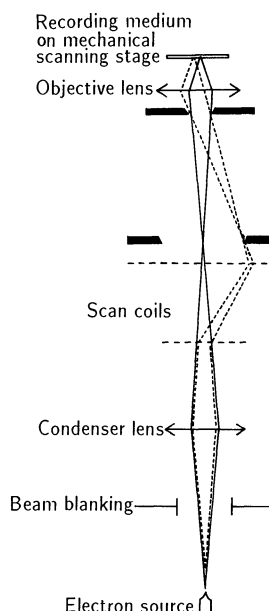


Figure 9.10. Schematic of an electron-beam lithography system.

has been selected out of the many methods reported⁽⁶⁻⁸⁾ since it is the easiest to compare with the direct writing techniques to be described later.

The method⁽⁹⁾ uses a high-resolution 100 keV EBL system based on a modified scanning transmission electron microscope (STEM). The electron source is a tungsten field emission tip that gives a brightness of higher than $10^{12} \text{ A m}^{-2} \text{ sr}^{-1}$ at an accelerating voltage of 100 kV, and a focused spot size of 1.16 nm. The maximum scan size (i.e., the maximum area over which accurate patterns can be drawn in one step) is $250 \times 250 \mu\text{m}$. Focusing and astigmatism correction are carried out by brightfield (transmitted electrons) and darkfield (scattered electrons) detectors consisting of combinations of scintillators and photomultipliers, using a transparent part of the recording substrate. The generation of the zone plate pattern is carried out using a microprocessor interfaced to a host computer, and the electron exposure at each area of the pattern is controlled by a programmable clock in the pattern generator. Field emission tips exhibit a decrease in emitted current with time, corresponding to about $1\% \text{ min}^{-1}$ in this case. This can be rectified by cleaning the tip by applying a large reverse voltage, but in the meantime it is corrected for by maintaining a constant exposure via analog feedback to the clock frequency.

The zone plate patterns are drawn on 120-nm-thick silicon nitride (Si_3N_4) membranes coated with between 150 nm and $0.8 \mu\text{m}$ of resist. The resist used is a mixture of polymethylmethacrylate (PMMA), the highest resolution resist known, and methylmethacrylate (MMA), incorporated to increase the sensitivity (at the expense of resolution). This is a positive resist, i.e., the electrons break up the long polymer molecules so that they dissolve more quickly in a solvent. The outermost zone widths vary from 50 nm for the thinnest resist layer to 200 nm for the thickest (aspect ratios of 3–4:1). Patterns are generated using a raster scan as shown in Figure 9.11, the step size being 6 nm. Each line shown in the figure is defined by three parameters y , x_1 , and x_2 , with

$$x_1 = \pm(r_m^2 - y^2)^{1/2}, \quad x_2 = \pm(r_{m+1}^2 - y^2)^{1/2} \quad (9.7)$$

or

$$x'_1 = -(r_{m+1}^2 - y'^2)^{1/2}, \quad x'_2 = +(r_{m+1}^2 - y'^2)^{1/2} \quad (9.8)$$

the zone radii being given by equation (8.16). A zone plate with 100 zones and an outermost zone width of 200 nm has a total exposed area of $630 \mu\text{m}^2$, needing a total exposure time of about 7 min, which is short enough that distortions caused by drift of the scanning stage, fluctuations

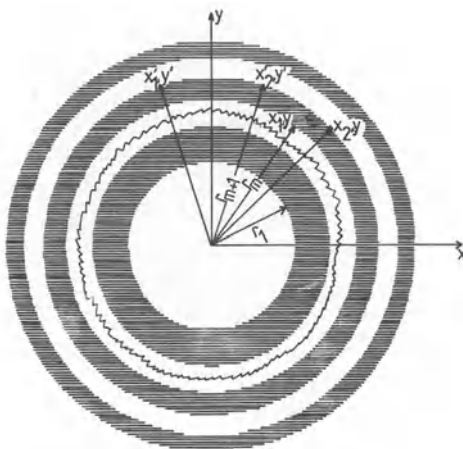


Figure 9.11. Generation of the zone plate pattern in a STEM resist exposure EBL system. (After Kratschmer *et al.*⁽⁹⁾)

in the scan coils, and so on, are negligible. The scale of possible error is therefore about 6 nm, the size of the scanning step, i.e., 12% of the outermost zone width for the finest zone plates made, falling well within the tolerances specified in Section 9.1. Elliptic distortion could, however, be introduced by nonperpendicular x and y scans.

The zone plate pattern in resist is transferred to a 50 nm-thick gold layer by ion milling, resulting in a zone plate with transmitting zones consisting of 120 nm of Si_3N_4 , and absorbing zones with the gold layer on top of the substrate. Using equation (9.5), these thicknesses give the theoretical maximum first-order diffraction efficiency (for perfectly positioned zones) as a function of X-ray energy shown in Figure 9.12.

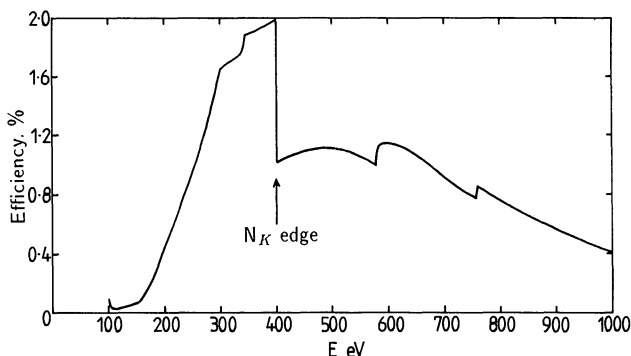


Figure 9.12. First-order diffraction efficiency of a 50-nm-thick gold zone plate on a 120-nm-thick silicon nitride support film,⁽⁹⁾ with correctly positioned zone boundaries.

The resolution of conventional EBL is limited by, among other things, scattering in the resist,^(10,11) which is important because the rate at which a solvent removes the exposed resist depends on the energy absorbed from the electron beam so that, after development, the pattern is determined by the energy distribution produced by the beam in the resist. Incident electrons enter the resist normally, or nearly so, to the surface and then undergo both elastic collisions, which change their direction, and inelastic collisions in which energy is deposited in the resist material and secondary electrons are emitted. Both these processes cause spreading of the beam. A significant number of electrons can also backscatter from the substrate into the resist since even relatively low-energy (~ 20 keV) electrons can penetrate several micrometers of resist. The likelihood of such backscattering occurring increases with the atomic weight of the substrate material. The best method of determining the effects of the scattering is to use Monte Carlo computer calculations.^(11,12) These show that for a low-energy (≤ 10 keV) beam there is a large lateral spreading of about 100 nm per 100 nm of resist thickness, while at higher energies (≥ 20 keV) this quickly reduces to about 25 nm per 100 nm of resist thickness. Thus, for high-resolution EBL, it is necessary to use high-energy beams and thin resist layers. However, these conditions increase the effects of backscatter from the substrate, leading to energy being deposited in the resist up to $\sim 1 \mu\text{m}$ from the beam position for substrates a few micrometers thick. This gives a general diffuse exposure reducing the contrast in the pattern, which can be minimized by using very thin substrates⁽¹³⁾ or by using a different type of EBL as described below.

The second electron beam method, which can be used for direct writing of zone plates, is based on a phenomenon that normally causes major problems when a STEM is used in studies of biological, and other, material. This is image degradation caused by deposition of a layer of contamination on the specimen surface. Although very high vacuums (pressure $\leq 10^{-7}$ Torr) are used, residual gas analyses of STEM column atmospheres show the presence of, among other molecules, water vapor, nitrogen, oxygen, and various heavy hydrocarbons.⁽¹⁴⁾ These hydrocarbons, from pumping oils, are the source of the contamination; they form a layer on the specimen surface and are fixed by the electron beam. Then the molecules can no longer diffuse and a buildup of the contamination occurs; leaving the beam in one position causes the formation of a "contamination cone," as shown in Figure 9.13. These cones are formed on both surfaces since many electrons pass through the specimen. Much work has been done to try to eliminate or reduce this contamination,^(15,16) while contamination lithography⁽¹⁷⁻²¹⁾ is an attempt to utilize it.

For the drawing of zone plate (or other) patterns, the specimen is

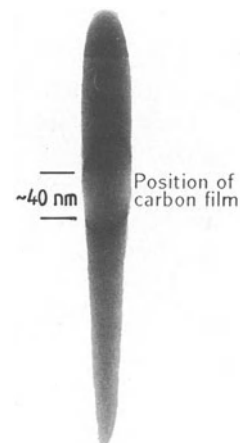


Figure 9.13. Electron micrograph of a contamination cone, rotated through 90° to show the profile.⁽²¹⁾

replaced by a thin (~10–20 nm) film of (for example) carbon or silicon nitride. The contamination process is enhanced by heating the specimen holder in which a small amount of suitable oil, arranged to increase the concentration of hydrocarbon molecules on the top side of the film only, is present. The electron beam strikes the film from below, so that electrons pass through the film and hydrocarbons diffusing into the path of the beam are fixed. As the thickness of the resulting cone increases, electron scattering increases leading to a decrease in the brightfield signal and an increase in the darkfield signal. Thus the cone can be made to a given thickness by monitoring the relative bright- and darkfield signal strengths. When the required signals are obtained, the beam is stepped on in a controlled (by microprocessor) fashion, resulting eventually in a pattern of constant thickness, irrespective of fluctuations in the field emission current.

Because of distortions caused by imperfect electron optics and scanning systems, and possibly nonperpendicular x/y scans, it is not possible using this technique to obtain the required positional accuracy over the whole area of the zone plate at once. The distortions are smallest on-axis and reduce to a simple nonorthogonality, within the required accuracy, over an axial scan of a few micrometers. The amount of error is then measurable and can be corrected for by modifying the data used to generate the pattern. Since zone plates are circularly symmetric, the zones can be accurately positioned if the distance of each part of a zone is a constant radius from an accurately defined center. By splitting the zone plate pattern into a series of narrow-angled sectors drawn radially outwards in the x direction, high-accuracy x -positioning

and corrections for nonorthogonal scanning and specimen drift are all that are needed to obtain the required accuracy. It is simple to correct for nonorthogonality over a $5\text{ }\mu\text{m}$ field, and thus each sector is divided into slightly overlapping drawing fields of this size. These fields must then be patched together very precisely, and this is done by drawing T-shaped registration marks on the left of each field. The first of these is drawn relative to a very accurately defined central circle, and subsequent ones by physically moving the film to the right and drawing the registration mark relative to the previous one. When sufficient marks have been drawn to define one sector, the film is rotated and those for the next sector drawn in the same way, until the whole circular pattern has been generated. Each field can be placed to an accuracy of 2.5 nm relative to an adjacent field, and thus the accuracy over a zone plate with radius $25\text{ }\mu\text{m}$ (requiring six overlapping fields in each sector) is about 6 nm .

If there are no errors present in their positioning, this pattern of registration marks could be used to define accurately the positions of the zones within each field. However, the registration marks could be mispositioned because of small magnification changes while drawing them. These can be caused by changes in the vertical position of the film during rotation and also by instabilities in the STEM control circuitry, and can be corrected for by intersector registration. This involves determining the position of a registration mark in one sector relative to the corresponding one in the adjacent sector by drawing an arc in each field and measuring the placement errors at the field overlaps. There is usually a component of the error constant in both magnitude and direction, and this is attributable to nonorthogonality of the x/y scans. Once measured, this component can be used to correct for the nonorthogonality. The residual errors then give the positional errors of the registration marks.

To draw a zone segment within any sector, the data for an arc representing the central radius of the zone are calculated using the zone plate equation (8.14), corrected for nonorthogonality. This arc is then drawn, relative to the relevant registration mark, a sufficient number of times at small displacements to form the zone segment, using the previously determined positional error of the registration mark as an offset. The remaining errors that can affect the zone positions are artifacts on the film, which can obscure or simulate registration marks, and magnification changes, which occur during the drawing of the zone segments. The effects of these are, however, not normally important since they apply to, at worst, a few of the fields and are not accumulative. Since it is possible to view the pattern during the drawing process (a major advantage of this technique), it is possible to correct for such errors in an *ad hoc* fashion. A drawback of the technique is that it takes

several hours to generate a zone plate pattern of, typically, $25\text{ }\mu\text{m}$ radius. Such a pattern is shown in Figure 9.14, along with examples of some of the possible errors, which are all well within the tolerance limits established in Section 9.1. Because each sector is drawn with the electron beam covering the same physical region and errors can be corrected for each sector independently, elliptic distortion does not arise. The zone plate shown has an outermost zone width of 40 nm, and the technique is capable of drawing lines as narrow as 20 nm or less.

Several indirect methods have been used to evaluate the quality of these zone plates.^(3,20) These involved using electron micrographs of the actual zone plates, and therefore could only give estimates of their

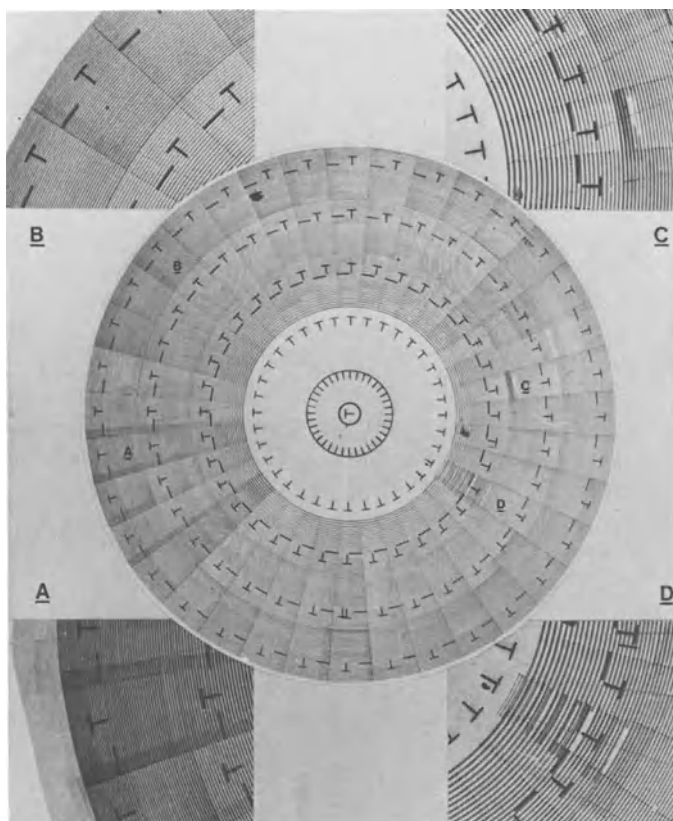


Figure 9.14. A 50- μm -diameter carbon zone plate made by contamination lithography,⁽²¹⁾ showing examples of possible errors: (A) nonorthogonality of the scans and (B) its correction, (C) variable zone thickness caused by changing brightfield detector gain, and (D) displacement of zones caused by an artifact near a registration mark. The secondary zone plate patterns are moire fringes caused by the reproduction of the figure from the original black and white photograph.

quality. Techniques used include study of the point spread functions of the micrographs (using HeNe laser light) and moire fringe measurements—two slightly displaced perfect zone plates give straight line fringes, and any departures from linearity are caused by errors in the zone boundary positions or shapes. These tests can only be qualitative, but allow the best zone plate of a batch to be chosen.

Because it is possible to draw lines with large aspect ratios (Figure 9.13 shows an aspect ratio of about 5:1), the carbon contamination zone plates are directly usable for some X-ray energies. Figure 9.15 shows the first-order diffraction efficiencies as functions of X-ray energy for perfectly made zone plates with the film and zone thicknesses illustrated. Measured efficiencies of about 1% have been obtained at a wavelength of 3.2 nm. Clearly, however, for energies toward the high end of the soft X-ray range, and also just lower than the carbon K_{α} absorption edge, it would be necessary to replicate the pattern into a heavier material using, for example, X-ray lithography.⁽²²⁾

A summary of the properties of zone plates made by various EBL methods is given in Table 9.1.

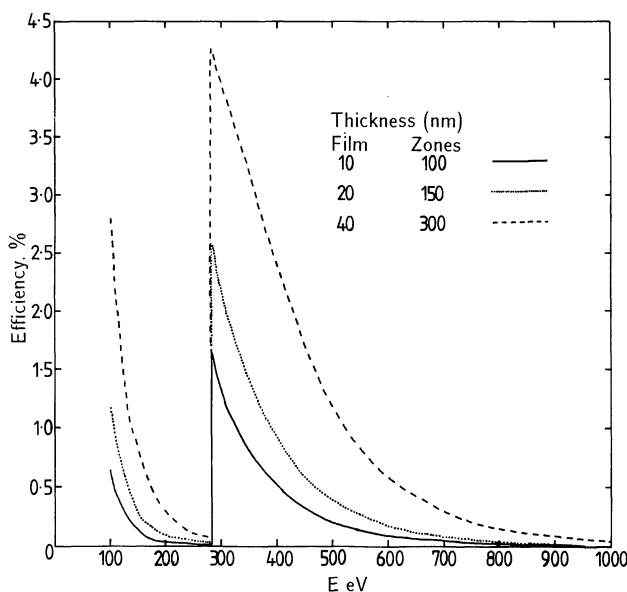


Figure 9.15. First-order diffraction efficiencies of carbon zone plates with correctly positioned zone boundaries.

Table 9.1. Some Zone Plates Made by Electron-Beam Lithography

Material/ thickness (μm)	Substrate/ thickness (μm)	No. of zones N	Radius r_N (μm)	Outermost zone width dr_N (μm)	Ref.
Gold/1.3	Free- standing			0.3	6
Gold/0.14	$\text{Si}_3\text{N}_4/0.1$	140	44.5	0.15	7
Gold/3	Free- standing	250	473	0.95	8
Gold/0.05	$\text{Si}_3\text{N}_4/0.12$	100	10	0.05	9
Gold/0.05	$\text{Si}_3\text{N}_4/0.12$	100	40	0.2	9
Carbon/0.15	Carbon/0.02	125	25	0.10	21
Carbon/0.15	Carbon/0.04	100	15	0.075	19
Carbon/0.15	Carbon/0.02	312	25	0.04	21

9.2.2. Interference Methods

Interference methods of making zone plates rely on the fact that the interference of two spherical, or one spherical and one plane, coherent wavefronts produces a zone plate pattern.^(23,24) The coherent wavefronts are produced by visible or ultraviolet lasers, and the schematic of a simple system⁽²⁴⁾ is shown in Figure 9.16. This system results in a centrally obstructed zone plate since one of the wavefronts only extends over the outer regions.

A problem with this, and any similar, setup arises since the zone plates are used at wavelengths different from that used for the construction. This results in spherical aberration, which can be corrected for by

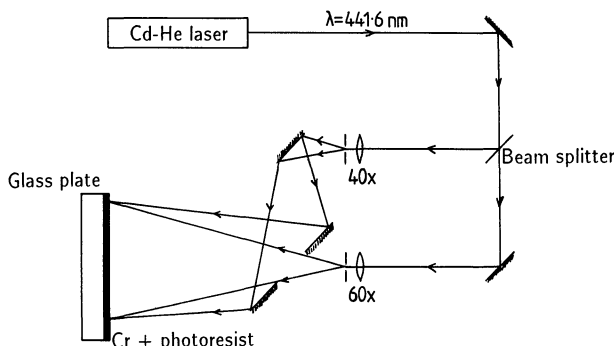


Figure 9.16. Schematic of a simple system for the manufacture of zone plates using interference. (After Dijkstra *et al.*⁽²⁴⁾)

introducing a corresponding spherical aberration into the wavefronts used for the construction. If the zone plate pattern is produced by one spherical wave and one plane wave, then the distance z_n from the effective source of the spherical wave to the zone plate pattern has to depend on the zone radius r_n via⁽²⁵⁾

$$z_n = z_1 [1 - (r_n/z_1)^2]^{1/2} \quad (9.9)$$

This aberration can be introduced to a good approximation by placing a plane parallel plate in the beam paths, as shown in Figure 9.17. Introducing the aberrations into the wavefronts makes these methods of zone plate manufacture analogous to holography. The zone plates are often referred to as holographic zone plates.

Most of the developments in interference, or holographic, manufacturing methods have been carried out by Schmahl and his colleagues at the University of Göttingen.⁽²⁶⁻²⁸⁾ They have developed systems for making two types of zone plate for use in X-ray microscopy, either with small radii ($\leq 50 \mu\text{m}$) and small numbers of zones (less than a few hundred) for use as objectives, or with larger radii (several millimeters) and large numbers of zones (usually several thousand) for use as condensers. These systems all use aberrated spherical wavefronts and the general principle used to generate these, and some specific examples, are discussed below.

The aberrated wavefronts are produced using aplanatic lens systems, which are constructed as indicated in Table 9.2 and Figure 9.18.⁽²⁶⁾ A spherical wavefront S converging to a point A is brought to a focus at D by the aplanatic lens system. When the radii and centers of the surfaces of the lenses are as given in Table 9.2, all the refraction takes place at the convex surfaces, the radiation passing normally through the concave surfaces. A wavefront focused at D is free of aberrations, while at positions just removed from D the wavefronts have the type of aberration

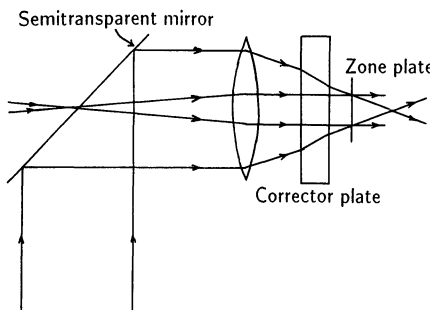


Figure 9.17. Correction of spherical aberration for holographic zone plates.

Table 9.2. Construction Scheme for a Three-Element Aplanatic Lens System^a

Lens. No.	Surface	Radius of lens surface	Coordinates of center of surface radius
1	Concave	$2r/n_g$	$r/n_g, 0$
	Convex	r	$0, 0$
2	Concave	$2rn_g$	$rn_g, 0$
	Convex	rn_g^2	$0, 0$
3	Concave	$2rn_g^3$	$rn_g^3, 0$
	Convex	rn_g^4	$0, 0$

^aSystems with larger numbers of lenses are obtained by continued application of the factor n_g , the refractive index of the lens material (measured with respect to air).

necessary for zone plate construction. Thus the zone plate interference structure is recorded in a plane near to the point D .

The outermost zone width of a zone plate made by these methods is⁽²⁶⁾

$$dr_N = \lambda_G / 4 \sin \alpha \quad (9.10)$$

where λ_G is the wavelength used to generate the zone plate pattern and α is the angle the outermost ray of the incoming spherical wave makes with the axis after passing through the lens system (Figure 9.18). Thus, for small dr_N , short wavelengths and highly convergent beams should be used. In practice, α is limited to be less than about 60° .

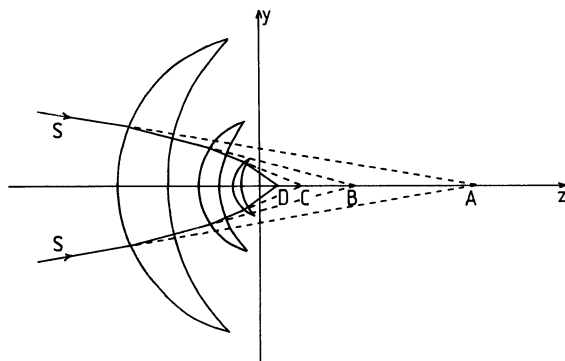


Figure 9.18. Production of aberrated wavefronts using an aplanatic lens system. (After Schmahl *et al.*⁽²⁶⁾)

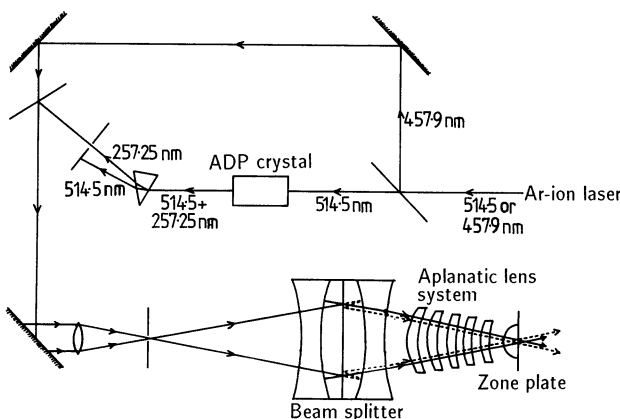


Figure 9.19. Realization of a holographic zone plate recording system using aplanatic lenses. (After Schmahl *et al.*⁽²⁶⁾)

A system that has been used to generate objective zone plate patterns is shown in Figure 9.19. An argon ion laser was used, the 457.9 nm radiation being used for optical alignment and the 514.5 nm radiation being frequency doubled to give a zone plate generating wavelength of 257.25 nm. The beam splitter resulted in two convergent spherical wavefronts, which then passed into the aplanatic lens system. Three aplanatic systems have been used—three-element, five-element, and six-element (as shown). In the latter two cases the zone plates were recorded in layers of photoresist parallel to the plane surface of the last lens with glycerol (refractive index = 1.5037) in between. This gave an effective generating wavelength of 171.1 nm so that outermost zone widths of ~ 50 nm (with $\alpha = 60^\circ$) were possible.

The larger condenser zone plates were manufactured in two ways, for two different types of microscope, imaging and scanning (see Chapter 10). Because of the different optical arrangements, the requirements for the condenser zone plate in a scanning microscope are less stringent than those for an imaging microscope, since in the latter the numerical apertures of the condenser and objective zone plates must be equal, which is equivalent to their outermost zones being of equal width. This is not necessary in a scanning microscope. An aplanatic lens system used to construct condenser zone plates for a scanning microscope is shown in Figure 9.20.⁽²⁸⁾ Two zone plates have been made with this system, the first requiring only the first two of the lenses after the beam splitter system, and the second all three.

In order to manufacture the condenser zone plates for imaging microscopy, more complicated procedures involving the generation of a

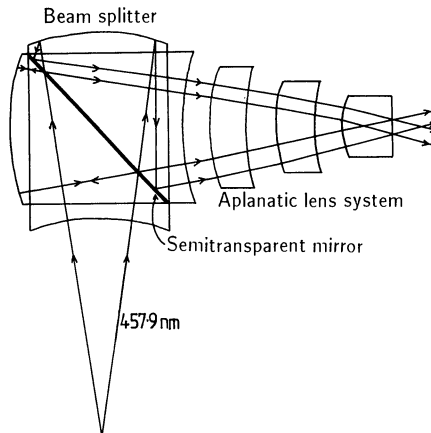


Figure 9.20. An aplanatic lens system used for generating patterns for condenser zone plates for scanning X-ray microscopy. (After Thieme.⁽²⁸⁾)

hologram followed by the use of this to generate the zone plate pattern are necessary.⁽²⁶⁾ One way of doing this, which results in a centrally obstructed zone plate, is illustrated in Figure 9.21. The hologram is generated in photoresist on a spherical surface using laser light of wavelength 457.9 nm and subsequently illuminated using 257.25 nm radiation. This generates two spherical wavefronts, from the zero and first diffracted orders of the hologram, which form the zone plate pattern.

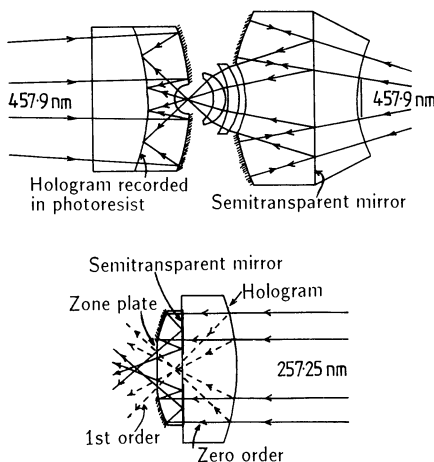


Figure 9.21. Two-stage process necessary for generating the patterns for condenser zone plates for imaging X-ray microscopy. (After Schmahl *et al.*⁽²⁶⁾)

Table 9.3. Zone Plates Made by Interference Methods

Material/ thickness (μm)	Substrate/ thickness (μm)	No. of zones N	Radius r_N (μm)	Outermost zone width dr_N (μm)	Ref.
Nickel	Freestanding	1,600	6250	2	24
Gold/0.04	Polyimide/0.1	845	500	0.3	26
Gold/0.04	Polyimide/0.1	625	150	0.12	26
Gold/0.04	Polyimide/0.1	100	11.6	0.058	26
Gold/0.04	Polyimide/0.1	251	27.8	0.055	26
Gold/0.04	Polyimide/0.1	630	1250	0.99	28
Gold/0.04	Polyimide/0.1	1,196	1250	0.52	28
Gold/0.04	Polyimide/0.1	2,600	2500	0.48	26
Gold/0.04	Polyimide/0.1	4,700	3000	0.32	26
Gold/0.04	Polyimide/0.1	15,000	4500	0.15	26
Gold/0.04	Polyimide/0.1	38,000	4500	0.06	26

The zone plate patterns were recorded in photoresist layers on a substrate of a glass plate, a polyimide layer, and a gold layer. After exposure and photoresist development, the gold was ion etched and the glass plate removed by etching with hydrofluoric acid, after attaching a support ring. This left gold zones, ~ 40 nm thick, on thin (~ 100 nm) polyimide foils. Properties of such zone plates are shown in Table 9.3 and the first-order focusing efficiencies (if perfectly made) over the soft X-ray region in Figure 9.22. The main source of error in this manufacturing method was probably over- or underexposure or development of the photoresist, leading to alternate zones being too wide and too narrow.

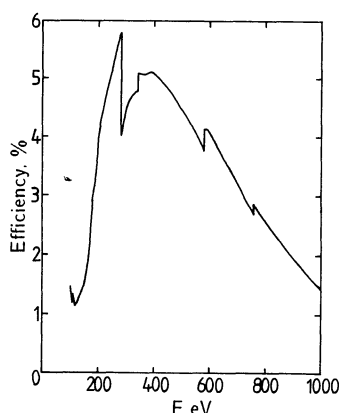


Figure 9.22. First-order diffraction efficiencies of holographic zone plates, consisting of 40-nm-thick gold zones on 100-nm-thick polyimide films, assuming correctly positioned zone boundaries.

This is the worst of the zone boundary placement errors (Section 9.1.1) and is almost certainly present in these zone plates since they were observed to have second-order foci.⁽²⁶⁾

9.2.3. Other Methods of Making Zone Plates

Several other possible methods of manufacturing zone plates have been reported. Some of these have not yet produced usable components and will be discussed in Chapter 11.

One type of technique is the reduction by electron-optical systems of accurately made large master patterns.⁽²⁹⁻³¹⁾ In these methods, large zone plates are either obtained from a commercial source⁽²⁹⁾ or engraved onto plastic plates.⁽³⁰⁾ In the latter case, a reduced photograph was made in a layer of (negative) photoresist on a glass plate covered with a thin (~300 nm) copper layer. After developing and etching, this left a copper on glass copy of the original master, which was then imaged to the required size using an electron-optical instrument consisting of, typically, an electron source with electrostatic acceleration, a magnetic lens, and quadrupole correction lenses. This gave a greatly reduced copy in a layer of photoresist on a silver-coated glass plate. After development of the photoresist the structure was copper plated and the exposed photoresist removed by vacuum heating. The zone plate was then removed from the glass by selective etching, leading to a freestanding copper zone plate. Properties of zone plates made in this way are shown in Table 9.4. This technique is limited to an outermost zone width of about 2 μm , and suffers from the same problems of over- or underexposure and development discussed above for interference methods.

Zone plates have also been made by 1:1 copying of master patterns, made either by EBL or holographically. The replication may be done using, for example, reactive sputter etching,⁽³²⁾ silicone rubber copies,⁽³³⁾ or X-ray lithography.⁽³⁴⁾ These methods have the advantage that many copies can be made of one original, although the performances of the resulting zone plates clearly depend on the quality of the original. It is

Table 9.4. Zone Plates Made by Reduction of a Master

Material/ thickness (μm)	Substrate/ thickness (μm)	No. of zones N	Radius r_N (μm)	Outermost zone width dr_N (μm)	Ref.
Copper/0.5	Freestanding	38	129	1.7	29
Copper/0.3	Freestanding	100	1550	7.75	30
Copper/0.3	Freestanding	100	1100	5.5	30
Copper/0.3	Freestanding	100	450	2.25	30

possible, however, to improve on the performance of the master by, for example, adjusting the bar to space ratio or the thickness of the zones, or by using better materials for the zone structure.

9.3. Stability of Zone Plates

The conditions of high irradiation under which zone plates may be used could lead to variation of the imaging properties with time. The most significant of these are likely to be degradation of the focused intensities caused by contamination deposits on the zones and substrates, and variations of the focal lengths caused by thermal expansion. The first of these has, up to now, not caused any problems⁽³⁵⁾ and is unlikely to in the future so long as some care is taken over the conditions of use. Thermal expansion is calculable, as below, and could conceivably cause problems. The zone plate will heat up due to the absorption of the soft X-ray energy, and thus the focal length will change by an amount Δf given by (for first-order imaging)

$$\Delta f = [\Delta(r_N^2)]/N\lambda \quad (9.11)$$

where $\Delta(r_N^2)$ is proportional to the change in area,

$$\Delta(r_N^2) = r_N^2\alpha\Delta T \quad (9.12)$$

α is the coefficient of area expansion, and ΔT is the temperature rise. In order to maintain the focal position, Δf should be less than the depth of focus, equation (8.12), so that

$$r_N^2\alpha\Delta T/N\lambda < f/2N = r_N^2/2N^2\lambda \quad (9.13)$$

i.e.,

$$\Delta T < 1/2N\alpha \quad (9.14)$$

Assuming that the zone plate is thermally isolated, this may be rewritten in terms of the energy E absorbed by the zone plate, the specific heat C of the material, and the zone plate mass M ,

$$E < MC/2N\alpha \quad (9.15)$$

For a 50-μm-diameter freestanding gold zone plate with 100 zones each 40 nm thick, this gives, using the accepted values of the specific heat and

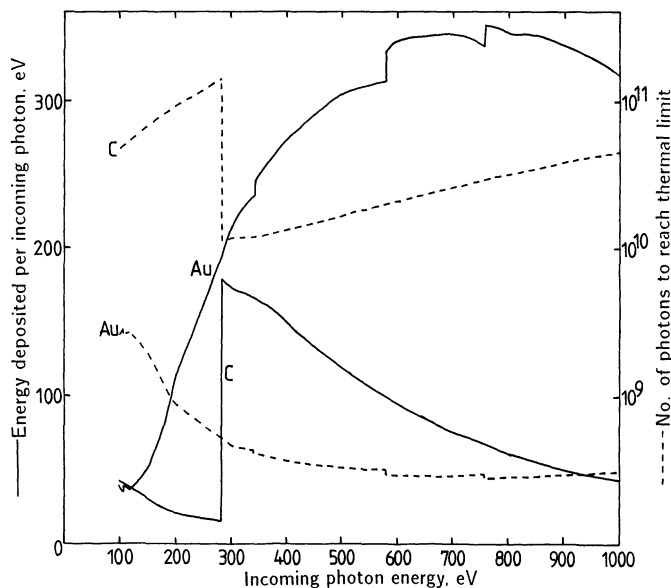


Figure 9.23. The energy deposited per incident photon and the number of photons needed to reach the thermal limit for a carbon zone plate (100-nm-thick zones on a 40-nm-thick substrate) and a freestanding gold zone plate (40-nm-thick zones), each with 100 zones and a radius of 25 μm .

the expansion coefficient,⁽³⁶⁾ $E \leq 10^{10}\text{--}10^{11}$ eV. For a similar carbon zone plate with 100-nm-thick zones on a 40 nm-thick substrate, $E \leq 10^{12}\text{--}10^{13}$ eV. The energy deposited per incident photon, and the corresponding numbers of photons needed to reach these limits, are shown as functions of incident photon energy in Figure 9.23. The total amounts of energy involved are very small and should easily be removed if the zone plate is in thermal contact with a larger piece of material, even if all the energy is deposited in 1 sec (which is conceivable at future synchrotron-based sources).

Applications of Soft X-Ray Focusing Systems

10.1. Introduction

Early X-ray imaging systems tended to use high-energy X rays, because of their greater penetrating power and the relative ease of production of useful fluxes. The advent of powerful sources and efficient detectors of soft X rays gave the impetus for designing and producing high-resolution optical systems and now the uses of these are many and varied. As improved optics become available it is to be expected that the range of applications will widen. In this chapter, current uses of soft X-ray optical systems will be discussed. It should be emphasized that this will not include, except in passing, uses of soft X rays that do not involve their focusing. Notable among these are lithography and contact microradiography (or microscopy).

10.2. Synchrotron Radiation Beam Lines and Monochromators

A large proportion of experiments using soft X rays are now carried out with synchrotron radiation, and thus a significant use of soft X-ray optical components is in beam lines and monochromators. Although, in principle, these are separate systems, in practice they must be considered together since the beam line optics should be designed to match^(1,2) the acceptance of the monochromator to the source emittances ε_x and ε_y , respectively in and perpendicular to the plane of the electron orbit. The emittance is defined as the product of the source size and its angular divergence, and is determined by the design and operating conditions of

the synchrotron. To obtain the maximum photon flux, the beam line should accept all of the vertical spread of radiation and as large a horizontal sweep as possible. It is common to have several beam lines, split by grazing incidence mirrors, from each beam port (see Section 1.3.1.1) and ϵ_x is limited by apertures in the storage ring or in the part of the beam line closest to the storage ring (the front end).

The overall layout of a beam line⁽³⁾ contains many components, in addition to the optical system, which will not be considered here. Although the optical system can be planned using standard optical design or ray-tracing procedures,⁽¹⁾ its construction depends on the feasibility of manufacturing the mirrors required.⁽²⁾ Two or more reflecting surfaces may be used, and it is important that high reflectivities are maintained over the entire wavelength range of interest. As discussed in Chapter 3, very flat surfaces can now be obtained on several materials so that losses of reflectivity due to roughness can be minimized. However, the performances of beam line mirrors can degrade with use for several reasons. The first mirror in a beam line is typically used to remove hard X rays and is thus subject to high heat loads and to radiation damage. If the first mirror performs any focusing, the second can be similarly affected. This causes shrinkage in the surface layers of glass mirrors,⁽⁴⁾ resulting in increased scattering and decreased reflectivity. Platinum-coated copper mirrors fitted with thermoelectric cooling devices have been used successfully⁽⁵⁾ and, more recently, water-cooled Kanigen-coated mirrors have been observed to withstand very high radiation loading⁽¹⁾ (Kanigen is a proprietary nickel coating). Silicon carbide mirrors (see Chapter 3) have also been used satisfactorily.

A second cause of performance degradation is carbon contamination of mirror surfaces,⁽⁶⁾ a similar process to that discussed in Chapter 9 for zone plate manufacture. This is related to photoelectrons emitted by the mirror, and thus increases with photon flux. Apart from ensuring that there are no sources of hydrocarbons (such as pumping oils) present in the system and that all components are very clean, the only way of reducing the contamination process is to improve the vacuum—significant partial pressures of hydrogen, carbon monoxide, and methane are present even in ultra-high-vacuum systems.⁽⁷⁾

The highest fluxes of soft X rays are obtained from undulators installed in storage rings, and thus the associated beam lines present more severe problems. Local heating and distortion are significant, because the radiation is highly collimated so that only small areas of mirrors are illuminated. For these high-power applications, water-cooled copper mirrors⁽¹⁾ or mirrors made from silicon carbide and other ceramic materials appear to be most suitable. In particular for soft X rays hafnium carbide has been suggested.⁽²⁾

A problem with the design of monochromators for synchrotron radiation arises from the continuum nature of the source. This is contamination of the spectral output with higher orders.⁽²⁾ In many cases, especially on high-energy synchrotrons, the intensity from the source in the higher orders can be greater than the incident first-order intensity. Filters can be used to reduce this problem, but the whole soft X-ray range cannot be covered satisfactorily in this way. Monochromators for synchrotron radiation should also have constant deviation over their range of use, since the source is immovable as is, in general, experimental apparatus.

10.2.1. Overlapping Range Grating Monochromator

One way of overcoming the contamination by higher orders is to use the principle of selective reflection,⁽⁶⁾ so that the grazing incidence angle is too large to reflect the higher orders while still giving reasonable efficiency in the first order. For soft X rays, this is only possible over a small part of the wavelength range, so that to give continuous coverage compound systems are necessary. The layout of such a monochromator,⁽⁹⁾ designed for the (now defunct) 5-GeV synchrotron at the Science and Engineering Council Daresbury Laboratory (U.K.), is shown in Figure 10.1. The first component, a rotatable plane blazed grating with $576 \text{ lines mm}^{-1}$, dispersed the radiation onto one of two concave mirrors, with radii of curvature 4 and 2 m. In such arrangements the condition for focus is

$$y = (R/2) \cos A_0 - x \cot 2A_0 \quad (10.1)$$

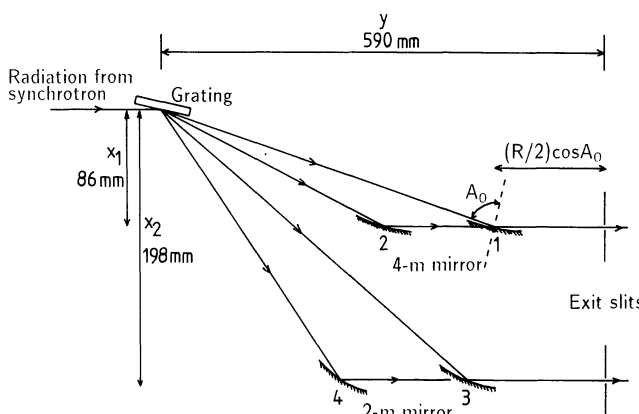


Figure 10.1. Double-slit overlapping range grating monochromator. (After West *et al.*⁽⁹⁾)

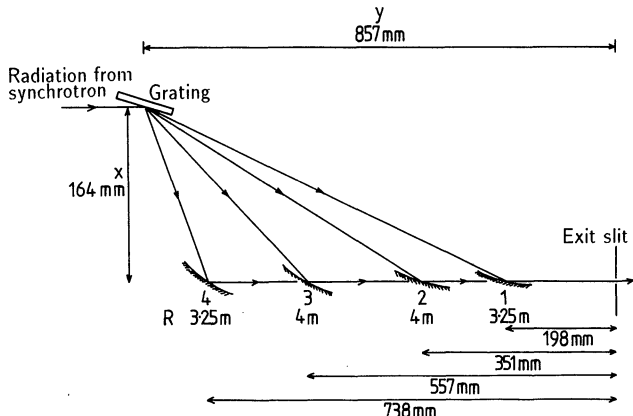


Figure 10.2. Single-slit overlapping range grating monochromator. (After Howells *et al.*⁽¹⁰⁾)

where R is the mirror radius of curvature and the angle A_0 and distances x and y are defined in Figure 10.1. For fixed values of x and y , there are then two positions of focus,⁽⁹⁾ i.e., two positions of each mirror. The monochromator had two exit slits, one for each mirror, only one of which was in use at any one time. The measured ranges of the monochromator, for which first-order radiation contributed over 95% of the output, were 4.4–7.5, 6–12, 9–22, and 14–34 nm for the mirror positions 1–4, respectively. The peak efficiency was about 5% and the resolution was about 0.02 nm, which, because the instrument worked in vertical dispersion, was limited by the vertical electron beam size in the synchrotron.

A later version of this monochromator⁽¹⁰⁾ used a laminar grating with a groove depth of 10 nm and $632 \text{ lines mm}^{-1}$, and eliminated the need for two exit slits by having interchangeable mirrors. The layout is shown in Figure 10.2, and the wavelength ranges were 6–13, 6.5–18, 9–23, and 20–50 nm for the mirror positions 1–4. In terms of resolution (0.03 nm) and efficiency (about 1%), this instrument did not perform as well as the earlier version. This was attributable to mirror imperfections.

10.2.2. The "Grasshopper" Monochromator

Spherical grating monochromators designed to work in the Rowland mounting require complicated motions and are therefore difficult to make UHV-compatible. This was, however, achieved in the "grasshopper" monochromator,⁽¹¹⁾ so called because of the appearance of the optical and scanning layout (Figure 10.3), used on the 4° beam line at the Stanford Synchrotron Radiation Laboratory (USA). The mirrors M_0 and

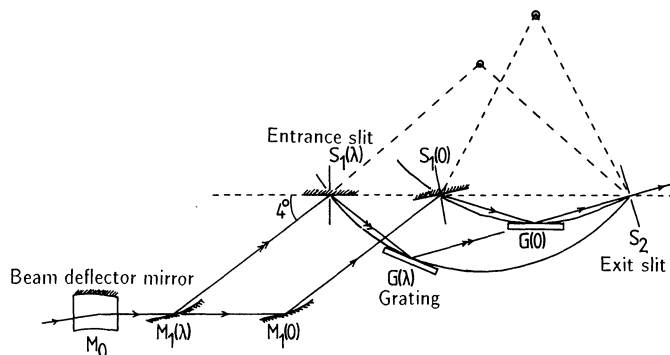


Figure 10.3. The grasshopper monochromator. (After Brown *et al.*⁽¹¹⁾)

M_1 can be considered as parts of the beam line. M_0 is a very smooth platinum-coated concave mirror, with a radius of curvature of 210 m, used to deflect the low-energy component of the X-ray beam by 4° and to collect and focus horizontally. It is maintained in UHV to minimize carbon contamination. M_1 is a platinum-coated quartz concave mirror that, as the monochromator scans, is moved parallel to the beam. In Figure 10.3, it is shown in two positions, zero order and for a wavelength λ . The monochromator is scanned using a Rowland circle geometry,⁽¹²⁾ a 1-m Rowland circle rotating about the exit slit S_2 to give constant exit beam direction. Simultaneously the grating arm S_1G pivots about the entrance slit/mirror combination S_1 , the slit mirror being a platinum-coated copper flat rotating at half the angular velocity of the grating. With a 600 lines mm^{-1} ruled replica grating and 15- μm entrance and exit slits, the monochromator gives a resolution of 0.015 nm in the range 1.5–62 nm. With a grating of 2400 lines mm^{-1} , the resolution is 0.003 nm in the range 2–50 nm with peak efficiencies varying from about 0.5 to 2.5% over this range. The main problems with this monochromator arise from higher orders in the output (about 10% at 10 nm⁽¹³⁾) and stray light levels.

Improved versions of the grasshopper monochromator have been built, incorporating refinements such as adjustable scanning arm lengths to compensate for grating radius errors, adjustable slits,⁽¹⁴⁾ and replacing M_1 by an aspheric mirror.⁽¹⁵⁾

10.2.3. Toroidal Grating Monochromators

The advantage of using a toroidal grating in a monochromator is that scanning can be achieved by rotating the grating about an axis through its pole (Figure 10.4). The toroidal grating monochromator (TGM) is thus a

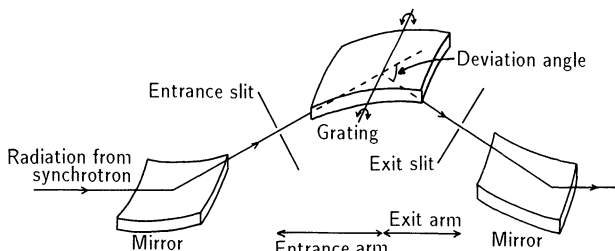


Figure 10.4. Schematic of a toroidal grating monochromator.

very simple instrument that is widely employed. However, they have poor resolution (which is not necessarily a disadvantage), and they quickly go out of focus. Better resolution can be obtained, at the expense of usable wavelength range, by designing an instrument with large dispersion. The short-wavelength limit of a TGM is primarily determined by the angular deviation, the grazing incidence angle being small for operation in the soft X-ray region to prevent absorption in the grating surface. Since toroidal gratings focus and disperse, it is only possible to optimize their performances over restricted ranges for fixed entrance and exit arm lengths. To compensate for astigmatism, the entrance and exit arms should be unequal, and the total distance between entrance and exit slits is typically several meters. Such large sizes cause TGMs to be particularly vulnerable to thermal and mechanical instabilities. The characteristics of several TGMs suitable for use over all or part of the soft X-ray region are shown in Table 10.1.⁽¹⁾ One of these,⁽¹⁶⁾ of particular interest, has been used to supply radiation to a scanning soft X-ray microscope (see Section 10.4.2.1) at the National Synchrotron Light Source (NSLS), Brookhaven (USA). This monochromator has no entrance slit, but uses the electron beam in the storage ring to define the

Table 10.1. Some Soft X-Ray Toroidal Grating Monochromators

Location	Wavelength range (nm)	Deviation angle (Figure 10.4)	Entrance arm length (m)	Exit arm length (m)	Grating lines mm ⁻¹
NBS ^a (Washington)	3–60	7°–17.8°			Variable
LURE (Orsay)	3–10	14°		4.255	
SRC (Wisconsin)	1.8–6.2	8°	2.927	7.045	800, 1200, 1800
BESSY ^a (Berlin)	1.5–5	8°	5.000	11.364	100, 1500, 1800
NSLS ^a (Brookhaven)	1.5–5	5.72°	3.024	6.061	600

^aNo entrance slit.

source. The resolution is therefore limited by the vertical size of the electron beam and has been measured to be 0.016 nm at a wavelength of 3.2 nm, i.e., at the midpoint of the range 1.5–5 nm. This resolution is about two times worse than the aberration-limited theoretical value. A 600 line mm^{-1} holographic laminar grating with grooves 12 nm deep over an area of $15 \times 50 \text{ mm}^2$ has been used. The two radii of curvature are 0.19 and 88 m and the total deviation of 5.72° is the smallest used in a TGM to date. The measured efficiency of the monochromator is about 15% at 3.2 nm. This reduces with time, due to carbon contamination, even though the TGM is housed at a base pressure of about 10^{-10} Torr. However, the grating is large enough that fresh (uncontaminated) areas can, when necessary, be exposed to the beam, so that refurbishment need only be carried out infrequently. Another problem with the operation of this TGM is the large higher-order spectral contamination in the output, about 15% at a wavelength of 3 nm.

10.2.4. Plane Grating Monochromators

Monochromators using plane gratings, like TGMs, only need a simple rotation of the grating to achieve wavelength scanning. However, since they perform no focusing, they are best suited to parallel light and thus should be preceded by a collimating mirror. Usually, however, the small vertical divergence of synchrotron radiation is utilized so that, sufficiently far from the source, parallelism may be assumed. The monochromators described in Section 10.2.1 used plane gratings but were not UHV-compatible. In this section, later types of plane grating monochromator (PGM) that are UHV-compatible will be discussed.

A typical PGM is the FLIPPER design,⁽¹⁷⁾ shown schematically in Figure 10.5. Two similar versions of this are in use at HASYLAB, at the DORIS synchrotron in Hamburg, West Germany. They use interchangeable mirrors with simple mechanical linkages to make UHV construction easier. Optimization of the monochromator output and the suppression of higher orders is achieved by choice of coatings on the six mirrors. The soft X-ray range is covered by mirrors M_1 , M_2 , and M_3 , with usable intensity at wavelengths down to 2.5 nm, although carbon on the mirror surfaces considerably reduces, in time, the flux below 4.4 nm. An ion-etched shallow blazed holographic grating is used and the paraboloidal mirror, used to focus the monochromatic radiation, is platinum-coated. The resolution is about 0.025 nm at the long-wavelength end of the soft X-ray region, and about 0.004 nm at a wavelength of 5 nm. The limit to the resolution is the 3-mm source height of the DORIS synchrotron (when operating at 3 GeV) rather than the optical components.

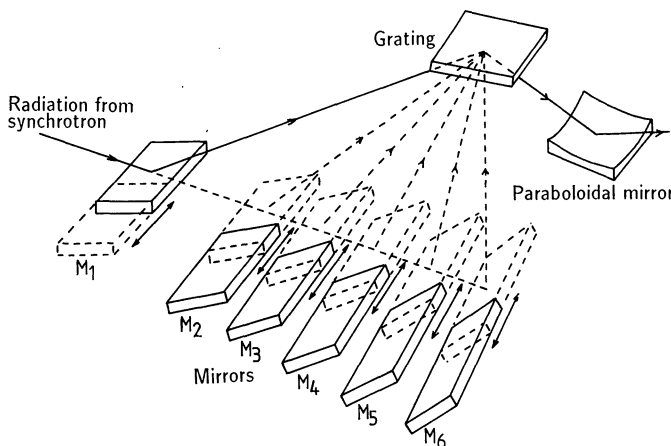


Figure 10.5. The FLIPPER plane grating monochromator.⁽¹⁷⁾

A simple design of a PGM, for use at DORIS, uses the same mirror and grating for the whole of its wavelength range of 1–250 nm,⁽¹⁸⁾ although additional gratings and mirrors could be used to extend the range. Figure 10.6 shows a schematic of the design. A premirror and a plane blazed grating, with 1200 lines mm⁻¹, rotate together to vary the wavelength. Since the mirror is not translated during the rotation, the height e of the entrance beam varies according to

$$e = D \sin \theta / \sin (\theta + 2\theta_b) \quad (10.2)$$

where θ is the grazing incidence angle on the grating with blaze angle θ_b , and D is the (constant) height of the exit beam. The predicted resolution of this monochromator is about 0.004 nm at a wavelength of 1 nm, and about 0.06 nm at a wavelength of 20 nm.

PGMs designed for storage rings with smaller source sizes can have high resolution over a large part of the soft X-ray range. Those for the NSLS at Brookhaven⁽¹⁹⁾ make use of the 0.26-mm height of the electron

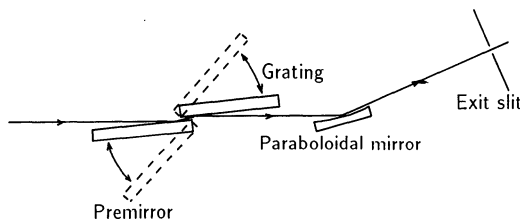


Figure 10.6. Rotating grating monochromator. (After Jark *et al.*⁽¹⁸⁾)

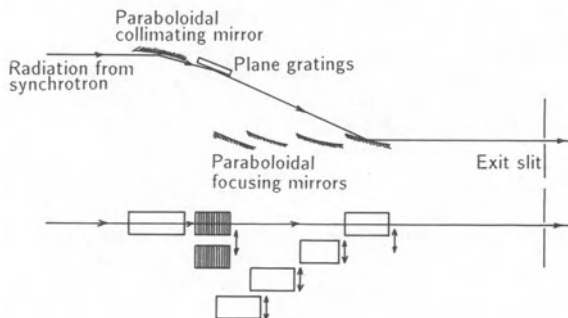


Figure 10.7. A plane grating monochromator for the NSLS VUV ring. (After Howells.⁽¹⁹⁾)

beam in the 750-MeV VUV storage ring. As shown in Figure 10.7, a paraboloidal premirror collimates the radiation onto one of two interchangeable gratings. Subsequent focusing is performed by one of four paraboloidal mirrors with different glancing angles and focal lengths, so that order sorting is obtained over four overlapping wavelength ranges. The paraboloidal mirrors must be of very high quality, and are made by diamond turning followed by light optical polishing. The alignment of the mirrors is facilitated by accurate reference surfaces machined at the diamond turning stage. The wavelength range of the instrument is 2–60 nm, and the resolution is about 0.002 nm in the soft X-ray region.

Another design utilizing a small source size is the SX-700 PGM for use at BESSY, Berlin.⁽²⁰⁾ This is shown in Figure 10.8, and has the advantages that it uses only three optical components and that it has fewer moving parts than normal for PGMs. The movements necessary are rotation of the grating and rotation and translation of the plane mirror. Using a grating of $1200 \text{ lines mm}^{-1}$, the wavelength range of the monochromator is 1.2–70 nm.

A type of PGM somewhat different from those already discussed has been proposed in which the grating is used in an extreme off-plane mounting,⁽²¹⁾ so that the incident beam is almost parallel to the grooves.

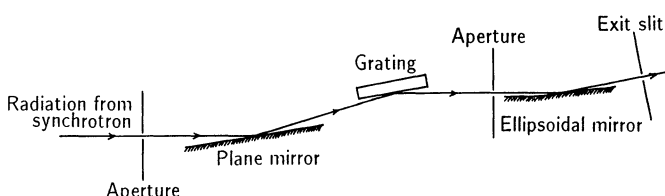


Figure 10.8. The SX-700 plane grating monochromator. (After Petersen and Baumgartel.⁽²⁰⁾)

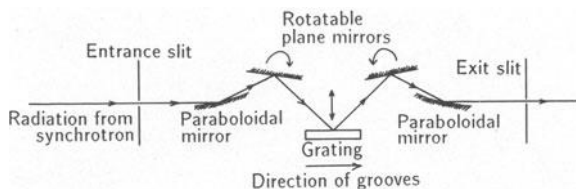


Figure 10.9. Extreme off-plane grating monochromator. (After Werner and Visser.⁽²¹⁾)

High efficiencies are possible with this arrangement, since the grating can remain on blaze at all wavelengths. Diffraction efficiencies of 70% have been achieved. The monochromator is shown in Figure 10.9 and, as can be seen, two paraboloidal and two plane mirrors are needed in addition to the grating. These ensure that the grating is kept illuminated and that the radiation incident on it is in a parallel beam. Wavelength scanning is achieved by displacing the grating normal to the grooves with simultaneous rotation of the paraboloidal mirrors. The wavelength range covered is 0.6–20 nm with a resolution of 0.013 nm for 100- μm entrance and exit slits.

10.2.5. Other Types of Monochromator

In addition to the grazing incidence reflection grating monochromators described above, the use of transmission gratings has been suggested.^(22,23) Although these are promising for the future, they have not yet been used in a practical system, and it is not clear whether they will have any significant advantages over reflection gratings.

Crystal monochromators can be used for soft X rays,⁽¹⁾ normally only over the short-wavelength part of the range where the performance of grating monochromators is degraded due to the small grazing angles that must be used. Liquid crystals in certain phases (where the long rodlike molecules constituting the crystal form layers with 3-nm spacing) can be used to cover the majority of the soft X-ray wavelength range.⁽²⁴⁾ A typical layout is shown in Figure 10.10 and the properties of some

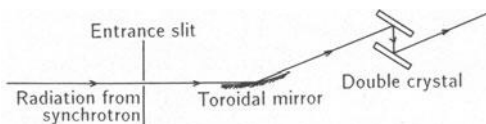


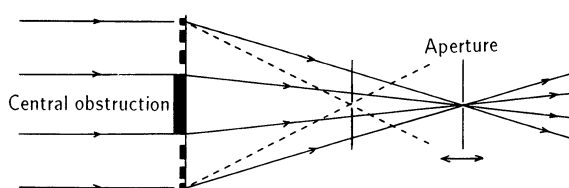
Figure 10.10. A double-crystal soft X-ray monochromator.

Table 10.2. Crystals for Soft X-Ray Monochromators

Crystal [orientation]	2d spacing (nm)	Wavelength range (nm)	Comments
Mica [002]	1.984	0.8–1.5	
Beryl [1010]	1.592	0.6–1.55	Resolution 0.0007 nm at $\lambda = 1.24$ nm
Sodium β -alumina	2.249	0.8–2.25	
Potassium acid phthalate (KAP)	2.66	0.95–2.65	Resolution 0.002 nm but susceptible to radiation damage
Liquid crystal ($C_4H_9O-C_6H_6-CHN-$ $C_6H_6-C_8H_{17}$, smectic A phase)	5.65	1.0–6.2	

suitable crystals are given in Table 10.2. Similar monochromators can be designed using multilayer mirrors, to cover large wavelength ranges, and these have the advantage that they can be formed on curved substrates and so can simultaneously focus the beam. Alternatively, multilayer mirrors on flat substrates can have laterally graded or stepped layers to allow simple wavelength scanning.

Because zone plates have wavelength-dependent focal lengths, they can be used as monochromators,²⁵ as discussed in Section 8.1.3 and shown in Figure 10.11. The central obstruction of the zone plate is to remove contamination from the zeroth order, while the aperture removes contamination from higher orders. By moving the aperture along the axis, different wavelengths are selected. The main contamination is due to higher focused orders of fractions of the selected wavelength—the third order of the wavelength $\lambda/3$ is focused at the same point as the first order of λ . The resolution of a zone plate monochromator is determined by the relative radii of the zone plate and the aperture [equation (8.65)], so that for high resolution the aperture must be small.

**Figure 10.11.** A zone plate monochromator.

10.3. Small-Angle X-Ray Scattering

Small-angle X-ray scattering or diffraction is a well-established method⁽²⁶⁾ for determining the large lattice spacings ($\sim 2\text{--}100\text{ nm}$) of complex molecules and for measuring the shapes and sizes of molecules $\leq 100\text{ nm}$ in diameter, e.g., colloidal suspensions, gels, large molecules in solution, precipitates in solid solutions and finely divided solids. The small-angle X-ray diffraction patterns of such particles are independent of the absorption coefficient and refractive index, and are characteristic only of the size, shape, and spacing of the structural units.⁽²⁷⁾ The technique requires that the beam incident on the specimen is very well defined with a small ($\leq 0.3\text{ mrad}$) angular divergence. The use of fine collimating apertures with a focusing system can lead to reductions of the exposure times by more than an order of magnitude.⁽²⁸⁾ Optical systems that have been used include crossed cylindrical mirrors⁽²⁸⁾ and toroidal mirrors.^(27,29) The former have the advantage that they can be formed by bending, allowing adjustment of the radii of curvature so that the mirrors can be used at optimum grazing incidence angles over a range of wavelengths, while the advantage of the latter is their greater collecting power. However, toroidal mirrors have fixed focal lengths and give a ring-shaped beam at the specimen.

10.4. X-Ray Microscopy

From very early in the 20th century, the possibilities have been discussed of using soft X rays to examine biological, and other, material.^(30,31) Most modern cell biology is dependent on the electron microscope, with some information coming from optical microscopy and X-ray diffraction. In principle, a soft X-ray microscope could be used to complement and supplement these types of data. Particularly in electron microscopy, specimens normally must undergo careful preparation such as drying, sectioning, and staining in order to allow images to be formed with sufficient contrast. Such preparation allows the possibility of introducing artifacts, and it would clearly be much more satisfactory to maintain specimens in, as far as possible, a natural environment, which means, in particular, not removing the water. This is not possible in conventional electron microscopy because of the stringent vacuum requirements and because the specimens would then be too thick so that the electrons would undergo multiple scattering. In comparison with optical microscopy, the shorter wavelengths of X rays allow, in principle, higher resolutions to be obtained.

As discussed in Chapter 1, the dominant attenuation process as soft

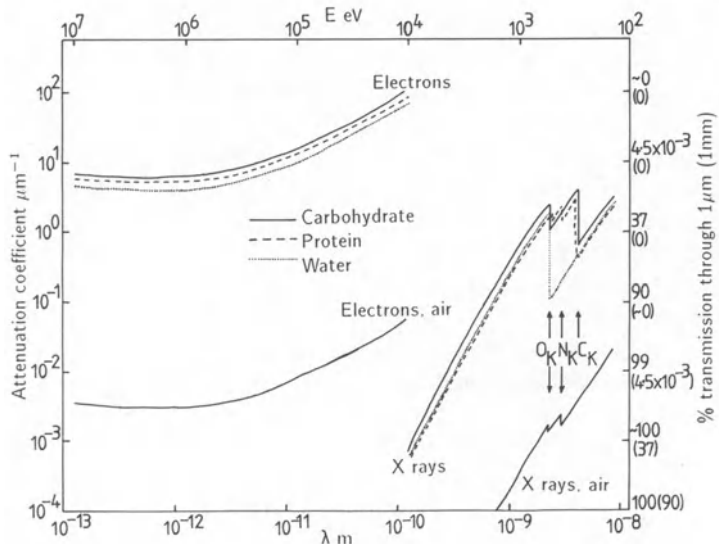


Figure 10.12. X-ray linear absorption and electron linear scattering coefficients.

X rays traverse matter is photoabsorption, with scattering cross sections being some six orders of magnitude lower. A comparison of soft X-ray linear absorption coefficients with electron scattering coefficients (Figure 10.12) shows three things. First, X rays are attenuated much less by materials than electrons are, and thus thicker (up to several micrometer) specimens can be imaged. Second, there are much larger differences from material to material for the X-ray coefficients, enabling contrast without staining. In particular, in the wavelength range 2.3–4.4 nm (between the oxygen and carbon K_{α} absorption edges), water is much less absorbing than is material containing carbon (e.g., protein, carbohydrate). Thus, in this so-called “water window,” images of specimens containing water can be obtained. Finally, there are several absorption edges in the water window wavelength range (e.g., the nitrogen K and calcium L edges) where the absorption coefficient changes by a large amount for a small wavelength difference. Subtraction of images taken on either side of such edges allows contrast enhancement and elemental analysis.⁽³²⁾ This is most likely to be useful in materials science applications since specimens need to contain several percent of an element for it to be detectable (above noise) in this way.

The concept of image formation in a soft X-ray microscope is simple. The specimen is placed between a source and a detector with, possibly, some system for focusing the X rays. The image is therefore a map of the variation in absorption coefficient across the specimen, since (usually) it

is only the transmitted X rays that are detected. In some cases, photoelectrons emitted when the X rays are absorbed can be detected,⁽³³⁾ and these give surface information (because of their short range). In the future, it may be possible to form images using fluorescence X rays. The simplest method of forming images, contact microradiography,⁽³⁴⁾ does not require focusing and so will not be discussed in detail here.

It is usually assumed that soft X-ray photons cause radiation damage by releasing photoelectrons on absorption, and thus the damage mechanism is closely related to that of low-energy electrons. It should be stressed that this has not been experimentally verified; however, assuming that this is how damage occurs, a radiation dose of 10^4 J kg^{-1} could be expected to kill a living cell while one of 10^7 J kg^{-1} would cause severe morphological damage.⁽³⁵⁾ It is possible to perform model calculations of feature resolution as a function of radiation dose and specimen thickness⁽³⁵⁾ and, although these are highly idealized, the results can be used to give an estimate of the resolution attainable before the onset of significant radiation damage. It appears that this will be around 10–20 nm. The same calculations can be carried out for electrons of the energy used in electron microscopy and the results indicate that, for an equivalent dose to a thick wet specimen, soft X rays can give resolutions an order of magnitude or more better.

The radiation damage limit to the resolution can be avoided if the image can be completed before the damage mechanism has caused any significant changes to the specimen. This requires that a very large flux of X rays is incident on the specimen in a very short time. The damage mechanism may be simply envisaged as proceeding as follows.⁽³⁶⁾ The absorption of X-ray photons, resulting in the production of ions and secondary electrons, takes place in about 10^{-17} sec . The electrons are captured by negative ions, or thermalized by further electron production, in about 10^{-13} sec . The electrons and ions cause the formation of free radicals, which persist for about 10^{-3} sec and are responsible for bond breaking and damage. The free radicals are formed in clusters within about 2 nm of the original photoabsorption event⁽³⁷⁾ and then diffuse outwards at a speed of about 2 m sec^{-1} so that they reach a diameter of 10 nm in about 2 nsec. Although, therefore, a large amount of damage takes place on nanosecond time scales, because of the persistence of the radicals the damage will only be total after about 1 msec. Thus, if sufficient X rays can be provided in less than 1 msec, the image will be formed before radiation damage is complete, and so the resolution limit can be circumvented. Laser plasma sources are capable of giving sufficient X rays in single pulses as short as 1 nsec⁽³⁸⁾ and thus allow image formation before the onset of any radiation damage, and then the resolution limit is determined by the X-ray wavelength, the optics, or the

properties of the detector. Note, however, that the specimen will not survive the radiation dose necessary to give such high resolution. At present, laser plasma sources are only suitable for contact microradiography, so that the radiation damage limit is still applicable to other forms of microscopy. In practice, to date the resolutions obtainable have been limited by the optics available to about an order of magnitude lower than this limit. In the remainder of this section, the use of microscopes with resolutions of around 100 nm will be discussed. Lower-resolution ($\sim 1 \mu\text{m}$) microscopes, used in imaging fusing plasmas, will be considered in Section 10.5.

10.4.1. Imaging X-Ray Microscopy

Apart from in contact microradiography, the highest resolutions to date, about 50 nm, have been obtained with an imaging system,⁽³⁹⁾ depicted schematically in Figure 10.13. This microscope has been operated by Schmahl and his colleagues, from the University of Göttingen, at the DESY synchrotron in Hamburg, the ACO storage ring in Paris (Orsay), and the BESSY storage ring in Berlin. The arrangement of the microscope is conventional, with a condenser and an objective each of which are zone plates (see Table 9.3). The condenser zone plate is centrally obstructed to prevent the specimen from being irradiated by the zero-order flux, and it also acts as a monochromator in conjunction with the aperture on which the specimen is mounted. Contamination of the image by higher orders of the objective zone plate (at the imaging wavelength) is prevented by the stop on its downstream side. Although this is, in principle, a very simple system, it has a major drawback due to the inefficiency of the optical components. At best, amplitude zone plates have efficiencies of about 10% in the first order, and thus only one in ten of the X-ray photons passing through the specimen contributes to the image. This clearly increases the radiation damage to the specimen. In practice, due to manufacturing inaccuracies and incomplete absorption in the absorbing zones, efficiencies are rather less than 10%, which

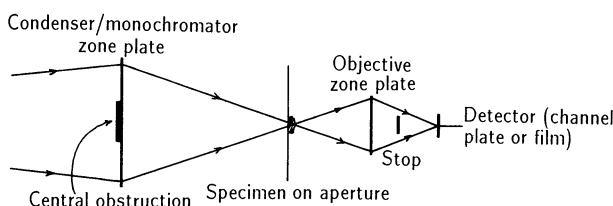


Figure 10.13. Schematic of an imaging soft X-ray microscope.

exacerbates the problem. In addition, this microscope has, to date, only been used with radiation of wavelength 4.5 nm, and thus has not utilized the water window. The resolution of ~ 50 nm was obtained, despite the use of an objective zone plate with an outermost zone width of 58 nm, because the zones were probably not of the correct widths and so there was a contribution to the image from the second order of wavelength 2.25 nm (Section 9.1.1).

An imaging microscope using a conventional X-ray tube and grazing incidence (Wolter) optics has been constructed,⁽⁴⁰⁾ but since it only has a resolution of $10\text{ }\mu\text{m}$ it is unlikely to be of significant use.

10.4.2. Scanning X-Ray Microscopy

In order to alleviate the problem of excessive irradiation of specimens due to inefficient optical components, it is necessary either to increase the efficiency or to eliminate postspecimen optics. Although the former may be possible in the future, using phase-modulating zone plates or multilayer mirrors, the latter is the method most likely to be successful in the short term. This requires the specimen to be scanned through a focused X-ray beam, at or near to the focus, so that the image is formed as a series of picture elements (pixels). A schematic diagram of such a scanning microscope is shown in Figure 10.14. Other advantages of this type of microscopy include the use of detectors, such as proportional counters, with high quantum detection efficiencies and, since the image is digital, it is in a form directly amenable to image processing. In addition, since all the pixels are imaged on the optical axis, aberrations are reduced. The major disadvantage is that the resolution depends on being able to scan the specimen in very fine steps of about half the desired

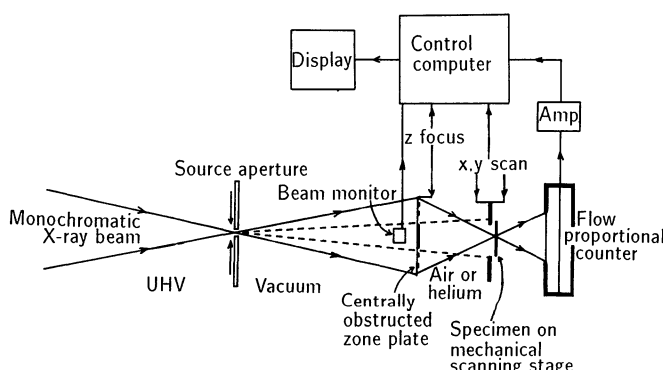


Figure 10.14. Schematic of a scanning soft X-ray microscope.

resolution. Thus it has been necessary to develop very-high-resolution two-dimensional scanning stages with repeatable, drift-free, movements. Since such development is largely mechanical, rather than optical, it is not appropriate to discuss it here. Suffice to say that repeatable steps smaller than about 50 nm, over a range of about 50 μm , have been obtained on a stage driven by piezoelectric transducers and monitored by linear variable differential transducers.⁽⁴¹⁾ Similar stages now being developed will be capable of finer movements, and other types of stage involving various types of lever reduction to obtain fine movements are also under consideration.^(42,43)

The first practical scanning X-ray microscope was developed at the Cambridge Electron Accelerator Synchrotron Source (USA).^(44,45) This, however, did not use any focusing optics in the microscope itself, although a grazing incidence ellipsoidal mirror was used as a condenser. The X-ray beam was defined by a pinhole, 1–2 μm in diameter, which was scanned across the sample. The resolution was limited to the size of these pinholes, diffraction effects preventing smaller pinholes from giving higher resolutions. An interesting feature of this microscope was the formation of images from fluorescence X rays as well as transmitted X rays.

Several more sophisticated scanning X-ray microscopes are now in use⁽¹⁶⁾ or under development,^(46–50) as indicated in Table 10.3. In most of these, the use of zone plate optics is intended, and the setup is then very close to the general schematic shown in Figure 10.14. One system, however, will use grazing incidence (Wolter) optics, as shown in Figure 10.15, and one will use normal incidence multilayer mirrors in the Schwarzschild configuration, as shown in Figure 10.16.

Table 10.3. Scanning X-Ray Microscopes

Location	Source	Optics	Scanning stage	Resolution (nm)	Ref.
Brookhaven	Synchrotron (NSLS)	Zone plate	Transducer	200	16
Berlin	Synchrotron (BESSY)	Zone plate	Lever reduction	60 ^a	46
Daresbury	Synchrotron (SRS)	Zone plate	Transducer or flexure	50 ^a	47
Hefei (China)	Synchrotron	Zone plate	Transducer	200 ^a	50
Brookhaven	Synchrotron (NSLS)	Multilayer mirrors	Transducer	50 ^a	48
NPL	Tube	Wolter type I	Flexure	<100 ^a	49

^aPredicted resolution.

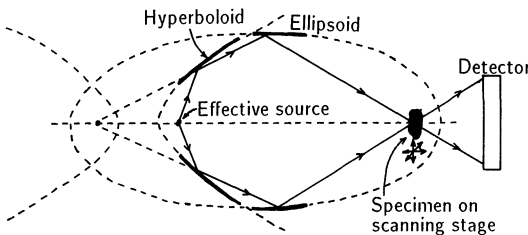


Figure 10.15. A Wolter type I grazing incidence scanning X-ray microscope.

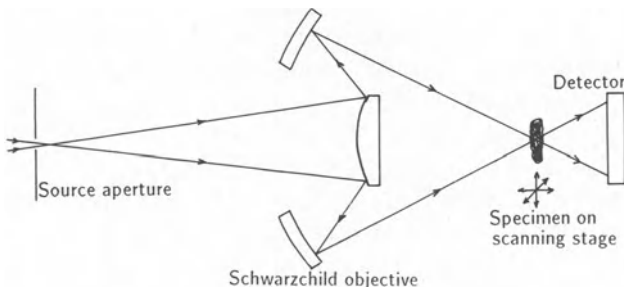


Figure 10.16. A normal incidence multilayer mirror scanning X-ray microscope.

10.4.2.1. The Stony Brook Scanning X-Ray Microscope

The only high-resolution scanning X-ray microscope presently in use is that built by Kirz and his colleagues at the State University of New York, Stony Brook, and the NSLS, Brookhaven.⁽¹⁶⁾ The source for this microscope is the ultraviolet ring at the NSLS (see Table 1.1), with a beam line constructed around the toroidal grating monochromator discussed in Section 10.2.3. The higher-order spectral contamination in the monochromator output is removed by grazing incidence reflection from a quartz flat that also serves to make the beam exactly horizontal. The beam is collimated using a pinhole (typically 30- μm diameter) and this serves as the source to be demagnified by the zone plate. Since the incident intensity can vary considerably over the time necessary to obtain an image, due to decay of the synchrotron beam, the input signal is monitored continuously using a transmission photodiode. This is used to normalize the image to the incident intensity.

The zone plate used in this microscope was produced by electron-beam lithography at the IBM Thomas J. Watson Research Center.⁽⁵¹⁾ The zone plate has 140 zones with an outermost zone width of 150 nm,

and is made of gold supported on a 120-nm-thick silicon nitride film. This zone plate suffered from elliptic distortion, which had to be corrected by tilting it through an angle of 12°. To eliminate unwanted diffracted orders, the zone plate is centrally obstructed (to a radius of 24 μm , i.e., the inner 40 zones) and a collimator is placed between the zone plate and the specimen, with the first-order focus in the shadow of the central obstruction.

The zone plate forms an image of the pinhole on the atmospheric side of a thin silicon nitride window so that the sample holder can be mounted outside the vacuum and attached magnetically to the scanning stage, to facilitate specimen changing. Specimens are positioned and focused using an optical alignment microscope, and the whole specimen area is surrounded by a dust-proof enclosure that can, if desired, be flooded with dry or humidified helium to give increased X-ray transmission as well as moisture retention for wet specimens. The scanning stage uses piezoelectric and linear variable differential transducers as described earlier.

The transmitted X rays are detected by a flow proportional counter with an efficiency of greater than 50%. The entrance window is 100-nm-thick carbon supported on a mesh and the detector works at atmospheric pressure using P10 gas (an argon/methane mixture). Although energy and spatial resolution are not of prime importance, at wavelengths around 3 nm the detector can discriminate against higher-order radiation from the monochromator.

Several interesting images of both wet and prepared material have been obtained with this microscope.^(16,41) Most of the work has been carried out using radiation of wavelength 3.2 nm, near the peak of the monochromator output. Typically, a $20 \times 20\text{-}\mu\text{m}$ image, containing about 10,000 pixels, of a 1- μm -thick wet object took about 1 h to form and showed a resolution of about 300 nm. A particularly interesting result has been the mapping of the calcium distribution in bone,⁽⁵²⁾ by comparison of two measurements of specimen absorptivity at wavelengths, of 3.55 and 3.58 nm, on either side of the calcium *L* absorption edge. In these experiments, resolutions of around 200 nm were obtained.

10.4.2.2. Other Zone Plate Scanning Microscopes

Two other scanning microscopes using zone plate optics are under construction, both differing in detail from the Stony Brook microscope. The one being installed at the BESSY synchrotron in Berlin, by Schmahl and his colleagues,⁽⁴⁶⁾ uses a centrally obstructed condenser zone plate that also acts as a monochromator, as well as an objective zone plate. These zone plates are made by interference techniques and resolutions of

about 50 nm are predicted. In the future, a sputtering method of zone plate manufacture (see Chapter 11) may allow resolutions as low as about 10 nm. The scanning mechanism for this microscope uses long (1 m) lever reduction, but the performance of this at the required resolution has not yet been reported.

The microscope to be installed at the Synchrotron Radiation Source (SRS) at Daresbury is being constructed by Burge, Duke, Michette, and colleagues from King's College London and the Daresbury Laboratory.⁽⁴⁷⁾ This will be the first microscope to utilize the more intense radiation available from an undulator source, and will use a plane grating monochromator. The zone plate objectives, made by contamination lithography (Section 9.2.1), will be centrally obstructed, and will have outermost zone widths as small as 40 nm in the first instance. Two types of scanning stage are being tested, one similar to the Stony Brook design and one based on flexure reduction.⁽⁴³⁾ Novel features of this microscope, which may be implemented after initial test experiments in 1986, include the use of multilayer mirrors to vertically divert the X-ray beam from the synchrotron to allow the scanning stage to be horizontal (preferable for some living specimens), and the possibility of three-dimensional imaging by displacing the specimen slightly from the zone plate focus and using the beam divergence.⁽⁵³⁾

10.4.2.3. A Grazing Incidence Reflection Scanning Microscope

A scanning microscope under construction by Franks at the National Physical Laboratory⁽⁴⁹⁾ uses Wolter type I grazing incidence optics (Figure 10.15) with small-diameter (about 30-mm bore) mirrors for stability. This is the only high-resolution (<100 nm) microscope at an advanced stage of planning that will not use synchrotron radiation. Instead an electron impact microfocus source,⁽⁵⁴⁾ with a source size of about 100 nm, will be used, the design of this allowing the target to be changed easily for wavelength selection. A flexure scanning stage is to be used.

10.4.2.4. A Normal Incidence Reflection Scanning Microscope

All of the microscopes discussed so far have small apertures and are prone to large aberrations. If normal incidence reflection is used, larger apertures and smaller aberrations are possible. For example, a Schwarzschild-type objective (Section 4.2), using two concentric spherical mirrors, can be almost free of aberrations and can, because of the simple shape of the mirrors, be made very accurately. However, because two reflections are needed, the efficiency will be low even when multilayer

mirrors are used, so that such an arrangement is unsuitable for imaging microscopy. In scanning microscopy, however, the effect is to give long imaging times, which need not be a major disadvantage for all specimens.

A scanning microscope with a multilayer mirror Schwarzschild objective is being constructed by Spiller at the NSLS,⁽⁴⁸⁾ and has undergone initial tests. The synchrotron source is demagnified by a grazing incidence ellipsoidal mirror onto an adjustable pinhole, with diameter 2–20 µm, which acts as a secondary source for further demagnification (by a factor of 64) by the objective. The objective mirrors are rhenium–tungsten/carbon multilayers designed for a wavelength of 6.7 nm i.e., outside the water window range. The estimated peak reflectivity of each mirror is about 10–15%, giving an overall throughput of about 1%.

10.4.3. A Comparison of Image Formation in Imaging and Scanning X-Ray Microscopes

Because of the unusual focusing properties of soft X-ray optical components, compared to those used, for example, at visible wavelengths, considerable care must be taken to ensure that images represent true features of objects. The discussion in this section is of particular relevance to zone plate microscopes,⁽⁵⁵⁾ but similar considerations could apply to other image-forming systems.

In a zone plate microscope, it is the unwanted diffraction orders that can cause problems in image formation. For a perfect Fresnel zone plate, the zero and first negative orders contain one-half and $2/\pi^2$, respectively, of the transmitted radiation, causing an intolerable contrast reduction and obscuration of image detail if the zone plate is used as a simple lens in its, most useful, first positive order. To reduce the effect of this background, the best option in microscopy is to use a combination of an axial obstruction in the plane of the objective zone plate and a pinhole some distance away. The image is formed in a shadow region from which most of the unwanted radiation has been removed. However, the optical system then has properties that are not normally encountered in a microscope.

The optical arrangements for imaging and scanning microscopy are shown in Figure 10.17a and 10.17b, respectively. The scanning arrangement is the same as that used in the Stony Brook microscope. If the pinhole/obstruction combinations were not present, there would be four main components to an image. For an imaging microscope, these are, in order of decreasing magnitude,

1. The radiation that is undiffracted by either the object or the objective zone plate and that forms a geometrical image of the

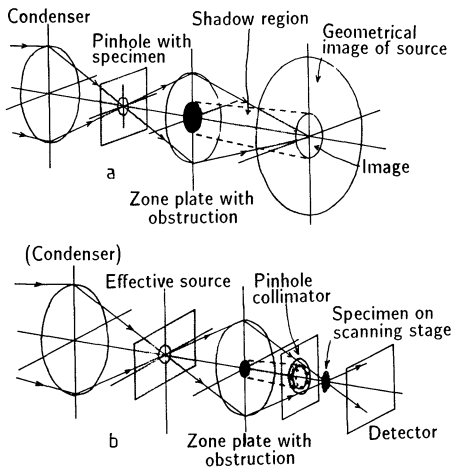


Figure 10.17. Schematic optical arrangements for microscopes using centrally obstructed zone plates: (a) imaging, (b) scanning.

source. This is the most prominent component of the image and greatly reduces the contrast.

2. The radiation that is diffracted by the object but transmitted in the zero order of the zone plate. The object behaves as a new source of radiation and a geometrical image is formed of it.
3. The desired image from the first positive order of the zone plate.
4. The radiation focused into the other diffraction orders of the zone plate.

These four components are also present in the images from a scanning microscope, where the optical arrangement may be considered to work as an imaging microscope in reverse to form a sampled image. The central obstruction of the objective zone plate along with the pinhole blocks the undiffracted radiation (component 1), and also removes the zero (component 2) and all negative diffraction orders from the image plane. In addition, in a scanning microscope most of the radiation in other unwanted orders (component 4) is removed.

For an imaging zone plate microscope it is convenient to mount the specimen on the pinhole so that the region of the specimen to be magnified must be chosen by, for example, using an optical microscope. The relationship between the pinhole radius r_p and the useful image radius r_a is then given geometrically by (Figure 10.18a)

$$r_p = r_0 - (z/z')(r_a - r_0) \quad (10.3)$$

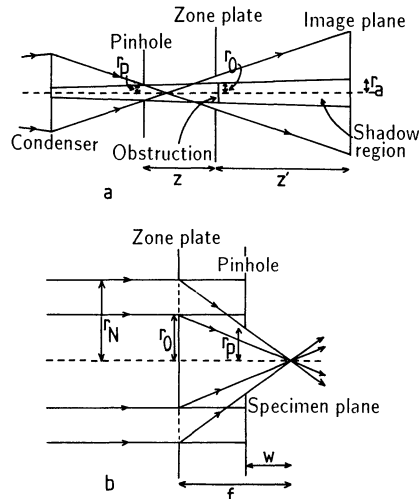


Figure 10.18. The relationship between the radii of the central obstruction and the pinhole for (a) an imaging microscope, and (b) a scanning microscope.

where z is the specimen–zone plate distance, z' is the zone plate–detector distance, and r_0 is the radius of the central obstruction of the zone plate. Since the apertures are large compared to the wavelengths used, they do not cause significant diffraction effects.

For a scanning microscope, the calculation of the pinhole size is more complicated since a working distance w , to allow the specimen to be scanned across the X-ray beam, must be left between the specimen and the pinhole. The equivalent arrangement in an imaging microscope would be if the specimen and pinhole were separated to allow, for example, dynamical positioning of the former. So that it does not obstruct any of the focused beam, the pinhole must have a minimum radius (Figure 10.18b)

$$r_{p\min} = r_N w / f \quad (10.4)$$

where r_N is the zone plate radius and f is the focal length, while the maximum radius is equal to that of the central obstruction of the zone plate. Compared to an imaging microscope, the scanning arrangement allows the obstruction of more of the unwanted radiation, the main limitation on this being the working distance.

Because of the difficulty in aligning the very small X-ray optical components, alternative arrangements such as obstructing the source (or condenser zone plate) in an imaging system,⁽³⁹⁾ or obstructing the detector in a scanning system,⁽⁵⁶⁾ have been suggested. Although these arrangements facilitate image formation, they both have nonlinear transfer functions that could lead to spurious results.

Image formation in imaging and scanning microscopes has been treated in detail by several authors.^(57–60) For a scanning system, the image intensity at a sample position x_s of a specimen with amplitude transmission t is given by

$$I(x_s) = K \int \int C(\nu_1, \nu_2) T(\nu_1) T^*(\nu_2) \exp [2\pi i(\nu_1 - \nu_2)x_s] d\nu_1 d\nu_2 \quad (10.5)$$

where T is the Fourier transform of t (i.e., the spatial frequency spectrum of the specimen) and K is a constant. Although equation (10.5) is one-dimensional, it can easily be extended to represent a two-dimensional image. The transfer of independent spatial frequencies ν_1 and ν_2 from object to image is determined by the transfer function

$$\begin{aligned} &C(\nu_1, \nu_2) \\ &= 2\pi \int_{-\infty}^{+\infty} S(q\xi, q\eta) D(q_0\xi, q_0\eta) A(\xi + \nu_1, \eta) A^*(\xi + \nu_2, \eta) d\xi d\eta \quad (10.6) \end{aligned}$$

where $q = z/f$, $q_0 = z_0/f$, z_0 is the specimen-detector distance, S is the source intensity distribution, D is the detector sensitivity to intensity, and A is the objective aperture function. The objective zone plate can be regarded as a perfect lens, perhaps with a central obstruction, if it is assumed that the obstructions completely block the unwanted radiation. The transfer function for one-dimensional objects can be evaluated by considering the integration areas of the constituent functions for different spatial frequency values. The integration area shown in Figure 10.19, for example, is for a scanning microscope with a point source (so that S is a delta-function) and a partially obstructed detector. Figure 10.20 shows the transfer functions for different detector arrangements in a scanning microscope with a point source. These are

1. A point (delta-function) detector. The system has a coherent transfer function and all combinations (ν_1, ν_2) of spatial frequencies are imaged perfectly.

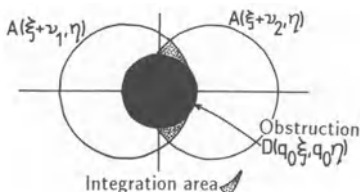


Figure 10.19. The integration area for evaluating the transfer function of a scanning microscope with a point source and a partially obstructed detector.

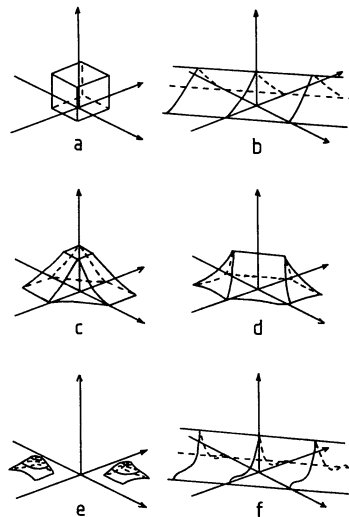


Figure 10.20. The transfer functions for different detector arrangements in a scanning microscope (after Refs. 58 and 59). (a) Point detector, coherent transfer function; (b) infinite detector, incoherent transfer function; (c) scaled detector smaller than the objective; (d) scaled detector larger than the objective; (e) finite obstructed detector; (f) obstructed objective (with infinite detector).

2. A detector of infinite extent, giving totally incoherent imaging with linear transfer of spatial frequency components equal to $(v_1 - v_2)$.
3. A scaled detector function smaller than the objective, resulting in nonlinear imaging for certain spatial frequency combinations.
4. A scaled detector function just larger than the objective, with a similar result to (c).
5. An annular detector, i.e., a finite obstructed detector, again leading to nonlinear imaging.
6. An obstructed objective (with point source and infinite detector), which alters the shape of the incoherent transfer function but retains the linear imaging properties.

For an imaging microscope, the same considerations apply with the source and detector interchanged, so that normally the detector sensitivity is described by a delta-function. Thus an obstructed source in an imaging microscope is equivalent to an obstructed detector in the scanning system. The resulting nonlinearity is shown qualitatively in Figure 10.21 for an imaging microscope—part of the zone plate is not illuminated by the radiation from a given object point, and this changes with the off-axis position. Thus different parts of the object are effectively imaged by different lenses (with correspondingly different point spread functions) and hence the transfer function is very nonlinear. A similar effect is obtained if a small source is used, so that the obstructed regions shown in Figure 10.21 become transmitting and vice versa.

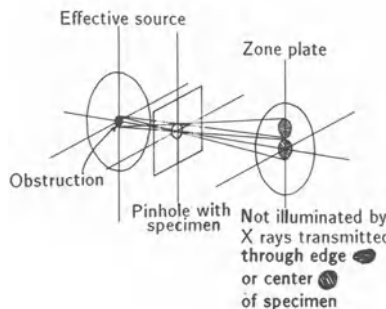


Figure 10.21. The effect of source (condenser) obstruction on zone plate illumination in an imaging microscope.

Thus, in conclusion, the axial obstruction must be in the plane of the objective zone plate for a linear transfer function. Obstruction of either the source or the detector produces nonlinear aberrations in the image that are not simple to characterize.

10.4.4. Other Types of X-Ray Microscope

In addition to the types of X-ray microscopy discussed above, several other methods have been used or proposed for imaging in the soft X-ray region. These will only be very briefly discussed, since (apart from possible optical components external to the instrument) no focusing of the X rays is performed.

In the first of these, projection microscopy,^(61,62) a specimen is placed at a distance d from a source of X rays of wavelength λ , and a shadow image is formed on a screen at a distance h from the specimen. Ideally, the source should be a point in which case the magnification is

$$M = (d + h)/d \quad (10.7)$$

and the resolution limit is determined by Fresnel diffraction,

$$\delta_f = (h\lambda)^{1/2} \quad (10.8)$$

In practice, the source will have a finite size s and then penumbral blurring will contribute to the resolution limit,

$$\delta_p = s(h/d) \quad (10.9)$$

In this type of microscopy, δ_p normally limits the resolution attainable to

several micrometers, and clearly it is an advantage to make h as small as possible compared to d . This leads to the idea of contact microscopy (more correctly called contact microradiography) in which the specimen is placed in intimate contact with an X-ray-sensitive resist. The value of h is now given by the thicknesses of the specimen and the resist but can clearly be very much less than d , leading to a magnification of, effectively, unity and a resolution determined either by (principally) δ_f or by the properties of the resist. After exposure and development, the resist contains an X-ray transmission map of the specimen that may subsequently be viewed by electron microscopy.

The contact process suffers most from saturation and nonlinearity of the resist. This may be overcome by replacing it with a photocathode layer used in transmission, followed by an emission electron microscope.^(63,64) This is then known as photoelectron microscopy.

10.5. Imaging of Laser Fusion Plasmas

As discussed in Chapter 1, plasmas can be used as sources of soft X rays. In laser-produced plasmas used in fusion research, the X-ray emission (along with α particle and neutron emission) is very important in characterizing the plasma.⁽⁶⁵⁾ X-ray imaging techniques can be of use in this in several ways, principally microscopy^(66,67) and coded aperture imaging.^(68,69) Transmission gratings⁽⁷⁰⁾ and multilayer mirrors⁽⁷¹⁾ have also been used.

10.5.1. X-Ray Microscopy of Fusing Plasmas

The optical arrangements of microscopes suitable for imaging plasmas are essentially the same as those discussed in Section 10.4 for biological imaging, with one restriction and two differences. The restriction is that the scanning arrangement cannot be used since the plasmas only exist over very short time scales (\sim nsec); they also typically have dimensions of several tens to hundreds of micrometers, so that the resolution of the microscope need only be in the range $1\text{--}10 \mu\text{m}$. The other difference is that the X-ray source and the object (specimen) are now one and the same—i.e., the object is self-luminous, emitting radiation over a range of wavelengths. Thus optics exhibiting severe chromatic aberration (zone plates) or designed for use at a particular wavelength (multilayer mirrors) are not suitable.

Wolter (type I) optics (Figure 10.22) are very well suited to this form of imaging. Such a microscope has been designed and built at the Los

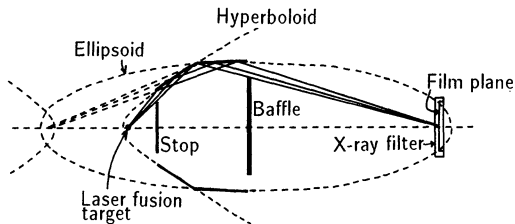


Figure 10.22. A Wolter type I grazing incidence imaging X-ray microscope used in laser fusion studies. (After Price.⁽⁶⁷⁾)

Alamos Scientific Laboratory, New Mexico.⁽⁶⁶⁾ This has a $10\times$ magnification, a field of view of several hundred micrometers, and an on-axis resolution of $1\text{--}2\ \mu\text{m}$. The ellipsoidal and hyperboloidal mirrors, each about 5 mm long, are made of electroless nickel on aluminum substrates, and are used at a grazing angle of 2° . The tolerances on the surface figures are around 25 nm, and the measured reflection efficiency is higher than 80%, indicating that the surface roughnesses are small.

Similar microscopes have been in use at the Lawrence Livermore National Laboratory (LLNL), California.⁽⁶⁷⁾ One of these has a $22\times$ magnification, a field of view of $800\ \mu\text{m}$, and a spatial resolution of $4\text{--}5\ \mu\text{m}$. Used in conjunction with an X-ray streak camera, a temporal resolution of 15 psec is possible. The performance of this microscope is limited by surface roughness of about 25 nm, so that only about 5% of the incident intensity is contained within the central $50\ \mu\text{m}$ of the point spread function.

Kirkpatrick–Baez microscopes (Section 2.4.1) have also been used at LLNL to image fusing plasmas.⁽⁶⁷⁾ The layout of a four-channel cylindrical mirror microscope is shown in Figure 10.23. Each channel of this

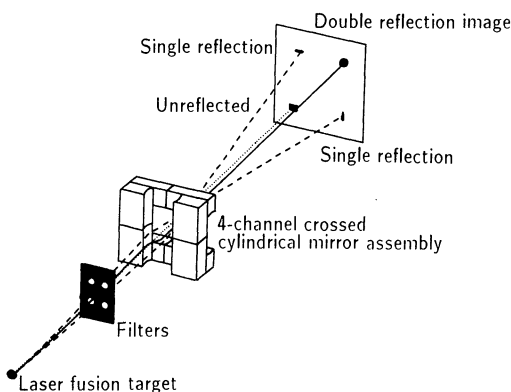


Figure 10.23. A four-channel Kirkpatrick–Baez X-ray microscope used in laser fusion studies. (After Price.⁽⁶⁷⁾)

produces a focused double-reflection image, two single-reflection line foci, and an unfocused spot from unreflected X rays. By a correct choice of filters, mirror materials, and grazing incidence angles, each channel can be used to image a different X-ray wavelength, which is clearly very useful for laser fusion diagnostics. The microscopes typically have object distances of 250–400 mm, magnifications of 3×–8×, and resolutions of 1–3 μm . Their major drawback is their small acceptance solid angles of, typically, 10^{-7} – 10^{-6} sr.

10.5.2. Coded Aperture Imaging

An alternative approach to X-ray imaging, initially suggested for astronomy^(72,73) and nuclear medicine,^(74,75) is to use coded apertures. In this, the X-ray source distribution casts geometrical shadows through a periodic array of openings in an opaque mask, producing a coded image that is subsequently decoded using optical or numerical techniques. For laser plasma diagnostics, zone plate coded imaging is used.^(68,69) In order that the shadows cast may be considered to be geometric, diffraction effects at the zone plate must be negligible, which means that the outermost zone width must satisfy⁽⁶⁸⁾

$$(dr_N)^2 > 4\lambda_{\max}zz'/(z + z') \quad (10.10)$$

where λ_{\max} is the longest wavelength to be imaged, z is the source to zone plate distance, and z' is the distance between the zone plate and the recording plane. The principle of zone plate coded imaging is illustrated in Figure 10.24. The (incoherent) source is considered to be a distribution of point sources, each of which casts a distinct shadow onto the recording medium. The spatial location of each source point is uniquely determined

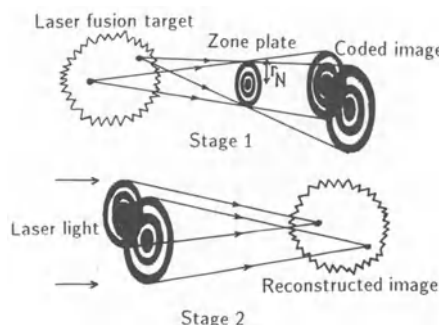


Figure 10.24. The principle of zone plate coded aperture imaging. (After Ceglio.⁽⁶⁹⁾)

by the size and position of its shadow—the more distant the point, the larger the shadow, while off-axis source points produce off-axis shadows. The shadowgraph may subsequently be decoded by coherent illumination with an optical laser, each zone plate shadow focusing the light to a diffraction-limited spot so that the original source distribution is reconstructed point by point.

Coded imaging techniques have significant advantages over conventional imaging methods for laser plasma diagnostics. Since the zone plate is not required to focus the X rays, polychromatic source radiation may be used, so long as the wavelength is short enough to satisfy equation (10.10), and long enough that the opaque zones absorb an appreciable fraction of the radiation. The zone plate can be large (radii, r_N , of 0.2–7.5 mm and outermost zone widths of 1–15 μm have been used), so that it has a large collection solid angle—typically four to six orders of magnitude higher than pinhole cameras⁽⁷⁶⁾ of similar resolution (~micrometers). The ratio of the signal to noise values for zone plate coded aperture and pinhole imaging is, for equal resolutions and a two-dimensional source distribution,⁽⁷⁷⁾

$$R = 0.32[(z + z')/z'](\pi r_N^2/A)^{1/2} \quad (10.11)$$

where A is the active source area. For a three-dimensional source,

$$R = 0.28[(z + z')/z']^{3/2}(\pi r_1^2 z/V)^{1/2} \quad (10.12)$$

where r_1 is the radius of the innermost zone of the coded aperture and V is the active source volume. Equations (10.11) and (10.12) show that, as the source size increases, zone plate coded imaging becomes less favorable. It is only successful if the diameter of the zone plate is large compared to that of the source.

A further advantage of zone plate coded imaging is, as intimated above, its capability for three-dimensional (tomographic) imaging, in which the reconstructed image is viewed in sections. The resolution is then about an order of magnitude lower than for planar imaging.⁽⁶⁸⁾

10.5.3. Transmission Grating Spectrometers

The design of a simple transmission grating spectrometer suitable for use in laser fusion experiments is shown in Figure 10.25.⁽⁷⁰⁾ The spectral resolution of such a system is

$$\Delta\lambda = (s + a)d/z + ad/z' \quad (10.13)$$

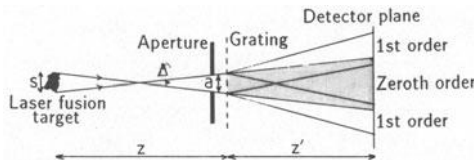


Figure 10.25. A transmission grating spectrometer used in laser fusion studies. (After Ceglio *et al.*⁽⁷⁰⁾)

where d is the grating period, s is the source size, a is the aperture size, z is the source to grating distance, and z' is the grating to detector distance. The maximum wavelength that can be recorded is

$$\lambda_{\max} = td/z' \quad (10.14)$$

where t is the detector size. The minimum wavelength is given either by

$$\lambda_{\min} = \delta d/z' \quad (10.15)$$

where δ is the detector spatial resolution, or by

$$\lambda_{\min} = \Delta\lambda \quad (10.16)$$

if the source size and the aperture cause the limitation (i.e., if the zeroth and first spectral orders overlap). Typically, gratings with $d \approx 300$ nm, z and z' equal to several hundred millimeters, and source and aperture sizes of ~ 100 μm have been used, leading to spectral resolutions of a few tenths of a nanometer. A streak camera used in conjunction with the spectrometer allows temporal resolutions of ~ 20 psec.

10.5.4. Multilayer Mirrors Used for Laser Plasma Spectroscopy

The spectral characteristics of laser plasmas have also been investigated in the soft X-ray region using multilayer mirrors.⁽⁷¹⁾ The system is shown schematically in Figure 10.26, and the multilayer characteristics

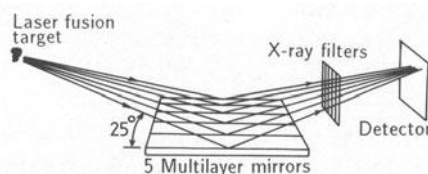


Figure 10.26. The use of multilayer mirrors in a spectrometer for laser fusion studies. (After Stradling *et al.*⁽⁷¹⁾)

Table 10.4. Multilayer Mirrors Used in Laser Plasma Diagnostics⁽⁷¹⁾

Channel wavelength/ width (nm)	<i>d</i> spacing (nm)	Bragg angle	Materials	Peak reflectivity % (calcd)	Filter	
					Material	Thickness (μm)
1.31/0.014	1.5	25°	W/C	1.6	Al	0.7
1.68/0.018	2.1	23.8°	W/C	5.1	Al	0.7
1.90/0.023	2.1	27.1°	W/C	5.1	Al	0.7
4.64/0.12	5.5	25°	Ti/C	10.6	C	2.65
12.14/0.12	17.8	25°	V/C	10.8	Be	1.0

are summarized in Table 10.4. The use of a streak camera allows temporal resolutions of 15 psec.

10.6. X-Ray Astronomy

Because of absorption in the atmosphere, X rays emitted by extraterrestrial sources cannot be detected at the earth's surface. Early experiments in X-ray astronomy were carried out using detectors mounted on balloons or rockets. Although it proved possible to use zone plates for focusing in rocket experiments,^(78,79) the only source suitable for imaging with these was the sun, which, because of its closeness, gives a sufficient X-ray flux density at the earth ($\sim 10^{-7} \text{ J m}^{-2} \text{ sec}^{-1}$ at solar minimum, $\sim 10^{-3} \text{ J m}^{-2} \text{ sec}^{-1}$ for a large flare) to overcome the small apertures of zone plates. Detection and measurement of the X rays from more distant sources had to await the launching of X-ray telescopes in satellites. Although these sources (such as pulsars, quasars, and black holes) can be very much stronger X-ray emitters than the sun, because of their vastly greater distances the received flux densities at the earth are extremely small ($\sim 4 \times 10^{-10} \text{--} 2 \times 10^{-17} \text{ J m}^{-2} \text{ sec}^{-1}$). Thus telescopes of large collecting power are necessary. Very large grazing incidence mirrors can be used, and the geometric collecting power can be increased further by using nested mirrors.⁽⁸⁰⁾ This is illustrated in Figure 10.27a for a Kirkpatrick-Baez telescope and in Figure 10.27b for a Wolter (type I) telescope. However, because a Kirkpatrick-Baez nest is not axially symmetric, the image is blurred for nonzero polar angles. Most of the systems that have been built or are planned consist of Wolter type I telescopes, but Wolter type II, single paraboloid, Wolter-Schwarzchild, and one- and two-dimensional Kirkpatrick-Baez systems have also been reported. Other systems, consisting of orthogonal arrays of plane mirrors (two-dimensional focusing collimator, Figure 10.28),⁽⁸¹⁾ or lobster-eye telescopes,⁽⁸²⁾ have also been proposed. Both of these can have larger

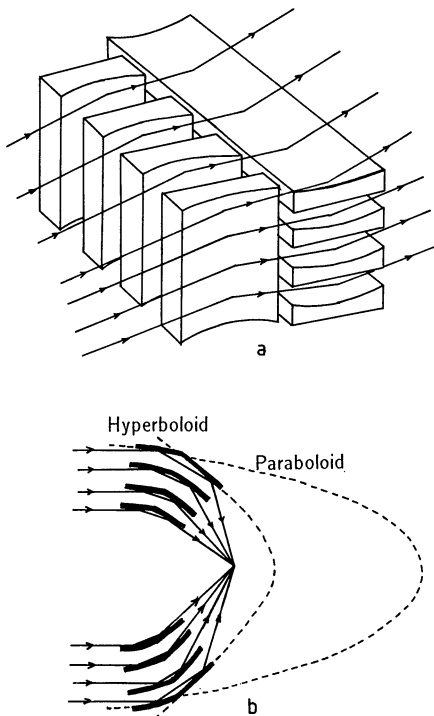


Figure 10.27. Nested mirror grazing incidence telescopes: (a) Kirkpatrick–Baez, (b) Wolter type I.

fields of view than Wolter or Kirkpatrick–Baez systems, but have reduced angular resolution. In the first of these designs, the mirrors are reflecting on both surfaces and the envelope of the upper edges of each stack forms a cylindrical section. The center lines of the upper and lower cylinders intersect at 90° at the coordinate system origin, and each mirror plane is aligned in the radial direction originating from the cylinder

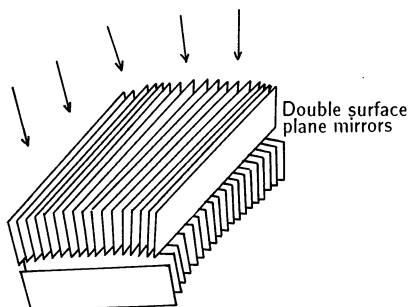


Figure 10.28. A two-dimensional focusing collimator telescope.⁽⁸¹⁾

center line of the corresponding stack. Each stack thus performs one-dimensional focusing on a cylindrical surface about halfway between the stack position and the center lines. However, because the individual mirrors have finite sizes along the radial direction, the focusing is not perfect. Also, radiation can pass through the system with only one, or no, reflection, giving respectively line-shaped and diffuse background in the image. The lobster-eye telescope is a variation of this design, and consists of a large number of small square-sided tubes, with internal reflecting walls, distributed over a spherical surface (of radius R) such that the axis of each tube is oriented along a radius of the sphere. Radiation reflected twice, from adjacent walls, within a single tube is focused onto a spherical surface with radius $R/2$, forming a two-dimensional image on this surface. The instrument suffers from the same disadvantages of single or no reflections discussed above. It derives its name from the reflective eyes of lobsters and shrimps, which work on the same principle.

It is important to be able to assess the performances of X-ray telescope mirrors before they are launched. In addition to the conventional metrological methods for surface finish evaluation discussed in Chapter 3, ray-tracing techniques have been used⁽⁸³⁻⁸⁹⁾ to determine the aberrations of grazing incidence telescopes. In these, the paths of an ensemble of individual rays are followed geometrically (by computer modeling) through the complete mirror system. A Monte Carlo ray-tracing procedure, for example, has been used to evaluate the optical characteristics of Wolter type I⁽⁸⁵⁾ and Wolter-Schwarzchild type I⁽⁸⁶⁾ telescopes. The input to the computer program is a geometrical description of the telescope, the surface material(s) of the reflectors, the location of the point source of X rays, and the X-ray wavelengths. Incident rays are required to go through points chosen at random on the front aperture of the telescope, and are followed through the system, using calculated reflectivities, until they reach the focal plane (or are lost). The output from the program gives the telescope effective collecting area and the rms radii for flat and optimally curved focal surfaces. The results show that the following empirical relation holds for the rms blur circle radius σ (in radians) on the optimally curved focal surface.

$$\sigma = A(\xi + 1)L_p \tan^2 \theta/f \tan \alpha + B \tan \theta \tan^2 \alpha \quad (10.17)$$

In equation (10.17), ξ is the ratio of the grazing incidence angles on the paraboloid and hyperboloid for an axial ray striking near to the intersection of the surfaces (for most telescopes, $\xi = 1$); L_p is the length of the paraboloid (the length of the hyperboloid was considered to be fixed by choice of L_p so that axial rays incident on the front of the paraboloid strike the back of the hyperboloid); θ is the angle between the

incident rays and the optical axis; f is the distance from the axial ray focus to the intersection plane of the surfaces, and may be considered to be the focal length of the system; and $\alpha = \tan^{-1}(r_0/f)$, where r_0 is the radius of the surfaces at their intersection. For Wolter telescopes, $A = 0.1$ and $B = 4$, while for Wolter–Schwarzchild telescopes, $A = 0.135$ and, since for these the Abbe sine condition is exactly satisfied, $B = 0$.

The analysis also gives the effective collecting area A_e as

$$A_e(\theta_i, E) \sim A_g R^2(\theta_i, E) = 8\pi f L_p \alpha^2 R^2(\theta_i, E) \quad (10.18)$$

where A_g is the geometrical collecting area, and $R(\theta_i, E)$ is the Fresnel reflectivity at a mean grazing incidence angle θ_i and energy E .

Ray-tracing has become the standard technique for designing and optimizing grazing incidence X-ray telescopes.⁽⁹⁰⁾ It has also been used for grazing incidence X-ray microscopes.⁽⁶⁶⁾

10.6.1. Examples of Grazing Incidence X-Ray Telescopes

The properties of X-ray telescopes that have already been used are summarized in Table 10.5. Some of these are discussed in more detail below.

10.6.1.1. The Skylab Telescopes

The telescopes ATM S-054⁽⁹¹⁾ and ATM S-056⁽⁹²⁾ were both flown aboard the manned Skylab mission in 1973. The ATM (Apollo telescope mount) was a very accurate and stable solar pointing platform, and the telescopes were used to obtain X-ray pictures of the sun at resolutions in the arc second range. The performances of the telescopes were limited by two things—the mirrors were made at a time when surface polishing technology was not at an advanced stage (in particular, the ability to measure surface smoothness was limited), and the images were recorded on photographic film so that very little spectral information was obtained. It was, however, possible to observe coronal holes (regions of low X-ray brightness in which the magnetic field is directed radially outwards from the surface), limb brightening (due to the existence of more hot material along the line of sight toward the limb), emission from hot coronal plasma, and emission from solar flares.⁽⁹³⁾

10.6.1.2. The Einstein Observatory

The Einstein observatory (High Energy Astronomy Observatory, HEAO-2) was launched in November 1978 into near earth orbit, and

Table 10.5. Some Grazing Incidence X-Ray Telescopes

Telescope/ type	Mirror/ substrate material	Focal length/ total mirror length (m)	Maximum diameter (m)/ geometric collecting area (m^2)	Wavelength range (nm)/ on-axis resolution (FWHM) (arc sec)	Ref.
ATM S-054/ Wolter I, 2 shells	Kanigen/ beryllium	2.13/ 0.342	0.304/ 0.0042	0.2–6/ 4	91
ATM S-056/ Wolter I	Fused silica	1.903/ 0.247	—/ 0.0015	0.6–6/ 2	92
AXT/ Wolter I	Nickel/ aluminum	2.28/ 1.05	0.66/ 0.028	0.6–8/ 20	94
Einstein/ Wolter I, 4 shells	Nickel/ fused silica	3.44/ 1.022	0.58/ 0.035	0.3–6/ 3	95
RT-4M/ Wolter I, 2 shells	Au–Ni/—	0.66/ 0.48	0.24/ — ^a	4.4–10/ —	98
MPI/ paraboloid		—/ 1.0	0.15/ —		99
MPI/ Wolter I	Kanigen/ aluminum	1.427/ 0.81	0.322/ 0.0106	0.6–12/ 5	99
Exosat/ Wolter I	Gold/ beryllium	1.090/ 0.4	0.278/ 0.0089	0.6–31/ 5	90

^aField of view 45' × 3°.

remained operational for almost 2½ years.^(95,96) It carried the largest X-ray telescope used to date. Several detector systems were used, including a high-resolution imager based on a channel plate device (possibly in conjunction with a transmission grating), an efficient imaging proportional counter, a solid-state spectrometer, a focal plane crystal spectrometer, and a collimated proportional counter. The telescope was controlled from the ground so that it pointed to preselected objects or areas, and almost 6000 observations covering a few percent of the total sky area have been carried out.⁽⁹⁷⁾ Typical objects studied include supernova remnants and pulsars.

10.6.1.3. The Max-Planck-Institut Telescopes

The MPI has developed two types of grazing incidence telescopes based on single paraboloidal reflectors and on Wolter type I optics.⁽⁹⁹⁾ Bundles of 12 paraboloidal mirrors have been flown twice on Aries

rockets (in 1977 and 1978), performing spectrophotometry of sources. The Wolter type I telescope has been flown on a Skylark rocket, using an imaging proportional counter as a detector (this limited the angular resolution to 1.5 arc min, although the optics themselves were capable of 5 arc sec). Images of supernova remnants were obtained. An obvious disadvantage of rocket-based observations is the short flight time (~minutes) compared to that for satellites.

10.6.1.4. The Exosat Observatory

The European Exosat observatory has been in operation since its launch in May 1983.⁽⁹⁰⁾ It has a highly eccentric orbit, extending to a height of 200,000 km and allowing long uninterrupted observations (up to 80 hr) of selected areas. It carries two identical Wolter I telescopes, each equipped with a focal plane detector consisting of a position-sensitive proportional counter (allowing spatial and spectral resolution) and a channel multiplier array (giving spatial resolution only). Additional spectral information can be obtained using filters, and each telescope is equipped with a movable transmission grating for spectroscopy. High-resolution images of, for example, supernova remnants have been obtained.

10.6.2. Future Telescopes

The properties of telescopes planned for launching over the next decade or so are summarized in Table 10.6. The MPI 0.8-m telescope⁽⁹⁹⁾ is similar to the 0.32-m telescopes previously developed there, apart from (for mechanical reasons) the choice of material. This telescope has been designed for launching by the Space Shuttle. The other planned instruments are discussed in more detail below.

10.6.2.1. Rosat

The German Röntgensatellit (Rosat),⁽¹⁰⁰⁾ to be launched by the Space Shuttle, will contain two telescopes, a Wolter type I and a wide-field camera based on a Wolter-Schwarzchild type I design (from the U.K.). The Wolter telescope will have three imaging detectors, only one of which can be used at a time. These are a high-resolution imager the same as that used on the Einstein observatory, and two identical position-sensitive proportional counters. For the wide-field camera, two identical multichannel plate detectors, with absorption filters to provide three different wavelength pass bands, will be used.

Table 10.6. Grazing Incidence X-Ray Telescopes Planned for the Future

Telescope/ type	Mirror/ substrate material	Focal length/ total mirror length (m)	Maximum diameter (m)/ geometric collecting area (m^2)	Wavelength range (nm)/ on-axis resolution (FWHM) (arc sec)	Ref.
MPI/ Wolter I, 4 shells	Au or Ni/ zerodur	0.24/ —	0.8/ 0.125	—/ 5	99
Rosat/ Wolter I, 4 shells	Gold/ zerodur	2.4/ 1.0	0.835/ 0.115	0.6–12/ 5	100
Rosat/ W-S ^a I, 3 shells	Gold/ aluminum	0.53/ 0.2	0.58/ — ^b	6–30/ 60	100
AXAF/ Wolter I, 4 shells	Au or Ni/ quartz or zerodur	10.0/ 1.65	1.20/ 0.15	0.1–12/ 0.5	101
AXIO/ W-S ^a I	Fused silica	0.475/ —	0.8/ 0.0175 ^c	0.6–30/ 0.5	102
LAMAR ^d / Wolter I, 10 shells	Au or Ni/ aluminum	3.6/ 0.69	0.86/ 0.135	0.2–12/ 20	103, 104
LAMAR ^d / K-B ^e	Au or Ni/ float glass	1.8/ —	0.25/ 0.027	0.2–12/ 60	103, 104

^aWolter–Schwarzchild.^bThis instrument is a wide-field camera with a circular field of view of 5°.^cEffective collecting area.^dLarge-area modular array of reflectors. The parameters given, in each case, are for single modules.^eKirkpatrick–Baez system with 11 front mirrors, 9 back mirrors, each 0.5 m long, 0.25 m wide.

The main objective of these telescopes is to carry out an all-sky survey, which will take about 6 months. For this, the two telescopes will look in parallel, so that spectral information will be simultaneously available over the wavelength range 0.6–30 nm. After the survey is completed, the telescopes will be used to perform detailed studies of selected sources.

10.6.2.2. The Advanced X-Ray Astrophysics Facility (AXAF)

AXAF⁽¹⁰⁾ is an observatory, planned in the United States, to be launched by the Space Shuttle. It has a design lifetime of over 10 years, and will be visited regularly for maintenance, with eventual retrieval. It will carry the largest grazing incidence telescope conceived so far, and will use a variety of detectors such as single photon counting imagers,

spectrometers, and polarimeters. It is intended to study, among other things, stellar structure and evolution, large-scale galactic phenomena, active galaxies and quasars, and galactic clusters.

10.6.2.3. Advanced X-Ray Imaging Observatory (AXIO)

AXIO⁽¹⁰²⁾ is designed to be a high-resolution solar X-ray astronomy observatory, and is thus intended to be able to image a large amount of structure over an extended area, rather than to study essentially point objects. This requires that the performance of the telescope should be represented, as for an X-ray microscope, by the modulation transfer function. A single Wolter type I system was chosen in the design for three main reasons: in a nested set of telescopes, the imaging properties tend to be governed by the worst mirror of the set; misalignments of the assembly could lead to degradation in image quality; and for solar observations it is not necessary to have such large collecting areas.

10.6.2.4. Large-Area Modular Arrays of Reflectors (LAMAR)

In single or nested telescopes, the collecting area is limited by the maximum feasible aperture. The collecting power may be increased by using several telescope modules in parallel. In the United States, several designs of LAMAR facilities have been considered, based on Wolter type I or Kirkpatrick–Baez optics.^(103,104) A typical Wolter I LAMAR design has seven modules, each consisting of ten nested telescopes, while a typical Kirkpatrick–Baez design has 64 modules each consisting of 11 front mirrors and nine back mirrors. In Europe, a similar concept, the X-Ray Multi-mirror Mission (XMM),⁽¹⁰⁵⁾ is being studied. This consists of two types of module, one for the wavelength range 0.6–12 nm, and one allowing imaging down to a wavelength of 0.1 nm.

10.6.3. Zone Plate Imaging in Astronomy

Fresnel zone plates have also been used, on rocket flights, to obtain solar images in a few cases. The earliest of these,⁽⁷⁸⁾ in 1967, obtained photographs (on X-ray film) of solar X rays in four wavelength ranges, the emission being from highly ionized atoms: 5.1 nm (Si X), 18 nm (Fe VIII–X), 30.4 nm (He II), and 58.4 nm (He I). For the soft X-ray imaging at 5.1 nm, a zone plate with 100 zones, a radius of 450 μm , an outermost zone width of 2.25 μm , and a first-order focal length of 0.4 m was used. The zone plate was not centrally obstructed and therefore the images suffered from contrast reduction due to radiation from the zero and other orders. However, the observations allowed the identification of

active prominences, limb brightening, pointlike emitting regions, and intense spots.

A similar experiment was carried out during a rocket flight in 1972.⁽⁷⁹⁾ In this case, the focused wavelength was 1.64 nm and the zone plate had 450 zones, a radius of 600 μm , an outermost zone width of 0.7 μm , and a focal length of 0.49 m. It, too, was not centrally obstructed. The experiment allowed the temperature and emission distributions of active regions to be determined, with an angular resolution of about 20 arc sec (limited by the film grain size). A later experiment, using a zone plate with a radius of 1.2 mm and a focal length of 0.75 m, allowed an angular resolution of about 15 arc sec.⁽⁷⁹⁾

10.7. X-Ray Spectroscopy

X-ray diffraction gratings have many applications in spectroscopy.^(106,107) In elemental analysis, for example, a sample is irradiated with X rays or electrons, exciting the characteristic spectra of the constituent elements and thereby allowing identification and measurement of concentration. In and around the soft X-ray region, there are 5 elements with *K* emission lines, 13 with *L* lines, more than 20 with *M* lines, and over 30 with *N* lines. These all lie within the wavelength range 2–20 nm, and thus the identification of light elements in the presence of heavier ones requires good wavelength resolution for which gratings, in the Rowland circle mounting, may be employed.

Gratings are also used in chemical shift analysis,⁽¹⁰⁸⁾ in which a particular chemical combination causes an X-ray line to be shifted in position and changed in intensity. This can allow, for example, the determination of chemical structure, bond strength, and the state of oxidation.

In astronomy, transmission gratings have been used in conjunction with Wolter type I telescopes,^(90,95,96) while reflection gratings have been used with paraboloidal reflectors.^(109,110) These experiments have mainly been concerned with the solar spectrum.⁽¹¹¹⁾

Future Developments

11.1. Introduction

As discussed in the previous chapters, the advances in soft X-ray optical systems have been rapid over the last few years, due to the development of intense sources, advances in manufacturing technology, and the desire to utilize the unique properties of X rays in the soft X-ray wavelength range. In this chapter the possibilities of further improvements in optical performance and additional uses of existing or improved systems will be discussed. First, however, a brief survey of advances and potential advances in soft X-ray sources will be given.

11.2. Sources of Soft X Rays

Developments are under way or planned for both synchrotron and laboratory-based sources. Typical designs for next-generation synchrotron sources have been presented both in Europe⁽¹⁻⁶⁾ and in the United States.⁽⁷⁾ The European Synchrotron Radiation Facility (ESRF) is to be situated at Grenoble, France, and the final design includes beam ports at conventional bending magnets as well as a number of insertion devices, i.e., wigglers and undulators, with a total of about 100 experimental stations. The main aim of this machine is to provide high-energy X rays, with output peaking in the wavelength range 0.1–1 nm and giving spectral brilliances several orders of magnitude higher than present-day sources in that range. This increase in brilliance will still hold in the soft X-ray region, although it is considered that a separate source optimized to the requirements of experiments involving lower-energy photons will be desirable. A design study of such a storage

ring has been carried out,⁽⁸⁾ with the performance goals being

- A characteristic wavelength of 2 nm
- High intensity
- Small horizontal and vertical electron beam dimensions and divergences
- A short bunch length
- Good extraction of synchrotron radiation
- A range of undulators
- Adequate beam lifetime

The published design of this machine envisages an electron energy of 800 MeV, a magnetic field of 1 T, a bending radius of 1.83 m, a stored current of 1 A, and a beam size of (horizontal \times vertical) $44 \times 38 \mu\text{m}$. The costs of building and operating such a machine would be very much less than those of the high-energy (5 GeV) ESRF, thus making this design attractive for soft X-ray studies.

In the United States, the Advanced Light Source (ALS), to be situated at the Lawrence Berkeley Laboratory, is designed to cover both the soft X-ray and higher-energy regime. The machine will operate at a nominal energy of 1.3 GeV, with a peak energy of 1.9 GeV, and will have several different wigglers and undulators to cover different spectral regions. The predicted spectral brilliances are of the same order of magnitude as those of the ESRF.

For smaller, laboratory, sources, development is continuing on conventional types of source utilizing electron impact, in particular to devise methods of increasing the electron current⁽⁹⁾ and to investigate target materials and geometries suitable for soft X-ray production.⁽¹⁰⁾ Considerable work has recently been carried out on laser plasma sources, using both high-⁽¹¹⁾ and low-power⁽¹²⁾ lasers, and in the near future systematic studies are planned of soft X-ray production as a function of laser pulse energy, length and shape, the frequency of the laser light, and the target material. The major development required for such sources is, however, in laser technology, the requirements being high energy per pulse, large pulse repetition rate, and compact size.

Perhaps the most exciting possibility, for the long term, is the development of X-ray lasers.^(13,14) Recently, amplification has been reported at wavelengths of 20.63 and 20.96 nm (corresponding to transitions in neonlike ions of selenium) and 15.50 and 15.71 nm (the same transitions in yttrium),^(15,16) and at a wavelength of 10.25 nm (corresponding to a transition in hydrogenlike ions of oxygen).⁽¹⁷⁾ Considerable effort is now going into achieving amplification at shorter wavelengths.^(18,19)

11.3. New Developments in Soft X-Ray Optics

Developments in the manufacture of grazing incidence optical system are likely to be, in the main, improvements on existing techniques such as surface figuring and assessment, and perhaps in the selection of new (e.g., ceramic) materials. The most significant developments in optical systems will probably be in the manufacture of multilayer mirrors and of amplitude and phase zone plates. In order to design and manufacture these to give efficiencies higher than currently obtainable, it will be necessary to know the optical constants of materials in the soft X-ray region, particularly the refractive index decrements, to a higher precision than at present. Methods of determining these are discussed below.

11.3.1. Measurement of Soft X-Ray Optical Constants

Optical constants for the X-ray region are usually derived from bulk reflectance⁽²⁰⁻²²⁾ or absorption⁽²³⁻²⁶⁾ measurements, using the Kramers-Kronig relation⁽²⁷⁾

$$\delta(\nu) = (2/\pi)P \int_0^{\infty} \nu' \beta(\nu') / (\nu'^2 - \nu^2) d\nu \quad (11.1)$$

where P stands for principal part. Thus, provided that the imaginary part of the complex refractive index, related to the absorption coefficient by equation (1.4), is known over the entire frequency range, the refractive index decrement may be calculated (or vice versa). In most cases, the knowledge of the absorption coefficient is fragmentary over some part of the frequency range, and so estimates have to be used.^(28,29) It would clearly be much more satisfactory to measure the absorption coefficients and the refractive index decrements directly at as many X-ray wavelengths as possible, and recently a method of doing this using transmission gratings⁽³⁰⁾ has been reported. Assuming ideal gratings with rectangular profiles (Figure 11.1), if the ratios of the first- to zeroth-order intensities for two gratings with parameters (g_1, d_1, w_1) and (g_2, d_2, w_2) are

$$A_1 = I_1^{(1)} / I_1^{(0)} \quad (11.2)$$

and

$$A_2 = I_2^{(1)} / I_2^{(0)} \quad (11.3)$$

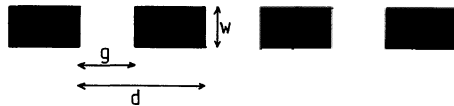


Figure 11.1. Profile of an ideal rectangular transmission grating.

then the optical constants δ and β may be obtained from⁽³¹⁾

$$(1 + B_1) \cos 2\pi w_1 \delta - \cosh 2\pi w_1 \beta + B_1 \cosh (2\pi w_1 \beta + r_1) = 0 \quad (11.4)$$

$$(1 + B_2) \cos 2\pi w_2 \delta - \cosh 2\pi w_2 \beta + B_2 \cosh (2\pi w_2 \beta + r_2) = 0 \quad (11.5)$$

where

$$r_1 = \ln [g_1/(d_1 - g_1)] \quad (11.6)$$

$$r_2 = \ln [g_2/(d_2 - g_2)] \quad (11.7)$$

$$B_1 = A_1(\pi^2/4)[\sin^2(\pi g_1/d_1) \cosh^2(r_1/2)]^{-1} \quad (11.8)$$

and

$$B_2 = A_2(\pi^2/4)[\sin^2(\pi g_2/d_2) \cosh^2(r_2/2)]^{-1} \quad (11.9)$$

If the grating profiles are not exactly rectangular, then equations (11.4) and (11.5) remain valid so long as

$$w \ll (d - g) \quad (11.10)$$

The gratings used in these experiments were up to 250 nm thick so that, for $d = 2g$ and $g = 10w$, gratings with 200 lines mm⁻¹ would be required, leading to very small amounts of dispersion. Thus it is better to use gratings with more lines per millimeter and with bars wider than $0.5d$ in order to maintain the condition (11.10). Gold gratings with between 400 and 3300 lines mm⁻¹ and thicknesses between 97.5 and 250 nm have been used to obtain optical constant data in the wavelength range 2.2–3.4 nm using the experimental arrangement shown schematically in Figure 11.2. The results are summarized in Table 11.1, the major source of error being poor repeatability of the grating wheel position. Other sources of error, relatively unimportant for the measurements carried out so far, include variations of g , d , and w over the grating surfaces, and the presence of harmonics in the incident radiation. Typical results from other determinations of the optical constants are also shown, for

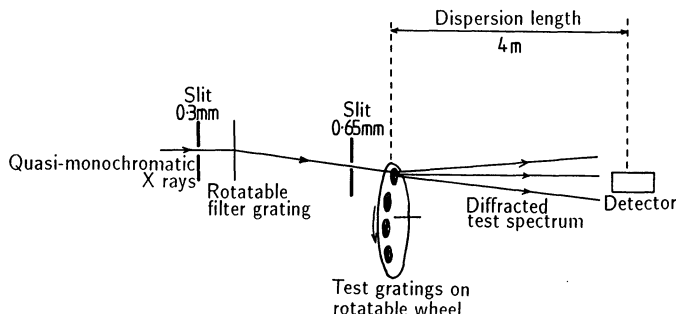


Figure 11.2. A schematic of the experimental arrangement for the measurement of optical constants using transmission gratings. (After Tatchyn *et al.*⁽³⁰⁾)

comparison, in Table 11.1. The main conclusion that can be drawn from this comparison is that the optical constants are not well determined, and in order to be able to use them with any confidence further measurements are required. In particular cases it may be desirable to measure the optical constants under conditions approaching their conditions of use, such as in the *in situ* measurements carried out in multilayer mirror manufacture. In this case, however, it is still not possible to design a multilayer mirror for incidence angles and wavelengths other than those monitored.

Another method, which has not yet been used, would be to measure the diffraction efficiencies of zone plates as functions of thickness,⁽³²⁾ thus utilizing the phase-changing properties of the zone material. This would

Table 11.1. Optical Constants of Gold Determined by Transmission Grating Measurements

Wavelength (nm)	Other measurements						
	A_1^a	A_2^b	δ (±50%)	β (±50%)	δ	β	Ref.
2.2	0.4078	0.685	0.0062	0.0044	0.0035	0.0029	21
					0.0044	0.0039	26
2.4	0.454	0.6996	0.0070	0.0040	0.0038	0.0038	21
					0.0048	0.0045	26
2.6	0.505	0.6946	0.0076	0.0038	0.0054	0.0051	26
					0.0062	0.0057	26
2.8	0.536	0.6788	0.0084	0.0038	0.0041	0.0061	21
					0.007	0.0064	26
3.1	0.568	0.718	0.0094	0.0038	0.0048	0.0062	21
					0.0039	0.0154	22
3.4	0.61	0.685	0.010	0.0039	0.0078	0.0071	26

^aGrating 1: $w_1 = 97.5 \text{ nm}$, $d_1 = 2.5 \text{ m}$, $l_1/d_1 = 0.31$.

^bGrating 2: $w_2 = 200 \text{ nm}$, $d_2 = 2.5 \text{ m}$, $l_2/d_2 = 0.56$.

require the replication of a master zone plate pattern into various thicknesses of material, so that differences in efficiency due to zone boundary placement errors could be minimized. Such measurements could be analyzed in two ways, the simplest being to experimentally determine which thickness gives the highest efficiency, i.e., to select which thickness gives the optimum phase-changing properties. The second approach, leading to more difficulties in analysis, would be to use equation (8.174) for the diffraction efficiency of a phase-modulating zone plate, to extract the optical constant information.

11.3.2. Advances in Multilayer Mirror Manufacture

The manufacturing technology for multilayer mirrors on flat substrates has now reached a relatively advanced stage, and such mirrors are now commercially available. Useful mirrors have also been manufactured on curved substrates. Most of the improvements foreseeable are to existing technologies such as the *in situ* monitoring techniques. When good data on optical constants become available, it will be possible to test mirrors at angles and wavelengths other than those for which they are designed, while still remaining confident about their performance under the design conditions.

Of the manufacturing techniques discussed in Chapter 5, only the laser deposition method has not been developed to a high degree of sophistication. The main element missing is *in situ* monitoring, but it should be possible to rectify this as indicated in Figure 11.3. The first laser pulse is loosely focused onto the evaporation target, causing the material to evaporate and be deposited on the multilayer mirror surface. The next pulse is tightly focused onto the monitoring target, causing the formation of a plasma and the emission of X rays that are reflected from

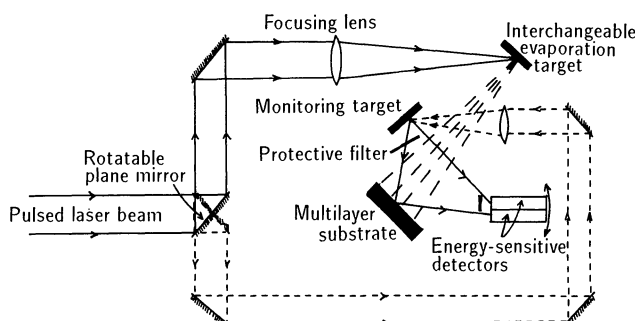


Figure 11.3. Schematic arrangement for multilayer mirror manufacture by laser deposition with *in situ* monitoring.

the mirror surface, which is protected from debris by a thin film, transparent to the X rays, as shown. The detectors must be energy sensitive because the plasma emits X rays over a range of wavelengths (Chapter 1), and the change in reflectivity of the multilayer mirror is measured by monitoring both the X-ray energy produced and that reflected. The process is repeated, using alternate pulses for evaporation and monitoring, until the reflectivity measurements indicate that a change of layer material is required, at which time the evaporation targets are interchanged. The monitoring target will also have to be movable so that a new area of the target can be presented to the laser beam every few pulses, to prevent large decreases in X-ray production due to cratering of the target surface.

11.3.3. Advances in Amplitude Zone Plate Manufacture

The methods discussed for zone plate manufacture in Chapter 9 would appear to be adequate for the short term. However, only the contamination lithography technique appears to be possibly applicable to higher-resolution zone plates, and even for this some development will be necessary to allow accurate patterns to be drawn and replicated into heavy metals. In this section, two other techniques possibly suitable for making zone plates with minimum line widths ~ 10 nm or less will be discussed. Some progress has been made toward the implementation of the first of these, while the second is more speculative.

11.3.3.1. Sputtered Sliced Zone Plates⁽³³⁾

In this process, the zones are formed by alternately sputtering materials with high and low absorption coefficients onto a rotating wire, which is then sliced to form the final zone plate. In order to obtain a wire with uniform diameter (variations smaller than the outermost zone width), the technique illustrated in Figure 11.4 is used.⁽³⁴⁾ In this, a glass tube containing a small amount of metal is heated in an oven until the glass softens and the metal melts. Suitable glasses are Pyrex, Duran, and Supramex, and alloys of gold with silicon or germanium can be used. If the softened glass is then quickly drawn into a tube of smaller diameter, a round metal filament is produced, the surface quality of which reproduces that of the fire-polished glass surface. After cooling, the glass covering the filament may be removed by etching with hydrofluoric acid. The roundness of the wire, which can be as small as $10\text{ }\mu\text{m}$ in diameter, can be determined by illuminating it with a laser and measuring the Fraunhofer diffraction pattern. This allows the diameter to be measured to an accuracy of about 10 nm, and variations can be detected by rotating the

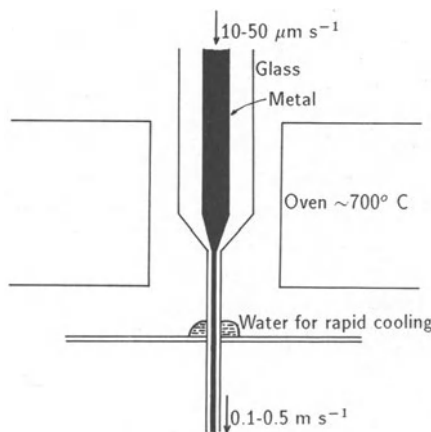


Figure 11.4. Technique for obtaining a uniform diameter wire for the core of sputtered sliced zone plates. (After Taylor.⁽³⁴⁾)

wire and repeating the measurements. Surface roughness can be derived from ripples in the interference maxima.

The layers are sputtered onto this wire using the apparatus shown schematically in Figure 11.5. The beam from the ion source hits a water-cooled arrangement that can hold three different target materials. After passing through a double slit, the sputtered material impinges on the rotating wire, behind which is a slab monitored by a microbalance. This allows the layer thicknesses to be measured. To reduce the effects of variations in the sputtering rate, each layer is deposited in two steps. After about 95–98% of the estimated deposition time, the slits are closed. The extra amount of material needed to complete the layer is then calculated from the microbalance measurements, and this is then sputtered onto the wire. The layer thicknesses can, in this way, be deposited to an accuracy of about one part in 10^4 .

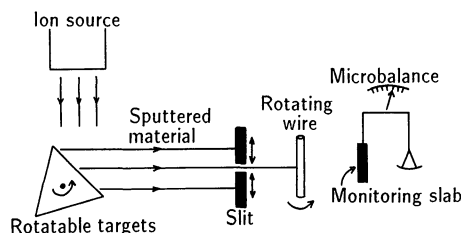


Figure 11.5. Arrangement for sputtering alternate layers of different material onto a rotating wire. (After Rudolf *et al.*⁽³³⁾)

After evaporation of all the layers the wire is strengthened by electroplating with about 100 µm of gold or copper, and then it is embedded in epoxy and sliced using a precision lathe with a diamond tool perpendicular to the wire axis. This causes distortion to a depth of about 200 nm, which is removed by ion milling. The ion-milled surface is glued to a supporting disk, and the other surface is turned and ion milled to give a final thickness of a few hundred nanometers.

Although very promising for the manufacture of high-resolution zone plates, this technique has not yet produced any usable components, mainly because of extreme difficulties in eliminating distortions caused by the slicing step.

11.3.3.2. *Electron Drilling of Metal β -Aluminas⁽³⁸⁾*

A focused electron beam, about 1 nm in diameter, will rapidly drill small holes about 2 nm wide in sodium β - and β'' -alumina, lithium β -alumina, potassium β -alumina, lead β -alumina, and silver β -alumina. This has two advantages over standard lithographic techniques, in that it has higher resolution and it is direct, involving no chemical development (in which it is similar to contamination lithography). Using a scanning transmission electron microscope, the same as those used in the lithographic processes described in Chapter 9, uniform 2-nm-diameter holes were cut through self-supporting 100-nm-thick polycrystalline specimens. Lines and holes greater than 2 nm wide could be drilled by moving the probe around. With a probe current density of about 10^8 A m^{-2} a drilling rate of 25 nm sec^{-1} was observed, with the holes growing inwards from each surface. There appeared to be no change in the quality of the drilled holes when the incident electron energy was varied between 40 and 100 keV. It is considered that the etching is due to the ionization of atoms in the specimen, which then react chemically to leave the hole.

Once cut, these materials are stable and, for example, will withstand exposure to air without degradation of the patterns. Thus it would be conceivable to use this technique to directly write freestanding zone plates. Using the etching rate quoted above, however, each 2-nm-wide hole would take 4 sec to drill in a 100-nm-thick substrate. The number of holes of radius r_h needed for a zone plate of radius r_N is $r_N^2/2r_h^2$, which, for a zone plate with 100 zones and an outermost zone width of 10 nm, is 2×10^6 . Thus the whole pattern would take about 100 days to draw, which is clearly too long. The way out of this would be to increase the probe current density (that used in contamination lithography is, for example, 10^{11} A m^{-2}); even so, some method of monitoring drift would have to be implemented. There has been no report on the quality of holes drilled, or the etching rate, for higher current densities.

Electron beam writing on the same scale has also been carried out on other materials. On sodium chloride crystals, for example, the process proceeds at a faster rate.⁽³⁶⁾ However, the crystals are not self-supporting.

11.3.4. The Manufacture of Phase Zone Plates

Using measured absorption coefficients and calculated refractive index decrements, a phase zone plate made of silver has been manufactured.⁽³⁷⁾ Designed for use at the aluminum K_{α} line (i.e., a wavelength of 0.834 nm), this zone plate has 100 zones each about 550 nm thick and a minimum zone width of 320 nm. The manufacture was a several stage process, the first being the generation of a pattern by electron-beam lithography. This was then replicated into resist on a polyimide-covered silicon substrate using X-ray lithography, and the resulting pattern was electroplated with silver to a thickness controlled by a profilometer. After the resist was dissolved, the zone plate was mounted on a brass ring and the silicon substrate was etched away, leaving the silver phase zone plate supported on a 500 nm-thick polyimide membrane.

The predicted diffraction efficiencies of this zone plate (using the calculated value of the refractive index decrement) are ~26% in the first order, ~4% in the zeroth order, and a total of ~38% in all other orders, with the remainder of the incident energy being absorbed. These values have not yet been experimentally verified, so that there is no confirmation that the correct values of the optical constants were used in the design.

11.4. New Uses of Soft X Rays

As soft X-ray sources and optical components continue to be developed, it is inevitable that they will be used in new and improved systems. It is impossible to give an exhaustive account of such uses, and in this section a selection of possibilities, most of which have already undergone some investigation, will be considered.

11.4.1. Applications of Multilayer Mirrors

Multilayer mirrors are, potentially, the most versatile of the various types of soft X-ray focusing device, because a large range of parameters are open to choice. Their use in spectrometers for laser plasma diagnostics has already been discussed, in Section 10.5.4, and an

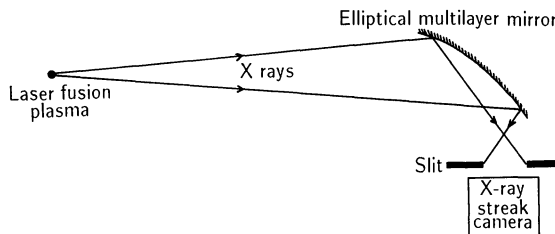


Figure 11.6. A spectrometer for laser fusion studies using a graded period elliptical multilayer mirror. (After Day *et al.*⁽³⁸⁾)

advanced design of such a system is shown in Figure 11.6.⁽³⁸⁾ This uses a long-focal-length elliptical or parabolic mirror⁽³⁹⁾ that has a period graded from one end to the other, allowing the complete wavelength range from 1 to 12 nm to be covered. After passing through a slit at the focus of the mirror, the reflected beam is dispersed along the entrance slit of an X-ray streak camera, giving time-resolved spectra with a resolution of ≤ 20 psec and a resolving power ($\lambda/\Delta\lambda$) of 20 to 50. Such a system would not be possible without the ability to freely design the diffracting system (i.e., the multilayer mirror).

Using multilayer mirrors on thin (transparent) substrates (or, ideally, freestanding multilayers), X-ray beam splitters can be constructed, as shown in Figure 11.7^(40,41). For a freestanding tungsten/carbon multilayer with 45 layer pairs designed for use at the oxygen K_{α} line ($\lambda = 2.36$ nm) and a Bragg angle of 45° , calculations show that about 8% of the s-polarized radiation is reflected and about 35% is transmitted. These figures can, of course, be varied, with increased reflection leading to decreased transmission and vice versa, the optimum setting depending on the experimental requirements.

Because the refractive index decrements are very small for X rays, the Brewster angle θ_B ,⁽⁴²⁾ given by

$$\tan \theta_B = 1 - \delta \quad (11.11)$$

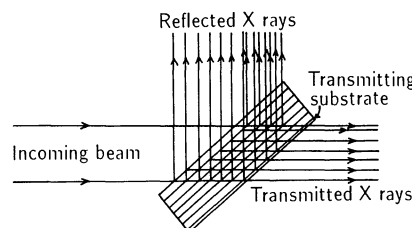


Figure 11.7. A multilayer beam splitter for X rays.

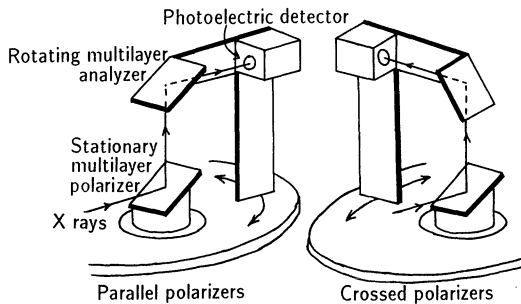


Figure 11.8. A double 45° crossed Bragg polarimeter for soft X rays. (After Khandar and Dhez.⁽⁴³⁾)

is very close to 45°. Thus the p-polarized component of the reflected radiation becomes very small at incidence angles near 45°, so that multilayer mirrors can be used as efficient linear polarizers.^(41,43) Figure 11.8 shows an experimental double 45° crossed Bragg polarimeter used to demonstrate the polarization effects of multilayer mirrors.⁽⁴³⁾ This has been used with a hafnium/silicon multilayer, with a period of 27 nm, at a wavelength of 30.4 nm, and a linear polarization

$$P = |(R_s - R_p)/(R_s + R_p)| \quad (11.12)$$

where R_s and R_p are the s- and p-polarized reflectivities, of 87% was obtained. Using measured refractive index decrements a polarization of 89% can be calculated; this demonstrates that such measurements could be used, in principle, to measure the optical constants.

Normal incidence multilayers are of interest for use in X-ray telescopes, and can overcome the problems of high cost, broadband response, and poor off-axis performance of grazing incidence telescopes. A tungsten/carbon-coated 1-m-diameter, 10-m-focal-length, parabolic mirror has, for example, been suggested for solar imaging purposes.⁽⁴¹⁾ This has a total geometric area of 0.78 m² and an effective collection area of about 0.18 m² for three strong solar emission lines at wavelengths of 4.922 nm (Si XI), 5.052 nm (Si X), and 5.534 nm (Si IX). Although the separation of the first two of these lines is only 0.13 nm, a multilayer collector tuned to one of them has a calculated background rejection of 26:1 at the other. The use of normal incidence X-ray telescopes in other areas of astronomy has also been considered.⁽⁴⁴⁾

Another use that has been discussed for normal incidence multilayer mirrors is in X-ray lasers.⁽⁴⁵⁾ As in conventional (longer wavelength) lasers, these will be used at the ends of the cavity to increase the path available for amplification.

11.4.2. Scanning Photoelectron Microscopy

Photoelectron microscopy was discussed briefly in Section 10.4.4 as an alternative imaging technique in contact microradiography. This involved no focusing of the X-ray beam, apart from that in a monochromator. Another technique using photoelectrons is scanning photoelectron microscopy.⁽⁴⁶⁾ In this, a sample with thickness less than the soft X-ray absorption length is placed on a thin metal foil and bombarded, from the foil side, by a rastered beam. Characteristic X rays are produced in the foil and these generate photoelectrons in the sample surface. The lateral resolution is approximately equal to the total thickness of the foil plus specimen and, to approach the theoretical limit of $\sim 1 \mu\text{m}$,⁽⁴⁷⁾ it will be necessary to use synchrotron radiation with a focusing monochromator such as a zone plate.

11.4.3. Three-Dimensional Imaging Using Soft X Rays

There are several possibilities for extracting three-dimensional information from soft X-ray images.⁽⁴⁸⁾ Of these, two techniques involving focusing could perhaps be implemented in the near future. The first of these⁽⁴⁹⁾ is similar to computerized tomography, and utilizes the natural divergence of the X-ray beam, along with object tilt. In principle, for 3-D image reconstruction, a complete angular set of 2-D image projections is required to give an unambiguous and unique reconstruction. In practice, in a zone plate scanning microscope for example, the tilting angle of the object will be geometrically restricted. Reconstructions from the resulting incomplete set of projections will be spatially distorted but can be improved using *a priori* information. In scanning X-ray microscopy, two arrangements are possible, the first using fan beam illumination and a linear array detector to provide a set of 2-D projections, and the second using cone beam illumination and a 2-D array detector. The latter method may place less stringent requirements on the scanning and tilting mechanisms.

The other 3-D imaging technique to be discussed here is X-ray holography.⁽⁵⁰⁾ Three possible recording geometries are shown in Figure 11.9. The first of these, the Gabor in-line hologram (Figure 11.9a), does not use a focusing system, the reference beam being formed by the radiation transmitted through the specimen. In order to separate the required wavefront it is best to place the recording surface in the far field of the object, and holograms of this type have been recorded using microfocus X-ray sources⁽⁵¹⁾ and synchrotron sources.^(50,52-54) Those recorded with the microfocus source suffered from long exposure times ($\sim 1 \text{ hr}$) and low resolution ($\geq 4 \mu\text{m}$), and useful holograms are only

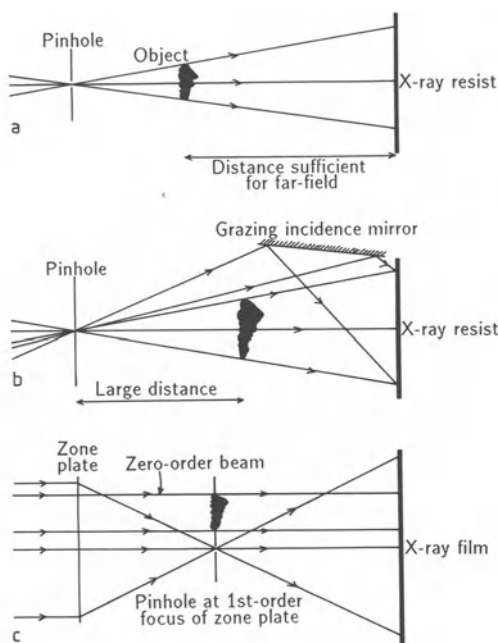


Figure 11.9. Hologram recording geometries: (a) Gabor, (b) Leith–Upatneiks, (c) Fourier transform. (After Howells.⁽⁵⁰⁾)

obtainable with brighter sources, synchrotrons allowing submicrometer resolutions with exposure times of a few minutes at wavelengths in the soft X-ray region. There has, however, been little success in reconstructing the holograms using visible light lasers, but it is considered that the problems (connected with spherical aberration caused by the wavelength change and resolution limitations due to recording conditions and the signal to noise ratio) are not insurmountable.

In the Leith–Upatneiks recording geometry (Figure 11.9b), a grazing incidence mirror is used to generate an off-axis reference beam, allowing separation of the two beams. However, this method requires a higher-resolution detector and a source with greater coherence length than for the Gabor geometry, and has not yet been used for recording X-ray holograms.

In the Fourier transform recording geometry (Figure 11.9c), the reference beam radiates from a point source that must be the same distance from the recording surface as the object is. For X-ray holography, the reference beam can be generated by placing a pinhole at the first-order focus of a zone plate, and the object is illuminated by the zero-order radiation from the same zone plate. To maintain temporal

coherence the lateral distance between the object and the pinhole should be approximately equal to the object size, which means that the interfering beams are at a small angle and the resulting fringes at the detector are coarsely spaced. The resolution is, in this case, not limited by the spatial resolution of the detector but by the size of the reference beam pinhole. The detector resolution does, however, limit the field of view. To date, X-ray holograms have not been recorded using this geometry.

Until X-ray lasers are developed, methods to isolate the coherent part of an incoherent source must be used in order to allow holograms to be recorded.⁽⁵⁰⁾ This may be done using the Van Cittert-Zernicke theorem,⁽⁵⁵⁾ according to which the output of a source is spatially coherent within the region defined by the first minimum of the Fraunhofer diffraction pattern of its spatial distribution. Thus, for a circular source of radius s , spatial coherence exists within the Airy cone of half angle α and the upper limit on the emittance of a coherent beam of wavelength λ is

$$\varepsilon_{\max} = s\alpha = 0.61\lambda \quad (11.13)$$

Thus, at the nitrogen K_α line ($\lambda = 3.2$ nm), $\varepsilon_{\max} = 1.95$ mrad μm so that, even for a source radius of ~ 50 μm (typical of the best current storage rings), only about 0.04 mrad of the angular spread of the radiation can be utilized. This applies to both the horizontal and the vertical emittance and, at best, only one in 10^7 of the photons emitted by the source can be used coherently.

For temporal coherence, it is necessary that the coherence length

$$l_c = \lambda^2/\Delta\lambda \quad (11.14)$$

should allow coherent illumination of the whole thickness of the specimen, as well as being longer than the largest path difference between the interfering beams. Since soft X rays can penetrate several micrometers of material, l_c should be ~ 10 μm , which, at a wavelength of 3.1 nm, requires $\Delta\lambda \sim 10^{-12}$ m (i.e., $\lambda/\Delta\lambda \sim 3 \times 10^3$), which is a higher resolving power than that easily attainable with most present soft X-ray monochromators. However, it is less difficult to holographically image specimens ~ 1 μm thick (needing $\lambda/\Delta\lambda \sim 300$).

The present limit to X-ray holographic imaging is in the fluxes available from current sources. For a signal to noise ratio of 5:1, the total flux I_G (photons sec^{-1}) needed for a Gabor hologram is given by⁽⁵⁰⁾

$$I_G t \geq 10^4 \lambda^3 w^4 / \delta^8 \Delta\lambda \quad (11.15)$$

where w is the working distance, δ is the resolution, and t is the recording time. For a Fourier transform hologram,

$$I_F t \geq 2.9 \times 10^2 N^4 \quad (11.16)$$

where N^2 is the total number of resolution elements in the image. For a 100×100 array the total number of photons required for a Fourier transform hologram is thus about 3×10^{10} and early synchrotrons are not capable of giving this number of (coherent) photons in reasonable times. The high-brightness synchrotron sources now under construction or planned will be able to give the necessary coherent power, particularly from undulator beam lines, and Fourier transform holography offers a good chance of achieving high-resolution three-dimensional biological imaging.

11.5. Conclusions

In any rapidly advancing field it is impossible to give a completely up-to-date account of achievements, and there can be little doubt that refinements to many of the concepts, techniques, and applications discussed in this and the preceding chapters will soon be accomplished. It is to be expected, in particular, that better and better optical systems will become available, and that these will be put to new uses that will allow the properties of soft X-ray photons to be more fully utilized. The next few years should see the realization of several goals in high-resolution imaging, for example in the study of living biological cells; in the study of laser plasmas, allowing advances in the quest for fusion energy sources; in the understanding of astrophysical sources of X rays; in the search for high-power soft X-ray sources; and other goals that have not yet been conceived.

References

Preface

1. G. Feinberg, *Solid Clues*, Heinemann, London (1985).
2. M. C. Hutley, *Diffraction Gratings*, Techniques of Physics 6 (N. H. March and H. N. Daglish, eds.), Academic Press, New York (1982).
3. G. W. Stroke, Diffraction gratings, in: *Handbuch der Physik XXIX* (S. Flugge, ed.), pp. 426–754, Springer, Berlin (1967).
4. M. J. Simpson, Design considerations of zone plate optics for a scanning transmission x-ray microscope, Ph.D. thesis, London University (1984).

Chapter 1

1. B. K. Agarwal, *X-Ray Spectroscopy*, Springer Series in Optical Sciences, Vol. 15, Chapters 3–5, pp. 121–239, Springer, Berlin (1979).
2. A. H. Compton and S. K. Allison, *X-Rays in Theory and Experiment*, 2nd ed., pp. 116–262 and 472–582, Van Nostrand, Princeton, N.J. (1935).
3. B. L. Henke, Low energy x-ray interactions: Photoionization, scattering, specular and Bragg reflection, in: *Low Energy X-Ray Diagnostics* (D. T. Attwood and B. L. Henke, eds.), AIP Conference Proceedings No. 75, pp. 146–155, American Institute of Physics, New York (1981).
4. W. T. Scott, *The Physics of Electricity and Magnetism*, 2nd ed., pp. 6–14, Wiley, New York (1966).
5. D. T. Cromer and D. Lieberman, Relativistic calculation of anomalous scattering factors for x-rays, *J. Chem. Phys.* **53**, 1891–1898 (1970).
6. M. S. Jensen, Some remarks on the anomalous scattering factors for x-rays, *Phys. Lett. A*, **74**, 41–44 (1979).
7. R. W. James, *The Optical Principles of the Diffraction of X-Rays*, pp. 166–167, Cornell University Press, Ithaca, N.Y. (1965).
8. S. T. Manson, Theory of sub-keV photoionization cross sections, in: *Low Energy X-Ray Diagnostics* (D. T. Attwood and B. L. Henke, eds.), AIP Conference Proceedings No. 75, pp. 156–161, American Institute of Physics, New York (1981).

9. H. A. Lorentz, *The Theory of Electrons and Its Application to the Phenomena of Light and Radiant Heat*, p. 48, Dover, New York (1952).
10. B. L. Henke, P. Lee, T. J. Tanaka, R. L. Shimabukuro, and B. K. Fujikawa, The atomic scattering factor, $f_1 + if_2$, for 94 elements and for the 100 to 2000 eV photon energy region, in: *Low Energy X-Ray Diagnostics* (D. T. Attwood and B. L. Henke, eds.), AIP Conference Proceedings No. 75, pp. 340–388, American Institute of Physics, New York (1981).
11. J. D. Jackson, *Classical Electrodynamics*, 2nd ed., pp. 672–679, Wiley, New York (1975).
12. A. A. Sokolov and J. M. Ternov, *Synchrotron Radiation*, Pergamon Press, Elmsford, N.Y. (1968).
13. S. Krinsky, M. L. Perlman, and R. E. Watson, Characteristics of synchrotron radiation and of its sources, in: *Handbook on Synchrotron Radiation* (E.-E. Koch, ed.), Vol. 1, pp. 65–171, North-Holland, Amsterdam (1983).
14. V. L. Ginzburg and S. I. Syrovatskii, Developments in the theory of synchrotron radiation and its reabsorption, *Ann. Rev. Astron. Astrophys.*, **7**, 375–420 (1969).
15. N. Marks and M. W. Poole, The choice of dipole magnetic field for the SRS, Daresbury Nuclear Physics Laboratory Report DL/TM129 (1974).
16. E.-E. Koch, D. E. Eastman, and Y. Farge, Synchrotron radiation—a powerful tool in science, in: *Handbook on Synchrotron Radiation* (E.-E. Koch, ed.), Vol. 1, pp. 1–63, North-Holland, Amsterdam (1983).
17. A. N. Chu, M. A. Piestrup, T. W. Barbee, Jr., R. H. Pantell, and F. R. Buskirk, Observation of soft x-ray transition radiation from medium energy electrons, *Rev. Sci. Instrum.*, **51**, 597–601 (1980).
18. Y. A. Bazylev and N. K. Zhevago, Intense electromagnetic radiation from relativistic particles, *Sov. Phys. Usp.*, **25**, 565–595 (1982).
19. A. H. Compton and S. K. Allison, *X-Rays in Theory and Experiment*, 2nd ed., pp. 97–115, Van Nostrand, Princeton, N.J. (1935).
20. B. K. Agarwal, *X-Ray Spectroscopy*, Springer Series in Optical Sciences, Vol. 15, pp. 35–46, Springer, Berlin (1979).
21. A. H. Compton and S. K. Allison, *X-Rays in Theory and Experiment*, 2nd ed., pp. 89–90, Van Nostrand, Princeton, N.J. (1935).
22. V. W. Slivinsky, X-ray emission from laser fusion targets, in: *Low Energy X-Ray Diagnostics* (D. T. Attwood and B. L. Henke, eds.), AIP Conference Proceedings No. 75, pp. 6–7, American Institute of Physics, New York (1981).
23. G. O'Sullivan, P. K. Carroll, T. J. McIlrath, and M. L. Ginter, Rare-earth plasma light source for VUV applications, *Appl. Opt.*, **20**, 3043–3046 (1981).
24. M. Kühne, Radiometric comparison of a laser-produced plasma and a BRV-source plasma at normal incidence, *Appl. Opt.*, **21**, 2124–2128 (1982).
25. D. J. Nagel, C. Brown, M. Peckarar, M. L. Ginter, J. Robinson, and T. J. McIlrath, Repetitively-pulsed soft x-ray plasma source, *Appl. Opt.*, **23**, 1428–1433 (1984).
26. M. L. Ginter, Laser produced plasma VUV and soft x-ray light sources, in: *X-Ray Microscopy* (G. Schmahl and D. Rudolph, eds.), Springer Series in Optical Sciences, Vol. 43, pp. 25–29, Springer, Berlin (1984).
27. R. A. McCorkle, High intensity pulsed electron beam plasma source, in: *Ultrasoft X-Ray Microscopy: Its Application to Biological and Physical Sciences*, (D. F. Parsons, ed.), Ann. N.Y. Acad. Sci. Vol. 342, pp. 53–64 (1980).
28. G. Ballofet, J. Romand, and B. Vodar, An emission source of continuous spectrum extending from the visible to the extreme ultraviolet, *C.R. Acad. Sci.*, **252**, 4139–4141 (1961).
29. J. Bailey, Y. Ettinger, A. Fisher, and R. Feder, Evaluation of the gas puff z pinch as an x-ray lithography and microscopy source, *Appl. Phys. Lett.*, **40**, 33–35 (1982).

30. K. W. Hill, M. Bitter, D. Eames, S. von Goeler, N. R. Sauthoff, and E. Silver, Low energy x-ray emission from magnetic fusion plasmas, in: *Low Energy X-Ray Diagnostics* (D. T. Attwood and B. L. Henke, eds.), AIP Conference Proceedings No. 75, pp. 8–24, American Institute of Physics, New York (1981).
31. L. P. Mix, E. J. T. Burns, D. L. Fehl, D. L. Hanson, and D. J. Johnson, Low energy x-ray emission from light ion targets, in: *Low Energy X-Ray Diagnostics* (D. T. Attwood and B. L. Henke, eds.), AIP Conference Proceedings No. 75, pp. 25–31, American Institute of Physics, New York (1981).
32. J. C. Riordan, J. S. Pearlman, M. Gersten, and J. E. Rauch, Sub-kilovolt x-ray emission from imploding wire plasmas, in: *Low Energy X-Ray Diagnostics* (D. T. Attwood and B. L. Henke, eds.), AIP Conference Proceedings No. 75, pp. 35–43, American Institute of Physics, New York (1981).
33. L. Spitzer, *Physics of Fully Ionized Gases*, Interscience, New York (1962).
34. G. O'Sullivan, The origin of line-free XUV continuum emission from laser-produced plasmas of the elements $62 \leq Z \leq 74$, *J. Phys. B*, **16**, 3291–3304 (1983).
35. D. Colombant and G. F. Tonon, X-ray emission in laser-produced plasmas, *J. Appl. Phys.*, **44**, 3524–3527 (1973).
36. J. G. Timothy and R. P. Madden, Photon detectors for the ultraviolet and x-ray region, in: *Handbook on Synchrotron Radiation* (E.-E. Koch, ed.), Vol. 1, pp. 315–366, North-Holland, Amsterdam (1983).
37. E. Spiller, Soft x-ray optics and microscopy, in: *Handbook on Synchrotron Radiation* (E.-E. Koch, ed.), Vol. 1, pp. 1091–1129, North-Holland, Amsterdam (1983).
38. J. H. Underwood and D. T. Attwood, The renaissance of x-ray optics, *Phys. Today*, **37**(4), 44–52 (1984).
39. M. Born and E. Wolf, *Principles of Optics*, 5th ed., pp. 38–41, Pergamon Press, Elmsford, N.Y. (1975).
40. E. Spiller, Low-loss reflection coatings using absorbing materials, *Appl. Phys. Lett.*, **20**, 365–367 (1972).
41. Lord Rayleigh, Resolution in optical images, *Philos. Mag. Ser. 5*, **8**, 261–274 (1879).
42. E. Abbe, Resolution of microscopes, *Arch. Mikrosk. Anat.*, **9**, 413–425 (1873).

Chapter 2

1. M. Born and E. Wolf, *Principles of Optics*, 5th ed., pp. 47–51, Pergamon Press, Elmsford, N.Y. (1975).
2. J. A. Prins, Reflection of x-rays by absorbing ideal crystals, *Z. Phys.*, **63**, 477–493 (1930).
3. V. Rehn, Focusing, filtering and scattering of soft x-rays by mirrors, in: *Low Energy X-Ray Diagnostics* (D. T. Attwood and B. L. Henke, eds.), AIP Conference Proceedings No. 75, pp. 162–169, American Institute of Physics, New York (1981).
4. L. A. Smirnov, Differential equations describing total external reflection of x-rays, *Opt. Spectrosc.*, **43**, 333–334 (1977).
5. C. G. Darwin, The theory of x-ray reflexion, *Philos. Mag.*, **27**, 315–333, 675–690 (1914).
6. R. W. James, *The Optical Principles of the Diffraction of X-Rays*, pp. 35–36, Cornell University Press, Ithaca, N.Y. (1965).
7. A. Franks and B. Gale, Grazing incidence optics for x-ray microscopy, in: *X-Ray Microscopy* (G. Schmahl and D. Rudolph, eds.), Springer Series in Optical Sciences, Vol. 43, pp. 129–138, Springer, Berlin (1984).

8. L. A. Smirnov, T. D. Sotnikova, B. S. Anokhin, and B. Z. Taibin, Total external reflection of x-rays from rough surfaces, *Opt. Spectrosc.*, **46**, 329–332 (1979).
9. A. Franks, Advances in x-ray optics at the National Physical Laboratory, *J. Phys. (Paris) C2*, **45**, 69–72 (1984).
10. P. Debye, Interference of Röntgen rays and heat motions, *Ann. Phys. (Leipzig)*, **43**, 49–95 (1914).
11. P. Kirkpatrick and A. V. Baez, Formation of optical images by x-rays, *J. Opt. Soc. Am.*, **38**, 766–774 (1948).
12. V. E. Cosslett and W. C. Nixon, *X-Ray Microscopy*, p. 87, Cambridge University Press, London (1960).
13. A. Franks, X-ray optics, *Sci. Prog. (London)*, **64**, 371–422 (1977).
14. E. Abbe, Resolution of microscopes, *Arch. Mikrosk. Anat.*, **9**, 413–425 (1873).
15. F. Jentzsch, Optische Versuch mit Röntgenstrahlen, *Phys. Z.*, **30**, 268–273 (1929).
16. J. Dyson, Optics of the focusing x-ray microscope, *Proc. Phys. Soc. London Sect. B*, **65**, 580–589 (1952).
17. A. V. Baez, Design of x-ray microscope mirrors using an electronic computer, in: *X-Ray Microscopy and Microradiography* (V. E. Cosslett, A. Engstrom, and H. H. Pattee, eds.), pp. 186–194, Elsevier, Amsterdam (1957).
18. J. F. McGee, D. R. Hesser, and J. W. Milton, X-ray reflection optics (recent developments), in: *Proc. Vth Int. Congress on X-Ray Optics and Microanalysis* (G. Mollenstedt and K. H. Gankler, eds.), pp. 11–26, Springer, Berlin (1969).
19. Y. T. Thathachari, Theory of image formation in combinations of X-ray focusing mirrors, *Proc. Indian Acad. Sci. A*, **37**, 41–62 (1953).
20. M. Montel, The x-ray microscope with catamegonic roof-shaped objective, in: *X-Ray Microscopy and Microradiography* (V. E. Cosslett, A. Engstrom, and H. H. Pattee, eds.), pp. 177–185, Elsevier, Amsterdam (1957).
21. H. H. Pattee, The compound, four-mirror, reflection x-ray microscope, in: *X-Ray Microscopy and Microradiography* (V. E. Cosslett, A. Engstrom, and H. H. Pattee, eds.), pp. 135–150, Elsevier, Amsterdam (1957).
22. H. Wolter, Mirror systems with grazing incidence as image-forming optics for x-rays, *Ann. Phys. 6th Ser.*, **10**, 94–114 (1952).
23. K. Schwarzschild, Untersuchungen zur Geometrischen Optik, *Abh. Ges. Wiss. Goettingen Math. Phys. Kl. N.F.4*, No. 1–3 (1905).
24. H. Wolter, Generalized Schwarzschild systems of mirrors with glancing reflection as optical systems for x-rays, *Ann. Phys. 6th Ser.*, **10**, 286–295 (1952).
25. R. C. Chase and L. P. Van Speybroeck, Wolter–Schwarzschild telescopes for x-ray astronomy, *Appl. Opt.*, **12**, 1042–1044 (1973).

Chapter 3

1. D. Korsch, C. L. Wyman, and L. M. Perry, Influence of alignment and surface defects on the performance of x-ray telescopes, *Space Optics—Imaging X-Ray Optics Workshop*, *Proc. SPIE 184*, 211–222 (1979).
2. B. Gale and M. Stedman, Non spherical mirrors in x-ray optics, *Aspheric Optics: Design, Manufacturing, Testing*, *Proc. SPIE 235*, 21–26 (1980).
3. E. Spiller, Soft x-ray optics and microscopy, in: *Handbook on Synchrotron Radiation* (E.-E. Koch, ed.), Vol. 1, pp. 1091–1129, North-Holland, Amsterdam (1983).
4. P. A. J. de Korte, R. Giralt, J. N. Coste, C. Ernu, S. Frindel, J. Flamand, and J. J.

- Contet, EXOSAT x-ray imaging optics, *Appl. Opt.*, **20**, 1080–1088 (1981).
5. M. Stedman, T. H. English, and A. Franks, New design of mirror bending block, *Reflecting Optics for Synchrotron Radiation*, *Proc. SPIE* **315**, 69–74 (1981).
 6. A. Franks, Advances in x-ray optics at the National Physical Laboratory, *J. Phys. (Paris) C2*, **45**, 69–72 (1984).
 7. A. Franks, The metrology of x-ray optical components, in: *Low Energy X-Ray Diagnostics* (D. T. Attwood and B. L. Henke, eds.), AIP Conference Proceedings No. 75, pp. 179–188, American Institute of Physics, New York (1981).
 8. K. Lindsey and A. Franks, Metal optics versus glass optics, *Advances in Optical Production Technology*, *Proc. SPIE* **163**, 46–54 (1979).
 9. R. E. Engdahl, Chemical vapour deposited (CVD) silicon carbide mirror technology, *Reflecting Optics for Synchrotron Radiation*, *Proc. SPIE* **315**, 123–130 (1981).
 10. V. Rehn and W. J. Choyke, SiC mirrors for synchrotron radiation, *Nucl. Instrum. Methods*, **177**, 173–178 (1980).
 11. A. Franks, X-ray telescope mirrors—materials, manufacture, tolerances and technology, *Space Optics—Imaging X-Ray Optics Workshop*, *Proc. SPIE* **184**, 110–122 (1979).
 12. K. Lindsey, R. Morrell, and M. J. Hanney, Ceramic materials as mirrors for synchrotron radiation, *Reflecting Optics for Synchrotron Radiation*, *Proc. SPIE* **315**, 140–147 (1981).
 13. M. M. Kelly and J. B. West, Fabrication and use of silicon carbide mirrors for synchrotron radiation, *Reflecting Optics for Synchrotron Radiation*, *Proc. SPIE* **315**, 135–139 (1981).
 14. H. L. Gerth, Introduction to precision machining of metal optics, *Reflecting Optics for Synchrotron Radiation*, *Proc. SPIE* **315**, 225–229 (1981).
 15. D. M. Miller and N. Laegreid, PNL—diamond turning capability, in: *Workshop on X-Ray Instrumentation for Synchrotron Radiation Research* (H. Winick and G. Brown, eds.), SSRL Report No. 78/04, pp. VII39–VII42, Stanford Linear Accelerator Center (1978).
 16. A. Franks, Materials problems in the production of high quality optical surfaces, *Mater. Sci. Eng.* **19**, 169–183 (1975).
 17. C. V. Muffoletto, Reflective and refractive scattering of ultraviolet radiation caused by state of the art optical grinding and polishing techniques, *Reflecting Optics for Synchrotron Radiation*, *Proc. SPIE* **315**, 85–88 (1981).
 18. G. M. Sanger, Optical fabrication technology, the present and future, *Contemporary Methods of Optical Manufacturing and Testing*, *Proc. SPIE* **433**, 2–18 (1983).
 19. R. L. Gentilman and E. A. Maguire, Chemical vapor deposition of silicon carbide for large area mirrors, *Reflecting Optics for Synchrotron Radiation*, *Proc. SPIE* **315**, 131–134 (1981).
 20. K. Parker and H. Shah, The stress of electroless nickel deposits on beryllium, *J. Electrochem. Soc.*, **117**, 1091–1094 (1970).
 21. R. E. Parks, Traditions of optical fabrication, *Reflecting Optics for Synchrotron Radiation*, *Proc. SPIE* **315**, 56–64 (1981).
 22. R. Lainé, R. Giralt, R. Zobl, P. A. J. de Korte, and J. A. M. Bleeker, X-ray imaging telescope on EXOSAT, *Space Optics—Imaging X-Ray Optics Workshop*, *Proc. SPIE* **184**, 181–188 (1979).
 23. P. A. J. de Korte, The current state of x-ray and XUV replica optics, in: *New Techniques in X-Ray and XUV Optics*, *Proc. RAL Symp.* (B. J. Kent and B. E. Patchett, eds.), RL-83-010, pp. 37–49, Rutherford Appleton Laboratory (1983).
 24. A. Franks, X-ray focusing by bent glass optics, in: *Workshop on X-Ray Instrumentation for Synchrotron Radiation Research* (H. Winick and G. Brown, eds.), SSRL Report No. 78/04, pp. VII128–VII141, Stanford Linear Accelerator Center (1978).

25. J. A. Howell and P. Horowitz, Ellipsoidal and bent cylindrical condensing mirrors for synchrotron radiation, *Nucl. Instrum. Methods*, **125**, 225–230 (1975).
26. J. H. Underwood and D. Turner, Bent glass optics, *X-Ray Imaging, Proc. SPIE* **106**, 125–135 (1977).
27. M. Stedman, A parabolic collimator of adjustable incidence angle and constant focal length, in: *Workshop on X-Ray Instrumentation for Synchrotron Radiation Research* (H. Winick and G. Brown, eds.), SSRL Report No. 78/04, pp. VII142–VII147, Stanford Linear Accelerator Center (1978).
28. R. A. Beth, Statics of elastic bodies, in: *Handbook of Physics* (E. U. Condon and H. Odishaw, eds.), 2nd ed., pp. 3.64–3.77, McGraw-Hill, New York (1967).
29. M. Stedman and V. W. Stanley, A machine for the rapid and accurate measurement of profile, *Advances in Optical Production Technology, Proc. SPIE* **163**, 99–102 (1979).
30. M. Stedman, Metrological evaluation of grazing incidence mirrors, *High Resolution Soft X-Ray Optics, Proc. SPIE* **316**, 2–8 (1981).
31. C. A. Wallace, D. F. Paul, and K. Lindsey, Production and evaluation of supersmooth x-ray synchrotron mirror surfaces, *Reflecting Optics for Synchrotron Radiation, Proc. SPIE* **315**, 186–192 (1981).
32. R. S. Longhurst, *Geometrical and Physical Optics*, 3rd ed., p. 352, Longmans, London (1973).
33. M. J. Downs, Surface Profile Interferometer, British Patent No. 8037689 (1980).
34. C. F. Bruce and B. S. Thornton, Obliquity effects in interference microscopes, *J. Sci. Instrum.*, **34**, 203–204 (1957).
35. J. M. Bennett, Measurement of RMS roughness, autocovariance function and other statistical properties of optical surfaces using a FECO scanning interferometer, *Appl. Opt.*, **15**, 2705–2721 (1976).
36. D. W. Butler, A stereo electron microscope technique for microtopographic measurements, *Micron*, **4**, 410–424 (1973).
37. P. S. Young, Fabrication of the high-resolution mirror assembly for the HEAO-2 x-ray telescope, *Space Optics—Imaging X-Ray Optics Workshop, Proc. SPIE* **184**, 131–138 (1979).
38. S. Mrowka, W. Harris, and R. J. Speer, Short wavelength interferometric testing of x-ray optics, *High Resolution Soft X-Ray Optics, Proc. SPIE* **316**, 16–20 (1981).
39. B. Aschenbach, H. Bräuninger, A. Ondrusch, and P. Predehl, X-ray scattering of superpolished flat mirror samples, *High Resolution Soft X-Ray Optics, Proc. SPIE* **316**, 187–193 (1981).
40. J. R. H. Herring, The evaluation of highly polished surface quality using grazing incidence soft x-ray reflection and scattering, in: *New Techniques in X-Ray and XUV Optics, Proc. RAL Symp.* (B. J. Kent and B. E. Patchett, eds.), RL-83-010, pp. 85–101, Rutherford Appleton Laboratory (1983).
41. J. C. Rife and J. F. Osantowski, Optical constants in the extreme ultraviolet and soft x-ray region, *Reflecting Optics for Synchrotron Radiation, Proc. SPIE* **315**, 103–107 (1981).
42. K. Lindsey and A. B. Penfold, Production and assessment of supersmooth optical surfaces, *Opt. Eng.*, **15**, 220–225 (1976).

Chapter 4

1. J. H. Underwood and T. W. Barbee, Jr., Synthetic multilayers as Bragg diffractors for x-rays and extreme ultraviolet: Calculations of performance, in: *Low Energy X-Ray*

- Diagnostics* (D. T. Attwood and B. L. Henke, eds.), AIP Conference Proceedings No. 75, pp. 170–178, American Institute of Physics, New York (1981).
2. J. H. Underwood and T. W. Barbee, Jr., Layered synthetic microstructures as Bragg diffractors for x-rays and extreme ultraviolet: Theory and predicted performance, *Appl. Opt.*, **20**, 3027–3034 (1981).
 3. L. G. Parratt, Surface studies of solids by total reflection of x-rays, *Phys. Rev.*, **45**, 359–369 (1954).
 4. A. E. Rosenbluth and P. Lee, Bragg condition in absorbing x-ray multilayers, *Appl. Phys. Lett.*, **40**, 466–468 (1982).
 5. R. Marmoret and J. M. Andre, Bragg reflectivity of layered synthetic microstructures in the x-ray anomalous scattering region, *Appl. Opt.*, **22**, 17–19 (1983).
 6. P. Lee, X-ray diffraction in multilayers, *Opt. Commun.*, **37**, 159–164 (1981).
 7. B. Videl and P. Vincent, Metallic multilayers for x-rays using classical thin-film theory, *Appl. Opt.*, **23**, 1794–1801 (1984).
 8. A. H. Saxena and B. P. Schoenborn, Multilayer neutron monochromators. *Acta Crystallogr. Sect. A*, **33**, 805–813 (1977).
 9. C. G. Darwin, The theory of x-ray reflexion, *Philos. Mag. Series 6*, **27**, 315–332 (1914).
 10. C. G. Darwin, The theory of x-ray reflexion, Part II, *Philos. Mag. Series 6*, **27**, 675–690 (1914).
 11. C. G. Darwin, Reflection of x rays from imperfect crystals, *Philos. Mag. Series 6*, **43**, 800–829 (1922).
 12. P. P. Ewald, The crystal-optics of x rays (I), *Ann. Phys. (Leipzig)*, **54**, 519–556 (1917).
 13. P. P. Ewald, The crystal-optics of x rays (II), *Ann. Phys. (Leipzig)*, **54**, 557–597 (1917).
 14. P. P. Ewald, Bragg's reflection law for Röntgen rays, *Phys. Z.*, **21**, 617–619 (1920).
 15. P. P. Ewald, The refractive index for x rays and the deviations from Bragg's law of reflection, *Z. Phys.*, **30**, 1–13 (1924).
 16. P. P. Ewald, Reflection of Röntgen rays, *Phys. Z.*, **26**, 29–32 (1925).
 17. W. H. Zachariasen, *Theory of X-Ray Diffraction in Crystals*, pp. 111–155, Wiley, New York (1945).
 18. B. L. Henke, P. Lee, T. J. Tanaka, R. L. Shimabukuro and B. K. Fujikawa, The atomic scattering factor, $f_1 + if_2$, for 94 elements and for the 100 to 2000 eV photon energy region, in: *Low Energy X-Ray Diagnostics* (D. T. Attwood and B. L. Henke, eds.), AIP Conference Proceedings No. 75, pp. 340–388, American Institute of Physics, New York (1981).
 19. J. A. Prins, Reflection of x-rays by absorbing ideal crystals, *Z. Phys.*, **63**, 477–493 (1930).
 20. A. V. Vinogradov and B. Y. Zeldovich, X-ray and far UV multilayer mirrors: Principles and possibilities, *Appl. Opt.*, **16**, 89–93 (1977).
 21. E. Spiller, High quality Fabry–Perot mirrors for the ultraviolet, *Optik (Stuttgart)*, **39**, 118–125 (1973).
 22. R.-P. Haelbich, A. Segmüller, and E. Spiller, Smooth multilayer films suitable for x-ray mirrors, *Appl. Phys. Lett.*, **34**, 184–186 (1979).
 23. P. Debye, Interference of Röntgen rays and heat motion, *Ann. Phys. (Leipzig)*, **43**, 49–95 (1914).
 24. E. Spiller, A scanning soft x-ray microscope using normal incidence mirrors, in: *X-Ray Microscopy* (G. Schmahl and D. Rudolph, eds.), Springer Series in Optical Sciences, Vol. 43, pp. 226–231, Springer, Berlin (1984).
 25. E. Spiller, Evaporated multilayer dispersion elements for soft x-rays, in: *Low Energy X-Ray Diagnostics* (D. T. Attwood and B. L. Henke, eds.), AIP Conference Proceedings No. 75, pp. 124–130, American Institute of Physics, New York (1981).

26. K. Schwarzschild, Untersuchungen zur Geometrischen Optik, *Abh. Ges. Wiss. Goettlingen Math. Phys. Kl. N.F.* 4, No. 1–3 (1905).

Chapter 5

1. A. E. Rosenbluth and J. M. Forsyth, The reflecting properties of soft x-ray multilayers, in: *Low Energy X-Ray Diagnostics* (D. T. Attwood and B. L. Henke, eds.), AIP Conference Proceedings No. 75, pp. 280–285. American Institute of Physics, New York (1981).
2. R.-P. Haelbich, A. Segmüller, and E. Spiller, Smooth multilayer films suitable for x-ray mirrors, *Appl. Phys. Lett.*, **34**, 184–186 (1979).
3. T. W. Barbee, Jr., Sputtered layered synthetic microstructure (LSM) dispersion elements, in: *Low Energy X-Ray Diagnostics* (D. T. Attwood and B. L. Henke, eds.), AIP Conference Proceedings No. 75, pp. 131–145, American Institute of Physics, New York (1981).
4. H. Koeppe, Dissertation, Giessen (1929).
5. W. Deubner, Reflection of x-rays from artificially prepared bodies of laminated structure, *Ann. Phys. (Leipzig)*, **5**, 261–280 (1930).
6. J. Dumond and J. P. Youtz, An x-ray method of determining rates of diffusion in the solid state, *J. Appl. Phys.*, **11**, 357–365 (1940).
7. J. Dinklage and R. Frerichs, X-ray diffraction and diffusion in metal film layered structures, *J. Appl. Phys.*, **34**, 2633–2635 (1963).
8. J. Dinklage, X-ray diffraction by multilayered thin-film structures and their diffusion, *J. Appl. Phys.*, **38**, 3781–3785 (1967).
9. E. Spiller, A. Segmüller, J. Rife, and R.-P. Haelbich, Controlled fabrication of multilayer soft x-ray mirrors, *Appl. Phys. Lett.*, **37**, 1048–1050 (1980).
10. S. V. Gaponov, S. A. Gusev, B. M. Luskin, N. N. Salaschenko, and E. S. Gluskin, Long-wave x-ray radiation mirrors, *Opt. Commun.*, **38**, 7–9 (1981).
11. E. Spiller, Evaporated multilayer dispersion elements for soft x-rays, in: *Low Energy X-Ray Diagnostics* (D. T. Attwood and B. L. Henke, eds.), AIP Conference Proceedings No. 75, pp. 124–130, American Institute of Physics, New York (1981).
12. E. Spiller, The design of multilayer coatings for soft x-rays and their application for imaging and spectroscopy, in: *New Techniques in X-Ray and XUV Optics, Proc. RAL Symp.* (B. J. Kent and B. E. Patchett, eds.), RL-83-010, pp. 50–69, Rutherford Appleton Laboratory (1983).
13. B. L. Henke, P. Lee, T. J. Tanaka, R. L. Shimabukuro, and B. K. Fujikawa, The atomic scattering factor, $f_1 + if_2$, for 94 elements and for the 100 to 2000 eV photon energy region, in: *Low Energy X-Ray Diagnostics* (D. T. Attwood and B. L. Henke, eds.), AIP Conference Proceedings No. 75, pp. 340–388, American Institute of Physics, New York (1981).
14. A. E. Rosenbluth, Reflecting properties of x-ray multilayer devices, Ph.D. thesis, University of Rochester (1982).
15. R.-P. Haelbich and C. Kunz, Multilayer interference mirrors for the XUV range around 100 eV photon energy, *Opt. Commun.*, **17**, 287–292 (1976).
16. E. Spiller, A scanning soft x-ray microscope using normal incidence mirrors, in: *X-Ray Microscopy* (G. Schmahl and D. Rudolph, eds.), Springer Series in Optical Sciences, Vol. 43, pp. 226–231, Springer, Berlin (1984).
17. A. N. Broers and E. Spiller, A comparison of high resolution scanning electron micrographs of metal film coatings with soft x-ray interference measurements of the film

- roughness, in: *Scanning Electron Microscopy I* (O. Johari, ed.), pp. 201–208, SEM Inc., AMF O'Hare (1980).
18. K. L. Chopra, *Thin Film Phenomena*, McGraw-Hill, New York (1970).
 19. L. J. Maissel and R. Glang (eds.), *Handbook of Thin Film Technology*, McGraw-Hill, New York (1971).
 20. J. L. Vossen and W. Kern (eds.), *Thin Film Processes*, Academic Press, New York (1978).
 21. S. Schiller, U. Heisig, and K. Goedcke, Use of the ring gap plasmatron for high rate sputtering, *Thin Solid Films*, **40**, 327–334 (1977).
 22. R.-P. Haelbich, Untersuchung der Eigenschaften von Mehrschichtinterferenzspiegeln aus absorbierenden materialen und ihre Verwendung in einem Rastermikroskop fur weiche Röntgenstrahlung, DESY Internal Report, DESY F41, HASYLAB 80/03 (1980).
 23. T. W. Barbee, Jr., Multilayers for x-ray optical applications, in: *X-Ray Microscopy* (G. Schmahl and D. Rudolph, eds.), Springer Series in Optical Sciences, Vol. 43, pp. 144–162, Springer, Berlin (1984).
 24. R. Kelly, J. J. Cuomo, P. A. Leary, J. E. Rothenberg, B. E. Braren, and C. F. Aliotta, Laser sputtering, Part I. On the existence of rapid laser sputtering at 193 nm, *Nucl. Instrum. Methods Phys. Res.*, **B9**, 329–340 (1985).
 25. S. V. Gaponov, F. V. Garin, S. A. Gusev, A. V. Kochemasov, Y. Y. Planonov, N. N. Salaschenko, and E. S. Gluskin, Multilayer mirrors for soft x-ray and VUV radiation, *Nucl. Instrum. Methods*, **208**, 227–231 (1983).
 26. S. V. Gaponov, E. S. Gluskin, S. A. Gusev, Y. Y. Planonov, and N. N. Salaschenko, Spherical and plane multilayer normal incidence mirrors for soft x-rays, *Opt. Commun.*, **48**, 229–232 (1983).
 27. R. Kelly and J. E. Rothenberg, Laser sputtering. Part III. The mechanism of the sputtering of metals at low energy densities, *Nucl. Instrum. Methods Phys. Res.*, **B7/8**, 755–763 (1985).

Chapter 6

1. M. C. Hutley, *Diffraction Gratings*, Techniques of Physics 6 (N. H. March and H. N. Daglish, eds.), Academic Press, New York (1982).
2. G. W. Stroke, Diffraction gratings, in: *Handbuch der Physik XXIX* (S. Flugge, ed.), pp. 426–754, Springer, Berlin (1967).
3. R. W. James, *The Optical Principles of the Diffraction of X-Rays*, pp. 1–6, Cornell University Press, Ithaca, N.Y. (1965).
4. H. A. Rowland, The concave diffraction grating, *Philos. Mag. Ser. 5*, **13**, 469–474 (1882).
5. H. G. Beutler, The theory of the concave grating, *J. Opt. Soc. Am.*, **35**, 311–350 (1945).
6. T. Namioka, Theory of the concave grating. I, *J. Opt. Soc. Am.*, **49**, 446–460 (1959).
7. F. L. O. Wadsworth, Mountings for concave diffraction gratings, *Astrophys. J.*, **3**, 47–53 (1896).
8. J. E. Mack, J. R. Stehn, and B. Edlén, On the concave grating spectrograph, especially at large angles of incidence, *J. Opt. Soc. Am.*, **22**, 245–261 (1932).
9. H. Noda, T. Namioka, and M. Seya, Geometric theory of the grating, *J. Opt. Soc. Am.*, **64**, 1031–1036 (1974).
10. H. Haber, The torus grating, *J. Opt. Soc. Am.*, **40**, 153–165 (1950).

11. T. Namioka, Theory of the ellipsoidal concave grating. I, *J. Opt. Soc. Am.*, **51**, 4–12 (1961).

Chapter 7

1. M. C. Hutley, *Diffraction Gratings*, Techniques of Physics 6 (N. H. March and H. N. Daglish, eds.), Academic Press, New York (1982).
2. A. Franks, X-ray optics, *Sci. Prog. (London)*, **64**, 371–422 (1977).
3. K. H. Hellwege, Über rasterformiger Reflexionsgitter, *Z. Phys.*, **18**, 625–655 (1933).
4. A. Franks, K. Lindsey, J. M. Bennett, R. J. Speer, D. Turner, and D. J. Hunt, The theory, manufacture, structure and performance of N.P.L. x-ray gratings, *Proc. R. Soc. London Ser. A*, **277**, 503–543 (1975).
5. H. A. Rowland, Imperfections in diffraction grating spectra, *Philos. Mag. Ser. 5*, **35**, 397–419 (1893).
6. V. W. Stanley, A. Franks, and K. Lindsey, A simple ruling engine for x-ray gratings, *J. Sci. Instrum. (J. Phys. E)*, *Ser. 2*, **1**, 643–645 (1968).
7. R. F. Stevens and M. C. Hutley, Interference techniques for generating diffracting optical components, *Advances in Optical Production Technology*, *Proc. SPIE* **163**, 84–91 (1979).
8. M. Breidne and M. Nevière, Grating efficiencies in the soft x-ray region: A comparison of different theories, *Opt. Acta*, **31**, 471–486 (1984).
9. R. Tatchyn, P. L. Csonka, and I. Lindau, Optimization of planar metallic non-refracting transmission grating profiles for nth order intensity maximization in the soft x-ray range, *J. Opt. Soc. Am.*, **72**, 1630–1638 (1972).
10. T. Merton, On the reproduction and ruling of diffraction gratings, *Proc. R. Soc. London Ser. A*, **201**, 187–191 (1950).
11. R. G. N. Hall and L. A. Sayce, On the production of diffraction gratings, II. The generation of helical rulings and the preparation of plane gratings therefrom, *Proc. R. Soc. London Ser. A*, **215**, 536–550 (1952).
12. R. F. Braybrook, A. Franks, F. J. Kirby, and K. Lindsey, Light element microprobe analysis with concave NPL x-ray gratings, in: *Quatrième Congrès International sur l'Optique des Rayons X et la Microanalyse* (R. Castaing, P. Deschamps, and J. Philibert, eds.), pp. 477–479, Hermann, Paris (1966).
13. A. Franks and K. Lindsey, Dispersion of 1A x-rays with NPL x-ray gratings, *J. Sci. Instrum. (J. Phys. E)*, *Ser. 2*, **1**, 144 (1968).
14. P. Predehl, H. Bräuninger, H. Kraus, and J. Trümper, Fabrication of transmission gratings for use in x-ray astronomy, *High Resolution Soft X-Ray Optics*, *Proc. SPIE* **316**, 128–133 (1981).
15. J. M. Bennett, Observation and measurement of surface relief of diffraction gratings using electron microscopy techniques, *J. Sci. Instrum. (J. Phys. E)*, *Ser. 2*, **2**, 816–817 (1969).
16. J. F. Verrill, Use of the Talystep in investigating diffraction grating groove profiles, *J. Sci. Instrum. (J. Phys. E)*, *Ser. 2*, **6**, 1199–1201 (1973).
17. H. Aritome, S. Matsui, K. Moriwaki, H. Aoki, S. Namba, S. Suga, A. Mikuni, M. Seki, and M. Taniguchi, Fabrication method and efficiency of new soft x-ray diffraction gratings: Bakable laminar gratings and transmission gratings for synchrotron radiation spectroscopy, *Nucl. Instrum. Methods*, **208**, 233–236 (1983).
18. A. G. Michette, M. T. Browne, P. Charalambous, R. E. Burge, M. J. Simpson, and P. J. Duke, Fabrication of small linewidth diffractive optics for use with soft x-rays, in:

- X-Ray Microscopy* (G. Schmahl and D. Rudolph, eds.), Springer Series in Optical Sciences, Vol. 43, pp. 109–118, Springer, Berlin (1984).
- 19. E. T. Arakawa and P. J. Caldwell, Holographically produced transmission gratings for soft x-rays, *Nucl. Instrum. Methods*, **172**, 293–296 (1980).
 - 20. H. I. Smith, E. H. Anderson, A. M. Hawryluk, and M. L. Schattenburg, Planar techniques for fabricating x-ray diffraction gratings and zone plates, in: *X-Ray Microscopy* (G. Schmahl and D. Rudolph, eds.), Springer Series in Optical Sciences, Vol. 43, pp. 51–62, Springer, Berlin (1984).
 - 21. Y. Vladimirska, E. Källne, and E. Spiller, Fabrication of free standing x-ray transmission gratings and zone plates, *X-Ray Lithography and Applications of Soft X-Rays to Technology*, *Proc. SPIE* **448**, 25–37 (1984).

Chapter 8

- 1. J. L. Soret, Concerning diffraction by circular gratings, *Ann. Phys. Chem.*, **156**, 99–106 (1875).
- 2. M. Born and E. Wolf, *Principles of Optics*, 5th ed., pp. 378–386, Pergamon Press, Elmsford, N.Y. (1975).
- 3. A. Boivin, On the theory of diffraction by concentric arrays of ring-shaped apertures, *J. Opt. Soc. Am.*, **42**, 60–64 (1952).
- 4. G. N. Watson, *A Treatise on the Theory of Bessel Functions*, Cambridge University Press, London (1922).
- 5. K. Kamiya, Theory of Fresnel zone plate, *Sci. Light (Tokyo)*, **12**, 35–49 (1963).
- 6. M. Born and E. Wolf, *Principles of Optics*, 5th ed., p. 441, Pergamon Press, Elmsford, N.Y. (1975).
- 7. M. Born and E. Wolf, *Principles of Optics*, 5th ed., pp. 397–398, Pergamon Press, Elmsford, N.Y. (1975).
- 8. J. W. Goodman, *Introduction to Fourier Optics*, p. 13, McGraw-Hill, New York (1968).
- 9. M. Born and E. Wolf, *Principles of Optics*, 5th ed., pp. 484–490, Pergamon Press, Elmsford, N.Y. (1975).
- 10. M. J. Simpson, Design considerations of zone plate optics for a scanning transmission x-ray microscope, Ph.D. thesis, London University (1984).
- 11. M. J. Simpson and A. G. Michette, Imaging properties of modified Fresnel zone plates, *Opt. Acta*, **31**, 403–413 (1984).
- 12. H. Rarback and J. Kirz, Optical performance of apodized zone plates, *High Resolution Soft X-Ray Optics*, *Proc. SPIE* **316**, 120–125 (1981).
- 13. H. F. A. Tschunko, Imaging performance of annular apertures, *Appl. Opt.*, **13**, 1820–1823 (1974).
- 14. W. T. Welford, *Aberrations of the Symmetrical Optical System*, p. 60, Academic Press, New York (1974).
- 15. H. E. Hart, J. B. Scrandis, R. Mark, and R. D. Hatcher, Diffraction characteristics of a linear zone plate, *J. Opt. Soc. Am.*, **56**, 1018–1023 (1966).
- 16. C. Gomez-Reino, J. M. Cuadrado, and M. V. P. Martinez, Optically produced linear zone plates, *Appl. Opt.*, **18**, 3032–3034 (1979).
- 17. L. C. Janicijevic, Diffraction characteristics of square zone plates, *J. Opt. (Paris)*, **13**, 199–206 (1982).
- 18. T. R. Welberry and R. P. Williams, On certain non-circular zone plates, *Opt. Acta*, **23**, 237–244 (1976).

19. C. Gomez-Reino, J. M. Cuadrado, and M. V. Perez, Elliptical and hyperbolic zone plates, *Appl. Opt.*, **19**, 1541–1545 (1980).
20. J. M. Cuadrado, R. C. Gomez, and M. V. P. Martinez, Zone Plates produced by cylindrical wavefronts: Recording and reconstruction, *Opt. Acta*, **29**, 717–723 (1982).
21. Z. Knittl and D. Lostakova-Roubova, Fresnel-Soret zone plates with manipulated focus patterns, *Opt. Acta*, **23**, 927–942 (1983).
22. K. K. Dey and P. Khastgir, Frequency dependence of a compounded microwave zone plate, *Proc. Natl. Acad. Sci. India Sect. A*, **51**, 45–48 (1981).
23. G. S. Waldman, Variations on the Fresnel zone plate, *J. Opt. Soc. Am.*, **56**, 215–218 (1966).
24. Lord Rayleigh, Wave theory, in: *Encyclopaedia Britannica*, 9th ed., Vol. 24, pp. 429–451 (1888).
25. R. W. Wood, Phase-reversed zone plates and diffraction telescopes, *Philos. Mag. Ser. 5*, **45**, 511–522 (1898).
26. J. Kirz, Phase zone plates for x-rays and the extreme uv, *J. Opt. Soc. Am.*, **64**, 301–309 (1974).
27. R. O. Tatchyn, Optimum zone plate theory and design, in: *X-Ray Microscopy* (G. Schmahl and D. Rudolph, eds.), Springer Series in Optical Sciences, Vol. 43, pp. 40–50, Springer, Berlin (1984).

Chapter 9

1. W. T. Welford, *Aberrations of the Symmetrical Optical System*, p. 206, Academic Press, New York (1974).
2. M. Born and E. Wolf, *Principles of Optics*, 5th ed., p. 468, Pergamon Press, Elmsford, N.Y. (1975).
3. M. J. Simpson, Design considerations of zone plate optics for a scanning transmission x-ray microscope, Ph.D. thesis, London University (1984).
4. M. J. Simpson and A. G. Michette, The effects of manufacturing inaccuracies on the imaging properties of Fresnel zone plates, *Opt. Acta*, **30**, 1455–1462 (1983).
5. I. Brodie and J. J. Muray, *The Physics of Microfabrication*, Plenum Press, New York (1982).
6. D. C. Shaver, D. C. Flanders, N. M. Ceglio, and H. I. Smith, X-ray zone plates fabricated using electron-beam and x-ray lithography, *J. Vac. Sci. Technol.*, **16**, 1626–1630 (1979).
7. D. P. Kern, P. J. Houzgo, P. J. Coane, and T. H. P. Chang, Practical aspects of microfabrication in the 100 nm region, *J. Vac. Sci. Technol.*, **B1**, 1096–1100 (1983).
8. H. Aritome, H. Aoki, and S. Namba, Focusing characteristics of x-ray zone plates fabricated by electron beam lithography and reactive ion etching, *Jpn. J. Appl. Phys. Part 2*, **23**, L406–L408 (1984).
9. E. Kratschmer, D. Stephani, and H. Beneking, High resolution 100 keV e-beam lithography, in: *Microcircuit Engineering 83* (H. Ahmed, J. R. A. Cleaver, and G. A. C. Jones, eds.), pp. 15–22, Academic Press, New York (1983).
10. J. M. Warlaumont, Status of microstructure fabrication, *High Resolution Soft X-Ray Optics*, *Proc. SPIE* **316**, 109–119 (1981).
11. C. D. Wilkinson, Fabrication of very small structures, in: *Examining the Submicron World* (R. Feder, J. Wm. McGowan, and D. M. Shinozaki, eds.), NATO ASI Series, Series B: Physics, Vol. 137, pp. 215–229, Plenum Press, New York (1986).
12. K. Murata, D. F. Kyser, and C. H. Ting, Monte Carlo simulation of fast secondary

- electron production in electron beam resists, *J. Appl. Phys.*, **52**, 4396–4405 (1981).
- 13. A. N. Broers, J. M. E. Harper, and W. W. Molzen, 250 Å linewidths with PMMA electron resist. *Appl. Phys. Lett.*, **33**, 392–394 (1978).
 - 14. P. Charalambous, Image data collection, contamination and beam writing in the STEM, Ph.D. thesis, London University (1982).
 - 15. L. Reiner and M. Wächter, Contribution to the contamination problem in transmission electron microscopy, *Ultramicroscopy*, **3**, 169–174 (1978).
 - 16. Y. Harada, T. Tomita, T. Watabe, H. Watanabe, and T. Etoh, Reduction of contamination in analytical electron microscopy, *Scanning Electron Microscopy II* (O. Johari and R. P. Becker, eds.), pp. 103–110, SEM Inc., AMF O'Hare (1979).
 - 17. A. N. Broers, J. Cuomo, J. Harper, W. Molzen, R. Laibowitz, and M. Pomerants, High resolution electron beam fabrication using STEM, *Ninth International Congress on Electron Microscopy*, Toronto, Vol. 3, pp. 343–354 (1978).
 - 18. M. T. Browne, P. Charalambous, and R. E. Burge, Uses of contamination in STEM: Projection electron lithography, *Inst. Phys. Conf. Ser.* **61**, 43–44 (1982).
 - 19. A. G. Michette, M. T. Browne, P. Charalambous, R. E. Burge, M. J. Simpson, and P. J. Duke, Fabrication of small linewidth diffractive optics for use with soft x-rays, in: *X-Ray Microscopy* (G. Schmahl and D. Rudolph, eds.), Springer Series in Optical Sciences, Vol. 43, pp. 109–118, Springer, Berlin (1984).
 - 20. A. G. Michette and R. E. Burge, Manufacture and tests of objective zone plates for use in a scanning transmission x-ray microscope, *J. Microsc. (Oxford)*, **138**, 303–309 (1985).
 - 21. C. J. Buckley, M. T. Browne, and P. Charalambous, Contamination lithography for the fabrication of zone plate x-ray lenses, *Electron-Beam, X-Ray and Ion-Beam Techniques for Submicrometer Lithography IV*, Proc. SPIE **537**, 213–217 (1985).
 - 22. E. Spiller and R. Feder, X-ray lithography, in: *X-Ray Optics* (H.-J. Queisser, ed.), Topics in Applied Physics, Vol. 22, pp. 35–92, Springer, Berlin (1977).
 - 23. G. Schmahl and D. Rudolph, High power zone plates as image forming systems for soft x-rays, *Optik (Stuttgart)*, **29**, 577–585 (1969).
 - 24. J. H. Dijkstra, W. de Graaff, and L. J. Lantwaard, Construction of apodized zone plates for solar x-ray image formation, in: *New Techniques in Space Astronomy* (F. Labuhn and R. Lust, eds.), pp. 207–210, Reidel, Dordrecht (1971).
 - 25. D. Rudolph, *Holographische Zonenplatten als abbildende Systeme für die Röntgenastronomie*, Forschungsbericht W74-07 des Bundesministeriums für wissenschaftliche Forschung (1974).
 - 26. G. Schmahl, D. Rudolph, P. Guttmann and O. Christ, Zone plates for x-ray microscopy, in: *X-Ray Microscopy* (G. Schmahl and D. Rudolph, eds.), Springer Series in Optical Sciences, Vol. 43, pp. 63–74, Springer, Berlin (1984).
 - 27. P. Guttmann, Construction of a micro zone plate and evaluation of imaging properties, in: *X-Ray Microscopy* (G. Schmahl and D. Rudolph, eds.), Springer Series in Optical Sciences, Vol. 43, pp. 75–90, Springer, Berlin (1984).
 - 28. J. Thieme, Construction of condenser zone plates for a scanning x-ray microscope, in: *X-Ray Microscopy* (G. Schmahl and D. Rudolph, eds.), Springer Series in Optical Sciences, Vol. 43, pp. 91–96, Springer, Berlin (1984).
 - 29. K. H. von Grote, G. Mollenstedt and R. Spiedel, Preparation of short focal length zone plates for x- and uv-rays, and of correction plates for electron microscopes, *Optik (Stuttgart)*, **22**, 252–269 (1965).
 - 30. B. E. Bol Raap, J. B. le Poole, J. H. Dijkstra, W. de Graaff, and L. J. Lantwaard, X-ray heliography by means of a Fresnel–Soret type zone plate camera, in: *Small Rocket Instrumentation Techniques* (Ken-Ichi Maeda, ed.), pp. 203–210, North-Holland, Amsterdam (1969).

31. H. W. P. Koops and J. Grob, Submicron lithography by demagnifying electron beam projection, in: *X-Ray Microscopy* (G. Schmahl and D. Rudolph, eds.), Springer Series in Optical Sciences, Vol. 43, pp. 119–128, Springer, Berlin (1984).
32. F. Kalk and D. Glocker, Thick zone plate fabrication using reactive sputter etching, *J. Vac. Sci. Technol.*, **19**, 170–172 (1981).
33. D. Glocker and R. Wiseman, A new method for the batch production of micro-Fresnel zone plates, *J. Vac. Sci. Technol.*, **20**, 1098–1100 (1982).
34. Y. Vladimirska, E. Källne, and E. Spiller, Fabrication of free standing x-ray transmission gratings and zone plates, *X-Ray Lithography and Applications of Soft X-Rays to Technology*, Proc. SPIE **448**, 25–37 (1984).
35. D. Rudolph and G. Schmahl, High power zone plates for a soft x-ray microscope, in: *Ultrasoft X-Ray Microscopy: Its Application to Biological and Physical Sciences* (D. F. Parsons, ed.), Ann. N. Y. Acad. Sci. Vol. 342, pp. 94–104 (1980).
36. Y. S. Touloukian and C. X. Ho (eds.), *Thermodynamic Properties of Matter*, IFI/Plenum Data, New York (1970).

Chapter 10

1. R. L. Johnson, Grating monochromators and optics for the VUV and soft x-ray region, in: *Handbook on Synchrotron Radiation* (E.-E. Koch, ed.), Vol. 1, pp. 173–260, North-Holland, Amsterdam (1983).
2. V. Saile and J. B. West, VUV and soft x-ray monochromators for use with synchrotron radiation, *Nucl. Instrum. Methods*, **208**, 199–213 (1983).
3. M. R. Howells, Beam line design for synchrotron spectroscopy in the VUV, *Appl. Opt.*, **19**, 4027–4034 (1980).
4. A. Franks, K. Lindsey, P. R. Stuart, and R. Morrell, Effects of synchrotron generated x-radiation on uncoated and gold-coated elastically bent silica mirrors, in: *Workshop on X-Ray Instrumentation for Synchrotron Radiation Research* (H. Winick and G. Brown, eds.), SSRL Report No. 78/04, pp. VII117–VII127, Stanford Linear Accelerator Center (1978).
5. F. C. Brown, R. Z. Bachrach, and N. Lien, The SSRL ultrahigh vacuum grazing incidence monochromator, *Nucl. Instrum. Methods*, **152**, 73–79 (1978).
6. D. A. Shirley, Beam line chemistry, in: *Workshop on X-Ray Instrumentation for Synchrotron Radiation Research* (H. Winick and G. Brown, eds.), SSRL Report No. 78/04, pp. VII80–VII100, Stanford Linear Accelerator Center (1978).
7. P. Charalambous, Image data collection, contamination and beam writing, Ph.D. thesis, London University (1982).
8. K. P. Miyake, R. Kato, and H. Yamashita, A new mounting of soft x-ray monochromator for synchrotron orbital radiation, *Sci. Light (Tokyo)*, **18**, 39–56 (1969).
9. J. B. West, K. Codling, and G. V. Marr, A grazing incidence monochromator for use with synchrotron radiation, *J. Phys. E*, **7**, 137–144 (1974).
10. M. R. Howells, D. Norman, G. P. Williams, and J. B. West, A grazing incidence monochromator for synchrotron radiation, *J. Phys. E*, **11**, 199–202 (1978).
11. F. C. Brown, R. Z. Bachrach, and N. Lien, The SSRL ultrahigh vacuum grazing incidence monochromator: Design considerations and operating experience, *Nucl. Instrum. Methods*, **152**, 73–79 (1978).
12. M. Salle and B. Vodar, A projected concave grating monochromator with oblique incidence for the far ultraviolet, *C. R. Acad. Sci.*, **230**, 380–382 (1950).

13. E. Källne, J. H. Dijkstra, R. Bartlett, T. Kitchens, R. O. Tatchyn, M. Hecht, and I. Lindau, Analysis of the throughput of a grazing incidence monochromator using transmission gratings, *Reflecting Optics for Synchrotron Radiation, Proc. SPIE* **315**, 178–184 (1981).
14. C. H. Pruett, E. M. Rowe, T. R. Winch, and F. H. Middleton, Recent instrumentation developments at the University of Wisconsin Synchrotron Radiation Center, *Nucl. Instrum. Methods*, **152**, 57 (1978).
15. F. C. Brown, S. L. Hulbert, and N. C. Lien, Extended range computer controlled monochromator for synchrotron radiation, *VI Int. Conf. on Vacuum Ultraviolet Radiation Physics*, Paper III-50 (1980).
16. H. Raback, J. M. Kenney, J. Kirz, M. R. Howells, P. Chang, P. J. Coane, R. Feder, P. J. Houzeg, D. P. Kern, and D. Sayre, Recent results from the Stony Brook scanning microscope, in: *X-Ray Microscopy* (G. Schmahl and D. Rudolph, eds.), Springer Series in Optical Sciences, Vol. 43, pp. 203–216, Springer, Berlin (1984).
17. W. Eberhardt, G. Kalkoffen, and C. Kunz, Grazing incidence monochromator FLIPPER, *Nucl. Instrum. Methods*, **152**, 81–83 (1978).
18. W. Jark, R.-P. Haelbich, H. Hogrefe, and C. Kunz, A new monochromator for the energy range $5 \text{ eV} < h\nu < 1000 \text{ eV}$, *Nucl. Instrum. Methods*, **208**, 315–318 (1983).
19. M. R. Howells, Plane grating monochromators for synchrotron radiation, *Nucl. Instrum. Methods*, **177**, 127–139 (1980).
20. H. Petersen and H. Baumgartel, BESSY SX/700: A monochromator system covering the spectral range $3 \text{ eV} < h\nu < 700 \text{ eV}$, *Nucl. Instrum. Methods*, **172**, 191–193 (1980).
21. W. Werner and H. Visser, X-ray monochromator designs based on extreme off-plane grating mountings, *Appl. Opt.*, **20**, 487–492 (1981).
22. R. Tatchyn and I. Lindau, New monochromator designs for the soft x-ray range, *Nucl. Instrum. Methods Phys. Res.*, **195**, 163–173 (1982).
23. R. Tatchyn, I. Lindau, and P. L. Csonka, Optimization of rectangular transmission gratings: Applications to new monochromator design, *Nucl. Instrum. Methods Phys. Res.*, **195**, 239–243 (1982).
24. J. Als-Nielsen, P. S. Pershan, H. W. Schnopper, E. H. Silver, and N. J. Westergaard, New crystal for 200–1200 eV soft x-ray spectroscopy, *Appl. Opt.*, **21**, 1894–1895 (1982).
25. E. Spiller, A zone plate monochromator for synchrotron radiation, in: *Workshop on X-Ray Instrumentation for Synchrotron Radiation Research* (H. Winick and G. Brown, eds.), SSRL Report No. 78/04, pp. VI44–VI49, Stanford Linear Accelerator Center (1978).
26. A. Guinier and G. Fournet, *Small-Angle Scattering of X-Rays*, Wiley, New York (1955).
27. B. L. Henke and J. W. M. DuMond, Submicroscopic structure determination by long wavelength x-ray diffraction, *J. Appl. Phys.*, **26**, 903–917 (1955).
28. A. Franks, Some developments and applications of microfocus x-ray diffraction techniques, *Br. J. Appl. Phys.*, **9**, 349–352 (1958).
29. A. Elliott, The use of toroidal reflecting surfaces in x-ray diffraction cameras, *J. Sci. Instrum.*, **42**, 312–316 (1965).
30. P. Goby, New applications of Röntgen rays: Mice radiography, *C.R. Acad. Sci.*, **156**, 686–691 (1913).
31. G. Schmahl and D. Rudolph (eds.), *X-Ray Microscopy*, Springer Series in Optical Sciences, Vol. 43, Springer, Berlin (1984).
32. F. Polack, S. Lowenthal, Y. Petroff, and Y. Farge, Selective x-ray absorption microanalysis with synchrotron radiation, *Nucl. Instrum. Methods*, **152**, 289–291 (1978).

33. F. Polack and S. Lowenthal, Photoelectron microscope for x-ray microscopy and microanalysis, *Rev. Sci. Instrum.*, **52**, 207–212 (1981).
34. R. Feder, E. Spiller, J. Topalian, A. N. Broers, W. Gudat, B. J. Panessa, Z. A. Zadunaisky, and J. Sedat, High resolution soft x-ray microscopy, *Science*, **197**, 259–260 (1977).
35. D. Sayre, J. Kirz, R. Feder, D. M. Kim, and E. Spiller, Transmission microscopy of unmodified biological materials: Comparative radiation dosages with electrons and ultrasoft x-ray photons, *Ultramicroscopy*, **2**, 337–349 (1977).
36. R. J. Rosser, X-ray microscopy at Imperial College, in: *X-Ray Microscopy* (G. Schmahl and D. Rudolph, eds.), Springer Series in Optical Sciences, Vol. 43, pp. 242–250, Springer, Berlin (1984).
37. J. L. Magee, Radiation chemistry, *Annu. Rev. Phys. Chem.*, **12**, 389–410 (1961).
38. R. J. Rosser, K. G. Baldwin, R. Feder, D. Bassett, A. Coles, and R. W. Eason, Soft x-ray contact microscopy with nanosecond exposure times, *J. Microsc. (Oxford)*, **138**, 311–319 (1985).
39. D. Rudolph, B. Niemann, G. Schmahl and O. Christ, The Gottingen x-ray microscope and x-ray microscopy experiments at the BESSY storage ring, in: *X-Ray Microscopy* (G. Schmahl and D. Rudolph, eds.), Springer Series in Optical Sciences, Vol. 43, pp. 192–202, Springer, Berlin (1984).
40. S. Aoki and Y. Sakanayagi, An x-ray microscope using grazing incidence toroidal mirrors, in: *Ultrasoft X-Ray Microscopy: Its Application to Biological and Physical Sciences* (D. F. Parsons, ed.), Ann. N. Y. Acad. Sci. Vol. 342, pp. 158–166 (1980).
41. J. Kirz and H. Rarback, Soft x-ray microscopes, *Rev. Sci. Instrum.*, **56**, 1–13 (1985).
42. B. Niemann, G. Schmahl, and D. Rudolph, Status of the scanning x-ray microscope, *High Resolution X-Ray Optics, Proc. SPIE* **316**, 106–108 (1981).
43. F. E. Scire and E. C. Teague, Piezo driven 50 μm range stage with subnanometer resolution, *Rev. Sci. Instrum.*, **49**, 1735–1740 (1978).
44. P. Horowitz and J. A. Howell, A scanning x-ray microscope using synchrotron radiation, *Science*, **178**, 608–611 (1972).
45. P. Horowitz, Some experiences with x-ray and proton microscopes, in: *Short Wavelength Microscopy* (D. F. Parsons, ed.), Ann. N. Y. Acad. Sci. Vol. 306, pp. 203–222 (1978).
46. B. Niemann, The Gottingen scanning x-ray microscope, in: *X-Ray Microscopy* (G. Schmahl and D. Rudolph, eds.), Springer Series in Optical Sciences, Vol. 43, pp. 217–225, Springer, Berlin (1984).
47. P. J. Duke, X-ray microscopy at the Daresbury Laboratory, in: *X-Ray Microscopy* (G. Schmahl and D. Rudolph, eds.), Springer Series in Optical Sciences, Vol. 43, pp. 232–241, Springer, Berlin (1984).
48. E. Spiller, A scanning soft x-ray microscope using normal incidence mirrors, in: *X-Ray Microscopy* (G. Schmahl and D. Rudolph, eds.), Springer Series in Optical Sciences, Vol. 43, pp. 226–231, Springer, Berlin (1984).
49. A. Franks and B. Gale, Grazing incidence optics for x-ray microscopy, in: *X-Ray Microscopy* (G. Schmahl and D. Rudolph, eds.), Springer Series in Optical Sciences, Vol. 43, pp. 129–138, Springer, Berlin (1984).
50. X. Xie, S. Kang, C. Jin, and T. Jin, Soft x-ray microscopy at the Hefei Synchrotron Radiation Laboratory, Preprint from Synchrotron Radiation Instrumentation Conference, Stanford (1985).
51. D. P. Kern, P. J. Houzege, P. J. Coane, and T. H. P. Chang, Practical aspects of microfabrication in the 100 nm regime, *J. Vac. Sci. Technol.*, **B1**, 1096–1100 (1983).
52. J. M. Kenney, C. Jacobsen, J. Kirz, H. Rarback, F. Cinotti, W. Thomlinson, R. Rosser, and G. Schidlovsky, Absorption microanalysis with a scanning soft x-ray

- microscope—Mapping the distribution of calcium in bone, *J. Microsc. (Oxford)*, **138**, 321–328 (1985).
- 53. L. M. Cheng and A. G. Michette, Three dimensional imaging in scanning soft x-ray microscopy, *J. Phys. (Paris) C2*, **45**, 97–100 (1984).
 - 54. D. J. Pugh and P. D. West, An electron source for a microfocus x-ray tube incorporating a single pole magnetic lens and novel focusing system, in: *Developments in Electron Microscopy and Analysis* (D. L. Misell, ed.), I.O.P. Conference Series No. 36, pp. 29–32, The Institute of Physics, London (1977).
 - 55. M. J. Simpson and A. G. Michette, Considerations of zone plate optics for soft x-ray microscopy, *Opt. Acta*, **31**, 1417–1426 (1984).
 - 56. H. Rarback, The development of a scanning soft x-ray microscope, Ph.D. thesis, State University of New York at Stony Brook (1983).
 - 57. H. H. Hopkins, On the diffraction theory of optical images, *Proc. R. Soc. London Ser. A*, **217**, 408–432 (1953).
 - 58. R. E. Burge and J. C. Dainty, Partially coherent image formation in the scanning transmission electron microscope (STEM), *Optik (Stuttgart)*, **46**, 229–240 (1976).
 - 59. C. J. R. Sheppard and A. Choudhury, Image formation in the scanning microscope, *Opt. Acta*, **24**, 1051–1073 (1977).
 - 60. C. J. R. Sheppard and T. Wilson, Image formation in scanning microscopes with partially coherent source and detector, *Opt. Acta*, **25**, 315–325 (1978).
 - 61. V. E. Cosslett and W. C. Nixon, *X-Ray Microscopy*, Cambridge University Press, London (1960).
 - 62. J. C. Buckland-Wright, Quantitative microfocal radiography in medicine, biological research and the quality control industry, *Microscopy—Techniques and Applications*, *Proc. SPIE* **368**, 9–16 (1982).
 - 63. L. Y. Huang, X-ray image convertor microscopy, *Z. Phys.*, **149**, 225–253 (1957).
 - 64. F. Polack and S. Lowenthal, Photoelectron x-ray microscopy: Recent developments, in: *X-Ray Microscopy* (G. Schmahl and D. Rudolph, eds.), Springer Series in Optical Sciences, Vol. 43, pp. 251–260, Springer, Berlin (1984).
 - 65. K. A. Brueckner, Energy deposition in laser heated plasmas, *Phys. Rev. Lett.*, **36**, 677–679 (1976).
 - 66. J. K. Silk, A grazing incidence microscope for x-ray imaging applications, in: *Ultrasoft X-Ray Microscopy: Its Application to Biological and Physical Sciences* (D. F. Parsons, ed.), Ann. N. Y. Acad. Sci. Vol. 342, pp. 116–129 (1980).
 - 67. R. H. Price, X-ray microscopy using grazing incidence reflection optics, in: *Low Energy X-Ray Diagnostics* (D. T. Attwood and B. L. Henke, eds.), AIP Conference Proceedings No. 75, pp. 189–199, American Institute of Physics, New York (1981).
 - 68. N. M. Ceglio, D. T. Attwood, and E. V. George, Zone plate coded aperture imaging of laser produced plasmas, *J. Appl. Phys.*, **48**, 1566–1569 (1977).
 - 69. N. M. Ceglio, The impact of microfabrication technology on x-ray optics, in: *Low Energy X-Ray Diagnostics* (D. T. Attwood and B. L. Henke, eds.), AIP Conference Proceedings No. 75, pp. 210–222, American Institute of Physics, New York (1981).
 - 70. N. M. Ceglio, M. Roth, and A. M. Hawryluk, A streaked x-ray transmission grating spectrometer, in: *Low Energy X-Ray Diagnostics* (D. T. Attwood and B. L. Henke, eds.), AIP Conference Proceedings No. 75, pp. 290–291, American Institute of Physics, New York (1981).
 - 71. G. L. Stradling, T. W. Barbee, Jr., B. L. Henke, E. M. Campbell, and W. C. Mead, Streaked spectrometry using multilayer x-ray interference mirrors to investigate energy transport in laser plasma applications, in: *Low Energy X-Ray Diagnostics* (D. T. Attwood and B. L. Henke, eds.), AIP Conference Proceedings No. 75, pp. 292–296, American Institute of Physics, New York (1981).

72. L. Mertz and N. O. Young, Fresnel transformation of images, in: *Proc. Internat. Conf. on Optical Instruments and Techniques* (K. J. Habell, ed.), pp. 305–312, Chapman & Hall, London (1961).
73. N. O. Young, Fresnel transformation of images, *Sky Telesc.*, **25**, 8–12 (1963).
74. H. L. Caulfield and A. D. Williams, An introduction to holography by shadow casting, *Opt. Eng.*, **12**, 3–7 (1973).
75. W. L. Rogers, L. W. Jones, and W. H. Beierwaltes, Imaging in nuclear medicine with incoherent holography, *Opt. Eng.*, **12**, 13–22 (1973).
76. P. Lee, D. B. van Hulsteyn, A. Hauer, and S. Whitehill, Low energy x-ray imaging of laser plasmas, *Opt. Lett.*, **6**, 196–197 (1981).
77. N. M. Ceglio, Zone plate coded imaging on a microscopic scale, *J. Appl. Phys.*, **48**, 1563–1565 (1977).
78. B. E. Bol Raap, J. B. Le Poole, J. H. Dijkstra, W. de Graaff, and L. J. Lantwaard, X-ray heliography by means of a Fresnel–Soret type zone plate camera, in: *Small Rocket Instrumentation Techniques* (Ken-Ichi Maeda, ed.), pp. 203–210, North-Holland, Amsterdam (1969).
79. G. Krämer, G. Elwert, H. J. Einighammer, H. Bräuninger, and H. H. Fink, Imaging of solar active regions with Fresnel zone plates, *X-Ray Imaging, Proc. SPIE* **106**, 79–84 (1977).
80. R. Giacconi and B. Rossi, A “telescope” for soft x-ray astronomy, *J. Geophys. Res.*, **65**, 773–775 (1960).
81. W. K. H. Schmidt, A proposed x-ray focusing device with wide field of view for use in x-ray astronomy, *Nucl. Instrum. Methods*, **127**, 285–292 (1975).
82. J. R. P. Angel, Lobster eyes as x-ray telescopes, *Space Optics–Imaging X-Ray Optics Workshop, Proc. SPIE* **184**, 84–85 (1979).
83. J. D. Mangus and J. H. Underwood, Optical design of a glancing incidence x-ray telescope, *Appl. Opt.*, **8**, 95–102 (1969).
84. J. D. Mangus, Optical design of glancing incidence extreme ultraviolet telescopes, *Appl. Opt.*, **9**, 1019–1025 (1970).
85. L. P. Van Speybroeck and R. C. Chase, Design parameters of paraboloid–hyperboloid telescopes for x-ray astronomy, *Appl. Opt.*, **11**, 440–445 (1972).
86. R. C. Chase and L. P. Van Speybroeck, Wolter–Schwarzchild telescopes for x-ray astronomy, *Appl. Opt.*, **12**, 1042–1044 (1973).
87. W. Werner, Imaging properties of Wolter I type x-ray telescopes, *Appl. Opt.*, **16**, 764–773 (1977).
88. W. Cash, D. L. Sheeley, and J. H. Underwood, Astronomical applications of grazing incidence telescopes with polynomial surfaces, *Space Optics–Imaging X-Ray Optics Workshop, Proc. SPIE* **184**, 228–233 (1979).
89. D. Korsch, Two-mirror grazing incidence telescopes with one conical surface, *Opt. Eng.*, **18**, 331–334 (1979).
90. B. Aschenbach, X-ray telescopes, *Rep. Prog. Phys.*, **48**, 579–629 (1985).
91. G. S. Vaiana, L. P. Van Speybroeck, M. V. Zombek, A. S. Krieger, J. K. Silk, and A. F. Timothy, The S-054 x-ray telescope experiment in Skylab, *Space Sci. Instrum.*, **3**, 19–76 (1977).
92. J. H. Underwood, J. E. Milligan, A. C. de Loach, and R. C. Hoover, S056 x-ray telescope experiment in the Skylab Apollo telescope mount, *Appl. Opt.*, **16**, 858–869 (1977).
93. J. L. Culhane and P. W. Sanford, *X-Ray Astronomy*, pp. 44–73, Faber & Faber, London (1981).
94. R. C. Catura, L. W. Acton, R. Berthelsdorf, J. L. Culhane, P. W. Sanford, and A. Franks, Cosmic x-ray telescopes for the ARIES rocket observations, *Space Optics–Imaging X-Ray Optics Workshop, Proc. SPIE* **184**, 23–29 (1979).

95. L. P. Van Speybroeck, Einstein Observatory (HEAO-B) mirror design and performance, *Space Optics—Imaging X-Ray Optics Workshop, Proc. SPIE* **184**, 2–11 (1979).
96. R. Giacconi, P. Gorenstein, S. S. Murray, F. Schreier, F. Seward, H. Tananbaum, W. H. Tucker, and L. Van Speybroeck, The Einstein Observatory and future x-ray telescopes, in: *Telescopes for the 1980's, Annu. Rev. Monograph* (G. Burbridge and A. Hewitt, eds.), pp. 195–256, Annual Reviews, Palo Alto, California (1981).
97. F. Seward and A. MacDonald, *Einstein (HEAO-2) Observing Catalog CFA/HEA83-039*, 4th ed. (1983).
98. S. L. Mandelstam, V. G. Kurt, B. I. Valnieck, L. A. Vainstein, E. K. Sheffer, V. A. Slemzin, and I. A. Zhitnik, Instruments for x-ray astronomy, *Adv. Space Res.*, **2**, 293–299 (1983).
99. J. Trümper, B. Aschenbach, and H. Bräuninger, Development of Imaging x-ray telescopes at Max-Planck-Institut Garching, *Space Optics—Imaging X-Ray Optics Workshop, Proc. SPIE* **184**, 12–19 (1979).
100. B. Aschenbach, H. Bräuninger, and G. Kettenring, Design and construction of the Rosat 5 arcsec mirror assembly, *Adv. Space Res.*, **2**, 251–254 (1983).
101. M. V. Zombeck, Advanced x-ray astrophysics facility (AXAF)—Performance requirements and design considerations, *Space Optics—Imaging X-Ray Optics Workshop, Proc. SPIE* **184**, 50–62 (1979).
102. J. M. Davis, A. S. Krieger, J. K. Silk, and R. C. Chase, Quest for ultrahigh resolution in x-ray optics, *Space Optics—Imaging X-Ray Optics Workshop, Proc. SPIE* **184**, 96–108 (1979).
103. R. C. Catura, W. A. Brown, and L. W. Acton, Comparison of Wolter I and Kirkpatrick-Baez x-ray optics for a Spacelab LAMAR facility, *Space Optics—Imaging X-Ray Optics Workshop, Proc. SPIE* **184**, 73–83 (1979).
104. P. Gorenstein, X-ray optics for the LAMAR facility, an overview, *Space Optics—Imaging X-Ray Optics Workshop, Proc. SPIE* **184**, 63–72 (1979).
105. J. Bleeker, J. L. Culhane, L. Koch-Miramond, H. Olthof, H. W. Schnopper, B. G. Taylor, and G. P. Whitcomb, *XMM—X-Ray Multi Mirror Assessment Study, ESA Rep. SCI(83) 2* (1983).
106. D. H. Tomboulian, The experimental methods of soft x-ray spectroscopy and the valence band spectra of the light elements, in: *Handbuch der Physik* (S. Flugge, ed.), Vol. 30, pp. 246–304, Springer, Berlin (1957).
107. A. Franks, X-ray optics, *Sci. Prog. (London)*, **64**, 371–422 (1977).
108. D. J. Fabian, *Soft X-Ray Band Spectra*, Academic Press, New York (1968).
109. E. C. Bruner, Jr., L. W. Acton, W. A. Brown, S. W. Salat, A. Franks, G. Schmidtke, W. Schweizer, and R. J. Speer, X-ray spectrometer spectrograph telescope system, *Space Optics—Imaging X-Ray Optics Workshop, Proc. SPIE* **184**, 270–277 (1979).
110. W. A. Brown, E. C. Bruner, Jr., L. W. Acton, A. Franks, M. Stedman, and R. J. Speer, Paraboloidal x-ray telescope mirror for solar coronal spectroscopy, *Space Optics—Imaging X-Ray Optics Workshop, Proc. SPIE* **184**, 278–284 (1979).
111. J. L. Culhane and L. W. Acton, The solar x-ray spectrum, *Annu. Rev. Astron. Astrophys.*, **12**, 359–381 (1974).

Chapter 11

1. Y. Farge, *European Synchrotron Radiation Facility—The Feasibility Study*, European Science Foundation (1979).
2. Y. Farge and P. J. Duke (eds.), *European Synchrotron Radiation Facility, Supplement I. The Scientific Case*, European Science Foundation (1979).

3. D. J. Thompson and M. W. Poole (eds.), *European Synchrotron Radiation Facility, Supplement II. The Machine*, European Science Foundation (1979).
4. B. Buras and G. V. Marr (eds.), *European Synchrotron Radiation Facility. Supplement III. Instrumentation*, European Science Foundation (1979).
5. D. J. Thompson, Development of an optimised x-ray synchrotron radiation facility, *Nucl. Instrum. Methods Phys. Res.*, **201**, 1–2 (1982).
6. B. Buras and S. Tazzari, European Synchrotron Radiation Facility, Report of the ESRP, 3rd edition, European Synchrotron Radiation Project, c/o CERN, Geneva, Switzerland (1985).
7. D. Attwood, B. Hartline, and R. Johnson, *The Advanced Light Source: Scientific Opportunities*, LBL Pub-5111, Lawrence Berkeley Laboratory, University of California (1984).
8. G. V. Marr and D. J. Thompson (eds.), *An Optimised Vacuum Ultraviolet Storage Ring*, European Science Foundation, North-Holland, Amsterdam (1981).
9. M. Yoshimatsu and S. Kozaki, High brilliance x-ray sources, in: *X-Ray Optics, Applications to Solids* (H.-J. Queisser, ed.), Topics in Applied Physics, Vol. 22, pp. 9–33, Springer, Berlin (1977).
10. A. G. Michette, X-ray microscopy with a rotating anode source, King's College London Internal Report (1985).
11. A. G. Michette, P. C. Cheng, R. W. Eason, F. O'Neill, Y. Owadano, R. J. Rosser, P. Rumsby and M. J. Shaw, Soft x-ray contact microscopy using laser plasma sources, *J. Phys. D.*, **19**, 363–371 (1986).
12. A. G. Michette, C. Hills, F. O'Neill, A. M. Rogoyski, E. Turcu and Y. Owadano, The use of low power pulsed lasers as plasma sources for soft x-ray contact microscopy, to be published in *Proc. 3rd Topical Meeting on Short Wavelength Coherent Radiation: Generation and Applications* (Monterey, 18–24 March, 1986).
13. R. C. Elton, Recent advances in x-ray laser research, in: *Advances in X-Ray Analysis* (C. S. Barrett, D. E. Leyden, J. B. Newkirk, and C. O. Ruud, eds.), Vol. 21, pp. 1–6, Plenum Press, New York (1978).
14. F. V. Bunkin, V. I. Derzhiev, and S. I. Yakovlenko, Prospects for light amplification in the far ultraviolet, *Sov. J. Quantum Electron.*, **11**, 981–997 (1981).
15. M. D. Rosen, P. L. Hagelstein, D. L. Matthews, E. M. Campbell, A. U. Hazi, B. L. Whitten, B. MacGowan, R. E. Turner, R. W. Lee, G. Charatis, G. E. Busch, C. L. Shepard, and P. D. Rockett, Exploding-foil technique for achieving a soft x-ray laser, *Phys. Rev. Lett.*, **54**, 106–109 (1985).
16. D. L. Matthews, P. L. Hagelstein, M. D. Rosen, M. J. Eckart, N. M. Ceglio, A. U. Hazi, H. Medecki, B. J. MacGowan, J. E. Trebes, B. L. Whitten, E. M. Campbell, C. W. Hatcher, A. M. Hawryluk, R. L. Kauffman, L. D. Pleasance, G. Rambach, J. H. Scofield, G. Stone, and T. A. Weaver, Demonstration of a soft x-ray amplifier, *Phys. Rev. Lett.*, **54**, 110–113 (1985).
17. D. L. Matthews, E. M. Campbell, K. Estabrook, C. W. Hatcher, R. L. Kauffman, R. W. Lee, and C. L. Wang, Observation of enhanced emission of the O VIII H line in a recombining laser produced plasma, *Appl. Phys. Lett.*, **45**, 226–228 (1984).
18. S. E. Harris and T. B. Lucatorto (eds.), *Second Topical Meeting on Laser Techniques in the Extreme Ultraviolet*, AIP Conference Proceedings No. 119, American Institute of Physics, New York (1984).
19. K. Boyer, Multiphoton processes and short wavelength lasers, *Proceedings of the Los Alamos Conference on Optics '83, Proc. SPIE* **380**, 348–352 (1983).
20. A. P. Lukirskii, E. P. Savinov, O. A. Ershov, and Y. F. Shepelev, Reflection coefficients of radiation in the wavelength range from 23.6 to 113 Å for a number of elements and substances and the determination of the refractive index and absorption coefficient, *Opt. Spectrosc.*, **16**, 168–172 (1964).

21. O. A. Ershov, I. A. Brytov, and A. P. Lukirskii, Reflection of x-rays from certain substances in the region from 7 to 44 Å, *Opt. Spectrosc.*, **22**, 66–69 (1967).
22. M. Yanagihara, S. Yamaguchi, M. Niwano, Y. Iguchi, A. Yagishita, T. Koide, S. Sato, and T. Sasaki, Optical constants in the soft x-ray region, *Photon Factory Activity Report* (1984).
23. V. A. Fomichev and A. P. Lukirskii, Absorption coefficients of aluminium in the 23.6–410 Å range of ultrasoft x-radiation, *Opt. Spectrosc.*, **22**, 432–434 (1967).
24. R. Haensel, C. Kunz, T. Sasaki, and B. Sonntag, Absorption measurements of copper, silver, tin, gold and bismuth in the far ultraviolet, *Appl. Opt.*, **7**, 301–306 (1968).
25. H. J. Hagemann, W. Gudat, and C. Kunz, Optical constants from the far infrared to the x-ray region: Mg, Al, Cu, Ag, Au, Bi, C, and Al_2O_3 , *J. Opt. Soc. Am.*, **65**, 742–744 (1975).
26. H. J. Hagemann, W. Gudat, and C. Kunz, DESY Report 74/7 (1974).
27. F. Bassani and M. Alterelli, Interaction of radiation with condensed matter, in: *Handbook on Synchrotron Radiation* (E.-E. Koch, ed.), Vol. 1, pp. 463–605, North-Holland, Amsterdam (1983).
28. B. A. Bethe and E. E. Saltpeter, *Quantum Mechanics of One- and Two-Electron Atoms*, Springer, Berlin (1957).
29. D. Y. Smith and E. Shiles, Finite-energy f-sum rules for valence electrons, *Phys. Rev. B*, **17**, 4689–4694 (1978).
30. R. Tatchyn, I. Lindau, E. Källne, M. Hecht, E. Spiller, R. Bartlett, J. Källne, J. H. Dijkstra, A. Hawryluk, and R. Z. Bachrach, The first use of transmission gratings for measurements of optical constants in the soft x-ray region, *Nucl. Instrum. Methods*, **195**, 423–428 (1980).
31. R. Tatchyn, I. Lindau, and E. Källne, Analysis of a new method determining optical constants in the soft x-ray region, *Opt. Acta*, **27**, 1505–1536 (1980).
32. A. G. Michette, Soft x-ray optical properties of materials, SERC Case studentship proposal (1984).
33. D. Rudolph, B. Niemann, and G. Schmahl, Status of the sputtered sliced zone plates for x-ray microscopy, *High Resolution X-Ray Optics, Proc. SPIE* **316**, 103–105 (1981).
34. G. F. Taylor, A method of drawing metallic filaments and a discussion of their properties and uses, *Phys. Rev.*, **23**, 655–660 (1924).
35. M. E. Mochel, C. J. Humphreys, J. A. Eades, J. M. Mochel, and A. M. Petford, Electron beam writing on a 20-Å scale in metal β -aluminas, *Appl. Phys. Lett.*, **42**, 392–394 (1983).
36. M. Isaacson and A. Murray, In situ vaporization of very low molecular weight resists using 1/2 nm diameter electron beams, *J. Vac. Sci. Technol.*, **19**, 1117–1120 (1981).
37. N. M. Ceglio, A. M. Hawryluk, and M. Schattenberg, X-ray phase lens design and fabrication, *J. Vac. Sci. Technol.*, **B1**, 1285–1288 (1983).
38. R. Day, J. Gross, R. Bartlett, and T. Barbee, Layered synthetic microstructures: Measurements and applications, *Nucl. Instrum. Methods*, **208**, 245–249 (1983).
39. B. L. Henke, Low energy x-ray spectroscopy with crystals and multilayers, in: *Low Energy X-Ray Diagnostics* (D. T. Attwood and B. L. Henke, eds.), AIP Conference Proceedings No. 75, pp. 85–96, American Institute of Physics, New York (1981).
40. P. Lee, Multilayer mirrors and beam splitters for soft x-rays, *Opt. Commun.*, **43**, 237–241 (1982).
41. P. Lee, R. J. Bartlett, and D. R. Kania, Soft x-ray optics using multilayer mirrors, *Opt. Eng.*, **24**, 197–201 (1985).
42. M. Born and E. Wolf, *Principles of Optics*, 5th ed., p. 43, Pergamon Press, Elmsford, N.Y. (1975).
43. A. Khandar and P. Dhez, Multilayer x-ray polarizers, *Applications of Thin-Film Multilayered Structures to Figured X-Ray Optics, Proc. SPIE* **563**, 158–163 (1985).

44. M. Elvis, Extra-solar astronomy with a 2.4 m normal incidence x-ray telescope at 0.1 arcsec resolution, *High Resolution X-Ray Optics, Proc. SPIE* **316**, 144–148 (1981).
45. P. Dhez, G. Jamelot, A. Carillon, P. Jaegle, P. Pardo, and D. Naccache, X-uv gain amplification studies in laser plasmas using normal incidence multilayer mirrors, in: *Second Topical Meeting on Laser Techniques in the Extreme Ultraviolet* (S. E. Harris and T. B. Lucatorto, eds.), AIP Conference Proceedings No. 119, pp. 199–206, American Institute of Physics, New York (1984).
46. J. Kirchner, Quantitative microanalysis with high resolution using soft x-rays—Possible applications, in: *X-Ray Microscopy* (G. Schmahl and D. Rudolph, eds.), Springer Series in Optical Sciences, Vol. 43, pp. 308–313, Springer, Berlin (1984).
47. J. Cazaux, Microanalysis and x-ray photoelectron spectroscopy: Principles and performance deductions, *Rev. Phys. Appl.*, **10**, 263–280 (1975).
48. D. Sayre, Review of image formation methods with the soft x-ray photon, in: *Ultrasoft X-Ray Microscopy: Its Application to Biological and Physical Sciences* (D. F. Parsons, ed.), Ann. N.Y. Acad. Sci. Vol. 342, pp. 387–391 (1980).
49. L. M. Cheng and A. G. Michette, Three dimensional imaging in scanning soft x-ray microscopy, *J. Phys. (Paris) C2*, **45**, 97–100 (1984).
50. M. R. Howells, Possibilities for x-ray holography using synchrotron radiation, in: *X-Ray Microscopy* (G. Schmahl and D. Rudolph, eds.), Springer Series in Optical Sciences, Vol. 43, pp. 318–335, Springer, Berlin (1984).
51. S. Aoki and S. Kikuta, X-ray holographic microscopy, *Jpn. J. Appl. Phys.*, **13**, 1385–1392 (1974).
52. S. Aoki, Y. Ichihara, and S. Kikuta, X-ray hologram obtained by using synchrotron radiation, *Jpn. J. Appl. Phys.*, **11**, 1857 (1972).
53. M. R. Howells, M. Iarocci, J. Kenney, J. Kirz, and H. Rarback, X-ray holographic microscopy experiments at the Brookhaven synchrotron light source, *Science with Soft X-Rays, Proc. SPIE* **447**, 193–203 (1984).
54. S. Aoki, K. Shinohara, A. Tanaka, Y. Iguchi, and M. Yanagihara, Recording x-ray holograms with x-ray resists, *Photon Factory Activity Report* (1984).
55. R. S. Longhurst, *Geometrical and Physical Optics*, 3rd ed., pp. 249–253, Longmans, London (1973).

Index

- Abbe criterion, 34
Abbe sine condition, 59, 62–64
Aberrated zone plate, 217
Aberrations, 31, 53, 109, 179–184, 276
Absorption, 1, 2, 3–4, 6, 29, 49, 96, 103–106, 255, 256, 285
Absorption coefficient, 3–4, 6, 7, 285
Absorption edge, 4, 6, 7, 255
Advanced X-ray astrophysics facility, 280–281
Advanced X-ray imaging observatory, 281
Airy pattern, 174–175, 186–187
Amplitude grating, 149, 150, 158
Amplitude reflection coefficient, 96
Anamorphotism, 59
Anomalous dispersion, 6
Aspheric grating, 139
Aspheric mirror, 57
Astigmatic image length, 136, 142
Astigmatism, 31, 54–55, 134, 136, 140, 142–143, 145, 183, 248
Astronomy, v, 1
 X-ray: *see* X-ray astronomy
Astrophysical sources of soft X rays, 298
Atomic scattering factor, 5, 7, 46, 97
AXAF, 280–281
AXIO, 281
- Bending block, 83, 84, 86
Bent mirror, 73
Bent mirror optics, 83–89
 beam bending equation, 84
 bending block, 83, 84, 86
 bending couple, 83
 bending of cylinders, 83, 86–89
- Bent mirror optics (*cont.*)
 bending of flats, 83–86
 bending mechanism, 83
 bending moment, 84
 bending of spheres, 83
 compliant systems, 86
 ellipsoidal figure, 88
 elliptical profile, 86
 focal length, 85
 magnification, 88
 noncompliant systems, 86
 parabolic profile, 84–86
 precision, 83
 stability, 83
 thin beam approximation, 83
 tolerances, 86
Blaze angle, 150
Blazed grating, 149–150, 155–157, 158
Bragg angle, 99, 106
Bragg condition, 95
Bragg diffraction, 1
Bragg law, 47
Bragg reflection, 44, 95, 96
 integrated reflectivity, 100, 101
 first-order, 99
 mth-order, 100
 peak reflectivity, 101
Bragg reflection peak, 96, 97, 107–108
Brewster angle, 294
- Cell biology, v, 298
Centrally obstructed zone plate, 188, 189–193, 237, 264, 265
 axial intensity distribution, 191

- Centrally obstructed zone plate (*cont.*)
background, 192
chromatic aberration, 191
contrast, 192, 193
improvement, 189
depth of focus, 191
diffraction, 189
efficiency, 190
energy in point spread function, 191–192
modulation transfer function, 192, 193
obstruction ratio, 189
point spread function, 189–190
resolution, 190, 193
resolving power, 191
shadow, 189
zone boundary radii, 189
- Channeling radiation, 18
- Charge-coupled devices, 27
- Chemical vapor deposition, 77, 80
- Chromatic aberration, 191
longitudinal, 176, 177
transverse, 176, 177
- Coherent scattering, 1, 2
- Coded aperture imaging, 224, 269
of laser fusion plasmas, 271–272
- Coma, 56, 57, 60, 134, 183
loss of resolution, 141
- Complex refractive index, 3, 28, 97
- Compound zone plate, 203
- Compton scattering, 1
- Computerized tomography
a priori information, 295
cone beam illumination, 295
fan beam illumination, 295
geometrical restriction, 295
- Composite zone plate, 189, 193–203
first/third-order, 193
axial intensity distribution, 196–197
background, 200
depth of focus, 198–199
diffraction patterns, 194–197
efficiency, 193, 200, 201
energy in point spread function, 199, 200
modulation transfer function, 200, 201
outermost zone width, 194
peak intensity, 195
point spread function, 195, 196
resolution, 193, 195, 196, 201
resolving power, 197–198
specification, 194
zone boundary radii, 193–194
- Composite zone plate (*cont.*)
higher-order, 193, 202–203
point spread function, 202
- Concave diffraction grating, 131–139
angular dispersion, 139
astigmatic image length, 136
astigmatism, 134, 136
coma, 134
Fermat's principle, 132
grating equation, 132
grating mounting, 132
grazing incidence, 132, 136
horizontal focus, 132
image width, 133, 136
least aberrated image, 132
modified Rayleigh criterion, 137, 138
optimum width, 137–138, 144
resolution, 134
resolving power, 137–138
Rowland circle, 133, 139
Rowland mounting, 133, 134–136, 137
spherical aberration, 137
stigmatic imaging, 133
vertical focus, 132
Wadsworth mounting, 133
- Conic sections, 57
- Conicoidal surfaces, 60, 68, 209
- Contact microradiography: *see* X-ray microscopy
- Contact microscopy: *see* X-ray microscopy
- Contamination lithography, 160, 161, 228–232
accuracy, 229–230
contamination cone, 228, 229
errors, 230, 231
minimum line width, 289
resolution, 231
zone plate efficiency, 232
zone plate testing, 232
- Critical angle, 31, 42, 51, 57, 71, 74, 96, 147, 150
- Crossed cylindrical mirrors, 58, 254
- Crystal monochromator, 252–253
liquid crystals, 252
wavelength range, 252
- Cylindrical mirror, 57
- Depth of focus, 29, 184–186, 191, 198–199, 240
- Detectors, 27, 28, 165, 243
photoconductive
charge-coupled devices, 27

- Detectors (*cont.*)
 photoconductive (*cont.*)
 scintillation counters, 27
 photoemissive
 ionization chamber, 27
 microchannel plate, 27, 278, 279
 proportional counter, 27, 261, 278, 279
 photographic
 film, 27
 resist, 27, 269
- Diamond turning, 73, 77–78
- Diffraction, 33
- Diffraction gratings, v, 127–145, 147–162, 282
 amplitude, 149, 150, 158
 aspheric, 139
 blazed, 149–150, 155–157, 158
 concave, 131–139
 design, 147
 diffuse scattering, 154
 efficiency, 127
 ellipsoidal, 139, 140, 142–145
 grass, 154
 grazing incidence, 136
 groove profiles, 127
 laminar, 149, 150–153, 158–159, 160
 linear, 129–130
 Lyman ghosts, 153–154
 manufacturing tolerances, 147
 reflection, 127, 147–154
 roughness, 154
 Rowland ghosts, 153–154
 satellites, 154
 spherical, 131–139
 toroidal, 139–141
 transmission, 127, 154–157, 159–163
- Diffraction-limited imaging, 34, 35, 71, 165
- Distortion, 184
- Einstein observatory, 277
 pulsars, 278
 supernova remnants, 278
- Electromagnetic radiation
 infrared, 1
 radio waves, 1
 reflection, 1
 refraction, 1
 visible, 1
- Electron-beam lithography, 160, 161, 225–228, 233, 292
- Electron-beam plasma, 23
- Electron drilling of metal β -aluminas, 291
 etching rate, 291
 free-standing zone plates, 291
 resolution, 291
- Electron impact microfocus source, 262
- Electron impact source
 target geometries, 284
 target materials, 284
- Electron microscopy, biological, 1
- Ellipsoidal grating, 139, 140, 142–145
 astigmatic image length, 142
 astigmatism, 142–143, 145
 optimum width, 143–145
 spherical aberration, 143
 stigmatic points, 142
- Ellipsoidal mirror, 58
- Elliptical zone plate, 203
 best focus, 205
 zone boundary radii, 204, 205
- Exosat observatory, 279
 supernova remnants, 279
- Extreme off-plane grating monochromator
 efficiency, 252
 resolution, 252
 wavelength range, 252
- Field curvature, 141, 183
- Field of view, 109
- Fermat's principle, 132, 179–180
- FLIPPER monochromator, 249, 250
 higher-order suppression, 249
 resolution, 249
 wavelength range, 249
- Fluorescence X rays, 256, 259
- Form factor, angle-dependent, 6
- Fourier transform hologram, 296
 coherence requirement, 297, 298
 flux, 298
 resolution, 297
- Freestanding zone plate, 203, 223, 239, 291
- Fresnel–Kirchoff diffraction integral, 170
- Fresnel coefficient, 105
- Fresnel diffraction, 268
- Fresnel equations, 30, 44, 45, 96
 reflection at a curved surface, 41
 reflection at a plane surface, 40
- Fresnel zone plate, 34, 165–166, 169; *see also* Zone plate
- Fresnel zones, 44–45, 50
- Fusion, v, 298

- Gabor in-line hologram
 flux, 297
 reconstruction, 296
 resolution, 295, 296, 298
- Gabor phase zone plate, 212
- Gabor zone plate, 205–207
 background, 207
 efficiency, 207
 focal point, 206
 sinusoidal amplitude transmittance, 205, 206
- Gas puff Z pinch plasma, 23
- Generalized blazed phase zone plate, 214, 215
- Glancing angle, 30, 31, 37, 51, 72, 74
- Grasshopper monochromator, 246
 efficiency, 247
 resolution, 247
 Rowland circle, 247
 wavelength range, 247
- Grating equation, 128, 129, 132, 170
- Grating mounting, 132
- Gratings, 3, 33; *see also* Diffraction gratings
- Grazing incidence angle, 37, 42, 44
- Grazing incidence diffraction grating, 136
- Grazing incidence optics, 37–94
 bent mirrors, 73
 bent mirrors optics: *see* Bent mirror optics
 critical angle, 71, 74
 diffraction-limited imaging, 71
 glancing angle, 37, 72, 74
 grazing incidence angle, 37
- Kirkpatrick–Baez systems, 58
- manufacture, 67
 blanks, 76, 77–79
 casting, 77
 chemical vapor deposition, 77, 80
 coating, 73, 76, 79–80
 diamond turning, 73, 77–78
 forging, 77
 fusing, 77
 grinding, 72, 73, 78–79
 hot isostatic pressing, 77
 lapping, 72, 73, 76, 80–81
 machining, 77
 polishing, 72, 73, 76, 80–81
 reaction bonding, 77
 replication, 73; *see also* Replica optics
 rolling, 77
 roughness, 77, 79
 sintering, 77
 spinning, 77
 surface figure, 76, 78
 vibrations, 78
- Grazing incidence optics (*cont.*)
 manufacturing tolerances, 58, 67
 misalignments, 67, 72
 roughness, 71, 74
 surface figure errors, 67–72
- materials evaluation
 homogeneity, 73, 74, 76
 machining, 75
 mechanical properties, 74, 75
 microstructure, 73, 74, 75–76
 polishability, 73
 stability, 73, 74
 surface damage, 75
 surface refurbishment, 75
 thermal properties, 75, 76
 vibration, 74–75
- metrology: *see* Metrology
 off-axis resolution, 65
 optical constants, 94
 ray-tracing, 65
 reflectivity, 74
 replica optics: *see* Replica optics
 resolution, 65, 70–71
 Snell's law, 37
 soft X-ray evaluation of surfaces, 93–94
 total external reflection, 37
 Wolter systems, 58
- Grazing incidence reflection, 32, 35, 46
 aberrations, 31
 astigmatism, 31
 reduction of aberrations, 58
- Grazing incidence reflectivity, 43
- Grazing incidence X-ray microscope, 45, 50
 scanning, 262
- Grazing incidence X-ray telescope, 73, 274–277
- Grinding, 72, 73, 78–79
- HEAO-2: *see* Einstein observatory
- High Energy Astronomy Observatory: *see* Einstein observatory
- Hildenbrand–Montel mirror, 59
- Hologram, 236, 237
- Holographic zone plates, 234
- Holography, 234; *see also* X-ray holography
- Huygens–Fresnel principle, 165
- Hyperbolic zone plate, 203
- Image formation, 1
- Image processing, 258
- Imaging X-ray microscopy: *see* X-ray microscopy

- Imploding wire plasma, 23
Incoherent scattering, 1, 2
Ion beam plasma, 23
Ionization chamber, 27
- Kirkpatrick–Baez systems, 58–60
 Abbe sine condition, 59
 anamorphotism, 59
 coma, 59
 cylindrical mirrors, 58
 magnification, 59
 spherical mirrors, 59
X-ray microscope, 270–271
 acceptance solid angle, 271
 magnification, 271
 resolution, 271
X-ray telescope, 274, 275
Kramers–Kronig relation, 285
- LAMAR, 281
- Laminar grating, 149, 150, 158–159, 160
 efficiency, 151–153
 land-to-groove ratio, 153
 polarization, 151
 primary maximum, 151, 152, 153
 reflection coefficient, 152
 shadowing, 152–153
- Lapping, 72, 73, 76, 80–81
- Large area modular array of reflectors, 281
- Larmor distribution, 8
- Laser fusion plasma
 characterization, 269
 coded apertures, 269, 271–272
 imaging, 269–274
Kirkpatrick–Baez X-ray microscope, 270–271
multilayer mirrors, 269
multilayer mirror spectrometer, 273, 292–293
soft X-ray emission, 269
transmission gratings, 269
transmission grating spectrometer, 272–273
Wolter X-ray microscope, 269–270
zone plate coded aperture imaging, 271–272
- Laser plasma sources: *see* Plasma sources,
 pulsed laser
- Leith–Upatnieks hologram, 296
 coherence requirements, 296
- Linear absorption coefficient, 3, 4
- Linear attenuation coefficient, 2
- Linear diffraction grating
 angular dispersion, 130
- Linear diffraction grating (*cont.*)
 diffraction pattern, 129
 main maxima, 129
 grating equation, 129
 reflection, 127
 resolving power, 129–130
 Rayleigh criterion, 129
 transmission, 127
- Linear polarizer, 294
- Linear zone plate, 203
- Linearly blazed transmission grating, 155
 efficiency, 156, 157
 optimum aperture size, 155
 optimum blaze slope, 155
 optimum thickness, 156
- Lyman ghosts, 153–154
- Mass absorption coefficient, 3–4, 6
- Materials evaluation: *see* Grazing incidence
 optics, materials evaluation; Multilayer
 mirrors, materials evaluation
- Materials science, v
- Max Planck Institut X-ray telescopes, 278–279
- Merton nut, 158
- Metrology, 89–93, 276
 axial profile, 73, 89, 90–91
 circularity, 73, 89, 90
 diameter, 89, 90
 fringes of equal chromatic order, 93
 interferometry, 89, 91, 93
 Linnik, 93
 multiple pass, 93
 normal incidence, 93
 sensitivity, 93
 Twyman–Green, 93
macrotopography, 89, 90–91
mechanical probes, 89–90, 92
- microtopography, 89, 91–93
- Nanosurf, 92
- Nomarski microscope, 92
- optical constants, 94
- optical heterodyne profilometry, 92
- optical probes, 89–90, 91, 92
- profile measuring machine, 90–91
- soft X-ray evaluation of surfaces, 93–94
- stereo electron microscopy, 93
- surface damage, 91
- surface figure, 89
- surface profile, 92
- surface roughness, 73, 89
- Talystep, 91–92
- thin film microstructure, 92–93

- Metrology (*cont.*)
 tolerances, 89
- Microchannel plate, 27, 278, 279
- Microscopy, X-ray: *see* X-ray microscopy
- Mirror manufacture: *see* Grazing incidence optics, manufacture; Multilayer mirrors, manufacture
- Mirrors, 3
- Modified zone plate, 34, 188
 centrally obstructed, 188, 189–193
 composite, 189, 193–203
 compound, 203
 elliptical, 203
 freestanding, 203
 hyperbolic, 203
 linear, 203
 missing-zone, 203
 spoked, 203
 square, 203
- Modulation transfer function, 187, 188, 192, 193, 200–201
- Monochromators, 33, 127, 177–178, 243, 245–253
 constant deviation, 245
 crystal, 252–253
 extreme off-plane plane grating, 251–252
 FLIPPER, 249, 250
 grasshopper, 246–247
 higher-order spectral contamination, 245
 multilayer mirrors, 253
 overlapping range plane grating, 245–246
 plane grating, 249–252
 spherical grating, 246
 SX-700, 251
 toroidal grating, 247–249, 260
 transmission grating, 252
- Moseley diagram, 21
- MTF: *see* Modulation transfer function
- Multilayer mirrors, 32, 33, 35, 95–126, 269, 273–274
 aberrations, 109
 absorption, 96
 absorption losses, 108
 absorption-free, 97–103
 advances in, 288
 in situ monitoring, 288
 laser deposition, 288–289
 amplitude reflection coefficient, 96
 amplitude reflectivity, 108
 aperiodic design, 108
 atomic scattering factors, 97
- Multilayer mirrors (*cont.*)
 bandpass, 108
 Bragg angle, 99
 Bragg condition, 95
 Bragg reflection, 95, 96
 first-order, 99
 integrated reflectivity, 100, 101
 mth-order, 100
 peak reflectivity, 101
 Bragg reflection peaks, 96, 97, 107–108
 complex refractive index, 97
 conicoidal surfaces, 109
 correlated roughness, 108
 critical angle, 96
 diffusion between layers, 99
 dynamical theory, 97–106
 Bragg angle, 106
 contaminant layers, 104
 Fresnel coefficient, 105
 optical constants, 105
 reflectivity, 105–106
 thin multilayer, 106
 effective number of layer pairs, 103
 efficiency, 109
 enhancement of reflectivity, 95
 field of view, 109
 focusing, 109
 Fresnel equations, 96
 kinematical theory, 97
 layer materials, 106
 compatibility, 108
 layer thickness, 106
 layer thickness variations, 97
 linear polarizer, 294
 manufacture, 111, 120–126
 control of layer thickness, 121, 122–123, 124
 deposition rate, 120, 121, 122
 diode sources, 120
 evaluation, 122
 evaporation, 122–123
 laser evaporation, 125–126
 laser plasma diagnostics, 292–293
 laser sputtering, 125
 magnetron sources, 120–121
 resolving power, 293
 ring gap plasmatron, 121
 sputtering, 120–122
 sputtering rate, 121, 125–126
 stability, 124
 substrates, 120

- Multilayer mirrors (*cont.*)
manufacture (*cont.*)
thin film technology, 120
triode sources, 120
vapor deposition, 120
wavelength range, 293
manufacturing tolerances, 111–117
cumulative thickness errors, 117
in situ corrections, 116
interfacial roughness, 111
figure errors, 111
layer thickness errors, 111–117
peak reflectivity, 115
peak width, 115
reflectivity, 111, 115, 116
reflectivity measurement, 116
resolving power, 115
materials evaluation, 118–119
optical constants, 118
reflectivity, 118
roughness, 118–119
stability, 118
monochromators, 253
laterally graded, 253
stepped, 253
wavelength range, 253
mosaicity, 97
new developments, 285
optical constant measurement, 287
optical constants, 122, 124
optical multilayer theory, 97
peak widths, 122
radiation damage, 120
reflectivity, 107–108, 123–124, 126
refractive index decrement, 100
resolution, 109
resolving power, 102–103, 108
rough interfaces, 108
roughness, 122, 123, 124
scattering amplitude density, 98
optical constants, 108
sinusoidal variation, 108
Schwarzchild optics, 109
structure, 96
spectrometer, 273, 292–293
 resolving power, 293
 temporal resolution, 274, 293
 wavelength, 293
thick multilayer, 101, 102
thin multilayer, 97, 101–103
X-ray beam splitter, 293
- Multilayer mirrors (*cont.*)
X-ray laser, cavity mirrors, 294
X-ray microscope, 109, 258, 259, 262
X-ray telescope, 109, 294
uncorrelated roughness, 108
- Nanosurf, 92
Negative zone plate, 166, 172
Nomarski microscope, 92
Normal incidence reflection, 31; *see also* Multilayer mirrors
Normal incidence X-ray microscope: *see* X-ray microscopy
Nonlinear imaging, 265, 267, 268
- Obliquity, 56, 57
Optical constants, 94, 105, 118, 122, 124; *see also* Absorption coefficient; Refractive index decrement
measurement
 absorption, 285
 absorption coefficient, 285
 bulk reflectance, 285
 comparison of methods, 286
 Kramers–Kronig relation, 285
 with multilayer mirrors, 287
 refractive index decrement, 285
 with transmission gratings, 285, 286, 287
 with zone plates, 287–288
Optical heterodyne profilometry, 92
Optical multilayer theory, 97
Optical transfer function, 187
Optimized profile zone plates, 213
 efficiency, 214, 215
OTF, 187
Overlapping range plane grating monochromator, 245
 efficiency, 246
 resolution, 246
 selective reflection, 245
 wavelength range, 246
- Parabolic mirror, 58
Penumbral blurring, 268
Phase grating, 150
Phase-modulating zone plate, 207, 258, 285,
 288
 with absorption, 208
 efficiency, 209–212, 292
 optimum phase shift, 210, 211, 212
 phase shift, 209

- Phase-modulating zone plate (*cont.*)
 with absorption (*cont.*)
 primary focus, 209
 signal-to-noise ratio, 211
 efficiency, 207
 Gabor, 212
 Rayleigh–Wood, 207
 efficiency, 208
 focal points, 208
 Photoelectron microscopy, 269
 scanning, 295
 resolution, 295
 Plane grating monochromators, 249–252
 order sorting, 251
 resolution, 250, 251
 wavelength range, 250, 251
 Plasma sources, 17, 23–26
 bremsstrahlung, 23
 continuum radiation, 23
 electron beam, 23
 gas puff Z pinch, 23
 imploding wire, 23
 light ion beam, 23
 line radiation, 23
 pulsed laser, 3, 23–25, 256–257
 angular distribution, 25
 bremsstrahlung, 24, 25
 continuous spectrum, 24, 25
 conversion efficiency, 23, 24, 25
 developments in laser technology, 284
 high-power, 23, 284
 line spectrum, 23, 24, 25
 low-power, 23, 284
 plasma equilibrium, 24
 soft X-ray production, 284
 spectral distribution, 23, 25
 tokamak, 23
 vacuum spark, 23
 Polishing, 72, 73, 76, 80–81, 83
 Positive zone plate, 166, 172
 Projection microscopy: *see* X-ray microscopy
 Proportional counter, 27, 261, 278, 279

 Radiation damage: *see* X-ray microscopy,
 radiation damage
 Ray tracing, 65, 244, 276
 Rayleigh criterion, 34, 35, 129, 148, 176,
 186
 modified, 137, 138
 Rayleigh scattering, 1
 Rayleigh $\lambda/4$ rule, 218

 Rayleigh–Wood phase reversal zone plate, 207
 efficiency, 208
 focal points, 208
 Reflection coefficient, 46, 48, 51
 amplitude, 96
 Reflection grating, 127, 147–154
 amplitude grating, 149, 150, 158
 blaze angle, 15
 blazed grating, 149–150, 158
 critical angle, 147, 150
 dispersion, 147
 efficiency, 148, 149, 150–151, 158, 159
 groove depth, 150
 groove profiles, 149
 groove spacing, 147
 laminar grating, 149, 150–153, 158–159,
 160
 manufacture
 interference methods, 149, 159
 etching, 158–159
 lithography, 149
 Merton nut, 158
 quality, 159
 replication, 149
 ruling, 149, 157
 ruling engine, 158
 ruling errors, 157
 minimum reflected wavelength, 148
 optimum grating width, 157
 phase grating, 150
 pitch upper limit, 150
 Rayleigh criterion, 148
 reflectivity, 148
 roughness, 148, 150
 shadowing, 149, 150
 Reflectivity, 74, 115, 118, 123–124
 Refractive index, 3, 29
 complex, 3, 28, 97
 decrement, 51, 57, 100, 285
 Replica optics, 81–83
 coating, 81, 82
 degradation, 83
 masters, 81
 polishing, 83
 quality, 82, 83
 scatter, 83
 stability, 82
 surface figure, 82
 for telescopes, 82
 Resolution, 70–71, 109, 134, 141, 186–187,
 190, 193, 201

- Resolution (*cont.*)
off-axis, 65
- Resolving power, 34, 57, 102–103, 108, 115, 129–130, 137–138, 176–178, 191, 197–198, 293
- Rosat, 279
all-sky survey, 280
wavelength range, 280
- Rotating anode source, 22
- Roughness, 44, 50–53, 71, 74, 78, 79, 89, 108, 118–119, 122, 123, 124, 148, 150, 154
interfacial, 111
- Rowland circle, 133, 139, 247, 282
- Rowland ghosts, 153–154, 158
- Rowland grating, 133
- Rowland mounting, 134–136, 137, 246
astigmatic image length, 136
astigmatism, 134, 136
coma, 134
grazing incidence, 136
image width, 136
resolution, 134
- Scanning photoelectron microscopy, 295
resolution, 295
- Scanning transmission electron microscope, 226, 227, 228, 230
- Scanning X-ray microscope: *see* X-ray microscopy
- Schwarzchild objective, 109, 259–260, 262
- Scintillation counter, 27
- Sinusoidal grating, 154
efficiency, 154
- Skylab telescopes
ATM S-054, 277
ATM S-056, 277
coronal holes, 277
hot coronal plasma, 277
limb brightening, 277
resolution, 277
solar flares, 277
solar images, 277
- Small-angle X-ray scattering, 254
with crossed cylindrical mirrors, 254
with toroidal mirrors, 254
- Snell's law, 37
- Soft X-ray attenuation
absorption, 1, 2, 3–4, 6, 29, 49
absorption coefficient, 7
linear, 3, 4
- Soft X-ray attenuation (*cont.*)
absorption coefficient (*cont.*)
mass, 3–4, 6
Bragg diffraction, 1
coherent scattering, 1, 2
Compton scattering, 1
elastic scattering, 1
incoherent scattering, 1, 2
inelastic scattering, 1
linear attenuation coefficient, 2, 3
photoionization cross section, 6
Rayleigh scattering, 1
scattering, 4
Thomson scattering, 1, 4, 6
- Soft X-ray energy range, 2
- Soft X-ray imaging, v
- Soft X-ray lens, 29–30
- Soft X-ray microscopy: *see* X-ray microscopy
- Soft X-ray optics, v, vi, 3, 28, 243; *see also*
Grazing incidence optics; Multilayer
mirrors; Zone plates
- aberrations, 35
- accuracy, 34
- aperture, 30
- diffraction-limited imaging, 34, 35
- efficiency, 30
- manufacturing inaccuracies, 35
- new developments, 285, 288–292
- numerical aperture, 34–35
- resolution
Abbe criterion, 34
Rayleigh criterion, 34, 35
resolving power, 34
- Soft X-ray physics, vi
- Soft X-ray refractive index: *see* Refractive
index
- Soft X-ray sources, v, 243; *see also* Plasma
sources; Solid target sources; Synchro-
tron radiation
comparison, 26, 27
continuum spectra, 7
line spectra, 7
new developments, 283–285
- Solid target sources, 17, 18–23
bremsstrahlung, 18
continuum spectrum
angular distribution, 18–19, 22
conversion efficiency, 20
cut-off, 19
polarization, 19
spectral distribution, 20

- Solid target sources (*cont.*)
 line spectrum, 18
 conversion efficiency, 22
 intensity, 22
 ionization energies, 21
 K series, 21
 L series, 21
 Moseley diagram, 21
 reabsorption, 22, 23
 rotating anode, 22
 target materials, 21
- Soret zone plate, 165, 169, 172
- Spectral lines, 4
 labeling, 4
- Spectrometer
 X-ray, 127, 272–273
- Spectroscopy: *see* X-ray spectroscopy
- Spherical aberration, 55–56, 137, 143, 182–183, 233–234
- Spherical diffraction grating: *see* Concave diffraction grating
- Spherical grating monochromator, 246
- Spherical mirrors, 53–57, 59
 aberrations, 53
 reduction of, 57
 astigmatism, 54–55
 collecting power, 57
 coma, 56–57
 magnification, 56
 meridian focal length, 55
 meridian focal line, 55
 obliquity, 56, 57
 resolving power, 57
 sagittal focal length, 55
 sagittal focal line, 55
 spherical aberration, 55–56
- Spoked zone plate, 203
 number of spokes, 203
 point spread function, 203
 width of spokes, 203
- Sputtered zone plates, 262, 289, 290
 resolution, 291
- Square zone plate, 203
- Strehl limit, 218, 221, 222
- Strehl ratio, 217–218, 219, 221, 222, 223
- Structure factor, 46
- Surface roughness: *see* Roughness
- SX-700 plane grating monochromator, 251
 wavelength range, 251
- Synchrotron radiation, v, 3, 7, 8–17, 243–253
 Advanced Light Source, 15, 284
- Synchrotron radiation (*cont.*)
 angular divergence, 9–10, 12
 coherence, 15
 critical frequency, 11, 12
 critical wavelength, 11, 12–13, 16
 European Synchrotron Radiation Facility, 14, 15, 283–284
 frequency distribution, 10–11
 polarization, 11
 radiated power, 10
 sources, 12–16, 73
 beam lines, 15, 86, 243–244
 divergence of beam, 86
 flux, 15
 monochromators, 243
 source emittance, 243
 temporal structure, 13
 undulators, 16–17, 18, 244
 wigglers, 16
 spectral distribution, 12
- Talystep, 91–92
- Telescope: *see* X-ray telescope
- Thomson scattering, 1, 4–5
- Three-dimensional imaging, 262, 295
a priori information, 295
 computerized tomography, 295
 cone-beam illumination, 295
 fan-beam illumination, 295
 X-ray holography, 295–298
- Tokamak, 23
- Tomographic imaging, 272
- Toric aberration, 141
- Toroidal mirror, 57, 254
- Toroidal grating, 139
 aperture, 141
 astigmatism, 140
 coma, 141
 loss of resolution, 141
 field curvature, 141
 optimum width, 142
 quasi-stigmatic wavelength range, 140
 resolution, 141
 stigmatic image, 140
 stigmatic points, 141
 toric aberration, 141
- Toroidal grating monochromator, 247, 260
 astigmatism, 248
 dispersion, 248
 efficiency, 249
 mechanical instability, 248

- Toroidal grating monochromator (*cont.*)
resolution, 248, 249
short wavelength limit, 248
thermal instability, 248
wavelength range, 248, 249
- Total external reflection, 31, 37, 38, 40, 42
- Transfer function, 266–267, 268
- Transition radiation, 18
- Transmission coefficient, 46, 48
- Transmission grating, 127, 269, 285–287
dispersion, 154
efficiency, 154, 155
free-standing, 163
linearly blazed, 155–157
manufacture, 159
coating, 163
contamination lithography, 160, 161
electron-beam lithography, 160, 161
holographic methods, 162
interference methods, 162
replication, 163
X-ray lithography, 163
- pitch, 154
- rectangular profile, 154–155
- Transmission grating monochromator, 252
- Transmission grating spectrometer, 272
spectral resolution, 273
temporal resolution, 273
- Undulator, 16, 262, 283, 284
beam line, 244
helical, 17
planar, 17
spectral distribution, 17, 18
- Vacuum spark plasma, 23
- Van Cittert–Zernicke theorem, 297
- Wadsworth mounting, 133
- Water window, 255, 258
- Wiggler, 16, 283, 284
multipole, 16
single-bump, 16
three-pole, 16
- Wollaston prism, 92
- Wolter optics, 58
Abbe sine condition, 62, 63
conicoidal surfaces, 60
type I, 61, 262, 274, 275, 276
type II, 61, 274
type III, 61
- Wolter X-ray microscope: *see* X-ray microscopy
- Wolter–Schwarzchild optics, 63, 274, 276
Abbe sine condition, 63, 64
- X-ray astronomy, 224, 274–282
Advanced X-ray Astrophysics Facility, 280–281
Advanced X-ray Imaging Observatory, 281
AXAF, 280–281
AXIO, 281
balloons, 274
black holes, 274
Einstein observatory, 277–278
Exosat, 279
HEAO-2, 277–278
High Energy Astronomy Observatory, 277–278
LAMAR, 281
Large Area Modular Array of Reflectors, 281
Max Planck Institut, 279
pulsars, 274
quasars, 274
rockets, 274
Rosat, 279–280
satellites, 274
Skylab, 277
solar imaging, 274
telescope: *see* X-ray telescope
- XMM, 281
- X-Ray Multi-mirror Mission, 281
- zone plate, 274
zone plate imaging, 281–282
- X-ray beam splitter, 293
- X-ray holography, 295–298
Fourier transform hologram, 296–297, 298
Gabor in-line hologram, 295, 296, 297–298
Leith–Upatneiks hologram, 296
- X-ray laser
amplification, 284
for holography, 297
multilayer cavity mirror, 294
- X-ray lithography, 163, 224, 225, 239, 243, 292
- X-ray microscopy, vi, 61, 109, 127, 224, 234, 236, 237, 238, 254–269
absorption, 256
absorption edges, 255
comparison with electron microscopy, 254–255

- X-ray microscopy (*cont.*)
 comparison of image formation in imaging and scanning, 263–268
 axial obstruction, 263
 background, 263
 centrally obstructed zone plate, 264–265
 components of image, 263–264
 detector arrangements, 266–267
 image radius, 264
 nonlinear imaging, 265, 267, 268
 objective zone plate, 266
 obstructed detector, 265
 obstructed source, 265
 optical arrangements, 263
 pinhole, 263
 pinhole radius, 264, 265
 sampled image, 264
 source arrangements, 267
 transfer function, 266–268
 working distance, 265
 zone plate microscope, 263
 comparison with optical microscopy, 254
 contact microradiography, 243, 256–257,
 269
 contact microscopy, 243, 256–257
 resolution, 269
 X-ray resist, 269
 contrast enhancement, 255
 contrast mechanism, 255
 detection of fluorescence X rays, 256, 259
 detection of photoelectrons, 256
 detection of transmitted X rays, 256, 259
 detector, resolution limit, 257
 elemental analysis, 255
 the Göttingen scanning microscope
 condenser zone plate, 261
 objective zone plate, 261
 resolution, 261–262
 scanning stage, 262
 grazing incidence microscope, 45, 50
 acceptance solid angle, 271
 efficiency, 270
 field of view, 270
 Kirkpatrick–Baez optics, 270, 271
 magnification, 270–271
 spatial resolution, 258, 269, 270, 271
 temporal resolution, 270
 Wolter optics, 269–270
 grazing incidence scanning microscope
 electron impact microfocus source, 262
 scanning stage, 262
- X-ray microscopy (*cont.*)
 grazing incidence (*cont.*)
 Wolter type I optics, 262
 hydrated specimens, 256
 image formation, 255
 imaging of laser fusion plasmas, 257, 269–274
 imaging microscopy, 257, 263–271
 condenser zone plate, 257
 efficiency, 257
 grazing incidence, 258
 objective zone plate, 257
 radiation damage, 257
 resolution, 258
 zone plate monochromator, 257
 the King's College scanning microscope
 objective zone plate, 262
 resolution, 262
 scanning stage, 262
 undulator source, 262
 vertical beam, 262
 three-dimensional imaging, 262
 laser plasma sources, 256–257
 multilayer mirrors, 258
 normal incidence scanning microscope
 efficiency, 262
 multilayer mirrors, 262
 reflectivity, 262
 Schwarzchild optics, 262–263
 optical system, resolution limit, 256
 phase-modulating zone plates, 258
 photoabsorption, 255
 photoelectron microscopy, 269
 projection microscopy, 268–269
 Fresnel diffraction, 268
 magnification, 268
 penumbral blurring, 268
 resolution, 268
 radiation damage, 256
 avoidance of resolution limit, 256
 comparison with electron microscopy, 256
 damage mechanism, 256
 resolution limit, 256–257
 scanning microscopy, 248
 detector, 258
 the Göttingen microscope, 261–262
 grazing incidence microscope, 262
 image processing, 258
 the King's College microscope, 262
 multilayer optics, 259–260
 normal incidence microscope, 262–263

- X-ray microscopy (*cont.*)
scanning microscopy (*cont.*)
picture element, 258
pinhole microscope, 259
pixel, 258
scanning stage, 259
schematic, 258
Schwarzchild objective, 259–260
the Stony Brook microscope, 260–261
reduction of aberrations, 258
resolution, 258–259
thick specimens, 256
Wolter optics, 259–260
zone plate optics, 259
scattering, 255
the Stony Brook scanning microscope
beam line, 260
calcium distribution in bone, 261
flow proportional counter, 261
imaging times, 261
objective zone plate, 260–261
resolution, 261
scanning stage, 261
specimens, 261
toroidal grating monochromator, 260
water window, 255, 258
wavelength resolution limit, 256
- X-ray monochromator, 127
- X-ray reflection, 44–50
from atomic surface layers, 44–50
surface roughness, 44, 50–53
- X-ray resist, 27
- X-ray spectrometer, 127
- X-ray spectroscopy
in astronomy, 282
chemical shift analysis, 282
elemental analysis, 282
Rowland circle, 282
wavelength resolution, 282
- X-ray telescope, 61, 73, 109, 127
collecting power, 274
grazing incidence, 274–277
aberrations, 276
angular resolution, 275
effective collecting area, 276–277
field of view, 275
geometrical collecting area, 277
Kirkpatrick–Baez optics, 274, 275
lobster-eye telescope, 274, 276
metrology, 276
nested mirrors, 274
- X-ray telescope (*cont.*)
grazing incidence (*cont.*)
ray-tracing, 276
single reflection, 274
two-dimensional focusing collimator, 274, 275, 276
Wolter type I optics, 274–276
Wolter type II optics, 274
Wolter–Schwarzchild optics, 274, 276
multilayer mirror, 294
- X-ray transitions, 5
selection rules, 5
- Zone plate, 35, 127, 165–241, 285, 289
astigmatism, 183
in astronomy, 274, 281–282
central zone radius, 168
centrally obstructed, 188–193, 265
chromatic aberration, 33
longitudinal, 176, 177
transverse, 176, 177
coded aperture imaging, 271
collection solid angle, 272
outermost zone width, 271
resolution, 272
three-dimensional source distribution, 272
tomographic imaging, 272
two-dimensional source distribution, 272
- coma, 183
- composite, 193–203
- compound, 203
- construction, 166
- depth of focus, 184–186
- diffraction orders, 169
- diffraction pattern, 170, 172
Airy pattern, 174–175
axial intensity distribution, 174
background, 175–176
higher-order real foci, 173
maximum intensity, 173
primary focus, 173
point spread function, 171, 187–188
radial intensity distribution, 173, 175
virtual foci, 173
width, 173
- diffraction-limited imaging, 165
- distortion, 184
- efficiency, 33, 178–179, 223–224, 232
- elliptical, 203, 204–205
- field curvature, 183
- freestanding, 203, 224, 291

- Zone plate (*cont.*)
 Fresnel, 34, 165–166, 169
 focal length, 33, 168
 focal positions, 172
 Gabor, 205–206
 Gabor phase-modulating, 212
 generalized blazed phase, 214
 geometrical aberrations, 179–181
 Fermat's principle, 179, 180
 grating equation, 170
 holographic, 234
 hyperbolic, 203
 imaging, vi, 168
 linear, 203
 magnification, 168
 manufacture, 217
 contamination lithography, 228–232, 289
 lithographic process, 219, 222
 holography, 234
 interference methods, 224, 233–239
 electron-beam lithography, 224, 225–228, 233, 292
 electron drilling of metal β -aluminas, 291
 electron-optical reduction, 239
 one-to-one copying, 239
 photographic process, 219
 sputtering, 262, 289–291
 supporting substrate, 217, 223
 manufacturing tolerances, 217–223
 aberrated zone plate, 217
 boundary errors, 218–222
 boundary placement accuracy, 219
 boundary shifts, 218
 discontinuous zones, 221–222
 distorted boundaries, 217
 efficiencies, 220–221
 elliptical zones, 222, 223
 even-order foci, 220, 221
 focal lengths, 218
 mispositioned boundaries, 217
 outermost zone width, 218
 Rayleigh $\lambda/4$ rule, 218
 refocusing, 218
 Strehl limit, 218, 221, 222
 Strehl ratio, 217–218, 219, 221, 222, 223
 Zone plate (*cont.*)
 microscope, 259–268
 missing zones, 203
 modified, 34
 modulation transfer function, 187–188
 as a monochromator, 177, 178, 253, 257
 resolution, 253
 negative, 166, 172
 negative foci, 169
 new uses, 287–288
 optical transfer function, 187
 optimized zone profiles, 213–215
 phase-modulating, 207–212, 258, 285, 292
 positive, 166, 172
 positive foci, 169
 resolution
 Airy pattern, 186–187
 extended object, 186–188
 outermost zone width, 186
 point source, 186
 Rayleigh criterion, 186
 resolving power, 176–177
 in combination with a pinhole, 178
 Rayleigh criterion, 176
 Soret, 165, 169, 172
 spherical aberration, 182–183
 blur circle, 182
 optimum number of zones, 183
 optimum radius, 182
 spoked, 203–204
 square, 203
 stability
 contamination, 240
 depth of focus, 240
 focal length variation, 240
 loss of intensity, 240
 thermal expansion, 240–241
 testing, 232
 thin lens approximation, 168, 181
 zone areas, 169
 zone boundaries, 33
 radii, 167–168
 zone definition, 166
 zone thickness, 223
 zone widths, 169–170